Behaviour and Design of Optimised Cold-Formed Steel Structures

THE UNIVERSITY OF SHEFFIELD

By:

Seyed Mohammad Mojtabaei

A thesis submitted in partial fulfilment for the degree of

Doctor of Philosophy

in the

Faculty of Engineering

Department of Civil and Structural Engineering

September 2019

T O

My Father and Mother

&

To my love Fariba

for their unconditional love and support

for their sacrifices and pray

ABSTRACT

Cold-formed steel (CFS) structural members are fabricated at room temperature from thin gauge steel sheets. They offer a higher strength-to-weight ratio than conventional hot-rolled steel products and have lower embodied carbon. Moreover, they are light-weight and easier to handle, transport and install. Due to their suitability of prefabrication into panels and standardized systems, they are suitable for modular systems and offer unrivalled construction speeds. However, literature study exposes a need for more efficient CFS structural components, particularly on bolted-moment connections, to improve performance, minimize material use and increase their environmental and economic benefits. This study aims to develop more efficient CFS structures at three different levels (i.e. element, connection, and frame), and to investigate the behaviour and design of CFS bolted connections subjected to both static and seismic loads.

At the element level, stiffness and buckling strength of CFS elements at Serviceability Limit State (SLS) and Ultimate Limit State (ULS), determined in accordance with the Eurocode 3 effective width method, were first optimised, respectively, and the efficiency of the optimum results were assessed using experimentally validated Finite Element (FE) models. CFS elements were then optimised based on their post-buckling behaviour by establishing a link between an optimisation algorithm and Python script in ABAQUS FE analysis. The optimisation process was carried out using either Particle Swarm Optimisation (PSO) algorithm, Genetic Algorithm (GA), or Big Bang-Big Crunch optimisation (BB-BC). The total coil width of the steel plate and its thickness were kept constant during the optimisation procedure to use the same amount of material in all cross-sections. The results demonstrated that noticeable improvements were achieved in stiffness, buckling strength and post-buckling behaviour of CFS element.

At the connection level, the behaviour of various CFS bolted connections under both monotonic and cyclic loading conditions was investigated using experimentally validated FE models. Extensive parametric studies were also conducted using the validated FE models by considering a wide range of design variables in order to eventually propose general design equations for the capacity of CFS bolted connections and identify the most efficient design solutions which considerably improve their seismic performance. In addition, the seismic performance of CFS bolted moment connections was further improved using optimised CFS beam elements with enhanced non-linear post-buckling behaviour. PSO algorithm was innovatively linked to Python script in ABAQUS FE analysis to optimise CFS bolted connections with respect to their energy dissipation capacity and ductility.

Finally, the efficiency of the optimised elements was then assessed at the frame level by incorporating them into CFS structural systems. It was shown that the proposed optimum design methodology at the element and connection levels leads to more resilient CFS moment-resisting portal frames with minimum structural weight.

RESEARCH CONTRIBUTION

Extensive analytical studies were carried out on behaviour and design of optimum cold-formed steel structural components such as elements, connections and frame. As a result of the work presented here and other collaborative projects, the following journal and conference papers were either published, submitted, or prepared for publication:

Journal Papers

Published

J1. S.M. Mojtabaei, M.Z. Kabir, I. Hajirasouliha, M. Kargar. (2018). "Analytical and experimental study on the seismic performance of cold-formed steel frames". *Journal of Constructional Steel Research*, 143, 18-31.

J2. J. Ye, J. Becque, I. Hajirasouliha, S.M. Mojtabaei, J.B.P. Lim. (2018). "Development of optimum cold-formed steel sections for maximum energy dissipation in uniaxial bending" *Engineering Structures*, 161, 55-67.

J3. J. Ye, S.M. Mojtabaei, I. Hajirasouliha. (2018). "Local-flexural interactive buckling of standard and optimised cold-formed steel columns". *Journal of Constructional Steel Research*, 144, 106-118.

J4. J. Ye, S.M. Mojtabaei, I. Hajirasouliha, Paul Shepherd, Kypros Pilakoutas. (2018). "Strength and Deflection Behaviour of Cold-Formed Steel Back-to-Back Channels". *Engineering Structures*, 181, 101-114.

J5. J. Ye, S.M. Mojtabaei, I. Hajirasouliha, K. Pilakoutas. (2019). "Efficient design of cold-formed steel bolted-moment connections for earthquake resistant frames". *Thin-Walled Structures*, 59, 49-61.

J6. J. Ye, S.M. Mojtabaei, I. Hajirasouliha. (2019). "Seismic performance of cold-formed steel bolted moment connections with bolting friction-slip mechanism", *Journal of Constructional Steel Research*, 27, 86-100.

J7. S.M. Mojtabaei, J. Ye, I. Hajirasouliha. (2019). "Development of optimum cold-formed steel beams for serviceability and ultimate limit states using Big Bang-Big Crunch optimisation". *Engineering Structures*, 106, 76-89.

J8. D.T. Phan, S.M. Mojtabaei, I. Hajirasouliha, J. Ye, J.B.P Lim. (2019). "Coupled element and structural level optimisation framework for cold-formed steel frames". *Journal of Constructional Steel Research*, 44, 79-91.

J9. S.M. Mojtabaei, I. Hajirasouliha, J. Becque. (2020). "Local buckling in cold-formed steel moment-resisting bolted connections: behaviour, capacity and design". *Journal of Structural Engineering (ASCE), (In press).*

Submitted

J10. S.M. Mojtabaei, I. Hajirasouliha, J. Becque, J. Ye. "Development of cold-formed steel bolted-moment connections for maximum ductility and energy dissipation in seismic applications". *Submitted to Engineering Structures.*

J11. D.T. Phan, S.M. Mojtabaei, I. Hajirasouliha, J.B.P Lim. "Design and optimisation of cold-formed steel bolted moment connections considering effect of bimoment". *Journal of Structural Engineering (ASCE).*

Ready for Submission

J12. S.M. Mojtabaei, I. Hajirasouliha, J. Becque. "Behaviour and design of cold-formed steel bolted connections under combined actions". *Journal of Structural Engineering (ASCE).*

J13. S.M. Mojtabaei, J. Becque, I. Hajirasouliha. "Shape optimisation of Cold-formed steel beam-column members". *Journal of Constructional Steel Research.*

Conference Papers

C1. S.M. Mojtabaei, J. Becque, I. Hajirasouliha. The capacity of bolted cold-formed steel connections in combined bending, International Colloquia on Stability and Ductility of Steel Structures (SDSS), Prague, Czech Republic, 11-13, September, 2019.

C2. D.T. Phan, J.B.P. Lim, H.G. Harno, I. Hajirasouliha, S.M. Mojtabaei, L.T. Lau, J.H. Lim. Effect of knee braces on optimum design of cold-formed steel portal frames. 9th International Conference on Steel and Aluminium Structures (ICSAS19), Bradford, UK, 3-5, July, 2019.

C3. S.M. Mojtabaei, I. Papargyriou, I. Hajirasouliha, J. Becque. Optimum seismic design of cold-formed steel moment-resisting frames. 9th International Conference on Steel and Aluminium Structures (ICSAS19), Bradford, UK, 3-5, July, 2019.

C4. S.M. Mojtabaei, J. Becque, I. Hajirasouliha. Behaviour of cold-formed steel bolted moment connections. 9th International Conference on Steel and Aluminium Structures (ICSAS19), Bradford, UK, 3-5, July, 2019.

C5. J. Ye, S.M. Mojtabaei, I. Hajirasouliha, Paul Shepherd, Kypros Pilakoutas, Verification of eurocode design models on the calculation of strength and deflections in cold-formed steel beams, Eighth International Conference on THIN-WALLED STRUCTURES - ICTWS 2018 - Lisbon, Portugal, July 24-27, 2018.

C6. S.M. Mojtabaei, I. Papargyriou, I. Hajirasouliha, J. Becque, K. Pilakoutas. Development of cold-formed steel moment-resisting frames using optimum beams in seismic applications. 16th European conference on earthquake engineering, 18-21 June 2018, Thessaloniki, Greece.

ACKNOWLEDGEMENTS

TABLE OF CONTENTS

LIST OF FIGURES

LIST OF TABLES

LIST OF SYMBOLS

h	cross-sectional web height
b, b_e	gross and the effective width of the plate
c, d	the length of edge stiffeners
$\theta°$	the angle of edge stiffener
t	plate thickness
y_0, z_0	shear centre coordinates
i_y, i_z, i_0	radius of gyration about the y-y and z-z axes, and polar radius of gyration
v, E, G	the Poisson's ratio and the Young's modulus, and shear modulus of the plate, respectively
I_t, I_w	torsional and warping constant of the gross cross-section, respectively
X	channel eccentricity
f_y	material yield stress
f_u	material ultimate stress
L	member length
l_e	effective length of beam
ω	ratio of effective length over total length of beam
L_{cr}	buckling length in relevant buckling plane
$A_{gross}, W_{gross}, I_{gross}$	gross cross-sectional area, section modulus, and second moment of area, respectively
$A_{eff}, W_{eff}, I_{eff}$	effective cross-sectional area, section modulus, and second moment of area, respectively
A_w	area of web element
W_{pl}	plastic section modulus
$W_{pp,eff}$	effective partially plastic section modulus
A_s, I_s	area and second moment of area of the stiffener about an axis through its centroid parallel to the plate
Z_f	section modulus about horizontal axis
k	buckling factor (Eurocode3)
ψ	ratio of the end stresses in the plate (Eurocode3)
ρ	reduction factor applied on the plate width (Eurocode3)
σ_{cr}	elastic local buckling stress of the plate
$\sigma_{cr.s}$	elastic buckling stress of the plate-stiffener assembly
f_{cr}	elastic buckling stress of the cross-section
K	stiffness of the continuously partial restraint supporting the edge stiffener

λ_l, λ_d	slenderness against local and distortional buckling, respectively
λ_s	cross-sectional slenderness
e_{Ny}, e_{Nz}	shift of effective centroid about y-y and z-z axes
N_{Ed}	applied axial compression load (herein taken as a axial capacity in beam-column member)
$N_{Ed,s}$	axial capacity of the beam-column member with standard sections
$M_{y,Ed}$, $M_{z,Ed}$	applied bending moments about y-y and z-z axes, respectively
eN_y	eccentricity of the compression load
$M_{cy,Rd,ten}$, $M_{cz,Rd,ten}$	design moment resistances for the maximum tensile stress in cross-section subjected to only bending moment about y-y and z-z axes
$M_{cy,Rd,com}$, $M_{cz,Rd,com}$	design moment resistances for the maximum compressive stress in cross-section subjected to only bending moment about y-y and z-z axes
$\Delta M_{y,Ed}$, $\Delta M_{z,Ed}$	additional moments due to shift of the effective centroidal axes about y-y and z-z axes
$N_{b,Rd}$	design buckling resistance of the compression member
$M_{b,Rd}$	design lateral-torsional buckling resistance moment
γ_{M1}	Eurocode 3 partial safety factor
γ_D, γ_L	dead load and live load factors, respectively
χ_{Fy}, χ_{Fz}, χ_T, χ_{FT}, χ_{LT}	reduction factors taking into account flexural buckling about y-y and z-z axes, torsional buckling, flexural-torsional buckling, and lateral-torsional buckling, respectively
$\bar{\lambda}$, $\bar{\lambda}_{LT}$	slenderness of the compression and flexural members for the relevant global buckling modes, respectively
$N_{cr,y}$, $N_{cr,z}$	elastic critical forces for flexural buckling about y-y and z-z axes, respectively
$N_{cr,T}$, $N_{cr,FT}$	elastic critical forces for torsional and flexural-torsional buckling, respectively
k_{yy}, k_{yz}, k_{zy}, k_{zz}	the interaction factors for combined axial load and bending moment
α, α_{LT}	imperfection factor for compression and flexural members, respectively
M_{cr}	critical moment of a beam-column subjected to lateral-torsional buckling
C_1, C_2, C_3	loading conditions coefficients
k_z, k_w	effective length factor for the support conditions
N	number of particle
ρ_i^k, V_i^k, G_i^k	position, velocity, and the best position of the ith particle in iteration k, respectively
r_1, r_2	the independent random numbers used for Particle Swarm Optimisation (PSO)
K_0	initial stiffness of bearing behaviour
R	bolt radius or radius of influence
D	bolt diameter
l_b	bolt group length
h_b	bolt group height

R	reduction factor applied on the connection capacity
M_{max}, P_{max}	maximum bending moment and compressive capacity of the connection, respectively
M_c, P_c	nominal flexural and compressive capacity of CFS bolted connection, respectively
M_u, P_u	ultimate flexural and compressive capacity of the back-to-back channel, respectively
M_y, P_y	yield moment and compressive strength of cross-section, respectively
M_{cr}, P_{cr}	elastic local buckling moment and load of the cross-section, respectively
V_V	nominal shear capacity of section
M, V, P	required flexural, shear and axial compressive strengths of the connection, respectively
K_V	shear buckling coefficient
D_n, L_n	nominal dead load and live load , respectively
ϕ	resistance factor
R_n	nominal resistance
r_d	design resistance
r_m	corresponding to resistance obtained by the mean values of all relevant variable
b	correction factor from model uncertainty (reliability)
$k_{d,\infty}$	target calibration level
$k_{d,n}$	a factor related to the number of specimen
α_R	sensitivity factor
δ	error term
α_δ, α_{rt}	weighting factors
Q_{rt}, Q_δ, Q	standard deviation of resistance calculated using proposed design equation, the standard deviation of the error term δ, and the overall standard deviation of resistance, respectively
V_{rt}, V_δ	coefficients of variation (COVs) of the calculated resistance and the error term δ, respectively
κ_i, σ_i	basic variable i and its standard deviation
β_0	target reliability index for CFS member in LRFD design
C_ϕ	LRFD design factor
M_m, F_m, E_m	mean values of material, fabrication factors, and mean value of FE modelling error against experimental tests, respectively
P_m	mean value of professional factor
V_M, V_E, V_F	COV of material, fabrication factors, and COV of FE modelling error against experimental tests, respectively
V_Q	COV of the load
V_P	COV of the ratios of the FE results over to proposed design equation
C_P	correction factor
n	number of test samples

CHAPTER 1

Introduction

1.1. BACKGROUND

Mitigating the environmental impact of buildings on human health and the natural environment is the key parameter to sustainable construction. This aim can be achieved by efficiently using energy and resources. Hot-rolled steel structures are commonly used in the construction of multi-storey buildings. However, hot-rolled sections are only available in a limited number of standard profiles and lengths, leading to higher carbon emissions and up to 30% redundant material (Yu and LaBoube, 2010).

Cold-formed steel (CFS) sections are generally formed by either a press brake machine or a roll-forming process, using galvanized steel sheets. Therefore, these sections can be designed in many different configurations, contrary to hot-rolled steel elements, leading to more efficient and economic design solutions with less redundant material and waste during manufacturing (Lawson et al., 2005). A noticeable reduction of embodied carbon in the built environment can also be achieved by using CFS sections. According to a study by the University of Cambridge, replacing hot-rolled steel by CFS solutions has the ability to reduce the self-weight of structures and the associated carbon emissions by 15%-40% due to their higher strength-to-weight ratio (Carruth et al., 2011). The other advantages of using CFS sections in construction over their hot-rolled counterparts are a higher stiffness-to-weight ratio, off-site manufacturing, full recyclability and even reuse without loss of quality, smaller foundations, better durability, a larger volume of production, faster erection with lesser labour and easier fabrication and transportation.

As a result, CFS sections are an attractive option to use in industrial and multi-storey residential structures (Fig. 1.1)

Fig. 1.1. Cold-formed steel (a) industrial structures with moment-resisting portal frames and (b) multi-storey residential building with stud wall system

1.2. **RESEARCH MOTIVATION**

The main motivation behind this study is to provide more resilient and robust CFS structures at a reduced economic cost by optimising their structural components. It helps to cope with climate change, as well as man-made and natural hazard such as a high level of carbon emission in the built environment. This is therefore expected to have a long term impact on the UK and European economic growth and contribute towards the target set by the UK government for 33% reduction in both the initial cost of construction and the whole life cost of assets by 2025 (HMG, 2013). The development of new optimised CFS products and systems with a lighter weight and a lower embodied carbon will also increase the competitiveness of the UK and European steel and construction industries in the global market. Furthermore, findings of this study aim to benefit manufacturers and fabricators, design engineers and contractors.

Therefore, the following research necessities are introduced and addressed in this research project:

1.2.1. **Element level optimisation (CFS beam and CFS beam-column elements) and Structural level optimisation (CFS frame)**

The flexibility in manufacturing CFS cross-sectional shapes provides an excellent opportunity to determine optimum relative dimensions of channel sections (i.e. size optimisation), and enhance the load-carrying capacity of the available standard sections (Tian and Lu, 2004, Lee et al., 2006, Ma et al., 2015, Wang et al., 2016c). There is a general consensus that a structure

must be designed to resist both service and extreme load conditions with an acceptable level of reliability during its effective life. However, previous research has mainly focused on the Ultimate Limit State (ULS), which conventionally represents the ultimate strength of CFS structures under extreme load events. It should be noted that the slenderness of CFS elements is normally higher than that of their hot-rolled steel counterparts, and therefore, the Serviceability Limit State (SLS) is often more critical for CFS structures and needs to be investigated. Further research is also required to provide a new methodology for the development of optimum CFS beam-column members subjected to combined bending and axial force.

This enhancement of capacity at the element level may subsequently improve the capacity of CFS frame systems, especially for medium to long-span CFS portal frame buildings. Therefore, a coupled framework needs to be developed for element and structural level optimisation of CFS portal frames, under serviceability limit state (SLS) and ultimate limit state (ULS) conditions.

1.2.2. Behaviour and design of CFS bolted connections

A relatively new development in CFS is the emergence of CFS portal frames, which are combined with CFS purlins, girts and cladding in building solutions provided by CFS contractors/fabricators. These CFS systems are used in industrial and agricultural buildings with large open spans, warehouses and hangars. However, their development is held back by a lack of knowledge about their structural behaviour and a consequent lack of available design guidance.

The connections between the main members of CFS frames play a fundamental role in the overall behaviour of the structure. These connections, however, bear no resemblance to the welded connections typically employed in frames with hot-rolled members, but consist of bolted connections between the column and rafter webs and stiffened gusset plates. While this type of connection is economical and fast to execute, it results in a complicated transfer of the internal forces, which makes the connection prone to shear lag effects and localized failure modes. In addition, the reduced stiffness results in a semi-rigid behaviour which increases the deflections under loading and affects the distribution of the internal forces. Hence, there is a need to study the behaviour and capacity of bolted connections in CFS portal frames and propose a safe and reliable methodology for their structural design.

1.2.3. Seismic performance of CFS bolted moment connections

Experimental and numerical investigations on bolted moment connections between CFS sections have generally demonstrated their satisfactory strength and stiffness and adequate deformation capacity for seismic applications (Lim et al., 2016a, Lim and Nethercot, 2003a). Recent experimental and analytical studies have shown that the buckling strength of CFS elements/connections can be significantly improved by using new cross-sectional shapes (Bagheri Sabbagh et al., 2012b, Bagheri Sabbagh et al., 2012a, Ye et al., 2016a). However, typical CFS bolted moment connections may exhibit very low ductility and energy dissipation capacity, especially when the width-to-thickness ratios of the CFS elements increase (Mojtabaei et al., 2018). This highlights the need to develop efficient design configurations for moment-resisting CFS bolted beam-to-column connections to improve their seismic performance and therefore facilitate their practical application in earthquake-resistant frames.

Analytical studies have previously been carried out on the rotational capacity of beam elements under cyclic load (Serror et al., 2016a). However, further research is required to accurately predict the cyclic performance of CFS bolted moment connections using a more reliable way of modelling the bearing and slippage behaviour.

1.2.4.   Optimisation of CFS structural components for improved post-buckling behaviour

It has previously been shown that optimum design solutions for the bending and compressive strength of CFS elements can result in significant material savings (Ma et al., 2015, Ye et al., 2016b, Ye et al., 2016a). However, CFS structural components (i.e. elements and connections) can also be optimised to improve their post-buckling behaviour while considering their seismic characteristics (i.e. ductility and energy dissipation). The prediction of the complex post-buckling behaviour of CFS elements (controlled by combinations of local, global and distortional buckling) in parallel with an optimisation algorithm can be a very tedious task. Therefore, no research has previously been carried out on the optimisation of CFS structural components to improve their post-buckling behaviour in terms of ductility and energy dissipation capacity.

1.3. **AIM AND OBJECTIVES**

The aim of this research is to investigate the behaviour and design of CFS structures, such as elements, connections and frames, and find the best design solutions based on either their buckling strength or post-buckling behaviour using two-level optimisation. This was achieved by fulfilling the following objectives at different levels of CFS structures:

❖   At the element level:

1. To develop the best design solutions for the stiffness and the strength of CFS elements using shape optimisation of their cross-sections. Optimum design of CFS beam cross-sections at Serviceability Limit State (SLS) and Ultimate Limit State (ULS) will be developed to maximise their stiffness and strength, respectively. A new methodology will be also offered for optimising CFS beam-column elements subjected to different combinations of bending and axial compressive force.

2. To develop an innovative optimisation framework to improve post-buckling behaviour of CFS elements, which results in improvements in their seismic characteristics.

❖   At the connection level:

3. To investigate the behaviour and capacity of bolted connections in CFS portal frames subjected to static load and to propose a safe and reliable design methodology.

4. To evaluate the seismic performance of CFS beam-to-column bolted moment connections under cyclic loads with FE analysis, using experimentally validated models. In addition, to develop a more efficient seismic design of CFS bolted moment connections, further parametric studies will be conducted on the key design parameters such as beam cross-sectional shape and thickness, bolt configuration, bolt-group length and etc.

5. To develop a methodology for the optimisation of CFS bolted moment connections based on their post-buckling behaviour (i.e. ductility and energy dissipation capacity).

❖   At the frame level:

6. To develop a coupled framework for element and structural level optimisation of CFS portal frames, under serviceability limit state (SLS) and ultimate limit state (ULS) conditions. The CFS elements and frame geometry can be simultaneously optimised to develop more efficient CFS frames with reduced structural weight.

1.4. **TASKS AND METHODOLOGY**

The following methodology is adopted to achieve the objectives.

1. To fulfil the objectives regarding optimisations at different levels of CFS structures, a comprehensive overall review of the state-of-the-art of the research is performed on optimum design of CFS elements and non-linear optimisation methods such as Particle Swarm Optimisation (PSO) algorithms, Genetic Algorithms (GA), and Big Bang-Big Crunch optimisation (BB-BC) [Objectives 1, 2, 5 and 6].

2. To determine the stiffness, the strength and the seismic behaviour of CFS structures, an overall review is performed on the design provisions for CFS structural members and the seismic design codes, such as the Eurocode and the AISI, AISC and FEMA standards [Objectives 1, 2, 3, 4, 5 and 6].

3. The possibility of the occurrence of different instability modes including local/distortional and global buckling will be evaluated according to the Eurocode 3 (EC3) effective width method. Therefore, to find the best design solutions for CFS elements at both ULS and SLS, two distinct functions in MATLAB are developed: a programme implementing the EC3 design rules and a programme carrying out the optimisation algorithm [Objectives 1, 6].

4. To simulate cyclic and monotonic behaviour of CFS structural components and to assess the accuracy of the optimisation results, detailed non-linear FE models are validated using the results of experiments [Objectives 1, 2, 3, 4, 5, and 6].

5. Develop Python scripts to generate ABAQUS-based FE models of the structural components (i.e. elements and connections). This task is essential for both the optimisation of the structural components based on their post-buckling behaviour and for eventually proposing design equations [Objectives 2, 3, 5].

6. Establish a link between three different pieces of software, namely PYTHON, ABAQUS and MATLAB to carry out the optimisation process on the post-buckling behaviour of CFS structural components [Objectives 2 and 5].

1.5. **THESIS LAYOUT**

This thesis is presented in an "alternative format" and consists of seven chapters and three appendices some of which were published (or submitted/prepared for publication) as journal

papers. The thesis combines three chapters written following the "traditional" thesis format (chapters 1, 2 and 7) with "stand-alone" journal papers (Chapters 3 to 6 and Appendixes A, B and C). It should be noted that while the main contributions of the PhD study are incorporated in Chapters 3 to 6, collaborative research projects are also included in Appendixes A, B and C as secondary contributions since they are aligned with the general scope of this thesis.

1.5.1. Chapter 1

Introductions

In this chapter, a general background to the research is briefly provided. In addition, an overall introduction to the problem, the research motivation, the aims and objectives, the tasks and methodology, and the thesis layout are presented.

1.5.2. Chapter 2

Literature review

A literature review is presented on the following topics:

- CFS cross-sectional shapes.

- Existing design guidelines

- Behaviour of CFS elements

- Optimisation of CFS elements

- CFS connections

- Optimisation of CFS structures

- Currently available optimisation techniques and a discussion on their advantages and limitations

1.5.3. Chapter 3

Shape optimisation of cold-formed steel beam-column members

This chapter, which addresses parts of objective 1, is based on a ready for-submission-journal paper: S.M. Mojtabaei, J. Becque, I. Hajirasouliha. "Shape optimisation of Cold-formed steel beam-column members", *Journal of Constructional Steel Research*. The main contribution of the author to this paper was the development of a new methodology for the optimum design

of CFS beam-column elements, programming Eurocode 3 design regulations, establishing a link between optimisation algorithm and EC3, and writing the first draft of the paper.

The main purpose of this chapter is to offer a novel methodology which provides the best design solutions for practical CFS beam-column members subjected to different load combinations. To the best of the author knowledge, it is the first time that CFS elements with both open and closed sections are optimised under combinations of bending moment and axial compression load. Well-known Genetic Algorithm (GA) is used to carry out optimisation process. The total coil width and the thickness of all CFS prototypes (i.e. open and closed sections) were fixed during the optimisation process. The optimisation was carried out on the load-bearing capacity of the CFS elements obtained following the provisions of the Eurocode 3 effective width method (CEN, 2005c).

1.5.4. Chapter 4

Development of optimum cold-formed steel beams for serviceability and ultimate Limit states using Big Bang-Big crunch optimisation

This chapter, which completes objective 1, is based on a published journal paper: S.M. Mojtabaei, J. Ye, I. Hajirasouliha. (2019). "Development of optimum cold-formed steel beams for serviceability and ultimate limit states using Big Bang-Big Crunch optimisation". *Engineering Structures*, 106, 76-89. The main contribution of the author to this paper was programming of Eurocode 3 regulations for the design of CFS elements at both serviceability and ultimate limit states, discussions on the optimised results at different limit states, FE validations, and writing the first draft of the paper.

Chapter 4 develops a practical methodology for optimum design of CFS beam cross-sections with maximum flexural strength and minimum deflection under ultimate and serviceability load conditions, respectively, in accordance with Eurocode 3. It should be noted that conducting optimisation based on two different limit states defined by Eurocode and comparing their optimum results are considered as the main novelty of this study. To provide practical CFS cross-sections, manufacturing and end-use design constraints are imposed. The optimisation process is performed on twelve different CFS cross-sectional prototypes using the population-based Big Bang–Big Crunch Optimisation method. To evaluate the accuracy of the optimum results, detailed nonlinear finite element (FE) models are developed using ABAQUS by considering both material nonlinearity and initial geometrical imperfections.

1.5.5. Chapter 5

Behaviour and design of cold-formed steel bolted connection

Chapter 5 addresses objective 3, based on one published journal paper: S.M. Mojtabaei, I. Hajirasouliha, J. Becque. (2020). "Local buckling in cold-formed steel moment-resisting bolted connections: behaviour, capacity and design". *Journal of Structural Engineering (ASCE)*, and one ready-for-submission journal paper, S.M. Mojtabaei, J. Becque, I. Hajirasouliha. "Behaviour and design of cold-formed steel bolted connections under combined actions". *Journal of Structural Engineering (ASCE)*. The main contribution of the author to these papers was development design equations, FE validations, discussions on the effect of shear lag, reliability analysis, and writing the first draft of papers.

This chapter investigates, the behaviour and design of CFS bolted connections between the main structural components of CFS moment-resisting frames. It should be noted that, for the first time, the performance of CFS bolted connections are profoundly investigated and design equations are proposed for their strength. Experimentally validated FE models of CFS bolted connections under a static monotonic load condition are used to investigate the influence of the beam cross-sectional shape and thickness, the bolt configuration, and the bolt-group length on the flexural strength and the compressive capacity of the connections. The predicted capacities are then employed to propose general design equations for the nominal flexural capacity and axial compressive strength of the connections. The interaction of bending and shear, and bending, shear and compression are evaluated against proposed design equations, and compared with the interaction curves recommended by the design standard (i.e. the AISI provisions) for CFS elements.

1.5.6. Chapter 6

Development of Cold-Formed Steel Bolted Moment Connections for Maximum Ductility and Energy Dissipation

This chapter, which addresses objective 5, is based on a journal paper which is ready for submission: S.M. Mojtabaei, I. Hajirasouliha, J. Becque, J. Ye. "Development of cold-formed steel bolted-moment connections for maximum ductility and energy dissipation in seismic applications". *Engineering Structures*. The main contribution of the author to this paper was the development of a novel optimisation methodology based on post-buckling behaviour of the structures, FE validations, establishing a link between different software for the optimisation process, and writing the first draft of the paper.

This chapter is dedicated to improving the seismic performance of CFS moment-resisting frames by developing more efficient bolted moment-resisting connections using optimised CFS beams with enhanced non-linear post-buckling behaviour. An innovative optimisation process based on post-buckling behaviour of the bolted moment-resisting connections is considered as the novelty of this research. By taking into account material non-linearity and geometrical imperfection effects, detailed Finite Element (FE) models of typical CFS bolted moment connections are developed using the ABAQUS software and then validated against experimental cyclic test results. A Particle Swarm Optimisation (PSO) algorithm is linked to GMNIA ABAQUS FE analyses to optimise the validated models with respect to their energy dissipation capacity and ductility. Five different beam cross-sections are selected for the optimisation process and their relative dimensions, the location of intermediate stiffeners and the inclination of the lip stiffeners are considered as the main design variables. To provide practical beam cross-sections, all plate slenderness limit values defined by Eurocode 3 (EC3) along with a range of manufacturing limitations are also imposed as design constraints in the optimisation process. This chapter can provide a basis for more efficient CFS multi-storey moment-resisting frames, suitable for high seismic regions.

1.5.7. Chapter 7

Summary and Conclusions, and Recommendations for Future Work

This chapter contains a summary of the results, followed by recommendations for future work.

1.5.8. Appendix A

Development of Optimum Cold-Formed Steel Sections for Maximum Energy Dissipation in Uniaxial Bending

This appendix, which addresses objective 2, is based on a published journal paper: J. Ye, J. Becque, I. Hajirasouliha, S.M. Mojtabaei, J.B.P. Lim. (2018). "Development of optimum cold-formed steel sections for maximum energy dissipation in uniaxial bending" *Engineering Structures*, 161, 55-67. The main contribution of the author to this paper was the development of detailed nonlinear FE models for the monotonic behaviour of CFS beams and validation against the results of experimental tests. In addition, the author carried out the optimisation of CFS beams with different cross-sectional shapes to maximise their energy dissipation and ductility ratio.

Appendix A discusses the seismic characteristics of CFS beam elements and introduces an innovative methodology for optimising the post-buckling behaviour in the highly nonlinear inelastic range. An innovative optimisation process based on post-buckling behaviour of the

CFS beam element is considered as the novelty of this research. A novel shape optimisation framework is presented using the Particle Swarm Optimisation (PSO) algorithm, linked to GMNIA ABAQUS finite element analyses. The relative dimensions of the cross-section, the location and number of intermediate stiffeners and the inclination of the lip stiffeners are considered to be the main design variables. All plate slenderness limit values and limits on the relative dimensions of the cross-sectional components as defined by Eurocode 3, as well as a number of practical manufacturing and construction limitations, are taken into account as constraints in the optimisation problem.

1.5.9. Appendix B

Efficient Design of Cold-Formed Steel Bolted Moment Connections for Earthquake Resistant Frames

This appendix, which addresses objective 4, is based on two published journal papers: J. Ye, S.M. Mojtabaei, I. Hajirasouliha, K. Pilakoutas. (2019). "Efficient design of cold-formed steel bolted-moment connections for earthquake resistant frames". *Thin-Walled Structures*, 59, 49-61. And, J. Ye, S.M. Mojtabaei, I. Hajirasouliha. (2019). "Seismic performance of cold-formed steel bolted moment connections with bolting friction-slip mechanism", *Journal of Constructional Steel Research*, 27, 86-100. The main contribution of the author to these papers was the development of experimentally validated CFS bolted moment connections for seismic applications by considering different design parameters (e.g. bolt slip resistance and beam cross-sectional shape). The author used Eurocode concepts of cross-section classification to obtain the class of recently developed channels with folded and curved flanges and also wrote the first drafts of both above-mentioned papers.

Appendix B presents a comprehensive parametric study on the structural behaviour of CFS bolted beam-to-column connections with gusset plates under cyclic loading, aiming to develop efficient design solutions for earthquake resistant frames. To simulate the hysteretic moment–rotation behaviour and failure modes of selected CFS connections, an experimentally validated finite element model using ABAQUS is developed, which accounts for both nonlinear material properties and geometrical imperfections. Connection behaviour is modelled using a connector element, simulating the mechanical characteristics of a bolt bearing against a steel plate and slip of the bolt. The model is used to investigate the effects of bolt arrangement, cross-sectional shape, gusset plate thickness and cross-sectional slenderness on the seismic performance of CFS connections under cyclic loading. Finally, the proposed connections are assessed in accordance with the AISC requirements for intermediate and special moment frames.

1.5.10. Appendix C

Coupled Element and Structural Level Optimisation Framework for Cold-Formed Steel Frames

This appendix, which addresses objective 6, is based on a published journal paper: D.T. Phan, S.M. Mojtabaei, I. Hajirasouliha, J. Ye, J.B.P Lim. (2019). "Coupled element and structural level optimisation framework for cold-formed steel frames". *Journal of Constructional Steel Research*, 44, 79-91. The main contribution of the author to this paper was conducting optimisation at the element level, and consequently, providing a range of optimum sections. The author also wrote the first draft of this paper.

In appendix C, a novel methodology is proposed to simplify simultaneous optimisation of cross-sectional dimensions and the overall geometry of the structural system by coupling the element and structural level optimisation. It the first time that the optimisations at two different levels of CFS structures (i.e. element and frame) are coupled. At the element level, a practical procedure is presented for the development of conventional CFS back-to-back lipped-channel beam sections with maximum flexural strength by taking into account local, distortional and global buckling modes. To provide a comprehensive range of optimum sections suitable for CFS portal frames, CFS beam members with different span lengths subjected to various levels of uniformly distributed loads (UDLs) are considered in this study. The efficiency of the proposed optimum CFS cross-sections is then investigated and compared to standard commercially available back-to-back sections. At the structural level, a long span CFS portal frame with knee braces subjected to different serviceability limit state (SLS) and ultimate limit state (ULS) design load combinations is first analysed using Finite Element (FE) ANSYS software (ANSYS Inc., 2009) to determine the internal forces in the elements and the lateral displacement of the joints. Subsequently, the GA program is adopted to find the best design solution (i.e. with minimum structural weight) by using both standard and optimum CFS sections and considering a set of predefined structural design constraints. The results are then used to assess the efficiency of the proposed coupled framework and to investigate the influence of knee brace configuration on the structural performance of the optimised frame.

The following flowchart clearly demonstrates the structure of the thesis.
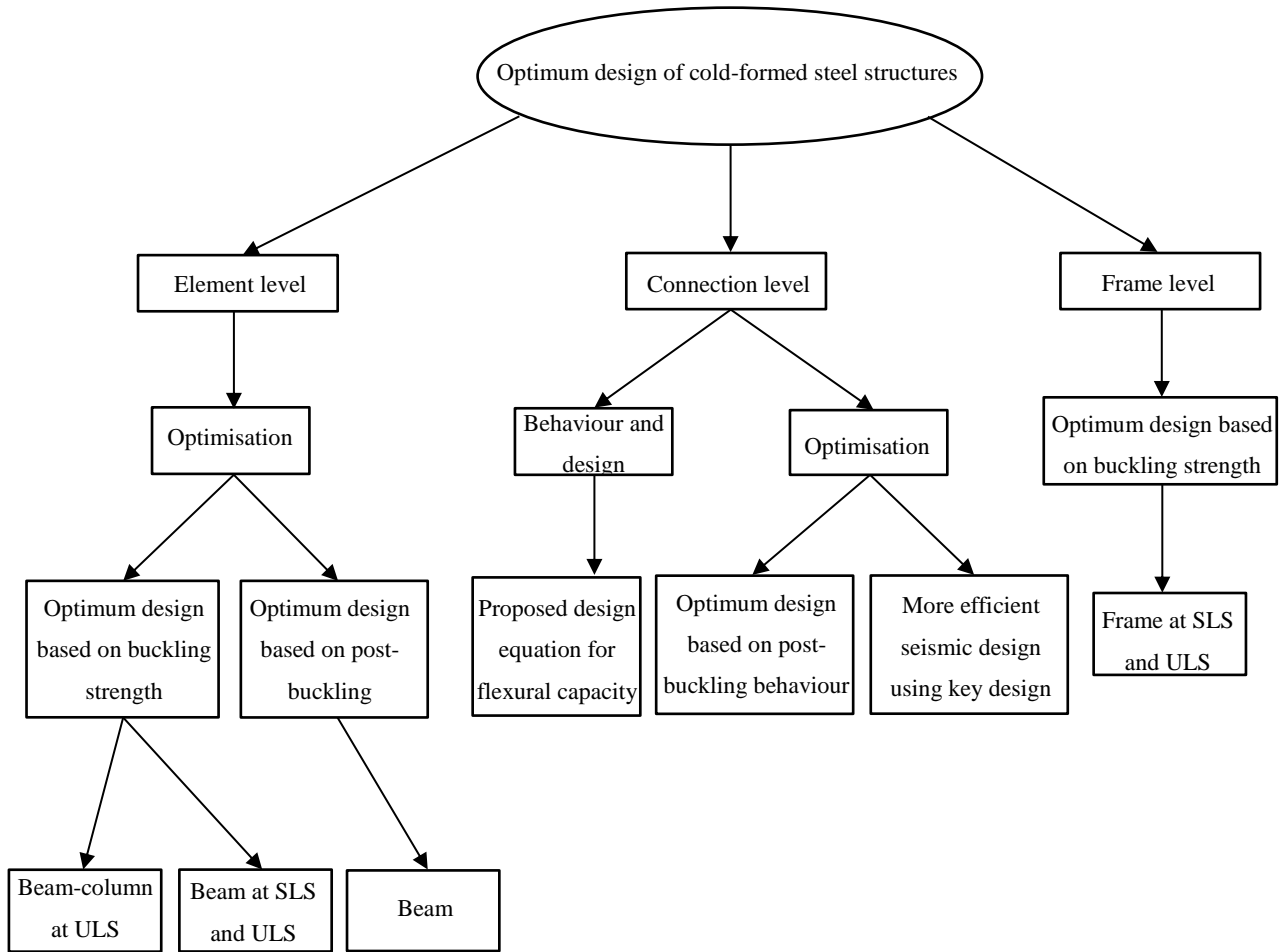
Fig. 1.2. A flowchart indicating the structure of the thesis
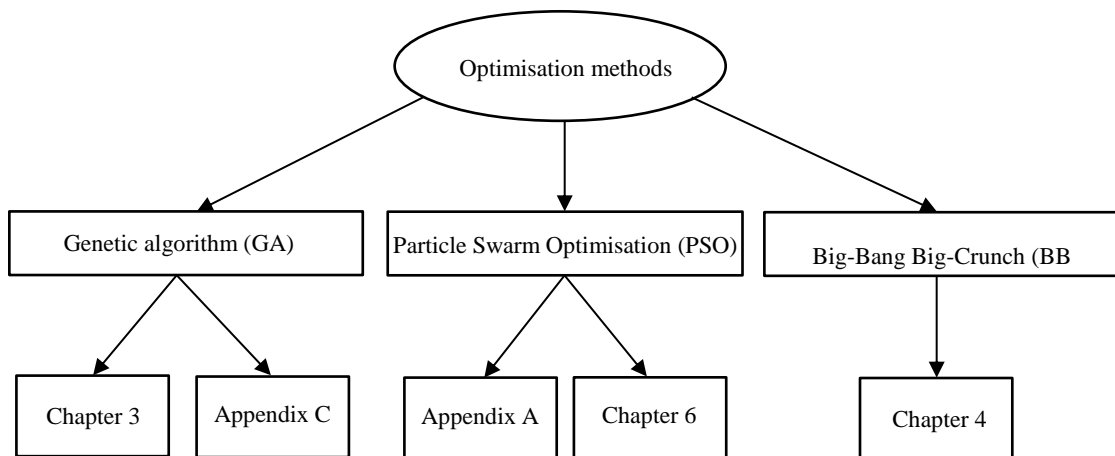
Fig. 1.3. A flowchart indicating the optimisation methods used in the thesis

CHAPTER 2

Literature Review

This chapter presents a comprehensive review of the available literature on the structural behaviour of CFS sections, CFS connections and CFS structural systems. The first part reviews previous research on the different cross-sectional shapes proposed for CFS elements (i.e. beams, columns, and beam-columns) and provides discussions on their structural performance. The governing design guidelines for the buckling resistance of CFS elements are then discussed. This is followed by a summary of previous research on the optimisation of CFS elements. In order to provide a background to Chapters 5 and 6 and Appendixes A and B the seismic behaviour of CFS elements and connections is also reviewed. At the end of this chapter, different systems of CFS frames are discussed.

2.1. BACKGROUND OF CFS SECTIONS

Cold-formed steel sections are normally manufactured by a rolling (Fig. 2.1 (a)) or a press-braking (Fig. 2.1 (b)) process. This offers flexibility in cross-sectional shapes (Fig. 2.2) and consequently an adaptability to various applications. CFS sections are made from either plain or dimpled steel sheets (Fig. 2.3 (a)). Generally, dimpled sheets are produced from plain steel sheets using the UltraSTEEL® process (Hadley Industries plc). Fig. 2.3 (b) shows an example of a CFS section formed with a dimpled sheet.

Fig. 2.1. Manufacturing process of CFS elements using (a) rolling (Tsang et al., 2018), or (b) press-braking (Bagheri Sabbagh et al., 2011)

Fig. 2.2. Variety of CFS sections (Yu and LaBoube, 2010)
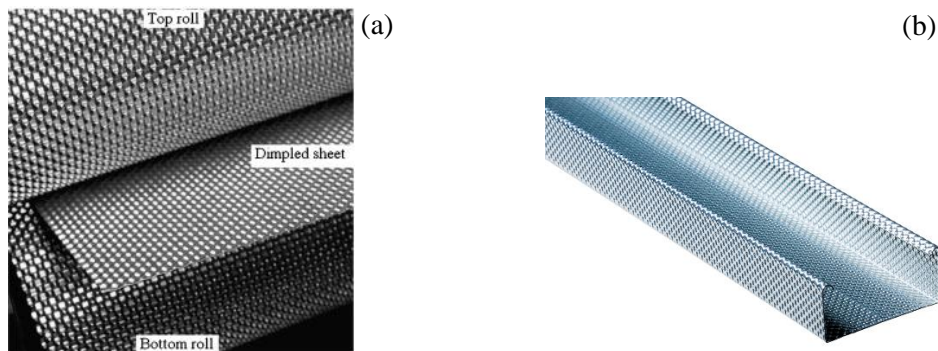
Fig. 2.3. (a) Typical dimpled steel sheet (Nguyen et al., 2012), (b) formed cross-sections with a dimpled steel sheet (Hadley Industries plc).

The manufacturing process can affect the stress-strain behaviour of the material, mainly as a result of strain hardening and residual stresses (Quach et al., 2010). As shown in Fig. 2.4, strain hardening enhances the yield stress and, to a lesser extent, the ultimate strength, but reduces the ductility of the material. Folding and coiling-uncoiling of steel sheets generate

residual stresses in CFS sections. It should be noted that residual stresses can noticeably affect the strength and ductility of CFS sections (Quach et al., 2010).

While coiling-uncoiling residual stresses are distributed in the flat portions of the sections, residual stresses caused by folding are localised in the corner zones of the sections (Yao et al., 2019). It has been demonstrated that longitudinal residual stresses in the corner zones of the CFS sections are higher than those in the flat portions (Weng and Pekoz, 1990). Further research also revealed that the forming process by rolling machine generates higher residual stresses than the forming by a press-braking machine (Batista and Rodrigues, 1992).
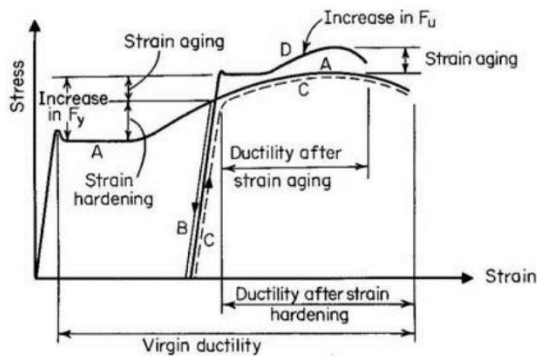
Fig. 2.4. Effect of manufacturing process on stress-strain curve of CFS (Yu and LaBoube, 2010)

CFS sections are more prone to local/distortional buckling than hot-rolled sections due to the large width-to-thickness ratio of their thin-walled elements. Over time, CFS sections have developed using modern manufacturing technologies into complex shapes aimed at delaying local-distortional buckling. Fig. 2.5 shows the evolution of CFS purlin sections. The conventional Z sections have evolved into more complex sections with edge and intermediate stiffeners placed into the webs and flanges (Davies, 2000).
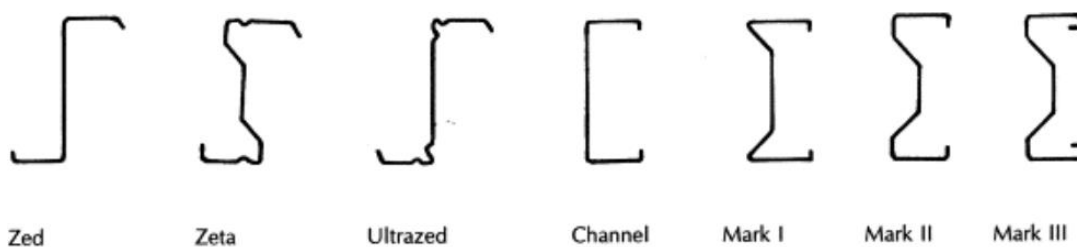
Fig. 2.5. Evolution of CFS purlin sections (Davies, 2000)

CFS members are employed in buildings as both structural and non-structural elements, including floor beams, roof trusses, stud wall panels, framing systems, guard rails, struts, mezzanine floors, cladding systems and storage racks. The buckling resistance of CFS beams has been improved by the development of more efficient cross-sections with different flange

shapes (see Fig. 2.6). These sections include the symmetrical I-beam with closed triangular hollow flanges (Perera and Mahendran, 2018), the LiteSteel beam with rectangular hollow flanges (Siahaan et al., 2018), delta hollow flange beams (Mohebkhah and Azandariani, 2015), rectangular hollow flange beams (Wanniarachchi and Mahendran, 2017), and beams with open and closed drop flanges (Magnucki and Paczos, 2009), sandwich flanges (Magnucki and Paczos, 2009) and also folded flanges (Ye et al., 2016b).

Extensive experimental and analytical studies have investigated local/distortional buckling and their interaction, global buckling and shear buckling. The results of these studies also revealed that more complex cross-sections can improve the flexural strength and stiffness of beam elements (Perera and Mahendran, 2018, Siahaan et al., 2018, Mohebkhah and Azandariani, 2015, Wanniarachchi and Mahendran, 2017, Magnucki and Paczos, 2009, Ye et al., 2016b). It was also demonstrated that the proposed innovative cross-sections are suitable for use as a main load-bearing element with long span.
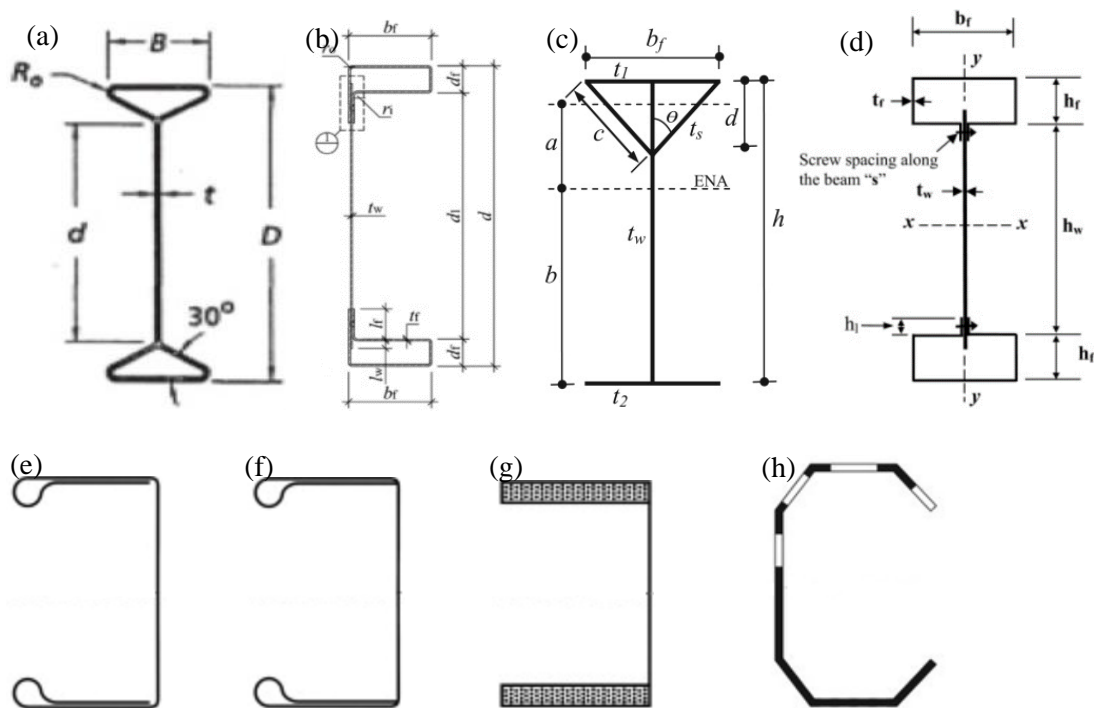
Fig. 2.6. Various cross-sectional shapes of the CFS beam elements with (a) closed triangular hollow flanges (Perera and Mahendran, 2018), (b) LiteSteel beam with rectangular hollow flanges (Siahaan et al., 2018), (c) delta hollow flange beams (Mohebkhah and Azandariani, 2015), (d) rectangular hollow flange beams (Wanniarachchi and Mahendran, 2017), (e) open and (f) closed drop flanges (Magnucki and Paczos, 2009), (g) sandwich flanges (Magnucki and Paczos, 2009), and (h) folded flanges (Ye et al., 2016b)

It has previously been shown that strength of CFS column elements can be more substantially increased compared to CFS beam elements using complex cross-sections. This can be attributed to the presences of (i) intermediate stiffeners which postpone local buckling of

individual plates, and (ii) edge stiffeners which can increase the distortional buckling strength. While the same can be said for the compressive zone of beam elements, the tension zone is not vulnerable to any instabilities. A large number of research projects were dedicated to the design of CFS columns with complex shapes including edge stiffeners (lip), intermediate stiffeners, stiffeners with inclined angle (e.g. (Yan and Young, 2002, Young, 2008, Chen et al., 2010, Wang et al., 2016d)), as shown in Fig. 2.7.
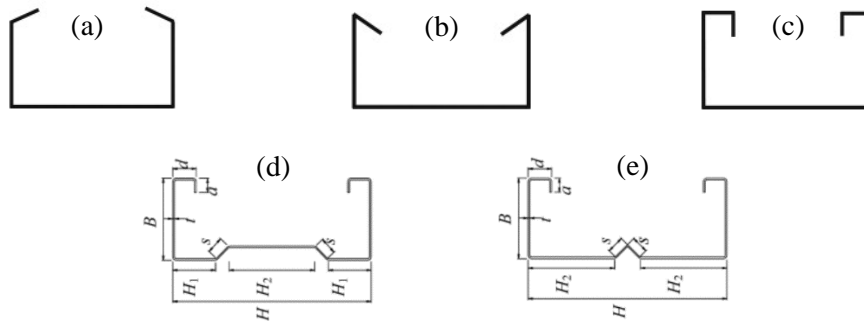
Fig. 2.7. CFS Columns with complex edge and intermediate stiffeners: (a) outwards edge stiffeners, (b) inwards edge stiffeners, (c) complex edge stiffeners, (d) Σ shape section with complex edge stiffeners, and (e) complex edge stiffeners and V type web intermediate stiffeners (Young, 2008, Wang et al., 2016d)

Narayanan and Mahendran (Narayanan and Mahendran, 2003) conducted experiments on CFS columns with innovative cross-sectional shapes (See Fig. 2.8). It was shown that the dominant failure modes were distortional buckling for all cross-sectional shapes and that local buckling was delayed due to the presence of stiffeners and the reduction in the flat width of the plates.
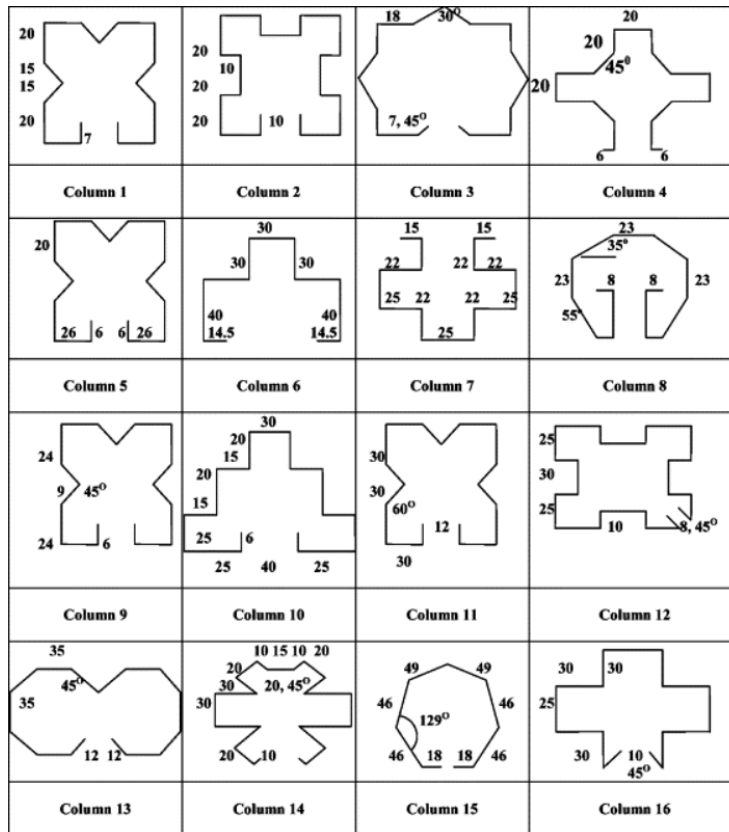
Fig. 2.8. Section geometries of innovative steel columns (All dimensions are measured values in mm)

As previously mentioned, CFS cross-sections are manufactured using either a rolling process or a press-braking machine, as shown in Fig. 2.1. Therefore, CFS elements generally have open cross-sections with singly-, point-, or asymmetric shapes. Relatively poor torsional properties are an inherent feature of open cross-sections compared to their closed counterparts. The dominant failure mode of open cross-sections would most likely be local/distortional buckling which can interact with global buckling modes (i.e. flexural, flexural-torsional and torsional modes) depending on the dimensions of the cross-sections and the element length. Built-up CFS sections can be an attractive alternative to improve the strength and stiffness of single sections, especially when the elements are used for longer spans. In general, a number of single channel sections are assembled using connectors to create a built-up section. It should be noted that no detailed design guidelines are currently available for CFS built-up sections. For instance, Eurocode 3 (CEN, 2005c) simply adds up the strength of all CFS channel sections, while the North-American Specification Specifications (AISI S100-12, 2012) use a modified slenderness ratio for the design of built-up columns. Fig. 2.9 shows examples of built-up cross-sections.
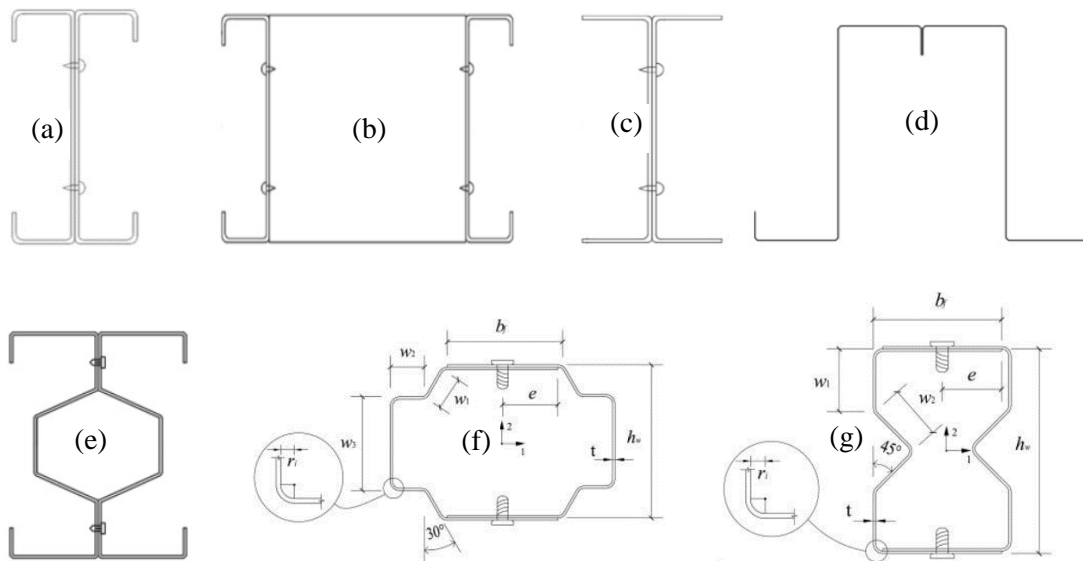
Fig. 2.9. CFS built-up sections: (a) (Ting et al., 2017), (b) (Roy et al., 2018), (c) (Roy et al., 2018), (d) (Georgieva et al., 2012), (e) (Zhang and Young, 2012), (f) (Wang and Young, 2016a), and (g) (Wang and Young, 2016b)

Several researchers have investigated the behaviour of CFS elements with built-up sections over the past decade. Roy et al. studied the nonlinear behaviour of axially loaded back-to-back built-up plain channel sections and built-up box sections (2018, 2019). The effect of longitudinal web stiffeners on the capacity of CFS built-up open section columns was investigated by Zhang and Young (2012). DSM equations were developed by Wang and Young (2016a, 2016b) for the flexural capacity of CFS built-up sections with intermediate stiffeners based numerical and experimental studies. More recently, Meza (2018) contrived comprehensive experimental programme with the aim of investigating the behaviour and the capacity of CFS built-up columns. In this study, the columns were designed to fail by interaction of cross-sectional buckling of the components, possible global-type buckling of the components between connectors and global buckling of the whole column, and all these failure modes were successfully achieved.

The widespread use of CFS as a construction material is also fuelling more research on its use in composite structures. Composite beams are commonly made of steel beam sections connected to a concrete slab at the top (see Fig. 2.10). Shear connectors are normally used to control the slip between two materials. Hanaor (2000) conducted experiments on CFS composite beams with different types of connectors under static loading. A state-of-art review of CFS-concrete composite systems was carried out by Lawan et al. (2015). A number of research projects also investigated CFS composite beams with bamboo and steel elements (Li et al., 2015) and CFS composite floors with wooden and steel elements (Kyvelou et al., 2015, Kyvelou et al., 2017).
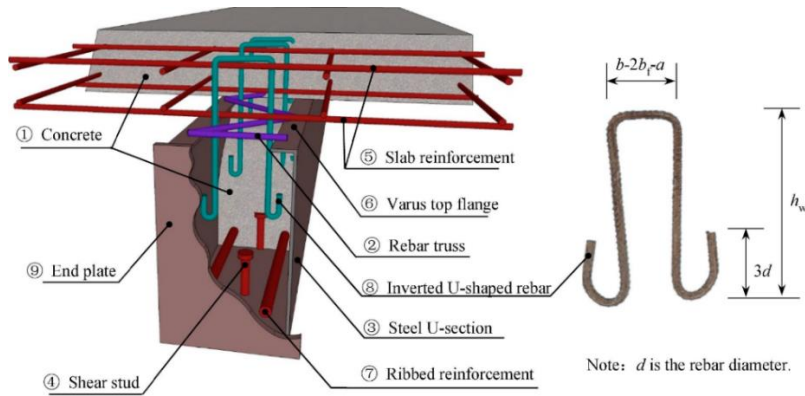
Fig. 2.10. Details of a typical CFS composite beam (Zhou et al., 2019)

2.2. DESIGN OF CFS MEMBERS

Failure of CFS members is generally characterised in terms of three basic modes of instabilities, namely local, distortional and global buckling, as illustrated in Fig. 2.11 (Schafer, 2006). The local buckling mode exhibits flexural deformations of the individual plates, without transverse displacements of the lines of intersection of adjacent plates. Distortional buckling involves distortion of the cross-section, leading to both in-plane and out-of-plane displacements of constituent plates. Global buckling consists of various modes, including flexural, torsional-flexural, torsional, or lateral-torsional buckling, and involves bending/twisting of CFS members without change of the cross-sectional shape. The design of CFS thin-walled structural components is governed by a number of specifications/guidelines such as the AISI standards (AISI S100-12, 2012), the ANZ standards (AS/NZS 4600, 2018) and Eurocode 3 (EC3) (CEN, 2005c). The European design guidelines (CEN 2005b) and the AISI provisions (AISI S100-12, 2012) have adopted two alternative design concepts for CFS elements, in particular the effective width method and the Direct Strength Method (DSM). While AISI allows both the effective width method and the DSM, EC3 is based on only effective width method.
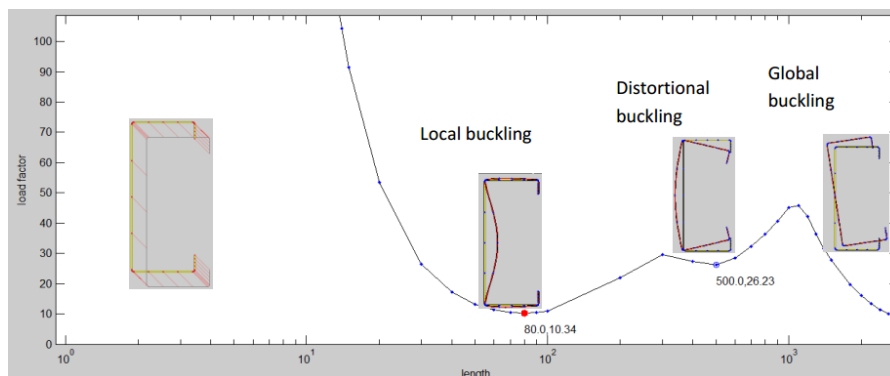
Fig. 2.11. Buckling modes of a CFS lipped-channel section under compression

2.2.1. Eurocode 3 (EC3) effective width method

The European design guidelines (EC3) (CEN, 2005c) are based on the effective width method. This method was first presented by Von Karman (1932) and is based on the fact that local buckling results in a shift of the load-bearing stresses towards the corner zones. Therefore, the efficiency of the central parts in carrying compressive loads is reduced. The reduction in the effectiveness of a locally buckled plate with a non-uniform stress distribution is taken into account in EC3 (CEN, 2005c) by defining an effective plate under a simplified linear stress distribution (see Fig. 2.12). The effective widths of a plate can be determined for different boundary conditions and stress gradients according to EC3 (CEN, 2005c).
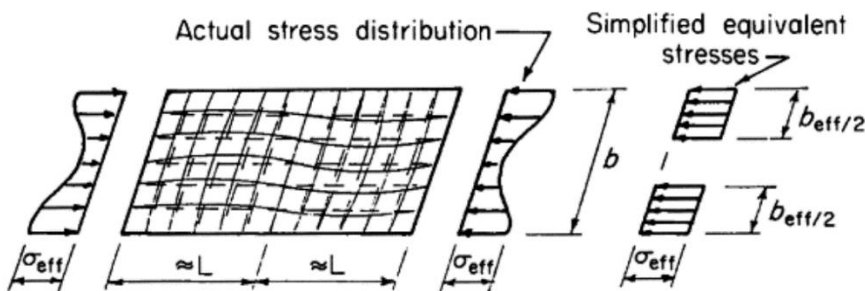
Fig. 2.12. Effective width of a plane element restrained along both edges (Davies, 2000)

EC3 (CEN, 2005c) accounts for distortional buckling based on the idea that the effective portion of an edge stiffener (lip) acts as a strut (Fig. 2.13) which is continuously supported by an elastic foundation along its centroidal axis with an equivalent spring stiffness of K. A reduction factor is then calculated and applied to the thickness of effective edge stiffener. This method is equally used by EC3 (CEN, 2005c) to determine the reduced thickness of intermediate stiffeners.

EC3 also determines the global buckling resistance of thin-walled CFS elements by using a global slenderness parameter based on the effective cross-sectional area (CEN, 2005e). It should be noted that the effective width method stipulated by EC3 is complex and requires the use of an iterative procedure. A number of research projects have recently focused on the improvement/development of the effective width method (e.g. (Batista, 2009, Yu and Yan, 2011, He and Zhou, 2014, Dubina and Ungureanu, 2014, Bernuzzi and Simoncelli, 2015, Bernuzzi and Maxenti, 2015, Bock and Real, 2015, Xingyou et al., 2016, Ye et al., 2016a)).
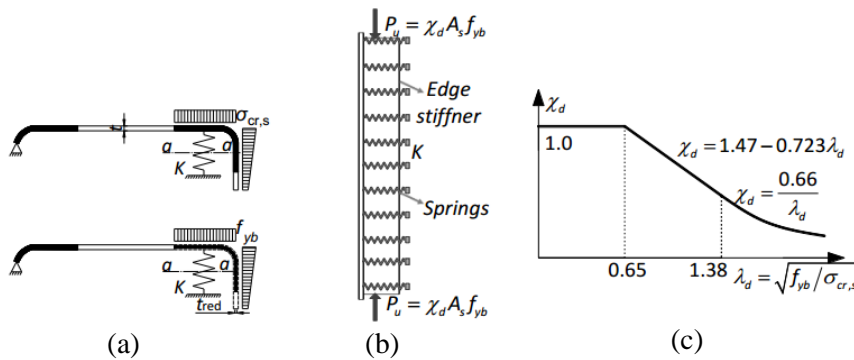
Fig. 2.13. Model of distortional buckling: (a) flange with edge stiffener, (b) flexural buckling of edge stiffener considered as a strut on an elastic foundation, and (c) flexural buckling curve for edge stiffener (CEN, 2005c)

2.2.2. Direct Strength Method (DSM)

The Direct Strength Method (DSM) adopted by the specifications (AISI S100-12, 2012) and the ANZ standards (AS/NZS 4600, 2018) is an alternative design approach to the traditional effective width method to predict the capacity of CFS members. This method is based on a computational stability analysis, where the elastic local, distortional and global buckling loads are determined. The local, distortional and global slenderness values of the cross-section are then obtained using the elastic buckling loads, and subsequently, the strength is directly predicted using a series of simple empirical equations (AISI S100-12, 2012). As discussed, the calculation of effective properties can be a tedious task, especially for complex CFS sections. However, only gross cross-sectional properties are needed in the DSM. The elastic buckling loads of CFS members can be computed using finite strip software such as CUFSM (Schafer, 2006). A comprehensive review of the DSM can be found in (Schafer, 2008).

It has been frequently demonstrated that the DSM can efficiently predict the capacity of typical "prequalified" CFS sections (AISI S100-12, 2012). However, the DSM was initially unable to design beam-column elements, as well as specific cross-sections such as plain channel and angle sections, and did not consider interactive buckling modes (e.g. local and flexural) (Ungermann et al., 2012). An extensive number of research projects developed the DSM for the design of CFS members under flexural, compression and shear loads, as well as combined actions (i.e. compression and bending). For example, design recommendations were proposed for columns by Kwon et al. (2009), Landesmann and Camotim (2013), Ajeesh and Arul Jayachandran (2016), Landesmann et al. (2016), Martins et al. (2017a), and Dinis et al. (2019), for beam elements by Nandini and Kalyanaraman (2010), Pham and Hancock (2013), Anbarasu (2016), Ren et al. (2016), Martins et al (2017b), and Nguyen et al. (2017), for elements under shear loads by Mahendran and Keerthan (2013), Degtyareva and Degtyarev (2016), and Pham et al. (2014, 2015, 2019), and for elements under combined actions by Pham

et al. (2012, 2014, 2015), (2016), and Torabian et al. (2015, 2016). Interactive buckling was also investigated by Kwon et al. (2009), Dinis et al. (2012), Dinis and Camotim (2015), Cava et al. (2016), Martins et al. (2017a, 2018), Ye et al. (2018c), and Matsubara et al. (2019). Pham and Hancock (2013) and Shifferaw and Schafer (2014) developed the DSM for the design of plain channel and angle sections, respectively. More recently, Schafer (2019) provided additional context on how DSM-based design fits within past design knowledge and summarised the current state of development and future potential of the approach.

Since the DSM depends mainly on the buckling signature curve concept, a significant number of research studies have been put forward presenting various methods of elastic buckling analysis for thin-walled sections. Finite Elements (FE) can be used to carry out an elastic buckling analysis of CFS sections which are susceptible to local/distortional, global buckling and their interactions. Other methods for the calculation of elastic buckling stresses have been developed:

- The constrained finite strip method (cFSM) was proposed by Ádány from Budapest University of Technology and Economics and Schafer from Johns Hopkins University (2006b, 2006c).

- The finite strip method (FSM) for shear buckling was developed by Pham and Hancock at the University of Sydney (2013).

- The general beam theory (GBT) was mainly developed by Gonçalves et al. (2010) at the Universidade de Lisbon.

- A novel modal decomposition methodology based on polarisation was proposed by Becque and Li at the University of Sheffield (2015) to construct the individual local, distortional, and global buckling modes of a thin-walled structural element under a given loading.

Recent developments on elastic buckling and modal decomposition can be found in Hancock and Pham (2015), Ádány (2016), Naderian and Ronagh (2015), and Becque et al. (2019).

2.3. OPTIMISATION OF CFS ELEMENTS

Although CFS elements are susceptible to local/distortional buckling, they can be more economical and efficient compared to similar hot-rolled sections, due to their high strength-to-weight ratio added to their flexibility in manufacturing various profiles and sizes through a cold-rolling or press-braking process at ambient temperature. The flexibility in CFS cross-sectional shapes provides an excellent opportunity to achieve higher load carrying capacities by optimising design solutions. However, this can be a challenging task due to typical manufacturing and end-use design constraints and the complex behaviour of CFS elements, which is controlled by combinations of local, global and distortional buckling modes. In general, optimisation of CFS members may aim to obtain an optimal cross-sectional shape without considering any restriction on the general shape of the sections (i.e. self-shape optimisation) (e.g. (Wang et al., 2016a, Madeira et al., 2015, Gilbert et al., 2012a, Gilbert et al., 2012b, Sharafi et al., 2014, Leng et al., 2011, Liu et al., 2004)), or determine optimum relative dimensions of a predefined cross-section (i.e. size optimisation) (e.g. (Leng et al., 2014, Wang et al., 2016b, Ye et al., 2016a, Lee et al., 2005, Magnucki et al., 2006, Ye et al., 2018d, Tran and Li, 2006, Adeli and Karim, 1997, Karim and Adeli, 1999, Ye et al., 2018a, Ma et al., 2015, Lee et al., 2006, Wang et al., 2016c, Tian and Lu, 2004, Ye et al., 2018c, Pastor et al., 2009)).

Different optimisation methods have been used for self-shape optimisation of thin-walled steel sections, including Genetic Algorithms (GA) (Gilbert et al., 2012a, Gilbert et al., 2012b, Wang et al., 2016a), the Direct Multi-Search (DMS) method (Madeira et al., 2015), graph theory, ant colony based algorithms (Sharafi et al., 2014), the gradient-based steepest descent method and simulated annealing (Leng et al., 2011). In most of these studies, a steel sheet with a predefined total width is allowed to be bent at a certain number of locations, while the DSM is generally adopted to estimate the compressive and bending capacity of the members. While a considerable enhancement of strength was reported in all aforementioned self-shape optimisation methods, they may lead to impractical complex shapes with high manufacturing costs and/or difficulty in connecting to other structural components (see Fig. 2.14).
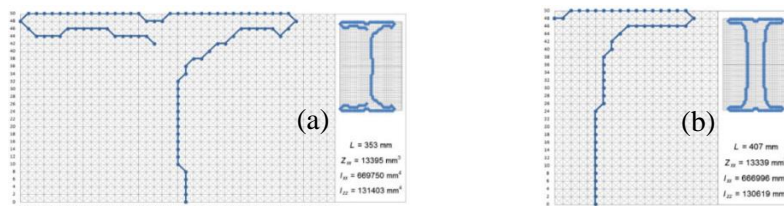
Fig. 2.14. Self-shape optimisation results on (a) open, and (b) close sections (Sharafi et al., 2014)

Early research on the size optimisation of CFS sections was started by Seaburg and Salmon (1971), who attempted to find the minimum weight of CFS hat-shaped sections based on the steepest descent method. Several investigations have also been conducted to optimise predefined standard CFS profiles, such as C channels, and I- and Z- shapes beams (e.g. (Karim and Adeli, 1999, Adeli and Karim, 1997, Ma et al., 2015)). It was shown that optimising the cross-sectional geometry of simply-supported CFS beams subjected to a uniformly distributed vertical load (Magnucki et al., 2006, Ye et al., 2016a, Ye et al., 2018d) or transverse load (Tran and Li, 2006) can substantially improve their flexural capacity. However, due to cross-sectional shape restrictions in size optimisation methods, the efficiency of the optimised sections may drop slightly compared to the self-shape optimisation solutions (Leng et al., 2014, Wang et al., 2016b).

Ye et al. (2016b) extended the effective width method in EC3 (CEN, 2005c, CEN, 2006a) to design a new type of 'folded-flange' cross-section by considering the possible occurrence of multiple distortional buckling modes. Subsequently, they used the Particle Swarm Optimisation (PSO) method to increase the maximum flexural capacity of different cross-sectional prototypes and demonstrate the efficiency of the proposed folded flange sections. It was shown that, for the same amount of material, optimised folded-flange sections can provide a bending capacity which is up to 57% higher than their standard counterparts. In another study, Ye et al. (2016a) adopted the Particle Swarm Optimisation (PSO) method to develop CFS beam sections with maximum flexural capacity, while the EC3 (CEN, 2005c, CEN, 2006a) design regulations and a number of manufacturing limitations were considered as design constraints. In a follow-up study, Ye et al. (2018a) proposed an advanced shape optimisation framework to achieve maximum energy dissipation of CFS sections in uniaxial bending by providing a link between detailed nonlinear finite element analyses and a PSO algorithm.

Various size optimisation methods have been also used to increase the compressive capacity of CFS axial members, such as Genetic Algorithms (GA) (Ma et al., 2015, Lee et al., 2006), Particle Swarm Optimisation (PSO) (Ye et al., 2018c) and the Hough Transform (Wang et al., 2016c). Lee et al. (2006) and Tian and Lu (2004) optimised the geometry of CFS columns under compressive axial loads and proposed optimum design curves for different prescribed load levels. The local-flexural buckling strength of single CFS channels and the global buckling strength of CFS storage pallet racking cross-sections, determined according to the relevant part of EC3 (CEN, 2005c), have been also optimised by Ye et al (2018c) and Pastor et al. (2009), respectively. In both studies, the adequacy of the optimum cross-sections was examined by detailed FE analysis and experiments (see Fig. 2.15).
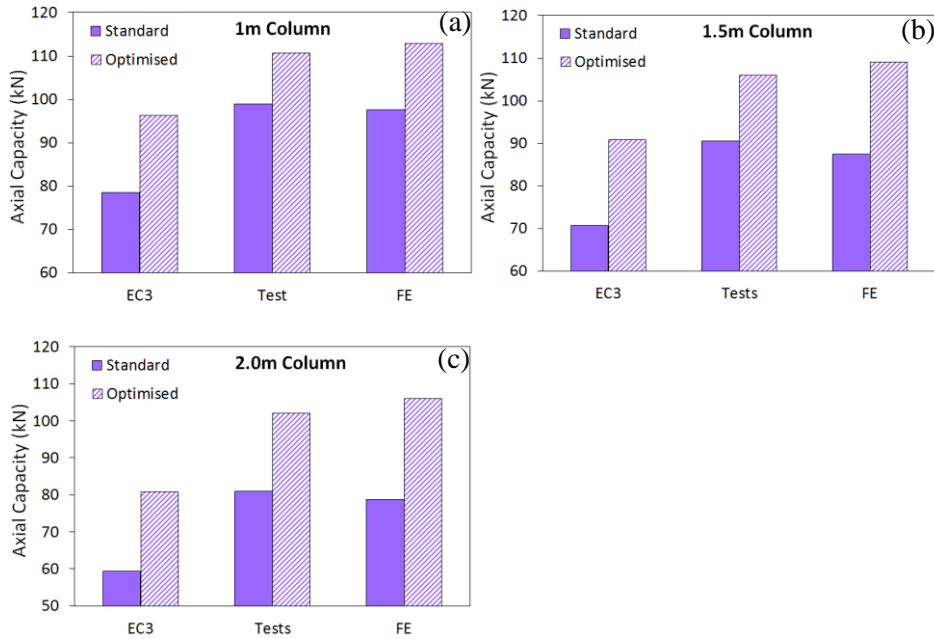
Fig. 2.15. Comparison between the compressive strength of the standard and the optimised lipped channels using the same amount of material (Ye et al., 2018c)

2.4. SEISMIC BEHAVIOUR OF CFS MEMBERS

The application of CFS members as main load-bearing components in seismic applications is limited to portal frames and low-rise stud wall frame systems with low energy dissipation capacity and ductility (Dubina D et al., 2012). As discussed in Section 2.1, CFS cross-sections with large width to-thickness ratios are generally susceptible to premature instabilities (i.e. local and distortional buckling) compared to their conventional hot-rolled counterparts. Therefore, conventional CFS structures (i.e. connections and frames) cannot provide sufficient strength and ductility for high seismic applications. This implies that the performance of CFS structures is not generally consistent with the strong-column weak-beam, and the strong-connection weak-components philosophies specified by seismic design codes (ANSI/AISC 341-16, 2016), due to the lack of ductility in elements and connections.

Existing studies on the cyclic performance of CFS elements are still limited in the literature. Calderoni et al. (2009a), as a pioneer in this field, conducted cyclic tests on CFS beams to evaluate the hysteretic behaviour and energy dissipation capacity. It was demonstrated that the strength degrades rapidly in the initial cycles because of local buckling and then remains almost constant in subsequent cycles due to the buckling deformations spreading throughout the cross-sections. Further experiments were conducted by Padilla-Llano et al. (2014, 2016) to investigate the cyclic behaviour and energy dissipation capacity of CFS elements experiencing local, distortional or overall buckling, as shown in Fig. 2.16. Abrupt drops in the

strength after the peak load/moment were observed, with subsequent stiffness degradation and pinching of the responses (i.e. load-deformation and moment-rotation), associated with straightening of the buckling deformations during loading direction reversals. It was also found that the energy dissipation capacity decreases with increasing cross-sectional slenderness.

Sabagh et al. (2011, 2012a) used improved detailing for connections, such as longitudinal and transverse stiffeners, to postpone failure in the CFS beam, and developed new CFS cross-sections with bent flanges to increase the capacity of the CFS cross-sections. They also counted on a bolt slip mechanism to dissipate the seismic energy and prevent premature buckling in CFS elements. More recently, CFS lipped channel and curved channel beams were tested in a moment-resisting connection subjected to a cyclic loading regime (Serror et al., 2016a). It was shown that the CFS beams with curved section are capable of providing higher ductility and dissipating more energy.
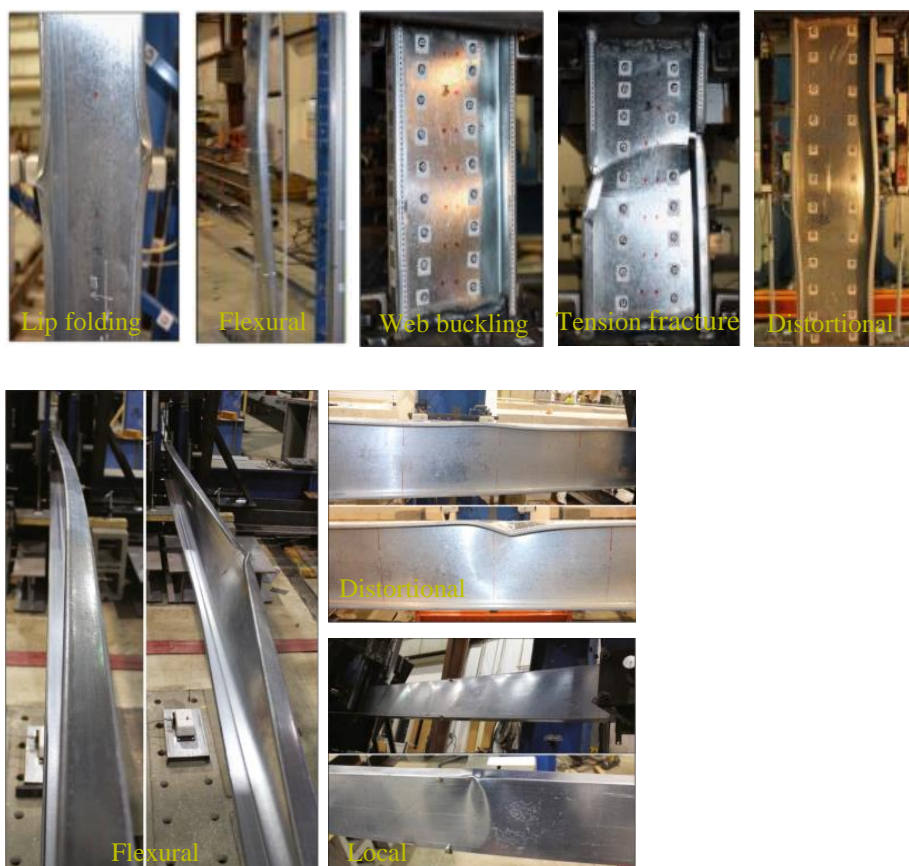
Fig. 2.16. Failure modes captured from cyclic tests on CFS column and beam elements (Padilla-Llano et al., 2014, Padilla-Llano et al., 2016)

2.5. CFS CONNECTIONS

A wide range of connections is currently used in the CFS construction industry using bolts or self-tapping screws (Yu and LaBoube, 2010). A relatively new development is the emergence of bolted connections to assemble CFS members in portal frames, due to their efficient assembly. These CFS portal frames are used in industrial and agricultural buildings with large open spans, warehouses and hangars. However, their development is held back by a lack of knowledge about the structural behaviour of the connections and a consequent lack of available design guidance. The most commonly used CFS bolted connections are: 1) bolted moment connections (i.e. beam-to-column with gusset plate joints (Fig. 2.17 (a)), eaves joints (Fig. 2.17 (b)), and rafters with apex joints (Fig. 2.17 (c))); 2) bolted axial connections used in truss elements (Fig. 2.18), and 3) sleeve or overlapped connections (i.e. beam-to-beam or purlins) (Fig. 2.19).
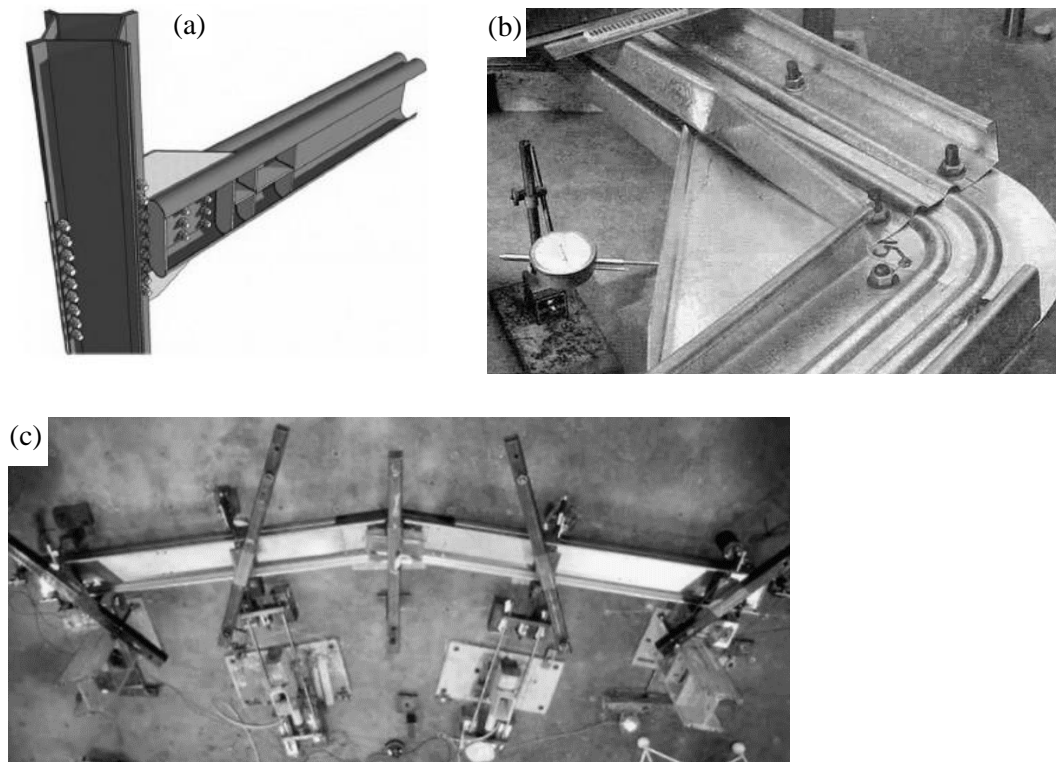
Fig. 2.17. Bolted moment connections: (a) Beam-to-column with gusset plate joints (Bagheri Sabbagh et al., 2012b), (b) eaves joints (Kirk, 1986), and (c) rafters with apex joints (Lim and Nethercot, 2003a)
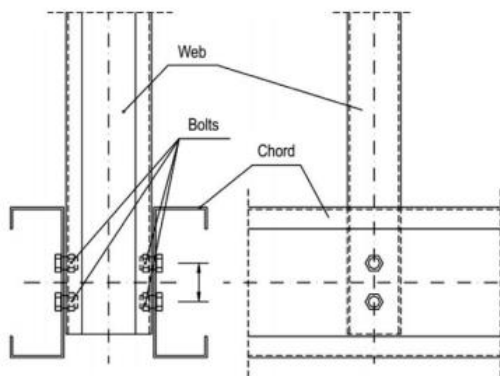
Fig. 2.18. CFS truss bolted connection (Zaharia and Dubina, 2006)

Fig. 2.19. Continuous lapped Z–purlin configuration (Pham et al., 2014)

2.5.1. Bolted moment connections

CFS portal frame connections are often executed by connecting the webs of both members to a gusset plate and these are economical and easy to assemble. However, the fact that a connection is made through the webs of the connecting members only, leaving the flanges unconnected, has obvious repercussions for the behaviour of the connection, both in terms of stiffness (they typically act as semi-rigid connections with a stiffness governed by bolt hole elongation properties) and strength. With respect to the latter, in a connection with properly sized bolts and gusset plates failure typically takes place within the connecting member, adjacent to the connection, as a result of cross-sectional instability (Mojtabaei et al., 2018, Lim and Nethercot, 2004b, Sabbagh et al., 2010). This instability is promoted by the introduction of both moment and shear through the web whereby the local stress concentrations at the bolt locations have to potential to further reduce the capacity below the calculated cross-sectional values. Unfortunately, current design standards do not account for this type of failure, which was first observed by Kirk (1986) in tests on CFS back-to-back lipped channel portal frame connections as early as 1986. It is also consistent with observations reported by Chung and Lau (1999) on CFS beam-to-column bolted moment connections.

Lim (2001) conducted a comprehensive study on CFS bolted moment connections, which also considered various failure modes of the bracket: overall lateral-torsional buckling, as well as local buckling modes of the bracket components. A large part of the study, however, was devoted specifically to local web buckling of the connecting members. With this purpose, an experimental program was carried out consisting of four apex connections tested in a four-point bending configuration, described in detail in (Lim and Nethercot, 2003a). The tests revealed a profound influence of the bolt group length (i.e. the distance between the centre lines of the outer bolt rows) on the capacity of the connections. The authors explained this by pointing out the reduced magnitude of the bolt forces in the longer connection. While this is of course true, the change in inclination of the bolt force in the shorter connection should also be noted. While the bolt forces in the first row of the longer connection are near vertical, a comparatively much larger horizontal component is introduced into the portion of the web adjacent to the connection in the shorter bolt group. This horizontal force adds to the compression already present as a result of bending and increases the risk of local buckling in the web of the connected member just outside the bolt group.

Lim et al. (2016b) dedicated a further study to the development of a design methodology for this type of connections based on the Direct Strength Method (DSM). The authors borrowed ideas from previous work by Baigent and Hancock (1982), who conducted experiments on frames composed of single CFS channels with rigid connections. Baigent and Hancock drew attention to the effect of the bi-moment in the channels, which reduced their capacity below the major axis bending capacity. They argued that the bi-moment is present because the bending moment is introduced into the web, which has an eccentricity relative to the shear centre, with the numerical value of the bi-moment being equal to the product of the moment and the distance from the web to the shear centre. This bi-moment causes bending in each of the flanges within their own plane, but in opposite directions for the top and bottom flanges. Lim et al. (2016b) argued that this bi-moment is also important in back-to-back channels where a moment is introduced in the web of each individual channel. Consequently, they proposed to calculate the cross-sectional capacity from the DSM local buckling equations, but using an elastic buckling stress obtained from a finite strip analysis while applying the stress distribution resulting from a combined bending moment and bi-moment. It was concluded that this results in conservative predictions for bolt-groups with reasonable lengths with the margin of safety increasing with the bolt group length.

In other noteworthy research, Chung and Lau (1999) tested six CFS connections under a linearly varying moment in the beam. Four of the connections failed by lateral-torsional buckling of the gusset plate, while the others failed by local buckling of the web. Wong and

Chung (2002) carried out 20 tests on both column base connections and beam-column connections. They observed four different failure modes, namely bearing failure of the bolts, lateral-torsional buckling of the gusset plate, flexural failure of the gusset plate and flexural failure of the beam. The latter mode corresponded to the local buckling failure of the web previously discussed. Öztürk and Pul (2015) carried out four-point bending tests on apex connection between back-to-back sigma channel rafters. Different connection configurations and stiffening arrangements of the bracket were considered. Similarly, the moment-rotation behaviour of the eaves, apex and base connections was evaluated experimentally and numerically by Rinchen and Rasmussen (2019). The study focused on local buckling of the bracket and local buckling of the beam web as failure modes. Bučmys et al. (2018) developed a component model for CFS joints consisting of three rotational springs, representing the stiffnesses of the bolt group in the beam, the gusset plate and the bolt group in the column. A comparison with the experiment showed that the stiffness of the tested joints was well predicted by the model.

A number of research projects have focused on the seismic performance of CFS bolted moment connections. Sabbagh et al. (2012b) conducted cyclic tests to evaluate the hysteretic behaviour of CFS beam-to-column bolted connections. The test specimens had an unusual cross-sectional shape with curved flanges. Unstiffened webs, as well as web reinforced with welded-in stiffeners, were considered. More recent studies by Ye et al. (2019c) demonstrated that the beam cross-sectional shape and slenderness, the gusset plate thicknesses and the bolt distribution can also significantly improve the seismic performance of bolted moment connections (by up to 250%). In a follow-up study, it was shown that incorporating a bolt friction slip mechanism can result in up to 200% higher ductility, energy dissipation capacity and damping coefficient of the connections, especially for CFS beams with thinner plates (Eurocode classes 3 and 4) (2019b). Sato and Uang (2009) also demonstrated that the ductility of CFS special bolted moment frames, as defined by the AISI S110 standard, can be enhanced through bearing action and slip of the bolts.

2.5.2. Bolted axial connections

CFS bolted connections under tensile loads are frequently used in trusses and lateral bracing systems (Zeynalian et al., 2016, Reda et al., 2019). They can be also employed in CFS frames to transfer the axial compressive loads of the column to the base (Mojtabaei et al., 2018, Phan et al., 2017b, McCrum et al., 2019). The ultimate load-carrying capacity of a bolted connection is governed by one of many possible failure modes such as tear-out, bearing, net-section fracture and bolt shear failure (Yu and LaBoube, 2010), as shown in Fig. 2.20.

In previous studies, it was frequently reported that non-uniform stress distribution exists in a tension member adjacent to a connection in which not all elements of the cross-section are directly connected. This phenomenon is commonly referred to as shear lag effect. The shear lag effect was first observed by Munse and Chesson (1963) in tension members with bolted or riveted end connections and a reduction factor for the net section was proposed. Further experimental and analytical studies were conducted on tension members with both bolted and welded end connections and design recommendations were made by Kulak and Wu (1997) and Easterling and Gonzalez (1993). Orbison et al. (2002) performed experiments on short tension member specimens to investigate the influence of varying connection eccentricity and length on the load capacity of the members. More recently, Teh et al. (2013a, 2012, 2013b) experimentally examined the accuracy of the equations specified by the North American and Australasian codes for determining the net section tension capacity of CFS angle braces bolted at one leg, flat steel sheets, and channel braces. Subsequently, more accurate design equations were proposed. In a follow-up study (Teh and Yazici, 2013), it was concluded that the net section is controlled by three factors: (i) the in-plane shear lag associated with the stress concentration around a bolt hole, (ii) the out-of-plane shear lag which exists in a bi-symmetric I-section bolted at the flanges only, and (iii) the bending moment resulting from the connection eccentricity with respect to the neutral axis.

The equations for the tensile capacity of CFS sheet in bolted connections with oversized holes and staggered bolts prescribed by the North American specifications (AISI S100-12, 2012) were also modified by Yu et al (2013) and Teh et al. (2012), respectively. In another study, Bolandim et al. (2013) used the results of a comprehensive experimental program to perform a reliability analysis on the tensile capacities of CFS members in bolted connections and subsequently proposed a smaller safety factor compared to the one specified by the AISI.
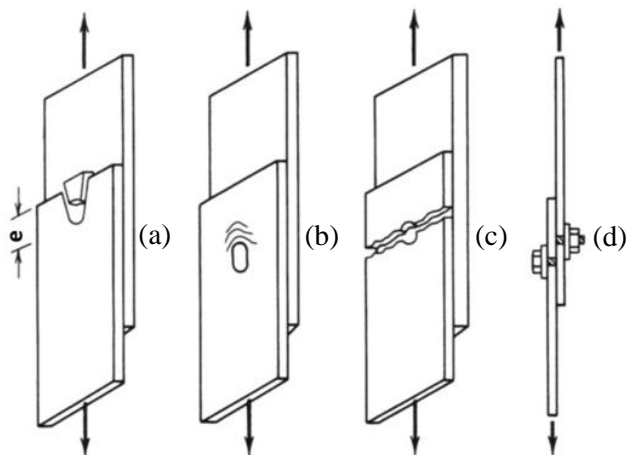
Fig. 2.20. Failure modes of bolted connections: a) tear-out failure of a sheet, b) bearing failure of a sheet, c) tension failure of net section, d) bolt shear failure (Yu and LaBoube, 2010)

2.6. CFS FRAME SYSTEMS

In general, there are two different types of CFS frame systems in the building industry, namely the shear/stud wall frame system, and the CFS portal frame.

The shear/stud wall frame system is widely used in residential low-rise and mid-rise buildings. The lateral performance of various CFS shear/stud wall frames has been investigated in an extensive number of experimental and analytical studies. Fülöp and Dubina (2004) conducted experiments on CFS stud wall frames to investigate the effects of different configurations, including diagonal strap braces, door openings and sheathing with a corrugated sheet or an Oriented Strand Board (OSB). The results showed that pinching behaviour can significantly change the energy dissipation capacity of the system, depending on the configuration used. Similarly, the behaviour of stud wall systems sheathed with calcium silicate board, gypsum, plywood and ply-bamboo was investigated experimentally by Miller and Pekoz (1994), Serrette et al. (1997), Pan and Shan (2011), Lin et al. (2014) and Gao and Xiao (2017). Recently, the effects of stud dimensions, stud spacing, fastener spacing and sheathing material were assessed experimentally by Ye et al. (2015, 2016c). Mohebbi et al. (2015) conducted an experimental program to investigate the behaviour of CFS shear walls consisting of single and double-sided steel sheathing, and reported different failure modes, such as sheathing-to-frame connection failure and stud buckling. They also showed that bearing failure of sheathing screws provides higher energy dissipation compared to other types of failure. In a follow-up study conducted by Mohebbi et al. (2016), the seismic performance of CFS stud walls sheathed with steel sheets and cladded with gypsum and fibre cement boards were experimentally investigated. It was demonstrated that using steel sheet along with cladding board leads to a more efficient design and an increased energy dissipation capacity compared to those with no cladding board. The performance of shear walls with different bracing systems, such as straps, steel sheets and K-bracing were evaluated experimentally in full-scale specimens under cyclic and monotonic loadings (Moghimi and Ronagh, 2009, Lin et al., 2014, Zeynalian et al., 2012).

Shamim et al. (2013) presented an experimental investigation on single and double storey steel-sheathed CFS shear walls using dynamic shake table tests. Experimentally validated models of CFS multi-storey frames with a typical V-braced system were analysed under a series of earthquake ground motions using linear time history method to examine their behaviour in a moderate earthquake (Dao and Lindt, 2013). Both test results and numerical analysis showed that the proposed system has acceptable ductility due to the use of innovative screwed plate connections. Two- and three-storey CFS shear walls with reinforced and

conventional end studs were tested by Wang and Ye (2016) under cyclic loading conditions, and their behaviour was compared. Full-scale shake table tests on a CFS framed building were conducted by Nakata et al. (2012) and Schafer et al. (2016) (see Fig. 2.21). The experimental programme was followed by a comprehensive numerical study to address characterisation and modelling of individual structural components including stud walls, beams and columns, screwed connections, and the whole building. Based on their findings, more detailed numerical models are needed to accurately simulate the behaviour of a full-scale CFS building system subjected to seismic load.

Fig. 2.21. A full-scale shake table test on a CFS framed building (Nakata et al., 2012, Schafer et al., 2016)

The above-mentioned studies have shown that the conventional CFS stud/shear wall system can normally maintain its lateral and vertical load-bearing capabilities up to the drift limits specified by most seismic codes. However, CFS stud walls may exhibit poor ductility due to the distortional buckling of the stud elements and the resulting rapid decrease in their load-bearing capacity (Xu et al., 2018). Fiorino et al. (Fiorino et al., 2016) conducted shake table tests on a full-scale two-storey sheathing-braced CFS building, where the results demonstrated the acceptable seismic lateral resistance of these structures under seismic loads. However, monotonic and cyclic tests on full-scale strap-braced CFS walls showed that the stud wall system may exhibit a non-ductile seismic performance (e.g. due to gusset-to-track connection failure) (Fiorino et al., 2016). In addition, using a CFS shear wall system restricts flexibility for space planning (e.g. opening sizes and proportions) and future alterations. Therefore, CFS portal frames made of beams, columns and moment-resisting connections are increasingly used as an alternative to CFS shear walls.

Several research projects have investigated the structural performance of CFS portal frames. Lim and Nethercot (2004b) and Yu et al. (2005) conducted experimental and numerical studies on the ultimate strength of CFS sub-frames. Dundu (Dundu, 2011) proposed an analytical design approach for structural components of a CFS portal frame, including the design of beams, columns and beam-columns according to the effective width method and the design of bolted moment connections. The geometry of CFS portal frames subjected to wind loads was

optimised by Phan et al. (2013a) using GA. In a follow-up study, Phan et al. (2013b) considered the effect of serviceability limits on the optimum design of CFS portal frame.

Comprehensive studies at the element and structural levels were conducted by Rasmussen et al. (2016) and Zhang et al. (2015, 2016a, 2016b) aiming to predict the behaviour of CFS members and portal frames. The researchers first developed a beam element using the Finite Element (FE) method which can take into account the deformations caused by local/distortional buckling modes. It was observed that considering local/distortional buckling deformations may lead to a noticeable reduction in the stiffness of CFS members. The calculated results were then validated against the results of FE models with shell elements. The developed element was used for the structural members (i.e. beam and columns) in locally and/or distortionally buckled frames. The results showed that the proposed method can accurately capture the true deformations and internal forces/moments of CFS portal frames.

Wrzesien et al. (2016) investigated the stressed skin diaphragm action in CFS portal frames by considering different types of joints and the existence of roof sheeting, and made a comparison with experimental results. It was demonstrated that the internal portal frame with roof sheeting could carry approximately three times more lateral load than the bare frame because of the stressed skin action which developed in the building. It was also shown that the deflection of the internal frame at the serviceability limit state could be significantly reduced (by up to 90%) compared to the bare frame. In another study, Phan et al. (2015) optimised the geometry of a CFS portal frame by considering the effect of stressed skin action. The results indicated that the proposed optimisation can considerably reduce the required structural weight of the CFS frame system by up to 53%.

The behaviour of CFS moment-resisting frames was investigated experimentally and numerically by several researchers. Sabbagh et al. (2010) evaluated the lateral performance of full-scale portal frames with concrete-filled CFS columns and CFS back-to-back beams, and they reported acceptable seismic performance (see Figure 2.22 (a)). Mojtabaei et al. (2018) investigated the seismic performance of innovative CFS moment-resisting portal frames consisting of two box-shaped columns, a back-to-back lipped channel beam section and moment-resisting bolted connections (see Figure 2.22 (b)). It was shown that the proposed system can offer good seismic performance provided the main structural elements are appropriately designed. Blum and Rasmussen (2019a) conducted numerical and experimental studies on a CFS portal frame composed of back-to-back lipped channel sections bolted through the webs, with additional back-to-back L-brackets bolted through the webs at the connections (see Figure 2.22 (c)). Experimentally validated FE models were then used to investigate the effects of the column-to-base and knee brace-to-column connection stiffness

on the frame capacity and behaviour. More recently, McCrum et al. (2019) investigated the seismic behaviour and failure modes of a single storey moment-resisting CFS portal frame subjected to cyclic loading conditions, as shown in Fig. 2.22 (d).

The progressive collapse behaviour of CFS portal frames in the event of fire was investigated by Johnston et al. (2015b, 2015a). The inclusion of accurate joint rigidity and geometric non-linearity (second-order analysis) were found to be key parameters in the modelling which greatly affect the collapse behaviour of the portal frame at elevated temperatures.
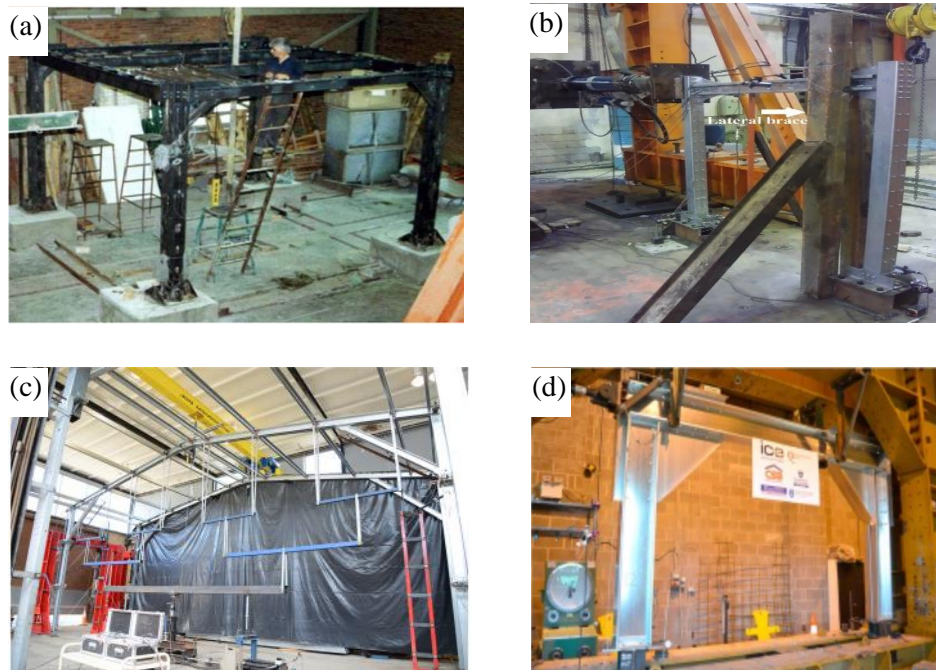
Fig. 2.22. Tested CFS moment-resisting portal frames by (a) Sabbagh et al. (2010), (b) Mojtabaei et al. (2018), (c) Blum and Rasmussen (2019b), and (d) McCrum et al. (2019)

2.7. SUMMARY

Based on the review of the literature discussed above, the following gaps in knowledge have been identified and will be addressed in more detail in the following chapters:

- It is apparent that the flexibility in the manufacturing of CFS sections allows the development of innovative shapes with improved resistance to local and distortional buckling. CFS sections can be stiffened by using intermediate stiffeners, edge stiffeners and increasing the folds within cross-sections. In addition, the manufacturing and constructional restraints should be taken into account when innovative cross-sections are developed. It should be noted that objectives 1, 2, 5, and 6 of thesis were formed based on this gap of knowledge.

- The literature is mainly focused on the Ultimate Limit State (ULS), which conventionally represents the ultimate strength of CFS structures under extreme load events. However, due to the high slenderness of CFS elements, the Serviceability Limit State (SLS) is often more critical for CFS structures and therefore needs to be investigated. This gap of knowledge shaping objective 1 of thesis is addressed in Chapter 4.

- A more practical methodology should be developed to optimise CFS beam-column elements subjected to different combinations of bending and axial compressive force. This gap of knowledge forming objective 1 of thesis is addressed in Chapter 3.

- While the behaviour and capacity of CFS bolted connections have been extensively investigated, there is still a need to investigate their behaviour in more depth and propose a safe and reliable design methodology to obtain their capacities. This gap of knowledge forming objective 3 of thesis is addressed in Chapter 5.

- While CFS structural components have previously been optimised based on their buckling resistance, they can also be optimised to improve their post-buckling behaviour, aiming to increase their energy dissipation capacity and ductility. This offers great potential to improve the seismic performance of CFS framing, sub-assemblies and full-scale systems. The aforementioned gap of knowledge shaping objectives 2 and 5 of thesis is addressed in Chapters 6 and Appendix A.

- The research on seismic behaviour of CFS bolted moment-resisting connections is still limited. An Efficient seismic design method for such connections should be developed by considering various key parameters (e.g. the beam cross-sectional shape and thickness, the gusset plate thickness, the slip resistance of the bolts, the bolt configuration and the bolt-group length). This gap of knowledge forming objective 4 of thesis is addressed in Appendix B.

- CFS elements and portal frames have both been individually optimised by other researchers. However, there is a need to develop a coupled framework for element and structural level optimisation of CFS portal frames, under serviceability limit state (SLS) and ultimate limit state (ULS) conditions. The CFS elements and frame geometry can be simultaneously optimised to develop more efficient CFS frames with reduced structural weight. This gap of knowledge forming objective 4 of thesis is addressed in Appendix C.

CHAPTER 3

Shape Optimisation of Cold-Formed Steel Beam-Column Members

3.1. INTRODUCTION

The use of cold-formed steel (CFS) elements as the main load-bearing structural components are gaining popularity in the construction industry. Flexibility in the manufacturing of their cross-sectional shapes provides a unique opportunity to improve the load-carrying capacity of these elements, led to more efficient and economic structural systems. This chapter addresses parts of objective 1 and aims to offer a practical methodology for the optimum design of CFS beam-column members, with different lengths and thicknesses subjected to various load combinations (i.e. compression and bending). Proposing an optimum design for CFS beam-column member is considered as a novelty of this chapter. In addition, the methodology developed in this study uses, for the first time, an eccentric load to provide different combinations of loads. Optimisation process is carried out using Genetic Algorithm (GA) with respect to either cross-sectional or member resistance of CFS elements determined according to the Eurocode 3 (EC3) effective width method and global buckling reduction factors, respectively. Six different cross-sections including single and built-up channel sections are selected, and their relative dimensions and inclination of the lip stiffeners are considered as main design variables. To provide more practical beam-column elements, EC3 design constraints for the plate slenderness as well as a range of practical manufacturing and construction limitations are imposed on the selected cross-sections. Standard commercially available single and back-to-back lipped channel sections are taken as starting points of optimisation and used to assess the efficiency of the optimised sections. The results show that,

for the given plate width and thickness, beam-column members with optimised sections are capable to provide up to 193% higher strength compared to those with standard cross-sections.

3.2. BACKGROUND

Cold-formed steel (CFS) structural members are fabricated at room temperature from thin gauge steel sheets. They offer several advantages than conventional hot-rolled steel products such as a higher strength-to-weight ratio, high flexibility in manufacturing, light-weight and easier to handle, transport and install. Recently, CFS members are progressively used as main structural elements subjected to combined axial compression and bending moment known commonly as beam-column elements. The strength and failure mode of a CFS beam-column element are highly dependent on the cross-section stress distribution generated by combined actions (Torabian et al., 2015, Torabian et al., 2016, Zheng et al., 2015, Huang and Young, 2014, Mojtabaei et al., 2018). In practical situations, the bending moment applied on the compression elements are resulted from (i): axial compressions with eccentricity (e.g. stud wall systems) (Fig. 3.1(a)), (ii): combined axial compressions and end moments (e.g. moment-resisting frames) (Fig. 3.1(b)), (iii): combined axial compressions and distributed transverse loads (e.g. CFS structures under lateral load actions) (Fig. 3.1(c)). In the absence of either axial compression ($N_{Ed} = 0$) or bending moment ($M_{Ed} = 0$), CFS elements behave as a pure beam or column, respectively. However, due to the existence of inevitable imperfections in framed structures, all CFS members generally act as beam-column elements.

(a)   (b)   (c)
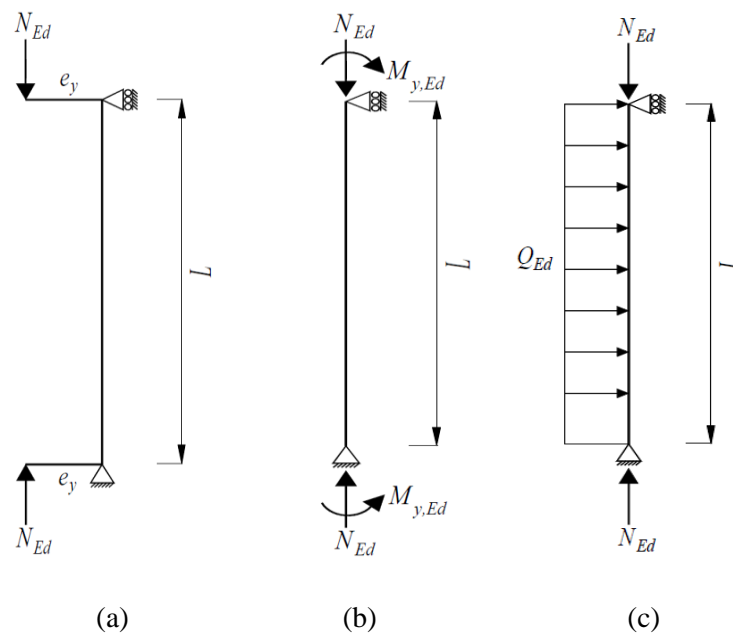
Fig. 3.1. Beam-column member subjected to; (a) axial compressions with eccentricity; (b) combined axial compressions and end moments; (c) combined axial compressions and distributed transverse loads

The behaviour of CFS beam-column members under different load combinations has been previously studied and compared with the available design codes. Torabian et al. (Torabian et al., 2015, Torabian et al., 2016) investigated experimentally the buckling resistance and failure modes of CFS beam-columns with lipped channel and Z sections under bi-axial moments and axial force. The results were then used to assess the reliability of the North American design standard (AISI S100-12, 2012), for predicting the strength of beam-columns, and to improve the current specification approach which utilizes a simple linear and conservative interaction equation. In other studies, experimental investigations were conducted on cold-formed stainless steel beam-columns with Square Hollow Section (SHS) and Rectangular Hollow Section (RHS) (Zheng et al., 2015, Huang and Young, 2014, Lui et al., 2014). It was demonstrated that while the codes' predictions are generally conservative, the European code (CEN, 2006b) provides quite conservative predictions for the beam-column specimens compared to the American Specification (SEI/ASCE-8-02, 2002) and Australian/New Zealand Standard (AS/NZS-4673) predictions.

Numerous research focused to improve the behaviour of CFS elements (i.e. beam and column) in terms of strength, stiffness, and energy dissipation by taking advantage of the high flexibility in cross-sectional shape. This was achieved through optimisation on their cross-sectional shapes for two different cases: (i) without any limitations on the general shape of the cross-section (i.e. unconstrained shape optimisation) (Liu et al., 2004, Leng et al., 2011, Gilbert et al., 2012a, Gilbert et al., 2012b, Sharafi et al., 2014, Madeira et al., 2015, Wang et al., 2016a), (ii) with a predefined cross-sectional shape (i.e. constrained shape optimisation) which is more practical and manufacturable (Adeli and Karim, 1997, Karim and Adeli, 1999, Tian and Lu, 2004, Lee et al., 2005, Magnucki et al., 2006, Tran and Li, 2006, Lee et al., 2006, Pastor et al., 2009, Leng et al., 2014, Ma et al., 2015, Ye et al., 2016a, Wang et al., 2016b, Wang et al., 2016c, Ye et al., 2018c, Ye et al., 2018a, Ye et al., 2018d, Mojtabaei et al., 2019b). Various optimisation methods have been employed to find the best design solutions for the CFS elements such as Graph Theory and Ant Colony (Sharafi et al., 2014), Hough Transform (Wang et al., 2016c), Genetic Algorithm (GA) (Wang et al., 2016a, Gilbert et al., 2012b, Lee et al., 2005, Ma et al., 2015), Particle Swarm Optimisation (PSO) (Ye et al., 2016a, Ye et al., 2018c, Ye et al., 2016b), Direct Multi-Search (DMS) (Madeira et al., 2015), Big Bang-Big Crunch (BB-BC) (Mojtabaei et al., 2019b), and simulated annealing and gradient-based steepest descent method (Leng et al., 2011). Ye et al. showed that the flexural capacity of CFS beams with standard sections can be noticeably enhanced by simply changing in cross-

sectional dimensions (2016a). To further improve the strength of the CFS beam element, they also optimised a wide range of cross-sectional shapes consisting of edge and intermediate stiffeners and folded-flanges (Ye et al., 2016b). Mojtabaei et al. (2019b) carried out optimisation to find the best design solutions for the CFS beam at both ultimate and serviceability limit state conditions. CFS beam sections were also optimised for maximum energy dissipation to improve the seismic characteristics of the commercially available section and subsequently make them competence in seismic applications (Ye et al., 2018a). The results of unconstrained shape optimisation on CFS columns (Leng et al., 2014) showed that the compressive capacity can be significantly increased (up to 140%) compared to standard cross-section, while this reaches 49% for those with practical constraints (Ma et al., 2015). Based on the results of constrained shape optimisation on CFS column, Lee et al. (2006) recommended optimum design curves for the various levels of load. In the other study conducted by Ye et al. (2018c), the compressive capacity of CFS lipped channel was optimised by considering the interactive buckling mode (i.e. local and flexural).

However, a very limited number of studies investigated the optimum design of CFS beam-column elements subjected to different load combinations. Wang et al. (2016a) and Parastesh et al. (2019) conducted shape optimisations using GA to increase the capacity of simply-supported CFS beam-columns with singly-symmetric open-section based on Direct Strength Method (DSM). However, their optimised sections have complex shapes, and therefore may not be suitable for practical applications. This study aims to provide a practical methodology for the optimum design of CFS beam-column members with different lengths and thicknesses subjected to various combinations of axial compression and uniform bending moment (see Fig. 3.1(a) and (b)). This can be a tedious task since the capacity of CFS element is simultaneously controlled by different types of instabilities (i.e. local, distortional and global buckling modes). The beam-columns are simply-supported so-called end-fork supports where twisting and lateral deflections are prevented, while free rotations and warping are permitted. Optimisation process is carried out using GA method with respect to either cross-sectional or member resistance of CFS elements determined according to the Eurocode 3 (EC3) effective width method and global buckling reduction factors, respectively (CEN, 2005e, CEN, 2005c, CEN, 2006a). Six different cross-sections including single and built-up channel sections are selected, and their relative dimensions and inclination of the lip stiffeners are considered as main design variables. To provide more practical beam-column elements, EC3 design constraints for the plate slenderness as well as practical manufacturing and construction limitations are imposed on the selected cross-sections. The strength of selected beam-columns and their resultant buckling modes are compared to those with the standard sections, and

subsequently, a trend in optimum shapes of the sections subjected to pure axial compression towards pure bending is discussed.

3.3. EUROCODE DESIGN PROCEDURE FOR BEAM-COLUMN MEMBERS

In this study, the strength of CFS beam-column elements are determined according to EN1993-1-1 (CEN, 2005e), EN1993-1-3 (CEN, 2005c), and EN1993-1-5 (CEN, 2006a) following two main steps: (i) cross-section resistance accounting for both local and distortional buckling modes; (ii) member resistance considering global instabilities. It should be noted that the flat widths of constituent plates of a cross-section are used to calculate the cross-sectional properties, and the effect of rounded corners is subsequently considered through a reduction factor.

3.3.1. Cross-section resistance

3.3.1.1. *Local buckling*

EC3 accounts for local buckling through effective width method, based on the fact that local buckling leads to a loss of compressive strength in the centre of a plate supported along both longitudinal edges or along the free edge of a plate supported along one longitudinal edge. Therefore, the corner zones remain as the main load-resistance parts of the cross-section. In general, local buckling causes the centroid of the effective cross-section to shift over a distance e_N relative to the original centroid of the gross cross-section, which affects the stress distribution. An iterative process is therefore required for calculations of the effective cross-section. Fig. 3.2 shows the effective areas of a lipped channel specified in solid black line under axial compression, bending about the major axis, and bending about the minor axis with either web in compression or tension.

(a)   (b)   (c)   (d)
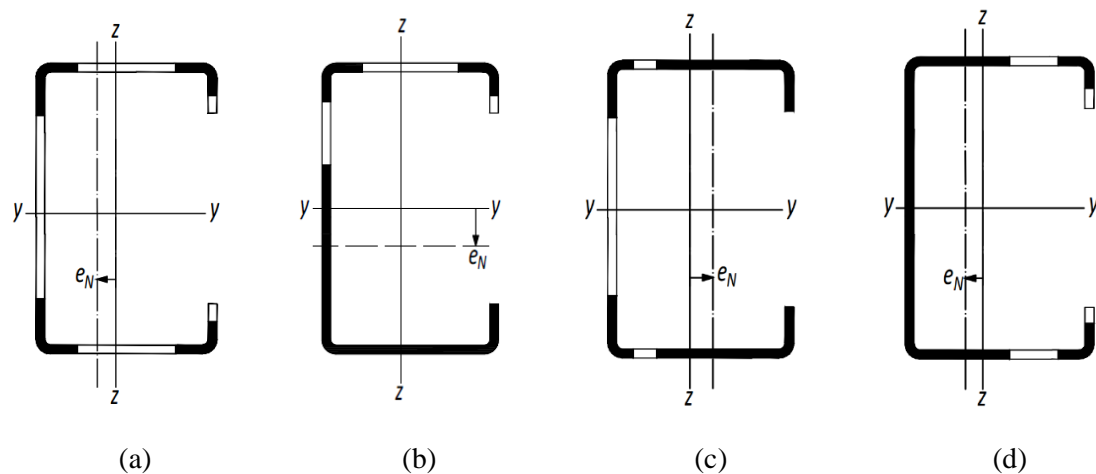
Fig. 3.2. Effective width of lipped channel subjected to; (a) axial compression; (b) bending about the major axis; (c) bending about the minor axis with web in compression; and (c) bending about the minor axis with web in tension

In the case of bending moment is applied about the weak axis leading web in compression (see Fig. 3.2 (c)), the initial yielding of the CFS cross-section is expected to emerge in the tension part of the flanges, while the compression part is still in elastic range. This results in an underestimation of cross-sectional capacity, and therefore, EN 1993-1-3 (CEN, 2005c) allows CFS cross-section to reserve the plastic stress in the tension zone without any strain limit (ε) until the furthest fibre in compressive zone reaches yield stress ($\sigma_c = f_y$). The inelastic reserve strength of the cross-sections is taken into account using the effective partially plastic section modulus $W_{pl,eff}$ obtained from a bilinear stress distribution (see Fig. 3.3).
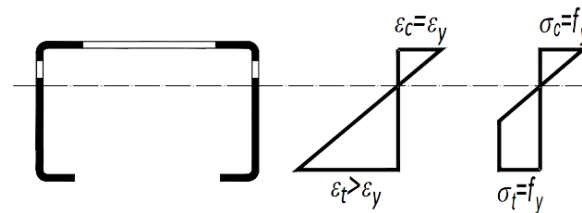
Fig. 3.3. Elastic reserved capacity for the CFS single channel subjected to minor bending moment with the web in compression

3.3.1.2. *Distortional buckling*

Distortional buckling is generally interpreted as flexural or flexural–torsional buckling of some of the constituent plates and is associated with both out-of-plane and in-plane movement of the fold-lines of the section. Distortional buckling can be seen as an example in the flange-lip subassembly of the lipped channel section (i.e. edge stiffener) or in the stiffened web of the channel section (i.e. intermediate stiffener). The effect of distortional buckling is taken into account by EC3 through reducing the thickness of the effective plate. This is based on the notion that the stiffener acts as a compression element supported continuously by elastic springs with the stiffness of K per unit length, as shown in Fig. 3.4. The elastic buckling stress of the stiffener on the elastic foundation ($\sigma_{cr,s}$) depends on the flexural stiffness of the adjacent plate and is calculated by:

$$\sigma_{cr,s} = \frac{2\sqrt{KEI_s}}{A_s} \tag{3.1}$$

where E is Young's modulus of the plate, I_s is the second moment of area of the stiffener about an axis through its centroid parallel to the plate, and A_s is the stiffener area.

Consequently, the distortional slenderness corresponds to yield stress of the material (f_y) and the elastic buckling stress of the stiffener ($\sigma_{cr,s}$):

$$\lambda_d = \sqrt{\frac{f_y}{\sigma_{cr,s}}} \tag{3.2}$$
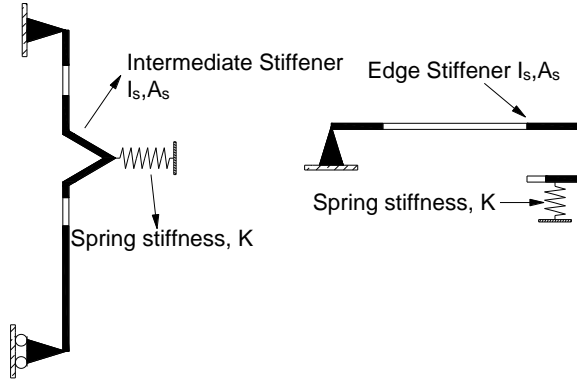
Fig. 3.4. Adopted EC3 model for the calculations of distortional buckling

3.3.1.3. *Cross-section check*

The cross-section of the beam-column element is required to carry combinations of the load without occurrence of either local or distortional buckling prior to considering the possibility of global buckling. Therefore, a CFS beam-column section under combined axial compression (N_{Ed}) and bending moments ($M_{y,Ed}$ and $M_{z,Ed}$) should satisfy the following requirement:

$$\frac{N_{Ed}}{N_{c,Rd}} + \frac{M_{y,Ed} + \Delta M_{y,Ed}}{M_{cy,Rd}} + \frac{M_{z,Ed} + \Delta M_{z,Ed}}{M_{cz,Rd}} \leq 1 \tag{3.3}$$

where $N_{c,Rd}$ is the design compression resistance, $M_{cy,Rd}$, $M_{cz,Rd}$ are the design moment resistances about major (y) and minor (z) axes, respectively. The additional moments $\Delta M_{y,Ed}$ and $\Delta M_{z,Ed}$ generated due to the shifts of centroidal axes of the effective cross-section relative to gross cross-section are given by:

$$\Delta M_{y,Ed} = N_{Ed}.e_{Ny} \tag{3.4}$$

$$\Delta M_{z,Ed} = N_{Ed}.e_{Nz} \tag{3.5}$$

where e_{Ny} and e_{Nz} are the shifts of y and z axes, respectively.

3.3.2. Member resistance

The resistance of the beam-column member deals with the problem of length, end-support, and restraint and requires the calculation of the global slenderness for pure compression and bending moment.

3.3.2.1. *Global buckling of a member subjected to pure compression*

The design buckling resistance of the compression member ($N_{b,Rd}$) for flexural about y and z axes, torsional or flexural-torsional buckling is determined by:

$$N_{b,Rd} = \frac{\chi A_{eff} f_y}{\gamma_{M1}} \tag{3.6}$$

where A_{eff} is the effective cross-sectional area, γ_{M1} is the partial safety factor prescribed by EC3, and χ is the reduction factor calculated for each type of instability and its corresponding slenderness ($\overline{\lambda}$) (i.e. flexural about y or z axis, torsional buckling, and flexural-torsional):

$$\chi = \frac{1}{\phi + \sqrt{\phi^2 - \overline{\lambda}^2}} \ , \ \begin{cases} \phi = 0.5[1 + \alpha(\overline{\lambda} - 0.2) + \overline{\lambda}^2] \\ \overline{\lambda} = \sqrt{\dfrac{A_{eff} f_y}{N_{cr}}} \end{cases} \tag{3.7}$$

where α considers the effect of imperfections through an appropriate buckling curve (e.g. buckling curve about minor axis z is used for the case of torsional or flexural-torsional buckling). N_{cr} is the elastic critical buckling load calculated for the relevant buckling mode:

Flexural about y: $$N_{cr,Fy} = \frac{\pi^2 EI}{L_{cr}^2} \tag{3.8}$$

Flexural about z: $$N_{cr,Fz} = \frac{\pi^2 EI}{L_{cr}^2} \tag{3.9}$$

Torsional: $$N_{cr,T} = \frac{1}{i_0^2}(GI_t + \frac{\pi^2 EI_w}{L_{cr}^2}) \tag{3.10}$$

Flexural-torsional: $$N_{cr,FT} = \frac{N_{cr,Fy}}{2\beta}[1 + \frac{N_{cr,T}}{N_{cr,Fy}} - \sqrt{(1 + \frac{N_{cr,T}}{N_{cr,Fy}})^2 - 4\beta\frac{N_{cr,T}}{N_{cr,Fy}}}] \tag{3.11}$$

In the above equations, I is the second moment of area of the gross cross-section, I_t and I_w are the torsional and warping constants of the cross-section (see Appendix A for the

calculation of warping constant), L_{cr} is the buckling length for relevant buckling mode, and $i_0 = i_y^2 + i_z^2 + y_c^2 + z_c^2$ is the polar radius of gyration (where i_y and i_z are the radius of gyration of the gross cross-section about the y and z axes, respectively, and y_c and z_c are the shear centre coordinates). Also, G is the shear modulus, and β is taken equal to $1 - (\frac{y_c}{i_0})^2$.

It is worth mentioning that EC3 (CEN, 2005e) implicitly accounts for the effects of applied compression force (N_{Ed}) and low slenderness of the member ($\bar{\lambda}$) on the global buckling resistance. For $N_{Ed}/N_{cr} \leq 0.16$ and $\bar{\lambda} \leq 0.2$, the reduction factor is ignored ($\chi = 1$) and only a cross-sectional check is required.

3.3.2.2. *Global buckling of a member subjected to pure bending*

For the case of laterally unbraced CFS elements subjected to major axis bending moment, out-of-plane lateral-torsional buckling may govern the behaviour and consequently decrease the design buckling resistance. Based on EN 1993-1-1 (CEN, 2005e), the design lateral-torsional buckling resistance moment ($M_{b,Rd}$) is determined by:

$$M_{b,Rd} = \chi_{LT} W_{eff,y} f_y / \gamma_{M1} \qquad (3.12)$$

where $W_{eff,y}$ is known as the effective section modulus about y axis, and χ_{LT} is the reduction factor taking into account lateral-torsional buckling:

$$\chi_{LT} = \frac{1}{\phi_{LT} + (\phi_{LT}^2 - \bar{\lambda}_{LT}^2)^{0.5}} \quad , \quad \begin{cases} \phi_{LT} = 0.5[1 + \alpha_{LT}(\bar{\lambda}_{LT} - 0.2) + \bar{\lambda}_{LT}^2] \\ \bar{\lambda}_{LT} = \sqrt{\dfrac{W_{eff,y} f_y}{M_{cr}}} \end{cases} \qquad (3.13)$$

where $\bar{\lambda}_{LT}$ is the cross-sectional slenderness for lateral-torsional buckling, M_{cr} is the critical moment, and α_{LT} reflecting the effect of imperfections is taken equal to 0.34 for buckling curve b. Similar to the elements under pure compression, EN 1993-1-3 (CEN, 2005c) recommends to ignore lateral-torsional buckling ($\chi_{LT} = 1$) for $\bar{\lambda}_{LT} \leq 0.4$ and $M_{Ed,y}/M_{cr} \leq 0.16$. The critical moment of a simply-supported CFS element (with free warping and rotation about minor axis z) subjected to end moments (e.g. see Fig. 3.1 (b)) is calculated by (Simões da Silva et al., 2010):

$$M_{cr} = \frac{\pi}{L}\sqrt{EI_z(GI_t + \frac{\pi^2 EI_w}{L^2})} \qquad (3.14)$$

where EI_z, GI_t, EI_w are the flexural rigidity about minor-axis, torsional rigidity, and warping rigidity, respectively. It should be noted that the CFS section with adequate restraint to the compression flange, and Square Hollow Sections (SHS) provide high torsional rigidity (GI_t) leading to prevent lateral-torsional buckling.

3.3.2.3. *Member check*

Based on Eurocode, the beam-column members which are subjected to combined bending and axial compression should satisfy the following equations:

$$\frac{N_{Ed}}{\chi_{Fy}N_{Rk}/\gamma_{M1}} + k_{yy}\frac{M_{y,Ed} + \Delta M_{y,Ed}}{\chi_{LT}M_{y,Rk}/\gamma_{M1}} + k_{yz}\frac{M_{z,Ed} + \Delta M_{z,Ed}}{M_{z,Rk}/\gamma_{M1}} \leq 1 \qquad (3.15)$$

$$\frac{N_{Ed}}{\chi_{Fz}N_{Rk}/\gamma_{M1}} + k_{zy}\frac{M_{y,Ed} + \Delta M_{y,Ed}}{\chi_{LT}M_{y,Rk}/\gamma_{M1}} + k_{zz}\frac{M_{z,Ed} + \Delta M_{z,Ed}}{M_{z,Rk}/\gamma_{M1}} \leq 1 \qquad (3.16)$$

with

$$\begin{aligned} N_{Rk} &= f_y A_{eff} \\ N_{y,Rk} &= f_y W_{eff,y} \\ N_{z,Rk} &= f_y W_{eff,z} \end{aligned} \qquad (3.17)$$

In Equations 3.15 and 3.16, χ_{Fy}, χ_{Fz} are the reduction factors for flexural buckling about y and z axes obtained from Equation 3.7. k_{yy}, k_{yz}, k_{zy}, and k_{zz} are the interaction factors which can be calculated using either Method 1 (Annex A) or Method 2 (Annex B) of EN1993-1-1 (CEN, 2005e). While the general formulae are the same for both methods, the main difference is in terms of interaction factors used for each method. In this study, since the specific coefficients used in Method 1 possess a wide range of applicability, Method 1 is preferably selected and explained in Appendix 3.2.

3.4. DEFINITION OF THE OPTIMISATION PROBLEM

This section is aimed to present a practical design methodology for the optimum design of CFS beam-column elements subjected to different combinations of axial compression load (N_{Ed}) and major axis bending moment ($M_{y,Ed}$). It is worth mentioning that shape optimisation or simply changing the relative dimensions of the cross-sections is used in this study to address the challenges faced by the UK CFS industries. However, using topology optimisation may results in less practical shapes for CFS structures unless more constraints are used. To this end, the bending moment is applied using the eccentric axial compression load ($M_{y,Ed} = N_{Ed}eN_y$), and therefore optimisation target is to maximise applied axial compression load without occurrence of any buckling:

$$\max \quad N_{Ed}(X) \qquad (X_i^L \leq X_i \leq X_i^U; i = 1, \cdots, n) \tag{3.18}$$

$$\text{Condition:} \quad \text{Satisfying member check (3.15 and 3.16)} \tag{3.19}$$

where X indicates a vector including cross-sectional design variables X_i listed in Table 3.1 with the lower bound X_i^L and upper bound X_i^U.

In this study, a simply-supported beam-column element with free rotations and warping and prevented twisting and lateral deflections (i.e. end-fork supports) is selected subjected to axial compression load and four different values of eccentricity $eN_y = 0, 0.25 \times 10^3, 1 \times 10^3, 100 \times 10^3$ mm. As shown in Table 3.1, six different cross-sections are chosen including three single sections (plain channel (①), lipped channel (②), and double lipped channel (③)) and three built-up sections (back-to-back (④), diamond (⑤), and RHS (⑥)). Each cross-section is individually optimised five times to find the best design solution for the capacity of CFS beam-column element. It should be noted that the interactions between the components of built-up section were neglected and consequently it was assumed that each single component could buckle individually. While it is more accurate to consider the column and beam elements as built-up members (Meza et al., 2019), this approach has been previously used (e.g. (Ye et al., 2018d, Ye et al., 2018c)) for the sake of simplicity and providing more conservative design solutions. Table 3.1 lists the buckling curve of the selected cross-sections which takes into account the effect of geometrical imperfection on the global buckling resistance of the member about major (y) and minor axes (z), as discussed in Section 3.3.

The total materials (i.e. coil widths) used for single and built-up sections are $l = 453$ mm and $l = 906$ mm, respectively, and are kept constant during optimisation process. Two different

plate thicknesses ($t = 1.5$ and 3) mm and three different element lengths ($L = 3000$ and 5000) mm are selected. The radius of the rounded corners (measured along the middle line of the section) was considered to be $2t$. The elastic modulus and the Poisson's ratio are taken as 210 GPa and 0.3, respectively. The yield and ultimate strength of the steel material are assumed to be $f_y = 350$ MPa and $f_u = 450$ MPa, respectively. To evaluate efficiency of the proposed optimisation process, standard single and back-to-back lipped channel sections are taken as benchmarks for the optimisation of the single and built-up sections, respectively, as shown in Fig. 3.5. It should be noted that, according to the cross-sectional classification determined by EN 1993-1-1 (CEN, 2005e), all studied cross-sections are categorized in either class 3 or 4 due to low slenderness of their constituent plates.

(a) Single channel   (b) Back-to-back channel
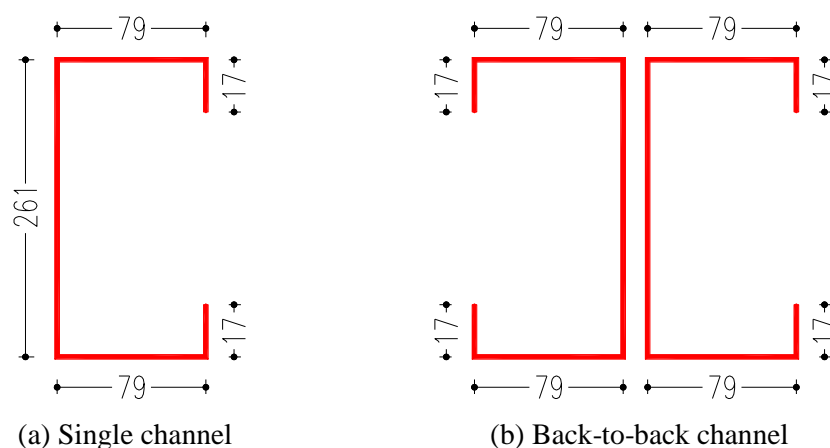
Fig. 3.5. Standard CFS beam-column cross-sections

To increase the practicality of the selected cross-sections, the following EC3 and manufacturing constraints are imposed, as listed in Table 3.1:

a) EC3 specifies the flange slenderness limits of $b/t \leq 50$, $b/t \leq 60$, and $b/t \leq 90$ for the CFS plain (①), lipped (②) channels (③), respectively. To meet the requirements of SCI Guide ED-017 (Way and Lawson, 2013) and make bolted connections of a CFS element to trapezoidal decking or plywood boards feasible, the minimum flange width of the channels (cross-sections ①, ②, ③, and ④) is assumed to be 50 mm. Since the constituent channels of the diamond cross-section (⑤) are connected through their flanges, the minimum flange width of these channels is set to 25 mm to provide enough space for the fasteners. The minimum dimension of RHS section (⑥) is also taken 100mm to ensure the practicality of the optimised section.
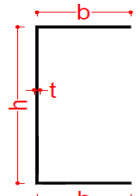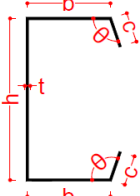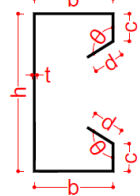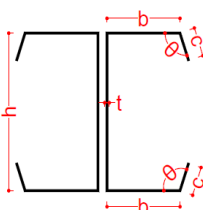
b) The edge stiffeners are constrained as suggested by EC3 using slenderness (e.g. $c/t \leq 50$) and dimension limits (e.g. $0.2 \leq c/b \leq 0.6$). Based on the recommendation of the
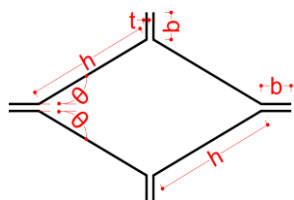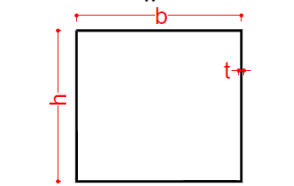
industrial partner of this project, the minimum length of the edge stiffeners is taken 10 mm (i.e. $c \geq 10$ mm, and $d \geq 10$ mm).

c) EC3 imposes particular limitations on the angle of edge stiffeners to be between $\pi/4$ and $3\pi/4$. For the diamond section, the inclination of the webs is restricted by $\pi/6 \leq \theta \leq \pi/3$ (see Table 3.1).

d) EC3 recommended that the web slenderness should be less than 500. To provide practical and maufacturable shapes for the cross-sections ②, ③, and ④, an additional constraint is also used to prevent the lips' length from exceeding half of the web.

Table 3.1. Selected beam-column cross-sections, design variables, constraints, and buckling curves

Cross-section No.	Cross-section shape	Total coil width (mm)	Design variables	Constraints based on EC3	Manufacturing & practical limitations (mm)	Buckling about axis	Buckling curve
①		453	$X_1=b/L$	$b/t \leq 50$ $h/t \leq 500$	$b \geq 50$	any	a
②		453	$X_1=c/b$ $X_2=b/L$ $X_3=\theta$	$0.2 \leq c/b \leq 0.6$ $b/t \leq 60$ $c/t \leq 50$ $h/t \leq 500$ $\pi/4 \leq \theta \leq 3/4\pi$	$b \geq 50$ $c \geq 10$ $h \geq 2c\sin(\theta)$	any	b
③		453	$X_1=c/b$ $X_2=d/b$ $X_3=b/L$ $X_4=\theta$	$0.2 \leq c/b \leq 0.6$ $0.1 \leq d/b \leq 0.3$ $b/t \leq 90$ $c/t \leq 60$ $d/t \leq 50$ $h/t \leq 500$ $\pi/4 \leq \theta \leq 3/4\pi$	$b \geq 50$ $c \geq 10$ $d \geq 10$ $h \geq 2c$	any	b
④		906	$X_1=c/b$ $X_2=b/L$ $X_3=\theta$	$0.2 \leq c/b \leq 0.6$ $b/t \leq 60$ $c/t \leq 50$ $h/t \leq 500$ $\pi/4 \leq \theta \leq 3/4\pi$	$b \geq 50$ $c \geq 10$ $h \geq 2c\sin(\theta)$	y-y z-z	a b

⑤		906	$X_1 = b/L$ $X_2 = \theta$	$b/t \leq 50$ $h/t \leq 500$	$b \geq 25$ $\pi/3 \leq \theta \leq \pi/6$	any b
⑥		906	$X_1 = b/L$	$b/t \leq 500$ $h/t \leq 500$	$b \geq 100$	any b

3.5. GENETIC ALGORITHM OPTIMISATION

Genetic algorithms (GAs) were initially developed by John Holland at the University of Michigan in the 1960s (Holland, 1962). Genetic Algorithm (GA) is known as an evolutionary computational technique that follows the Darwin evolution theory called "survival of the fittest". While heuristic search methods such as simulated annealing or taboo search use one solution during their process to find the optimum point, GA evolves a population of potential solutions through special selection rules to optimise the fitness function (i.e. optimisation target in Equation 3.18) (Holland, 1962, Gerald et al., 1989, Andre et al., 2001). This method initially generates a primitive population of chromosomes (each chromosome represents a candidate solution for the problem). The selected chromosomes are then evaluated according to the optimisation target. The evaluation process is based on the fact that the best design solutions (i.e. with higher values of fitness function) have a better chance of re-producing the problem answers. The formulation of this evaluation process is a key parameter to obtain convergence towards a global optimum solution and to increase the computational efficiency. It should be also noted that using the value of fitness function instead of a gradient vector and Hessian enables GA to provide a faster convergence and to avoid a lot of local optima around the optimum solution (Goldberg, 1989).

Six selected cross-sections (Table 3.1) for the beam-column members are individually optimised by changing the relative geometrical dimensions, and the angle of edge stiffener considered as variables in optimisation process. The optimisation framework is conducted by the development of two distinct pieces of program developed in MATLAB (Mathworks, 2011) for (I) EC3 design rules, and (II) GA optimisation. The GA population size was taken equal to 80 for all beam-column sections while the number of GA generations was kept 100, which convergence was achieved in the most efficient way. The sensitivity analysis on the other GA parameters was also carried out, and subsequently, the following values were selected: crossover probability $P_c = 0.9$; mutation probability $P_m = 0.01$; niching radius $R_n = 0.25$;

termination criterion $C_t = 100$ generations (i.e. the maximum number of function evaluations allowed was 8000); distribution coefficient for mutation $M_d = 1.0$; distribution coefficient for crossover $C_d = 1.0$. In this study, optimum solution is achieved after approximately 60 steps during the optimisation process.

As shown in the flowchart of Fig. 3.6, optimisation process of the beam-column elements is carried out according to following steps:

1) The cross-sectional dimensions of a beam-column member are randomly generated by GA method.

2) Gross cross-sectional properties including centroid (y_0, z_0), shear centre (y_c, z_c), second-moment of area (I_y, I_z), torsional and warping constant (I_w, I_t), and radius of gyration (i_y, i_z, i_0) are determined for the generated cross-section.

3) Effective cross-sectional properties $(A_{eff}, I_{eff}, W_{eff})$ and the corresponding shift of centroidal axis about y and z are calculated (e_{Ny}, e_{Nz}).

4) Design resistances of the cross-section for uniform compression $(N_{c,Rd})$ and bending moments about y $(M_{cy,Rd})$ and z $(M_{cz,Rd})$ are calculated, as explained in Section 3.3.

5) A very small eccentric axial compression load (N_{Ed}) is taken and applied on the beam-column element along with its corresponding bending moment $(M_{y,Ed} = N_{Ed} e_{Ny})$ and additional bending moments $\Delta M_{y,Ed}$ and $\Delta M_{z,Ed}$ caused by the shifts of centroidal axes.

6) As discussed in Section 3.3, beam-column element should satisfy the cross-section check stipulated by EC3 (see Equation 3.3). If the selected cross-section fails to pass the check, N_{Ed} is taken as a resistance of the element, and subsequently, GA generates another section for a new loop (step 1). Otherwise, the next steps taking into account the global instability has to be performed.

7) The reduction factors are calculated for different types of global buckling (i.e. flexural about y (χ_{Fy}) and z axes (χ_{Fz}), torsional (χ_T) and flexural torsional (χ_{FT}), and lateral-torsional (χ_{LT})) (see Section 3.3).

8) The design global buckling resistances of the beam-column element subjected to pure compression $(N_{b,Rd})$ and bending $(M_{b,Rd})$ are computed. It should be noted that the reduction factor used for the calculation of $N_{b,Rd}$ is taken as the minimum of $\chi_{Fy}, \chi_{Fz}, \chi_T$, and χ_{FT}.

9) The interaction factors (k_{yy}, k_{yz}, k_{zy}, k_{zz}) for combined compression force and bending moment are calculated using Equations 3.25-28 in Appendix 3.2.

10) Member resistance check is taken as the main condition in this study and conducted using Equations 3.15 and 3.16. If both Equations 3.15 and 3.16 are less than 1, selected eccentric axial compression force (N_{Ed}) is increased by a small increment (back to Step 5). This loop is repeated until the maximum capacity of the beam-column element is achieved (i.e. either Equations 3.15 or 3.16 reaches its limit). Subsequently, the optimisation process is continued by generating another cross-section in step (1).

Start

A → Generate dimensions of cross-section by using GA

Compute the gross cross-section properties → $I_y, I_z, I_w, I_t, i_y, i_z, i_0$, y_0, z_0, y_c, z_c

Calculate the effective properties of the section as well as shift of centroidal axes → A_{eff}, e_{Ny}, e_{Nz}, $W_{eff\ y}, W_{eff\ z}$

Calculate the design resistances of the cross-section for uniform compression and bending moments about y and z axes → $N_{c,Rd}$, $M_{cy,Rd}, M_{cz,Rd}$

B → Apply eccentric compression load with its corresponding moments and additional moments due to shift of centroid → $N_{Ed}, \Delta M_{y,Ed} = N_{Ed}.e_{Ny}$, $M_{y,Ed} = N_{Ed}e_y, M_{z,Ed} = N_{Ed}e_z$

Cross-section resistance check

$\dfrac{N_{Ed}}{N_{c,Rd}} + \dfrac{M_{y,Ed} + \Delta M_{y,Ed}}{N_{cy,Rd}} + \dfrac{M_{z,Ed} + \Delta M_{z,Ed}}{N_{cz,Rd}} \leq 1$ — *No* → Take N_{Ed} as a maximum capacity of the cross-section → To A

Yes

Compute reduction factors for various types of global buckling (i.e. flexural, torsional, flexural torsional, lateral-torsional) → $\chi_{Fy}, \chi_{Fz}, \chi_T, \chi_{FT}, \chi_{LT}$

Calculated the design buckling resistances of the beam-column element subjected to pure compression and bending → $N_{b,Rd} = \dfrac{\chi A_{eff} f_y}{\gamma_{M1}}$, $\chi = \min(\chi_{Fy}, \chi_{Fz}, \chi_T, \chi_{TF})$, $M_{b,Rd} = \dfrac{\chi_{LT} W_{eff,y} f_y}{\gamma_{M1}}$

Calculate the interaction factors → $k_{yy}, k_{yz}, k_{zy}, k_{zz}$

Member resistance check

Take N_{Ed} as the maximum capacity of the cross-section ← *Yes* — Eq. 15=1 or Eq. 16 =1 — *No* → Increase an eccentric compression load (N_{Ed}) by a small increment → To B

To A

Fig. 3.6. Optimisation process flowchart of beam-column elements

3.6. OPTIMISATION OF CFS SINGLE SECTION BEAM-COLUMN ELEMENTS

The optimum cross-sectional dimensions and capacities of the CFS single section beam-column elements with different plate thicknesses ($t = 1.5$ and 3 mm) and lengths ($L = 3000$ and 5000 mm) subjected to various load eccentricity (eN_y) are listed in Table. 3.2. While no bending moment is applied on the beam-column element with no eccentricity of the load (i.e. $eN_y = 0$), the results show that the beam-column element with the highest selected eccentricity of the load (i.e. $eN_y = 100 \times 10^3$ mm) can act as a beam carrying a significant bending moment and a negligible compression load. For the same amount of material, the capacities of the beam-column members with optimised cross-sections (N_{Ed}) are compared to those with standard conventional cross-sections ($N_{Ed,s}$), as shown in Fig. 3.7.

Based on the optimisation results, following conclusions can be made:

- In general, optimum cross-sectional shapes of CFS beam-column elements under negligible compression loads ($eN_y = 100 \times 10^3$ mm) tend to provide the maximum specified web height, as shown in Table 3.3. However, by increasing applied compression load (i.e. reducing eN_y), the optimised shapes adopt larger flange width and lip length (i.e. minimum web height).

- The results demonstrated that the adopted optimisation method possesses the highest efficiency for the beam-column element with larger length and cross-sectional thickness under pure axial compression load (i.e. $eN_y = 0$). Using optimised cross-sections ①, ②, and ③ can increase the strength of the CFS beam-column element by up to 50%, 193%, and 112%, respectively, compared to those with the standard conventional section. The results also show that while the beam-column elements with optimised plain channel section (①) are always less efficient than those with edge stiffeners (②, and ③), incorporating double edge stiffeners (③) may increase (up to 17%) the capacity of the beam-column element with optimum lipped channel section (②). These are especially evident for the CFS beam-column members with the short length and thin elements.

- As shown in Table 3.3, while the optimum lips' angle is calculated to be always above 90° in the beam-column elements with lipped ②, and double lipped ③ channel sections, generally releasing the lips' angle as an optimisation variable leads to a negligible increase in the strength of the member.

Table 3.2. Optimisation results of the single section beam-column elements with different length and thickness subjected to various eccentricity of the load

L (mm)	t (mm)	eN_y ×10³ (mm)	Optimum results*																		
			Plain channel (①)				Lipped channel (②)						Double lipped channel (③)								
			h	b	N_{Ed} (kN)	$\dfrac{N_{Ed}}{N_{Ed,s}}$	h	b	c	$\theta°$	N_{Ed} (kN)	$\dfrac{N_{Ed}}{N_{Ed,s}}$	h	b	c	d	$\theta°$	N_{Ed} (kN)	$\dfrac{N_{Ed}}{N_{Ed,s}}$
3000	1.5	0	303	75	29.67	0.54	194	81	49	112	82.76	1.51	128	90	54	18	91	97.12	1.77
		0.25	303	75	13.88	0.63	234	90	20	135	24.03	1.09	206	78	36	10	91	25.65	1.16
		1	304	75	6.00	0.67	259	67	29	117	9.02	1.01	243	64	31	10	90	10.05	1.13
		100	353	50	0.10	0.82	306	50	24	93	0.14	1.16	285	50	24	10	90	0.15	1.28
	3.0	0.00	179	137	120.19	0.95	136	107	51	118	291.07	2.30	112	91	55	25	93	241.65	1.91
		0.25	253	100	46.51	0.86	192	102	28	124	64.53	1.20	186	96	28	10	91	62.44	1.16
		1	275	89	19.22	0.83	236	79	30	122	24.08	1.04	234	76	24	10	90	23.47	1.02
		100	353	50	0.32	1.01	301	50	26	118	0.36	1.13	306	50	14	10	90	0.35	1.08
5000	1.5	0	303	75	16.6	0.55	165	90	54	134	55.41	1.83	145	90	54	10	91	54.78	1.81
		0.25	303	75	9.08	0.62	199	90	37	135	18.46	1.26	180	90	36	10	91	18.52	1.26
		1	303	75	4.69	0.66	234	90	20	135	7.66	1.07	212	77	34	10	90	7.89	1.10
		100	353	50	0.09	0.81	305	50	24	93	0.13	1.16	286	50	24	10	90	0.15	1.28
	3.0	0	153	150	92.59	1.50	124	112	52	135	180.60	2.93	121	98	59	10	92	131.08	2.12
		0.25	213	120	34.53	1.05	180	100	36	135	48.76	1.49	166	106	27	11	92	45.03	1.38
		1	250	101	15.37	0.89	208	89	34	135	19.83	1.15	200	92	25	10	91	18.84	1.09
		100	353	50	0.316	0.99	301	50	26	118	0.36	1.13	305	50	14	10	90	0.34	1.07

All dimensions in (mm)

(a) $eN_y=0\times10^3$

(b) $eN_y=0.25\times10^3$

(c) $eN_y=1\times10^3$

(d) $eN_y=100\times10^3$
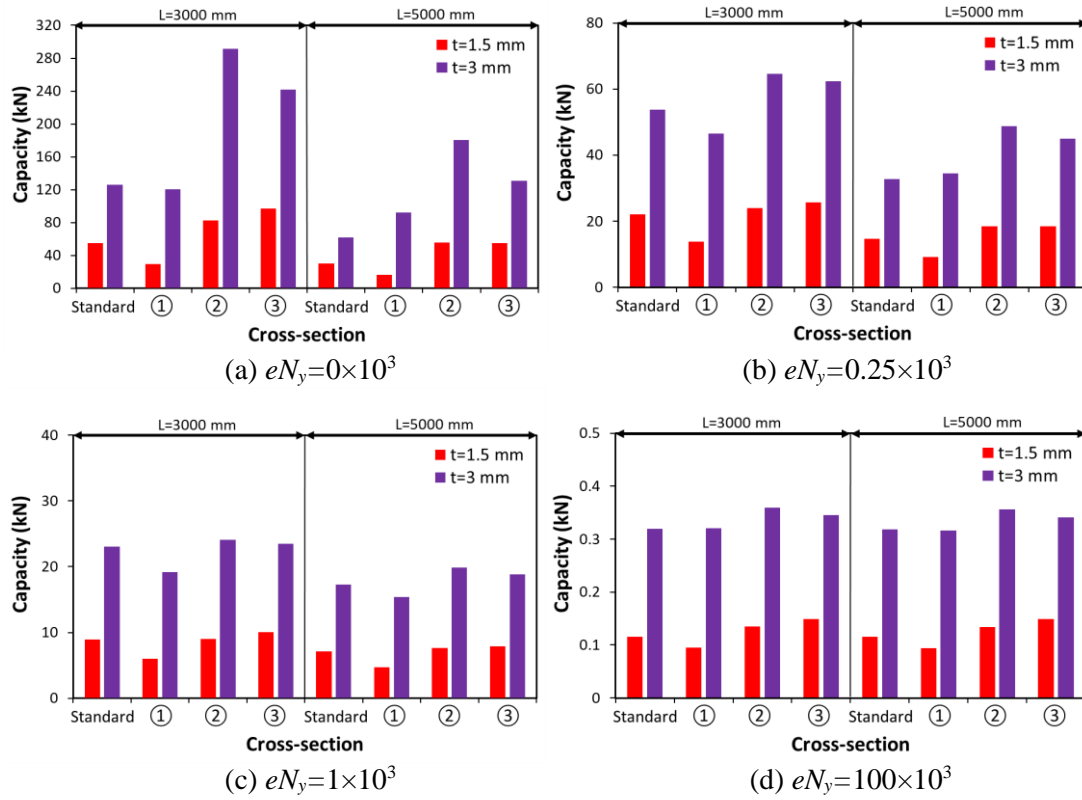
Fig. 3.7. Comparison between the capacities of the standard and optimised single section beam-column elements with different length and thickness subjected to various eccentricity of the load

Table 3.3. Optimised shapes of the single section beam-column elements with different length and thickness subjected to various eccentricity of the load

Cross-section No.	t (mm)	$eN_y=0\times10^3$		$eN_y=0.25\times10^3$		$eN_y=1\times10^3$		$eN_y=100\times10^3$	
		L=3000 (mm)	L=5000 (mm)	L=3000 (mm)	L=5000 (mm)	L=3000 (mm)	L=5000 (mm)	L=3000 (mm)	L=5000 (mm)
①	1.5								
	3.0								

Table 3.4 lists calculated reduction factors for the single section beam-column elements with different length and thickness values subjected to various eccentricity of the load. As expected, for the CFS elements under pure compression ($eN_y = 0$), either flexural or interaction of flexural and torsional buckling is dominant, while lateral-torsional buckling mode is critical for those acting as beams ($eN_y = 100 \times 10^3$ mm). It is also demonstrated that by increasing the length and thickness of the beam-column member under a significant bending moment ($eN_y = 100 \times 10^3$mm), larger reduction is applied to the cross-sectional capacity of the beam-column elements to take into account the effect of lateral-torsional buckling. Except for the case of significant bending moment ($eN_y = 100 \times 10^3$ mm), the failure mode of the beam-column plain channel section (①) with thin elements ($t = 1.5$ mm) is always flexural buckling about minor axis (z), however this is transformed to flexural-torsional buckling for the member with the thicker elements ($t = 3$ mm) (see Table 3.4). It is worth mentioning that

CFS beam-column member with thin plain channel section ($t = 1.5$ mm) subjected to compression and small bending ($eN_y = 0.25 \times 10^3$ mm) are highly likely to experience lateral-torsional buckling due to close values of reduction factors for flexural buckling and lateral-torsional buckling (especially for the longer members ($L = 5000$ mm)). Using beam-column elements with edge stiffeners in their cross-sections (e.g. cross-sections ② and ③) usually leads to flexural-torsional buckling, which governs the resistance of the element (see Table 3.4).

Table 3.4. Calculated reduction factors for the optimised single section beam-column elements with different length and thickness subjected to various eccentricity of the load

L (mm)	t (mm)	$eN_y \times 10^3$ (mm)	Plain channel (①) χ_{Fy}	χ_{Fz}	χ_T	χ_{FT}	χ_{LT}	Lipped channel (②) χ_{Fy}	χ_{Fz}	χ_T	χ_{FT}	χ_{LT}	Double lipped channel (③) χ_{Fy}	χ_{Fz}	χ_T	χ_{FT}	χ_{LT}
3000	1.5	0	1	0.5999	0.6463	0.6453	1	0.9467	0.7709	0.7248	0.7002	1	0.8018	0.6766	0.6543	0.5388	1
		0.25	1	0.5999	0.6463	0.6453	0.6263	1	0.7694	0.6902	0.6817	0.7421	1	0.639	0.624	0.6046	0.7007
		1	1	0.5999	0.6463	0.6453	0.6263	1	0.6441	0.6635	0.6585	0.6378	1	0.5141	0.5778	0.5707	0.5556
		100	1	1	1	1	0.3011	1	1	1	1	0.3687	1	1	1	1	0.3579
	3.0	0.00	0.9256	0.7972	0.5437	0.524	1	0.8099	0.7479	0.4857	0.4177	1	0.635	0.5562	0.5814	0.4028	1
		0.25	1	0.6281	0.5841	0.5784	0.6809	1	0.7292	0.5469	0.5227	0.7471	1	0.6268	0.49	0.4633	0.7092
		1	1	0.5438	0.5558	0.5526	0.5941	1	0.6066	0.5806	0.5696	0.6238	1	0.4928	0.5062	0.4967	0.5559
		100	1	1	1	1	0.1997	1	1	1	1	0.3407	1	1	1	1	0.2668
5000	1.5	0	1	0.3146	0.3741	0.3731	1	0.8107	0.6112	0.4069	0.3628	1	0.6352	0.3786	0.3353	0.2708	1
		0.25	1	0.3146	0.3741	0.3731	0.3187	0.872	0.5544	0.3987	0.3768	0.5669	0.7952	0.4073	0.3211	0.2943	0.5008
		1	1	0.3146	0.3741	0.3731	0.3187	1	0.4735	0.3829	0.3733	0.44	1	0.32	0.3189	0.3045	0.3739
		100	1	1	1	1	0.1276	1	1	1	1	0.1578	1	1	1	1	0.1519
	3.0	0	0.754	0.6178	0.2574	0.2379	1	0.5111	0.5095	0.2061	0.1673	1	0.3908	0.3055	0.2707	0.1851	1
		0.25	0.8411	0.4648	0.3395	0.3266	0.5355	0.7643	0.4445	0.2789	0.2546	0.5046	0.6867	0.3661	0.2241	0.2014	0.4859
		1	1	0.348	0.3398	0.3334	0.3928	1	0.3857	0.3117	0.2937	0.4231	1	0.2978	0.2549	0.2395	0.3778
		100	1	1	1	1	0.0915	1	1	1	1	0.1536	1	1	1	1	0.1211

3.7. OPTIMISATION OF CFS BUILT-UP SECTION BEAM-COLUMN ELEMENTS

Table 3.5 lists the optimum results of the CFS built-up section beam-column elements with different plate thicknesses and lengths subjected to various load eccentricity (eN_y). Similar to the optimisation of single section, the results show that the beam-column element with the highest selected eccentricity of the load (i.e. $eN_y = 100 \times 10^3$ mm) can be identified as a beam element. To assess the efficiency of the optimisation, comparisons between maximum capacities of the beam-column elements with the optimised built-up sections (N_{Ed}) and those with the standard back-to-back sections ($N_{Ed,s}$) are provided in Fig. 3.8 (note that the total coil width of the cross-sections remained constant).

Table 3.5. Optimisation results of the built-up section beam-column members with various thickness, length and load eccentricity

L (mm)	t (mm)	eN_y ×10³ (mm)	Back-to-back channels (④)						Diamond (⑤)					RHS (⑥)			
			h	b	c	$\theta°$	N_{Ed} (kN)	$\frac{N_{Ed}}{N_{Ed,s}}$	h	c	$\theta°$	N_{Ed} (kN)	$\frac{N_{Ed}}{N_{Ed,s}}$	h	b	N_{Ed} (kN)	$\frac{N_{Ed}}{N_{Ed,s}}$
3000	1.5	0	165	90	54	101	182.73	1.39	156	35	45	199.81	1.52	226	227	133.85	1.02
		0.25	243	66	39	116	50.86	1.11	177	25	57	43.53	0.95	312	141	48.19	1.05
		1	277	55	33	115	19.29	1.14	177	25	60	13.84	0.82	353	100	18.13	1.07
		100	305	50	24	88	0.27	1.30	177	25	60	0.15	0.74	353	100	0.22	1.06
	3.0	0.00	152	100	51	92	666.85	1.83	142	42	44	649.13	1.78	226	227	479.57	1.32
		0.25	208	86	37	116	146.50	1.14	177	25	60	120.24	0.93	312	141	157.82	1.23
		1	250	67	34	125	52.61	1.05	177	25	60	39.06	0.78	344	109	61.00	1.21
		100	301	50	26	118	0.72	1.13	177	25	60	0.43	0.67	353	100	0.71	1.11
5000	1.5	0	165	90	54	117	153.02	1.80	171	28	45	178.30	2.10	226	227	126.31	1.49
		0.25	207	77	46	123	41.05	1.20	177	25	56	38.97	1.14	309	144	41.53	1.22
		1	247	64	39	121	16.14	1.10	177	25	60	13.44	0.91	341	112	16.64	1.13
		100	305	50	24	91	0.27	1.30	177	25	60	0.15	0.73	353	100	0.22	1.06

	0	157	102	46	115	487.47	2.58	155	36	44	516.76	2.74	226	227	437.00	2.32
	0.25	179	96	41	126	121.11	1.42	177	25	53	105.10	1.23	226	176	139.84	1.64
3.0	1	219	81	36	129	45.13	1.12	177	25	60	35.95	0.89	315	138	52.98	1.31
	100	301	50	26	119	0.72	1.12	177	25	60	0.43	0.67	353	100	0.71	1.11

All dimensions in (mm)

Following conclusions can be drawn according to the optimisation results:

- As a general trend, by increasing applied bending moment on the beam-column member, optimum cross-sectional shapes adopt larger vertical internal elements (e.g. web), and subsequently, smaller horizontal internal and outstand elements (e.g. flanges and lip). Similar to optimisation of the beam-column elements with single sections, the highest productivity of the optimisation can be seen for the CFS members with the thicker elements and larger length under pure compression load (i.e. $eN_y = 0$).

- By optimising the relative dimensions of the standard back-to-back channel section, the strength of the CFS beam-column element is increased up to 158% and 12% when it acts as a column and a beam, respectively. The results also show that the optimum lips' angle of back-to-back channel section (④) is calculated to be always above 90˚.

- In the case of pure axial compression load (i.e. $eN_y = 0$), the optimum beam-column member with diamond cross-section (④) is capable to provide up to 174% and 17% higher capacity than those with standard and optimised back-to-back channel sections (⑤), respectively. The capacity of the beam-column members with the optimised diamond sections can be significantly reduced by increasing the applied bending moment (up to 76% compared to the optimum back-to-back channel section (⑤)).

- Optimised beam-column elements with RHS sections (⑥) can provide higher strength up to 132% compared to the elements with standard back-to-back sections. While using optimum RHS section as a beam (i.e. $eN_y = 0$) and a column (i.e. $eN_y = 0$) is not as efficient as optimised back-to-back channel section (④), optimised thick RHS sections ($t = 3$ mm) under combined compression and bending (i.e. $eN_y = 0.25 \times 10^3$ mm and $eN_y = 1 \times 10^3$ mm) can provide 17% more capacity than optimised back-to-back channel sections. The results also showed that using CFS beam-column elements with optimised RHS sections (⑥) under compression and bending moment is always more efficient than those with diamond sections (⑤).

(a) $eN_y=0\times10^3$

(b) $eN_y=0.25\times10^3$

(c) $eN_y=1\times10^3$

(d) $eN_y=100\times10^3$
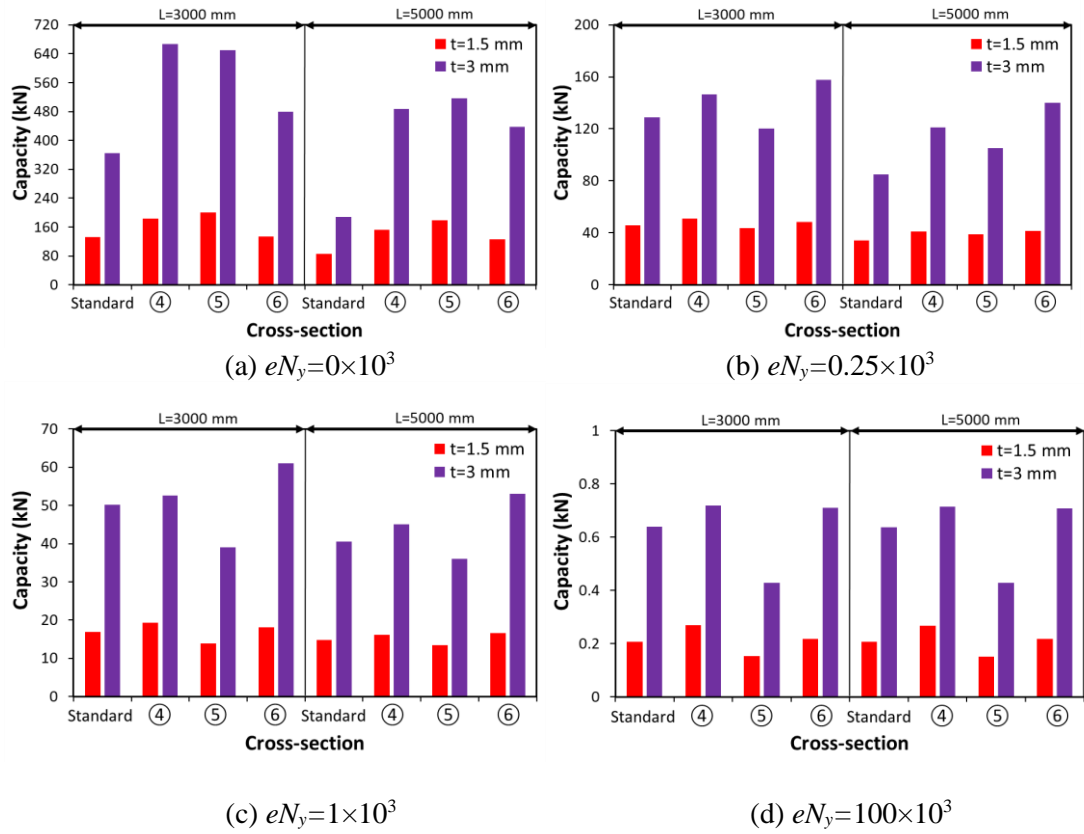
Fig. 3.8. Comparison between the capacities of the standard and optimised built-up section beam-column elements with different length and thickness subjected to various eccentricity of the load

Table 3.6. Optimised shapes of the built-up section beam-column elements with different length and thickness subjected to various eccentricity of the load

Cross-section No.	t (mm)	$eN_y=0\times10^3$		$eN_y=0.25\times10^3$		$eN_y=1\times10^3$		$eN_y=100\times10^3$	
		L=3000 (mm)	L=5000 (mm)	L=3000 (mm)	L=5000 (mm)	L=3000 (mm)	L=5000 (mm)	L=3000 (mm)	L=5000 (mm)
④	1.5								
	3.0								

Table 3.7 lists reduction factors for the optimised CFS beam-column elements with built-up sections. Since the interaction of flexural and torsional modes does not govern the buckling resistance of the beam-column elements with doubly symmetric cross-sections, the reduction factors for flexural-torsional buckling (χ_{FT}) were not presented in Table 3.7. The results show that flexural buckling about minor axis (z) is always a critical failure mode of the beam-columns with back-to-back sections ((④)), except for the cases subjected to significant bending moment (i.e. $eN_y = 100 \times 10^3$ mm) which experience lateral-torsional buckling. While torsional buckling is critical for the beam-column elements with optimised diamond sections ((⑤)) under pure compression (i.e. $eN_y = 0$), the dominant failure mode shifts to flexural buckling about minor axis (z) by applying combined compression and bending. As expected, the optimised members with RHS sections ((⑥)) are not susceptible to torsional or lateral-torsional buckling ($\chi_T = \chi_{LT}$). Also, these elements under combined compression and bending experience flexural buckling about minor axis (z). As can be seen in Table 3.7, some of the optimised beam-column members with diamond and RHS sections (especially shorter and thinner ones) do not have global buckling modes ($\chi_{Fy} = \chi_{Fz} = \chi_T = \chi_{LT} = 1$), and therefore, cross-sectional instabilities are governed in these cases.

Table 3.7. Calculated reduction factors for the optimised built-up section beam-column elements with different length and thickness subjected to various eccentricity of the load

L (mm)	t (mm)	$eN_y \times 10^3$ (mm)	Back-to-back channels (④)				Diamond (⑤)				RHS (⑥)			
			χ_{Fy}	χ_{Fz}	χ_T	χ_{LT}	χ_{Fy}	χ_{Fz}	χ_T	χ_{LT}	χ_{Fy}	χ_{Fz}	χ_T	χ_{LT}
3000	1.5	0	0.9543	0.9037	0.9273	1	0.9404	0.940	0.913	1	0.99	0.99	1	1
		0.25	1	0.7887	0.8698	0.8164	1	1	1	1	1	0.9513	1	1
		1	1	0.6611	0.8025	0.6947	1	1	1	1	1	1	1	1
		100	1	1	1	0.5026	1	1	1	1	1	1	1	1
	3.0	0.00	0.8889	0.8355	0.8504	1	0.8801	0.878	0.831	1	0.9592	0.9592	1	1
		0.25	1	0.7891	0.838	0.8309	1	0.836	0.891	1	1	0.9025	1	1
		1	1	0.6865	0.7946	0.7259	1	1	1	1	1	0.8528	1	1
		100	1	1	1	0.4679	1	1	1	1	1	1	1	1
5000	1.5	0	0.873	0.7791	0.8148	1	0.8503	0.8495	0.7884	1	0.9339	0.9339	1	1
		0.25	0.9199	0.6745	0.7708	0.7251	0.8961	0.779	0.8224	1	1	0.7793	1	1
		1	1	0.5021	0.6716	0.5514	1	0.7387	1	0.8931	1	0.794	1	1
		100	1	1	1	0.2322	1	1	1	0.8917	1	1	1	1
	3.0	0	0.7147	0.6421	0.6537	1	0.7219	0.7206	0.6253	1	0.8742	0.8742	1	1
		0.25	0.8082	0.6203	0.6579	0.7038	0.8275	0.7003	0.7227	1	0.9057	0.8179	1	1
		1	1	0.4996	0.6204	0.5676	1	0.594	1	0.8409	1	0.7384	1	1
		100	1	1	1	0.2173	1	1	1	0.8409	1	1	1	1

3.8. SUMMARY

This chapter presented a practical method for the optimum design of CFS beam-column members with different length and thickness subjected to various combinations of axial compression and bending moment. The GA method was used to obtain the best design solutions for the beam-column member according to European design guidelines (EC3). Six different cross-sections including single and built-up channel sections were selected, and their relative dimensions and inclination of the lip stiffeners were considered as main design

variables, while EC3 and practical design constraints were taken into account. Standard conventional cross-sections were used to evaluate the efficiency of the optimised beam-column cross-sections. It should be noted that while this chapter optimised CFS elements at ultimate limit state, the next chapter (i.e. Chapter 4) will present the best design solutions for CFS beams at both ultimate and serviceability limit state conditions and compare their results.

3.9. CONCLUDING REMARKS

Based on the results, the following conclusions can be made:

- The highest efficiency of the optimisation in terms of strength was observed for the CFS members with the thicker elements and larger length under pure compression load. In general, by increasing applied bending moment on the beam-column member, optimum cross-sectional shapes adopted larger vertical internal elements (e.g. web), and hence, smaller horizontal internal and outstand elements (e.g. flanges and lip).

- By simply changing the relative cross-sectional dimensions of the standard single and back-to-back lipped channel sections, the capacity of CFS beam-column elements was increased up to 193%, and 158%, respectively. The results also showed that while the beam-column elements with optimised plain channel sections are always less efficient than those with edge stiffeners, incorporating double edge stiffeners may increase the strength of the beam-column members depending on the thickness of their elements. The optimum lips' angles of the channel sections were also found to be always above 90˚.

- The results demonstrated that optimised beam-column elements with diamond and RHS sections can provide higher strength (up to 174%) compared to standard back-to-back lipped channel sections. It was also shown that the beam-column members with optimum diamond sections are capable to carry more pure axial compression load compared to those with the optimised back-to-back channel and RHS sections (up to 50%). However, the efficiency of diamond sections was considerably reduced under combined compression and major axis bending moment.

APPENDIX 3.1. CALCULATION OF WARPING CONSTANT

The warping constant for the close thin-walled sections is considered equal to zero, while According to Galambos (1968) and Chen and Lui (1987), the general expression to calculate the warping constant of open thin-walled sections is given as follows:

$$I_w = \int_0^L (\overline{w}_s - w_s)^2 \, t \, ds \tag{3.20}$$

where $w_s = \int_0^s r \, ds$ is unit warping with respect to the shear centre, and r equals the distance from the shear centre of the cross-section to the tangent at any point around the cross-section. $\overline{w}_s = \frac{1}{s} \int_0^s w_s \, ds$ is defined as the average value of w_s over the entire cross-section, t is the thickness of the thin-walled element, and s is the length of the midline of the entire cross-section. These integration formulae can be rewritten as the summation of warping constants for the constituent elements of the cross-section:

$$I_w = \frac{1}{3} \sum_{i=1}^n (\overline{w}_{si}^2 + \overline{w}_{si} \overline{w}_{sj} + \overline{w}_{sj}^2) t_{ij} L_{ij} \tag{3.21}$$

where,

$$\overline{w}_{si} = \left(\frac{1}{2A} \sum_{i=1}^n (w_{si} + w_{sj}) t_{ij} L_{ij} \right) - w_{si} \tag{3.22}$$

$$\overline{w}_{sj} = \left(\frac{1}{2A} \sum_{i=1}^n (w_{si} + w_{sj}) t_{ij} L_{ij} \right) - w_{sj} \tag{3.23}$$

$$w_{sj} = w_{si} + r_{ij} L_{ij} \tag{3.24}$$

where w_{si} and w_{sj} are the corresponding values of w_s at the ends of element, t_{ij} is the thickness of plate element ij, r_{ij} is the distance between the tangent of element ij and the shear centre, and L_{ij} the length of element ij as shown in Fig. 3.9.
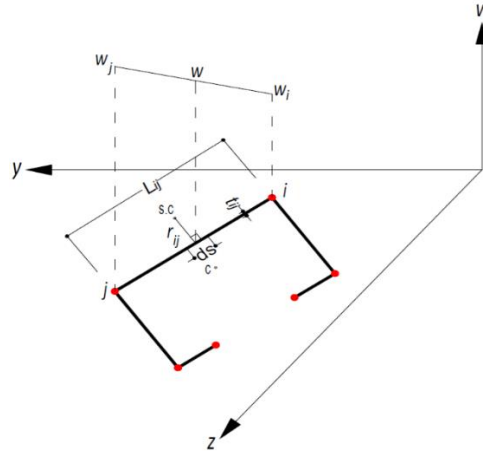
Fig. 3.9. Calculation of warping constant

APPENDIX 3.2. CALCULATION OF INTERACTION FACTORS

k_{yy}, k_{yz}, k_{zy}, and k_{zz} are the interaction factors for Method 1 which is given by Annex A, EN-1993-1-1:

$$k_{yy} = C_{my} C_{mLT} \frac{\mu_y}{1 - \dfrac{N_{Ed}}{N_{cr,Fy}}} \tag{3.25}$$

$$k_{yz} = C_{mz} \frac{\mu_y}{1 - \dfrac{N_{Ed}}{N_{cr,Fz}}} \tag{3.26}$$

$$k_{zy} = C_{my} C_{mLT} \frac{\mu_z}{1 - \dfrac{N_{Ed}}{N_{cr,Fy}}} \tag{3.27}$$

$$k_{zz} = C_{mz} \frac{\mu_z}{1 - \dfrac{N_{Ed}}{N_{cr,Fz}}} \tag{3.28}$$

where,

$$\mu_y = \frac{1 - \dfrac{N_{Ed}}{N_{cr,Fy}}}{1 - \chi_y \dfrac{N_{Ed}}{N_{cr,Fy}}} \qquad \mu_z = \frac{1 - \dfrac{N_{Ed}}{N_{cr,Fz}}}{1 - \chi_z \dfrac{N_{Ed}}{N_{cr,Fz}}} \tag{3.29}$$

$$
\left\{
\begin{aligned}
C_{my} &= C_{my,0} \\
C_{mz} &= C_{mz,0} \\
C_{mLT} &= 1
\end{aligned}
\right\}
\quad (\text{If } \bar{\lambda}_0 \leq 0.2\sqrt{C_1}\sqrt[4]{(1-\frac{N_{Ed}}{N_{cr,Fz}})(1-\frac{N_{Ed}}{N_{cr,TF}})})
\tag{3.30}
$$

$$
\left\{
\begin{aligned}
C_{my} &= C_{my,0} + (1-C_{my,0})\frac{\sqrt{\varepsilon_y}\,a_{LT}}{1+\sqrt{\varepsilon_y}\,a_{LT}} \\
C_{mz} &= C_{mz,0} \\
C_{mLT} &= C_{my}^2\frac{a_{LT}}{\sqrt{(1-\frac{N_{Ed}}{N_{cr,Fz}})(1-\frac{N_{Ed}}{N_{cr,T}})}} \geq 1
\end{aligned}
\right\}
\quad (\text{If } \bar{\lambda}_0 > 0.2\sqrt{C_1}\sqrt[4]{(1-\frac{N_{Ed}}{N_{cr,Fz}})(1-\frac{N_{Ed}}{N_{cr,TF}})}) \tag{3.31}
$$

where $\bar{\lambda}_0$ is defined as non-dimensional slenderness for lateral-torsional buckling due to uniform bending moment. $C_{mi,0}$ is equivalent uniform moment factor which is $C_{mi,0} = 1 + 0.2412\frac{N_{Ed}}{N_{cr,i}}$ for the equal applied bending moments at the ends acting in the opposite direction. A given factor C_1 is a factor depending on the loading and end conditions and can be taken as $C_1 = 1$ for the uniform bending moment. The other parameters are defined:

$$
\varepsilon_y = \frac{M_{y,Ed}A_{eff}}{N_{Ed}W_{eff,y}} \tag{3.32}
$$

$$
a_{LT} = 1 - \frac{I_t}{I_y} \geq 0 \tag{3.33}
$$

CHAPTER 4

Development of Optimum Cold-Formed Steel Beams for Serviceability and Ultimate Limit States Using Big Bang-Big Crunch Optimisation

4.1. INTRODUCTION

Cold-formed steel (CFS) elements are increasingly used as main structural members in modern construction practice. While flexibility of CFS cross-sectional shape allows achieving higher load carrying capacities by using more efficient shapes, obtaining optimum design solutions can be a challenging task due to end-use constraints and complex behaviour of CFS elements controlled by local, global and distortional buckling modes. While previous chapter (i.e. Chapter 3) focused on optimisation of CFS beam-column elements at ultimate limit state, this chapter aims to develop a practical methodology for optimum design of CFS beam sections with maximum flexural strength and minimum deflection under both ultimate and serviceability load conditions, respectively, in accordance with Eurocode 3 by taking into account manufacturing and end-use design constraints. The results are then compared, for the first time, to evaluate the best design solutions at different limit states. This is considered as the main novelty of this chapter. Population-based Big Bang–Big Crunch Optimisation method is employed to obtain optimum design solutions for twelve different CFS cross-sectional prototypes. To verify the flexural strength and stiffness of the optimum beam sections, detailed nonlinear finite element (FE) models are developed using ABAQUS by considering both material nonlinearity and initial geometrical imperfections. It is shown that the optimised sections based on serviceability limit state (SLS) and ultimate limit state (ULS)

Chapter 4. Development of optimum cold-formed steel beams for serviceability
and ultimate limit states using Big Bang-Big Crunch optimisation

71

can provide, respectively, up to 44% higher effective stiffness and 58% higher bending moment capacity compared to a standard lipped channel beam section with the same plate width and thickness. Using plain channel and folded-flange sections generally lead to the best design solutions for SLS and ULS conditions, respectively. Finally, the results of detailed FE models are used to evaluate the adequacy of EC3 proposed procedures to estimate CFS beam capacity and deflection at ULS and SLS, respectively.

4.2. BACKGROUND

Cold-formed steel (CFS) load-bearing members and structural systems are increasingly used in modern construction, for example in modular buildings, stud wall systems, purlins, trusses, side rails and cladding. Although CFS elements are susceptible to local/distortional buckling, they can be more economical and efficient compared to similar hot-rolled sections, due to their inherent advantages such as high strength-to-weight ratio, speed and efficiency of construction, and especially higher flexibility in manufacturing various profiles and sizes through cold-rolling or press-braking process at ambient temperature. The flexibility in CFS cross-sectional shapes provides an excellent opportunity to achieve higher load carrying capacities by using more efficient design solutions. However, this can be a challenging task due to typical manufacturing and end-use design constraints and complex behaviour of CFS elements controlled by combinations of local, global and distortional buckling modes. In general, optimisation of CFS members may aim to obtain an optimal cross-sectional shape without considering any restriction on the general shape of the sections (i.e. self-shape optimisation) (e.g. (Wang et al., 2016a, Madeira et al., 2015, Gilbert et al., 2012a, Gilbert et al., 2012b, Sharafi et al., 2014, Leng et al., 2011, Liu et al., 2004)), or determine optimum relative dimensions of a predefined cross-section (i.e. size optimisation) (e.g. (Leng et al., 2014, Wang et al., 2016b, Ye et al., 2016a, Lee et al., 2005, Magnucki et al., 2006, Ye et al., 2018d, Tran and Li, 2006, Adeli and Karim, 1997, Karim and Adeli, 1999, Ye et al., 2018a, Ma et al., 2015, Lee et al., 2006, Wang et al., 2016c, Tian and Lu, 2004, Ye et al., 2018c, Pastor et al., 2009)).

Different optimisation methods have been used for self-shape optimisation of thin-walled steel sections including Genetic Algorithm (GA) (Gilbert et al., 2012a, Gilbert et al., 2012b, Wang et al., 2016a), Direct Multi-Search (DMS) method (Madeira et al., 2015), graph theory and ant colony based algorithms (Sharafi et al., 2014), and gradient-based steepest descent method and simulated annealing (Leng et al., 2011). In most of these studies, a steel sheet with a predefined total width is allowed to be bent at a certain number of locations, while the Direct

Chapter 4. Development of optimum cold-formed steel beams for serviceability and ultimate limit states using Big Bang-Big Crunch optimisation

72

Strength Method (DSM) (AISI S100-12, 2012) is generally adopted to estimate the compressive and bending capacity of the members. While considerable enhancement of strength was reported in all aforementioned self-shape optimisation methods, they may lead to impractical complex shapes with high manufacturing costs and/or difficulty in connecting to other structural components.

Several investigations have previously been conducted to optimise predefined standard CFS profiles such as C channels, and I and Z shape beams (e.g. (Adeli and Karim, 1997, Karim and Adeli, 1999, Ma et al., 2015)). It is shown that optimising the cross-sectional geometry of simply-supported CFS beams subjected to uniformly distributed vertical (Magnucki et al., 2006, Ye et al., 2016a, Ye et al., 2018d) or transverse load (Tran and Li, 2006) can substantially improve their flexural capacity. However, due to cross-sectional shape restrictions in size optimisation methods, the efficiency of the optimised sections may drop slightly from self-shape optimisation solutions (Leng et al., 2014, Wang et al., 2016b).

Ye et al. (2016b) extended the effective width method in EC3 (CEN, 2005c) to design a new type of 'folded-flange' cross-section by considering the possible occurrence of multiple distortional buckling modes. Subsequently they used Particle Swarm Optimisation (PSO) method to increase the maximum flexural capacity of different cross-sectional prototypes and demonstrate the efficiency of the proposed folded flange sections. It was shown that, for the same amount of material, optimised folded-flange sections can provide up to 57% higher bending capacity compared to their standard counterparts. In another study, Ye et al. (2016a) adopted the Particle Swarm Optimisation (PSO) method to develop CFS beam sections with maximum flexural capacity, while Eurocode 3 (EC3) (CEN, 2005c) design regulations and a number of manufacturing limitations were considered as design constraints. By using an extended EC3 effective width method, to take into account the possibility of multiple distortional buckling modes, they developed an optimum innovative 'folded-flange' cross-section which could provide up to 57% higher flexural capacity compared to a standard benchmark section with the same plate width and thickness. In a follow-up study, Ye et al. (2018a) proposed an advanced shape optimisation framework to achieve maximum energy dissipation of CFS sections in uniaxial bending by providing a link between detailed nonlinear finite element analyses and PSO algorithm.

Various size optimisation methods have been also used to increase the compressive capacity of CFS axial members, such as Genetic Algorithm (GA) (Ma et al., 2015, Lee et al., 2006), Particle Swarm Optimisation (PSO) (Ye et al., 2018c) and Hough Transform (Wang et al., 2016c). Lee et al. (2006) and Tian and Lu (2004) optimised the geometry of CFS columns

under compressive axial loads and proposed optimum design curves for different prescribed load levels. The local-flexural buckling strength of single CFS channels and global buckling strength of the CFS storage pallet racking cross-sections, determined according to the relevant EC3 (EN1993-1-3), have been also optimised by Ye et al (2018c) and Pastor et al. (2009), respectively. In both studies, the adequacy of the optimum cross-sections was examined by the results of detailed FE analysis and experimental tests.

There is a general consensus that a structure must be designed to resist both service and highest load conditions with the acceptable level of reliability during its effective life. However, the aforementioned literatures mainly focused on Ultimate Limit State (ULS), which conventionally represents the ultimate strength of the CFS structures under extreme load events. It should be noted that the level of slenderness for CFS elements is normally higher than hot-rolled steel counterparts, and therefore, the Serviceability Limit State (SLS) is generally more critical for CFS structures. For example, previous studies indicated that the serviceability criteria can govern the design of CFS frame systems especially in low-seismic regions and wind load conditions (Phan et al., 2013c). Violation of serviceability requirements (e.g. deflection limits) implies that the structure would be unfit for normal service operations.

To address to above-mentioned research gaps, this study aims to provide a new framework for size optimisation of CFS beam members under both serviceability and ultimate limit states by considering manufacturing and design constraints. To obtain optimum cross-sections designed according to Eurocode design guidelines (CEN, 2005c, CEN, 2005b, CEN, 2005e), a computationally efficient Big Bang–Big Crunch (BB-BC) algorithm is adopted. The relative dimensions of the cross-sections, inclination of the flanges and lips, and adding features like different edge and intermediate stiffeners are considered as the main design variables in the proposed optimisation process. The efficiency of the optimum cross-sections is then compared with a standard conventional lipped-channel called "benchmark" section. Subsequently, detailed GMNIA Finite Element (FE) models accounting for both material nonlinearity and initial geometrical imperfections are employed using ABAQUS (2007) to evaluate the adequacy of EC3 methodology to estimate CFS beam capacity and deflection at ULS and SLS, respectively.

4.3. EUROCODE DESIGN PRINCIPALS

Eurocode 3 (EC3) part 1-3 (CEN, 2005c) specifies design requirements for CFS products made from thin gauge coated or uncounted steel sheet or strip. The EC3 design requirements are mainly based on limit state design, in which the structural performance is evaluated against

various limiting conditions (e.g. ULS and SLS). In this paper, the flexural strength and stiffness of CFS beam elements are quantified according to the Effective Width Method adopted from EC3 part 1-3 (CEN, 2005c) and EC3 part 1-5 (CEN, 2005b). The following subsections describe briefly the EC3 design procedure.

4.3.1. Local buckling

The EC3 effective width method can take into consideration the non-linear effect of local buckling, which leads to loss of strength in the middle of an internal plate element supported along both longitudinal edges, or in the free edge of an outstand element supported along one longitudinal edge. Therefore, the main load-bearing areas of the cross-section in compression zone are considered to be in the corner zones. Subsequently, the centroidal axis shifts towards the tensile part of the gross cross-section. The effective width of each internal and outstand compression element is calculated through the following equation in EC3 part 1-5:

$$\rho = \frac{b_e}{b} = \begin{cases} \dfrac{1}{\lambda_l}\left(1 - \dfrac{0.055(3+\psi)}{\lambda_l}\right) & \text{for interal compression element} \\[3mm] \dfrac{1}{\lambda_l}\left(1 - \dfrac{0.188}{\lambda_l}\right) & \text{for outstand compression element} \end{cases} \tag{4.1}$$

where ρ is the plate width reduction factor, and b_e and b are the effective width and the total width of the plate, respectively. The effect of applied stress gradient is expressed by ψ, which is defined as the ratio of the plate end stresses. λ_l is the slenderness ratio against local buckling and relates the material yield stress f_y to the elastic local buckling stress of the plate σ_{cr}:

$$\lambda_l = \sqrt{\frac{f_y}{\sigma_{cr}}} \tag{4.2}$$

Estimation of the effective cross-section subjected to bending moment in EC3 generally requires an iterative process. This is referred to the fact that the stress gradient is changed due to shift of neutral axis of the effective cross-section, which dependents on the loss of effective section in compression zone. While the iterative process is considered optional by EC3, in this study full iterations were carried out to achieve convergence.

4.3.2. Distortional buckling

Distortional buckling describes the distortion of the cross-section with rotation and translation at interior elements, leading to both in-plane and out-of-plane displacements of constituent plates. EC3 takes into account the local buckling and distortional buckling of CFS sections by reducing the effective width and the effective thickness of the constituent plates, respectively.

The distortional slenderness, λ_d, can be calculated based on a simplified model, in which the restraining effects of the adjacent plates in the cross-section are taken into account by using equivalent elastic springs:

$$\lambda_d = \sqrt{f_y / \sigma_{cr,s}} \tag{4.3}$$

where $\sigma_{cr,s}$ is the elastic buckling stress of the plate-stiffener assembly given by:

$$\sigma_{cr,s} = \frac{2\sqrt{KEI_s}}{A_s} \tag{4.4}$$

In the above equation, K and A_s are the stiffness of the spring (per unit length) and the effective cross-sectional area of the stiffener, respectively. E is the Young's modulus and I_s is the moment of inertia of the stiffener about the centroid parallel to the plate element. K is a function of the flexural stiffness of the adjacent plates and can be calculated based on the deflection of the stiffener assembly under a unit load u=1 (per unit length). EC3 also recommends to use an iterative process to update the local slenderness ratio of the plates, λ_l, by replacing $\lambda_{l,red} = \lambda_l \sqrt{\chi_d}$. χ_d is the reduction factor corresponding to the distortional buckling resistance and can be calculated by using the relative slenderness λ_d. It should be mentioned that f_y should be substituted by $\sigma_{com} = \chi_d \cdot f_y$ in each iteration for the calculation of λ_d. This optional iteration loop was considered in this study until $\chi_{d,n} \approx \chi_{d,(n-1)}$. In this study, optional iteration loop was considered when the ratio of two consecutive loops ($\frac{\chi_{d,n}}{\chi_{d,(n-1)}}$) is between 0.99 and 1.01.

4.3.3. Global buckling

Based on EC3 part 1-1 (CEN, 2005e), the design global buckling resistance moment of CFS beam members is taken as:

$$M_{b,Rd} = \frac{\chi_{LT} W_{eff} f_y}{\gamma_{M1}} \tag{4.5}$$

where W_{eff} is the effective modulus of the cross-section and γ_{M1} is the partial safety factor prescribed by EC3, which is equal to 1.0. Also, χ_{LT} is the reduction factor corresponding to the lateral-torsional buckling (or global slenderness ratio), which is calculated based on the elastic critical moment of the beam member using the following equation:

$$\chi_{LT} = \sqrt{\frac{W_{eff} f_y}{M_{cr}}} \tag{4.6}$$

In common practice the CFS beams are generally laterally restrained by a floor system, which means the global instability (e.g. lateral-torsional buckling) of the CFS beam elements are practically prevented. Therefore, the global buckling modes are not considered in the optimum design of CFS beams in this study.

4.4. PROBLEM DEFINITION

The aim of the optimisation process in this study is to maximise the flexural capacity and stiffness of CFS beams under ULS and SLS conditions, respectively, calculated based on EC3. A standard lipped channel section that satisfies all EC3 design constraints (see Fig. 4.1) was selected as the starting point of the optimisation process. This section was also used as a benchmark to confirm the efficiency of the optimum design solutions. The total coil width of the steel plate L=453 mm and its thickness t=1.8 mm were kept constant during the proposed optimisation procedure to use the same amount of material in all cross-sections. The radius of the rounded corners for all cross-sections was assumed to be 3 mm which is typical in CFS industries. The elastic modulus, yield stress and Poisson's ratio of the steel material were taken as 210 GPa, f_y=450 MPa, and 0.3, respectively.
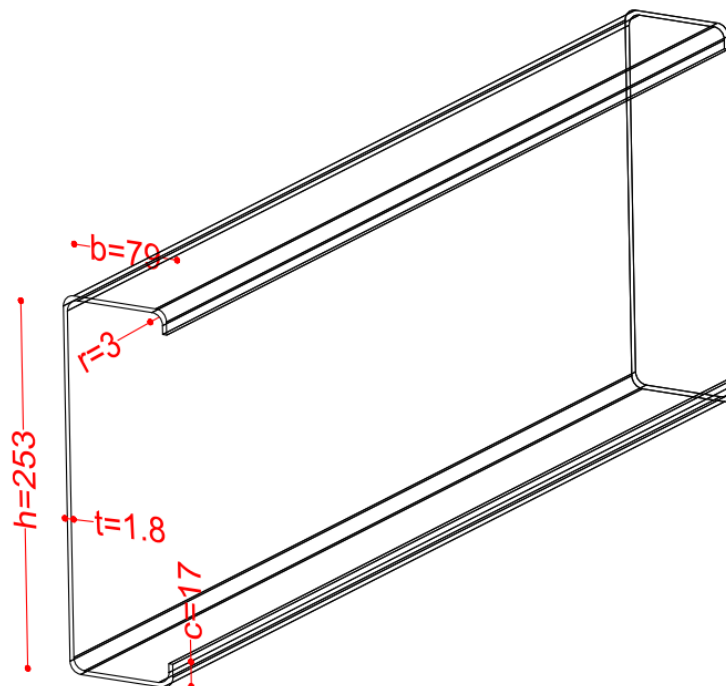
Fig. 4.1. Standard CFS lipped channel section used as a benchmark (dimensions in mm)

In this study, 12 different prototypes were selected including conventional plain and lipped channels as well as those with single and double intermediate stiffeners (in web or flanges), single and double inclined edge stiffeners, and a newly developed folded flange channel. All selected shapes can be manufactured through cold-rolling or press-braking process (see Table 4.1) and can be potentially used in practical applications. Each prototype was individually optimised using different optimisation targets (ULS and SLS). The following EC3 design constraints and practical and manufacturing limitations were imposed to each type of cross-sections as listed in Table 4.1:

a) The minimum width of the flange (bearing width) was set to be 50mm as suggested by SCI Guide ED-017 guidance (Way and Lawson, 2013). This criterion was imposed to provide enough space for the connection of gypsum or wood based boards and decking to the CFS beams by using screws.

b) Based on the advice from the industrial collaborators of this project, the size of single and double lips was taken to be $c \geq 10$ mm, and $d \geq 5$ mm (see Table 4.1) to make the forming of edge stiffeners (lips) feasible by using conventional rolling or press-brake machines.

c) It is common in the CFS industries to take the minimum depth of the channel sections equal to 200 mm, which allows a bolted connection or bridging to be constructed. By considering the standard floor depth, the maximum height of the web (beam depth) was also limited to 400 mm.

d) R_1 and R_2 factors were determined so that the web and flange intermediate stiffeners would be placed within the web height and flange width, respectively.

e) The EC3 limitations on the plates' slenderness ratios (width to thickness), relative dimensions of the channels and angle of edge stiffeners were considered as design constraints as listed in Table 4.1.

f) The opening angle and the leg length of the intermediate stiffeners used in the web and flanges were set to be $\pi/6$ and 15 mm, respectively, which is common in the CFS industries.

Table 4.1. Selected beam-column cross-sections, design variables, constraints and buckling curves

Prototypes	①	②	③	④	⑤	⑥
Cross-section						
Design variables	$X_1=b/L$	$X_1=b/L$ $X_2=R_1$	$X_1=b/L$ $X_2=R_1$	$X_1=c/b$ $X_2=b/L$ $X_3=\theta_1$	$X_1=c/b$ $X_2=b/L$ $X_3=R_1$ $X_4=\theta_1$	$X_1=c/b$ $X_2=b/L$ $X_3=R_1$ $X_4=\theta_1$
EC3 design constraints	$b/t\leq50$ $h/t\leq500$	$b/t\leq50$ $h/t\leq500$	$b/t\leq50$ $h/t\leq500$	$0.2\leq c/b\leq0.6$ $b/t\leq60$ $c/t\leq50$ $h/t\leq500$ $\pi/4\leq\theta_1\leq3/4\pi$	$0.2\leq c/b\leq0.6$ $b/t\leq60$ $c/t\leq50$ $h/t\leq500$ $\pi/4\leq\theta_1\leq3/4\pi$	$0.2\leq c/b\leq0.6$ $b/t\leq60$ $c/t\leq50$ $h/t\leq500$ $\pi/4\leq\theta_1\leq3/4\pi$
Practical & manufacturing limitations (mm)	$200\leq h\leq400$ $b\geq50$	$200\leq h\leq400$ $b\geq50$ $0.1\leq R_1\leq0.9$	$200\leq h\leq400$ $b\geq50$ $0.1\leq R_1\leq0.4$	$200\leq h\leq400$ $b\geq50$ $c\geq10$	$200\leq h\leq400$ $b\geq50$ $c\geq10$ $0.1\leq R_1\leq0.9$	$200\leq h\leq400$ $b\geq50$ $c\geq10$ $0.1\leq R_1\leq0.4$

Prototypes	⑦	⑧	⑨	⑩	⑪	⑫
Cross-section						
Design variables	$X_1=c/b$ $X_2=d/b$ $X_3=b/L$ $X_4=\theta_1$	$X_1=c/b$ $X_2=d/b$ $X_3=b/L$ $X_4=R_1$ $X_5=\theta_1$	$X_1=c/b$ $X_2=d/b$ $X_3=b/L$ $X_4=R_1$ $X_5=\theta_1$	$X_1=c/b$ $X_2=b/L$ $X_3=R_1$ $X_4=R_2$ $X_5=\theta_1$	$X_1=c/b$ $X_2=d/b$ $X_3=b/L$ $X_4=R_1$ $X_5=R_2$ $X_6=\theta_1$	$X_1=\theta_1$ $X_2=\theta_2$ $X_3=b$ $X_4=c$ $X_5=d$
EC3 design constraints	$0.2\leq c/b\leq0.6$ $0.1\leq d/b\leq0.3$ $b/t\leq90$ $c/t\leq60$ $d/t\leq50$ $h/t\leq500$ $\pi/4\leq\theta_1\leq3/4\pi$	$0.2\leq c/b\leq0.6$ $0.1\leq d/b\leq0.3$ $b/t\leq90$ $c/t\leq60$ $d/t\leq50$ $h/t\leq500$ $\pi/4\leq\theta_1\leq3/4\pi$	$0.2\leq c/b\leq0.6$ $0.1\leq d/b\leq0.3$ $b/t\leq90$ $c/t\leq60$ $d/t\leq50$ $h/t\leq500$ $\pi/4\leq\theta_1\leq3/4\pi$	$0.2\leq c/b\leq0.6$ $b/t\leq60$ $c/t\leq50$ $h/t\leq500$ $\pi/4\leq\theta_1\leq3/4\pi$	$0.2\leq c/b\leq0.6$ $0.1\leq d/b\leq0.3$ $b/t\leq90$ $c/t\leq60$ $d/t\leq50$ $h/t\leq500$ $\pi/4\leq\theta_1\leq3/4\pi$	$7/12\pi\leq\theta_1\leq5/6\pi$ $\pi/4\leq\theta_2\leq3/4\pi$ $30\leq b\leq48$ $50\leq c\leq60$ $15\leq d\leq60$
Practical & manufacturing limitations (mm)	$200\leq h\leq400$ $b\geq50$ $c\geq10$ $d\geq5$	$200\leq h\leq400$ $b\geq50$ $c\geq10$ $d\geq5$ $0.1\leq R1\leq0.9$	$200\leq h\leq400$ $b\geq50$ $c\geq10$ $d\geq5$ $0.1\leq R1\leq0.4$	$200\leq h\leq400$ $b\geq50$ $c\geq10$ $0.1\leq R_1\leq0.4$ $0.2\leq R_2\leq0.8$	$200\leq h\leq400$ $b\geq50$ $c\geq10$ $d\geq5$ $0.1\leq R_1\leq0.4$ $0.2\leq R_2\leq0.8$	$200\leq h+2b\sin(\theta_1)\leq400$

It should be noted that the design constraints listed in Table 4.1, especially in terms of channel dimensions, are typically related to the other elements connected to the CFS beam such as trapezoidal decking, plywood boards and angle cleats.

4.5. BIG BANG-BIG CRUNCH ALGORITHM

Big bang-big crunch (BB-BC) optimisation method was first proposed by Erol and Eksin (2006) based on the big bang and big crunch theories of the universe evolution. In this method, the randomness of the candidates and their convergence to the optimum solution represent the energy dissipation and gravitational attraction in nature. Previous studies demonstrated that, in general, the BB–BC optimisation method can offer several advantages such as lower computational time, higher convergence speed, and simpler programming compared to other conventional heuristic algorithms such as Genetic Algorithm (GA), Particle Swarm Optimisation (PSO) and Ant Colony Optimisation (Kaveh and Talatahari, 2009, Hasançebi and Kazemzadeh Azad, 2012, Prayogo et al., 2018). This is especially important for the complex optimisation of CFS elements due to their nonlinear behaviour affected by local and distortional buckling modes.

In the BB–BC optimisation process, the candidate solutions are randomly distributed over the search space (Big Bang phase) and then a convergence operation is used to calculate a weighted average of the candidate solutions (Big Crunch phase). In the big bang phase, the candidate solutions are uniformly distributed over the search space. The convergence operator in Big Crunch phase is then used to calculate the fitness function of each candidate and update its current position. The "centre of mass" is defined as the weighted average of the position of candidate solutions with respect to the inverse of the penalized fitness function, and is calculated as:

$$X_{cm} = \frac{\sum_{i=1}^{nc} \frac{1}{f_i} X_i}{\sum_{i=1}^{nc} \frac{1}{f_i}} \tag{4.7}$$

where X_{cm} and X_i are the position of the centre of mass and i^{th} candidate in the n-dimensional search space, f_i is the penalized fitness function for i^{th} candidate, and nc is the candidate population size.

The positions of the candidate solutions for the next iteration of the Big Bang are normally distributed around the centre of mass, X_{cm}, using the following equation:

$$X_i^{new} = X_{cm} + \sigma \tag{4.8}$$

where X_i^{new} is the position of the new candidate solution i, and σ is the standard deviation corresponding to a subset of the search space. In the proposed method, σ decreases inversely with each succeeding Big Bang iteration using the following equation:

$$\sigma = \frac{r\alpha(X_{max} - X_{min})}{s} \tag{4.9}$$

where r is a random number from a standard normal distribution, α is a parameter used to limit the size of the search space, X_{min} and X_{max} represent the lower and upper limits of the selected design variables, and s is the number of Big Bang iterations. In this study, the number of candidate population size (nc) and number of Big Bang iterations (s) were taken, respectively, as 150 and 100 for the first 6 prototypes of cross-sections, and 200 and 150 for the other prototypes. Parameter α was also selected equal to 1.0. Fig. 4.2 shows the details of the flowchart for the BB-BC algorithm used in this study.

It should be noted that, for the optimisation problems in this study, the only design constraints are EC3 and manufacturing restrictions imposed on the input design variables (see Table 4.1). Therefore, the constraints can be easily handled by using a domain (max and min values) for each design variable.

```
                              ┌─────────────────┐
                              │      Start       │
                              │  BB-BC algorithm │
                              │     (MATLAB)     │
                              └─────────────────┘
                                       │
                                       ▼
                              ┌─────────────────┐
                              │ Generate a random│
                              │  initial         │
                              │  population      │
                              │ (cross-section   │
                              │  dimensions)     │
                              └─────────────────┘
                                       │
                                       ▼
                              ┌─────────────────┐
                              │ Start iteration  │
                              └─────────────────┘
                                       │
   Iteration=Iteration+1               ▼
                              ┌─────────────────────┐
              ┌──────────────▶│ Compute fitness      │
              │               │ function of each     │
              │               │ candidate            │
              │               │ (e.g. flexural       │
              │               │ strength and stiffness)│
              │               └─────────────────────┘
              │                        │
              │                        ▼
   ┌──────────────────┐       ┌─────────────────┐
   │ Regenerate new   │       │ Select the best  │
   │ candidate around │       │ centre of mass   │
   │ the centre of    │       └─────────────────┘
   │ mass             │                │
   │ (cross-section   │                ▼
   │ dimensions)      │       ┌─────────────────┐
   └──────────────────┘       │ Identify the     │
              ▲               │ centre of mass   │
              │               └─────────────────┘
              │                        │
              │                        ▼
              │  No            ◇─────────────────◇   Ye   ┌────────┐
              └────────────────  Iteration=Max iteration ─────────▶│  End   │
                                ◇─────────────────◇              └────────┘
```

Fig. 4.2. Optimisation process flowchart of beam-column members

4.6. OPTIMUM DESIGN OF CFS BEAMS

The optimisation framework was conducted on the selected prototypes (see Table 4.1) by developing two programmes MATLAB (Mathworks, 2011) to design CFS beams based on EC3 design regulations and to carry out BB-BC. The optimisation process was aimed at obtaining the optimum relative dimensions of each cross-section as well as the best positions of the edge and intermediate stiffeners in web and flanges.

To ensure that the optimum results are consistent, each prototype was optimised three times using randomly selected candidates. While the maximum difference between the results obtained from the three runs was always less than 1%, the best design solution was selected. During the optimisation process, the convergence was normally achieved after approximately 20 and 50 steps for the ①, to ⑥ and ⑦ to ⑫ prototypes, respectively. As an example, the

iteration history of the optimisation process for the prototype ④ is shown in Fig. 4.3, where the convergence is achieved after 18 iterations for all three cases.
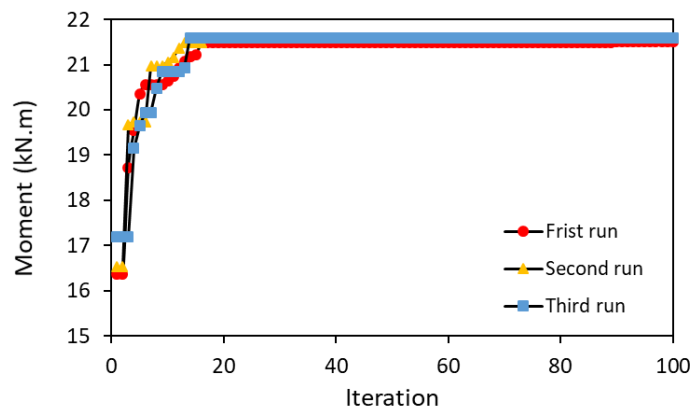
Fig. 4.3. Iteration history of the optimisation algorithm (BB-BC) for prototype ④

4.6.1. Optimisation for Ultimate Limit State (ULS)

This section is aimed to optimise laterally braced CFS beams in order to maximize their bending capacity at ULS. In this case, the optimisation target can be represented as a function of the effective property of the cross-section defined by:

$$\text{Max} \quad M(x) = W_{eff} f_y / \gamma_{M_0} \qquad X_i^L \leq X_i \leq X_i^U, \qquad (i = 1, \cdots, n) \quad (4.10)$$

where $M(x)$ and W_{eff} are the design moment resistance and effective section modulus of a cross-section about the major axis, respectively. W_{eff} is the ratio of effective second moment of inertia I_{eff} to the distance from effective centroid to furthest compression fibre, calculated by considering the contribution of all effective parts of the cross-section. γ_{M_0} is a partial safety factor used for ultimate limit state and is considered to be 1.0 as prescribed by the EC3 . The lower and upper bound of each design variable (X_i^L and X_i^U) are obtained based on the EC3 design requirements and the practical and manufacturing limitations listed in Table 4.1.

Table 4.2 compares the flexural capacity and dimensions of the standard section and those optimised based on maximum bending moment capacity for all selected prototypes using the same amount of material. The standard lipped channel section has been used as a benchmark to assess the efficiency of the proposed optimisation methodology. It is shown that the proposed optimisation method could considerably (up to 58%) increase the maximum bending capacity of the standard section. For better comparison, the effective cross-sections of the optimum solutions are presented in Table 4.3, in which the effective parts of cross-sections are drawn by thick solid black lines. The thicknesses of the effective parts are reduced in the

location of the intermediate and edge stiffeners to take into account distortional buckling modes as discussed in Section 4.3.2.
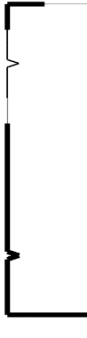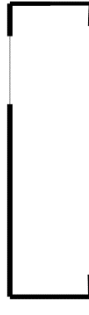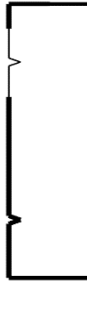
Based on the ULS optimisation results in Table 4.2, the following conclusions can be drawn:

- The flexural capacity of the benchmark lipped channel is increased by 30% only by optimising its relative cross-sectional dimensions (prototype ④). An additional 10% higher flexural capacity can be obtained by using an optimised CFS channel with double edge stiffener (prototype ⑦). It should be noted that the efficiency of the proposed optimisation method would be considerably increased by using more flexible design constraints (i.e. a wider range of input design variables).

- In general, plain channel sections (prototypes ①, ② and ③) do not provide efficient design solutions even after optimisation. This is referred to the fact that plain channels are generally highly susceptible to the local buckling of flanges.

- The flexural capacity of the optimum single and double lipped channels (prototypes ④ and ⑦) are not generally enhanced by incorporating intermediate stiffeners in the web (prototypes ⑤, ⑥, ⑧, and ⑨). This is especially evident in the case of double intermediate web stiffeners (prototypes ⑥ and ⑨). This shows the inefficiency of using web stiffeners in the tension zone of the cross-section. Besides, folding the intermediate stiffeners into the section results in a reduction of the web height (noting that total coil width is kept constant), which in turn reduces the flexural capacity of the section.

- Comparison between prototypes ⑥ and ⑩, and prototypes ⑨ and ⑪ indicates that adding intermediate flange stiffeners can increase (up to 17%) the moment capacity of the sections. The optimum location of the flange intermediate stiffener is approximately in the middle of the flange.

- As a general trend, it can be seen that optimised cross-sections tend to adopt taller web and subsequently narrower flanges. Therefore, all prototypes were optimised towards minimum specified flanges of 50 mm. As shown in Table 4.2, using folded flange section (prototype ⑫) provides the highest flexural capacity among all selected prototypes and offers 58% more flexural strength compared to the benchmark section. The folded flange cross-section can be easily manufactured (only 6 bends are needed) compared to the channels with intermediate stiffeners, and therefore, can provide a practical and efficient design solution.

Table 4.2. Dimensions and flexural capacity of standard and optimum CFS beams for different prototypes at ULS

Prototypes	h (mm)	b (mm)	c (mm)	d (mm)	θ_1°	θ_2°	R_1	R_2	M_{max} (kN.m)	$\frac{M_{max}}{M_{max,standard}}$
Standard	261	79	17						16.47	1
①	353	50							15.56	0.94
②	338	50					0.842		17.16	1.04
③	323	50					0.195		15.81	0.96
④	305	50	24		89				21.40	1.30
⑤	290	50	24		91		0.774		21.22	1.29
⑥	274	50	25		92		0.215		19.68	1.19
⑦	285	50	27	7	90				23.63	1.43
⑧	276	50	24	7	135		0.760		22.03	1.34
⑨	263	50	24	6	135		0.250		20.41	1.24
⑩	262	50	15		135		0.100	0.545	23.75	1.44
⑪	258	50	12	6	135		0.256	0.555	21.86	1.33
⑫	217	48	50	20	100	79			25.97	1.58

Table 4.3. The effective cross-section of optimum CFS beams for different prototypes at ULS

Prototypes	Benchmark	①	②	③	④	⑤	⑥
Effective sections							

Prototypes   ⑦   ⑧   ⑨   ⑩   ⑪   ⑫

Effective sections

4.6.2. Optimisation for Serviceability Limit State (SLS)

The serviceability limit state (SLS) is generally defined as the condition beyond which a structure becomes unfit for service. Unlike ULS, SLS depends more on the stiffness rather than the strength of a structural system. Based on Eurocode (CEN, 2002), the structural reliability under either SLS or ULS can be represented by the following inequality:

$$R_d \geq R_{Ed} \tag{4.11}$$

where R_d is the design resistance and R_{Ed} is the design load effect calculated for persistent and transient design situations as follow:

$$R_{Ed} = \sum_{j \geq 1} \gamma_{G,j}.G_{k,j} + \gamma_{Q,l}.Q_{k,l} \tag{4.12}$$

In Equation 4.12, $\gamma_{G,j}$ and $G_{k,j}$ are the partial safety factor and characteristic value for permanent action j, while $\gamma_{Q,l}$ and $Q_{k,l}$ are the partial safety factor and characteristic value of the leading variable action l, respectively. Eurocode (CEN, 2002) distinguishes between SLS and ULS by means of partial safety factors, which are $\gamma_{G,j} = 1.35$ and $\gamma_{Q,l} = 1.5$ for ULS and $\gamma_{G,j} = \gamma_{Q,l} = 1$ for SLS. While in general serviceability limit state loading condition should be determined for each specific project, the ratio of service to ultimate loads (or the ratio of average partial safety factors for SLS over those for ULS) in this study was taken as 0.7 and kept constant for different prototypes during the optimisation process. Therefore, to design for serviceability based on EC3 (CEN, 2005b), the maximum compressive stress $\sigma_{com,Ed,ser}$ in each cross-section was calculated based on the effective cross-section under $M_{Ed,ser}=0.7 M_{max}$ as shown in Fig. 4.4:

Chapter 4. Development of optimum cold-formed steel beams for serviceability and ultimate limit states using Big Bang-Big Crunch optimisation

86
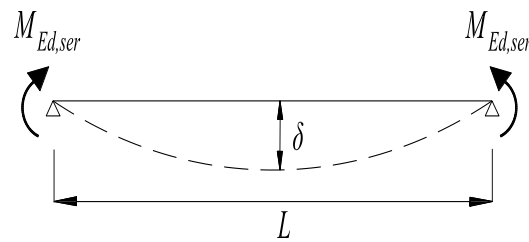
Fig. 4.4. Beam deflection at SLS subjected to a uniform pure bending ($M_{Ed,ser}$)

To determine the effective second moment of area (I_{eff}) of the CFS beam section, the slenderness ratio is calculated from:

$$\bar{\lambda}_{p,ser} = \bar{\lambda}_p \sqrt{\frac{\sigma_{com,Ed,ser}}{f_y}} \qquad (4.13)$$

For serviceability design, the optimisation problem can be formulated as a minimisation of beam deflection subjected to pure bending moment, which is defined by:

$$\text{Min} \qquad f(x) = \frac{M_{Ed,ser}L^2}{8EI_{fic}} \qquad X_i^L \le X_i \le X_i^U, \qquad (i=1,\cdots,n) \qquad (4.14)$$

where $f(x)$ is the deflection of the CFS beam. X_i is the design variables with the lower and upper bounds of X_i^L and X_i^U, specified in Table 4.1, respectively. In order to provide a reasonable comparison between the behaviour of each prototype at its SLS, the length of the beam is kept constant and equal to $L=5000$ mm. I_{fic} is the effective second moment of area, which is based on the service load. Eurocode 3 part 1-3 (CEN, 2005c) stipulates that the properties of the effective cross-section explained in Section 4.3 must be used in all SLS checks for CFS members. Also, it has been mentioned that the second moment of area of CFS sections can be estimated by an interpolation between effective and gross cross-sections for the design load combination using the following expression:

$$I_{fic} = I_{gr} - \frac{\sigma_{gr}}{\sigma}(I_{gr} - I(\sigma)_{eff}) \qquad (4.15)$$

where I_{gr} is the second moment of area of the gross cross-section, σ_{gr} is the maximum compressive bending stress based on the gross cross-section at serviceability limit state (SLS), and $I(\sigma)_{eff}$ is the second moment of area of the effective cross-section by considering local buckling estimated based on maximum stress $\sigma \ge \sigma_{gr}$ (σ is the highest absolute value of stress within the beam length). Subsequently, σ and σ_{gr} can be calculated based on the following equations:

$$\sigma_{gr} = \frac{M_{Ed,ser}}{W_{ser}} = \frac{M_{Ed,ser}}{I_{gr} / z_{c,ser}} \tag{4.16}$$

$$\sigma = \frac{M_{max}}{W_{eff}} = f_y \tag{4.17}$$

In the above equations, W_{ser} and W_{eff} are the section modulus for the SLS and ULS, respectively, and $z_{c,ser}$ represents the distance of neutral axis to extreme compression fibre in a CFS section associated with SLS. By substituting Equation 4.10 in Equation 4.17, the maximum stress corresponding to local buckling, σ, would be equal to the yield stress f_y.

The cross-sectional dimensions, second moment of area and flexural capacity of optimum sections for each prototype under service load level are calculated as presented in Table 4.4. Based on the results, the following observations can be drawn:

- The dimensions of the optimum plain channels (prototypes ①, ② and ③) for SLS are very similar to those optimised for ULS (the only difference is in the optimum locations of the web stiffeners). Unlike optimisation for ULS, optimum plain channels at SLS could provide considerably higher effective stiffness (up to 44%) compared to the benchmark lipped channel section. However, the flexural capacity of the sections may be slightly (up to 10%) lower than the benchmark channel. This implies that, in general, optimum plain channels are more efficient to satisfy SLS checks.

- The flexural stiffness of optimum plain and single/double lipped channels (prototypes ①, ④ and ⑦) were reduced by incorporating intermediate web stiffeners. Similar to the ULS optimisation, this reduction is more evident in the case of double intermediate web stiffeners (prototypes ③, ⑥ and ⑨). However, it can be seen from Table 4.4 that using optimised intermediate flange stiffeners (prototypes ⑩ and ⑪) could increase the effective stiffness and capacity of the sections by up to 10% and 27%, respectively.

- By optimising the relative dimensions of the standard benchmark section at SLS, the flexural stiffness and capacity of the section can be increased by 37% and 11%, respectively. However, for the same amount of material, optimisation of the channel section with folded flanges (prototype ⑫) resulted in a noticeable increase (up to 52%) in both effective stiffness and capacity of the standard section. This highlights the efficiency of folded flange sections for both ultimate and serviceability limit states.

- While a negligible difference (less than 4%) is seen between the effective stiffness of the optimum beams with single and double edge stiffeners (prototypes ④ and ⑦,

respectively) at SLS, the flexural capacity of the section with double edge stiffener is 13% higher than the one with single edge stiffener. A similar trend is observed for the sections with the intermediated web stiffeners (prototypes ⑤ and ⑥ compared to prototypes ⑧ and ⑨).

Table 4.4. Dimensions, effective second moment of area and flexural capacity of standard and optimum CFS beams for different prototypes at SLS

Prototypes	$\dfrac{M_{ser}}{M_{max}}$	h (mm)	b (mm)	c (mm)	d (mm)	θ_1°	θ_2°	R_1	R_2	I_{fic} $\times 10^6$ (mm^4)	$\dfrac{I_{fic}}{I_{fic,standard}}$	M_{max} (kN.m)	$\dfrac{M_{max}}{M_{max,standard}}$
Standard	0.7	261	79	17						7.22	1	16.47	1
①	0.7	353	50							10.39	1.44	15.53	0.94
②	0.7	338	50						0.9		10.33	1.43	16.29	0.99
③	0.7	323	50						0.1		9.01	1.25	14.86	0.90
④	0.7	333	50	10		135				9.88	1.37	18.24	1.11
⑤	0.7	318	50	10		135		0.9		9.20	1.27	17.68	1.07
⑥	0.7	303	50	10		135		0.1		8.55	1.18	16.69	1.01
⑦	0.7	323	50	10	5	90				9.65	1.34	20.61	1.25
⑧	0.7	308	50	10	5	135		0.9		8.91	1.23	19.34	1.17
⑨	0.7	293	50	10	5	135		0.1		8.23	1.14	17.96	1.09
⑩	0.7	273	50	10		135		0.1	0.800	9.31	1.29	22.29	1.35
⑪	0.7	263	50	10	5	135		0.1	0.319	8.71	1.22	20.86	1.27
⑫	0.7	227	48	50	15	105	65			10.10	1.41	24.99	1.52

- Similar to the ULS optimisation, optimised cross-sections tend to use taller web and narrower flanges. Therefore, all optimised sections have the minimum specified flange width of 50 mm. The main differences between optimised shapes for ULS and SLS are the size and angle of the edge stiffeners and the location of the intermediate web and flange stiffeners.

- Optimisation of the CFS beam sections at SLS on average increased the flexural stiffness and strength of the standard benchmark section by 30% and 14%, respectively. However, comparisons between the results presented in Tables 2 and 4 indicates that the sections optimised at SLS exhibit on average 9% lower flexural strength compared to those optimised at ULS.

4.7. ANALYTICAL INVESTIGATION

The ultimate flexural capacity and deflection of the standard and optimised cross-sections listed in Table 1 were determined at ULS and SLS using detailed nonlinear FE models in ABAQUS (2007), where the effects of material nonlinearity and initial geometric imperfections were taken into account. The results were then used to evaluate the efficiency of the proposed optimisation method in obtaining sections with reduced maximum deflection at SLS and increased ultimate capacity at ULS. The detailed FE models were also used to assess the accuracy of Eurocode predictions for different prototypes. It should be noted that the capability of detailed finite element (FE) models to simulate both pre- and post-buckling behaviour of CFS sections has been demonstrated in previous studies provided that appropriate element types, material models and geometric imperfections are adopted (Becque and Rasmussen Kim, 2009, Becque and Rasmussen, 2009, Yu and Schafer, 2007, Ye et al., 2018c). The adopted FE models have been also validated against a series of experimental tests on CFS back-to-back channels conducted at The University of Sheffield by the authors (Ye et al., 2018d).

4.7.1. Detailed FE models

The detailed FE models of the CFS sections corresponding to the selected prototypes were developed in ABAQUS (2007) using a 4-noded quadrilateral shell element with reduced integration (S4R). Based on a comprehensive mesh sensitivity analyses, a mesh size of 10×10 mm was found to be appropriate since a further mesh refinement did not make any noticeable change in the results. The stress-strain behaviour of CFS plates was modelled by using the widely adopted constitutive model proposed by Haidarali and Nethercot (2011a):

$$\varepsilon = \frac{\sigma}{E} + 0.002 \left(\frac{\sigma}{\sigma_{0.2}} \right)^n \qquad for \ \sigma \le \sigma_{0.2}$$

$$\varepsilon = \varepsilon_{0.2} + \frac{100(\sigma - \sigma_{0.2})}{E} \qquad for \ \sigma \ge \sigma_{0.2}$$

(4.18)

where $\sigma_{0.2}$ and $\varepsilon_{0.2}$ are the 0.2% proof stress and the total strain at $\sigma_{0.2}$, respectively. n is a shape parameter recommended by Gardner and Ashraf (2006) to be taken as 28 for grades 350

Chapter 4. Development of optimum cold-formed steel beams for serviceability
and ultimate limit states using Big Bang-Big Crunch optimisation

90

and 450 steel, and E is the elastic modulus which is taken equal to 210 GPa. The effects of geometrical imperfections were taken into account in CFS sections by performing eigenvalue elastic buckling analysis which is available in ABAQUS library (2007) on the CFS beams. The obtained dominant buckling mode (either local or distortional) was then incorporated in the initial perfect geometry of the cross-section and scaled to the certain magnitude extracted from the Cumulative Distribution Function (CDF) values suggested by Schafer and Peköz (1998). In this study, a CDF value of 50% was adopted (corresponding to $0.34t$ and $0.94t$ for local and distortional imperfections, respectively). These values are the best representative of the majority of CFS sections determined by Schafer and Peköz (1998) based on loads of imperfection measurements. It should be mentioned that the adopted CDF values are valid for the sections with the thickness (t) less than 3mm (Schafer and Peköz, 1998), so they are suitable for the sections considered in this study.

As shown in Fig. 4.5, the pinned support at the two ends of the CFS beam about major axis was simulated by coupling the nodes at each end section to the reference point defined in the mid-web, while the rotation about the minor axis was prevented. The end sections were also prevented from warping to be consistent with the assumption made for the EC3 design calculations in Section 4.6. To avoid lateral-torsional buckling, lateral bracings (representative of transitive beams in the roof systems) were used at each $L/4$ along the length of beam (see Fig. 4.5).

While the pure bending moments at SLS (equal to 70% of the calculated flexural capacity according to EC3) were directly imposed at the two end sections of the beam, the external loads at ULS were simulated by applying uniform rotations about the major axis of the two end sections using a displacement control regime. FE analysis was carried out using "Static, General" method analysis available in ABAQUS library (2007), which has been shown to be capable of accurately predicting the flexural capacity and deformation of CFS elements at both pre- and post-buckling range (Ye et al., 2018a, Mojtabaei et al., 2018, Ye et al., 2016a).

Chapter 4. Development of optimum cold-formed steel beams for serviceability
and ultimate limit states using Big Bang-Big Crunch optimisation

91
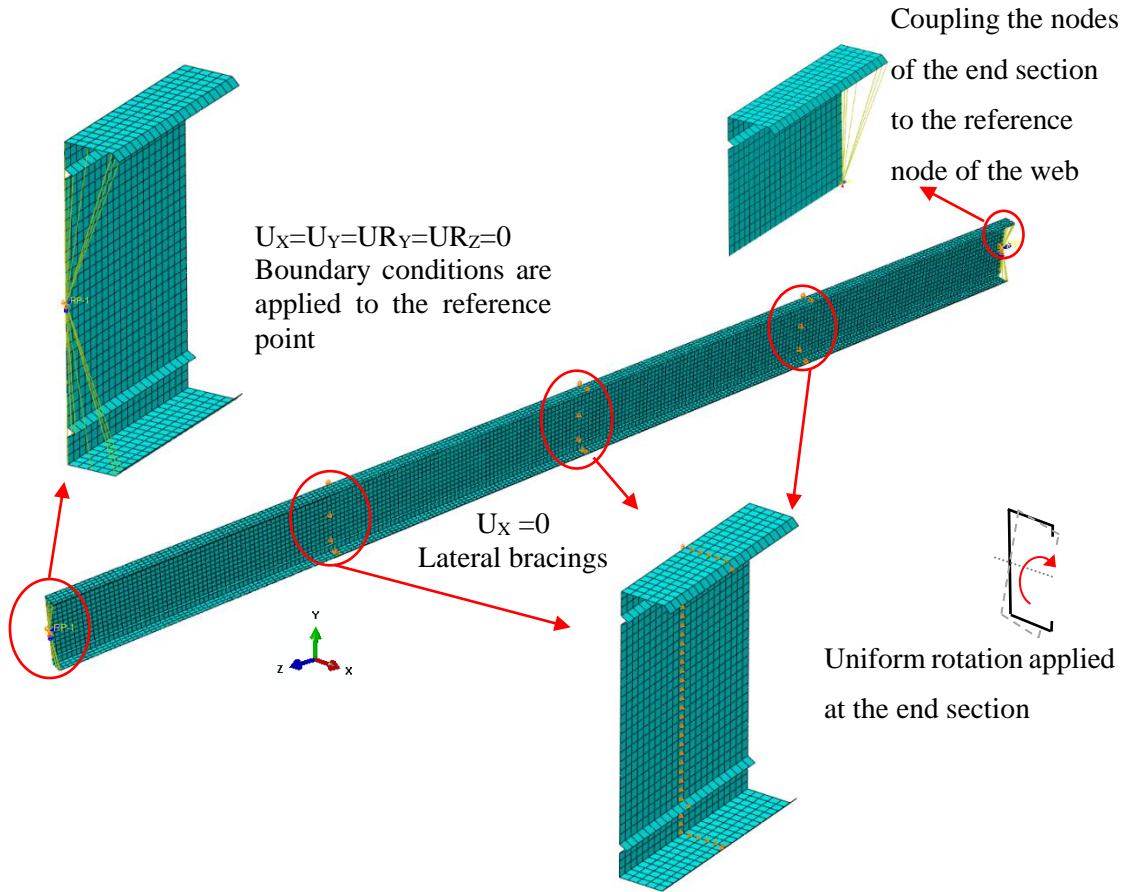
Fig. 4.5. Boundary conditions in the FE models subjected to pure bending moment

4.7.2. FE results of the standard and optimum sections

The results of the non-linear FE analyses were used to assess the efficiency of the CFS beam sections optimised using different prototypes (obtained in Section 4.6) compared to the benchmark section. Table 4.5 lists the maximum deflections and flexural capacities of the 12 selected prototypes as well as the benchmark channel predicted by EC and FE at SLS and ULS. Generally, the results obtained from EC are shown to be reliable for both SLS and ULS. The average ratios of the calculated mid-span deflection and flexural capacity using EC3 to the corresponding FE results were 1.01 and 1.02 with standard deviation of 8% and 5%, respectively. This implies that effective stiffness (I_{fic}) and effective second moment of area (I_{eff}) calculated based on EC3 effective width method provide reasonable predictions.

Fig. 4.6 compared the moment versus mid-span deflection curves for the CFS beam with standard and optimum cross-sections (under ULS) for prototypes ④ and ⑨ as representative examples. It is shown that the proposed optimisation algorithm could increase both stiffness and maximum capacity of the sections. Fig. 4.7 also illustrates the typical failure mode of the CFS beam at ULS, which is due to the local/distortional buckling at the compression zone.

Chapter 4. Development of optimum cold-formed steel beams for serviceability
and ultimate limit states using Big Bang-Big Crunch optimisation

92

Table 4.5. EC3 and FE results of CFS beam with benchmark and optimum cross-sections in terms of maximum deflection and flexural capacity at SLS and ULS, respectively

Prototypes	SLS			ULS		
	δ_{EC} (mm)	δ_{FE} (mm)	$\dfrac{\delta_{EC}}{\delta_{FE}}$	$M_{max,EC}$ (kN.m)	$M_{max,FE}$ (kN.m)	$\dfrac{M_{max,EC}}{M_{max,FE}}$
Standard	23.8	22.9	1.04	16.47	16.94	0.97
①	15.5	17.6	0.88	15.56	14.94	1.04
②	16.5	17.9	0.92	17.16	16.36	1.05
③	17.2	18.0	0.95	15.81	15.11	1.05
④	19.2	21.9	0.88	21.40	22.36	0.96
⑤	20.0	21.4	0.94	21.22	21.93	0.97
⑥	20.3	19.4	1.05	19.68	19.62	1.00
⑦	22.3	22.2	1.00	23.63	24.22	0.98
⑧	22.7	20.3	1.12	22.03	22.68	0.97
⑨	22.8	21.1	1.08	20.41	19.72	1.03
⑩	25.0	23.2	1.08	23.75	21.12	1.12
⑪	24.9	23.1	1.08	21.86	19.97	1.09
⑫	25.8	24.3	1.06	25.97	23.92	1.09
Average			1.01			1.02
Standard deviation			0.082			0.055
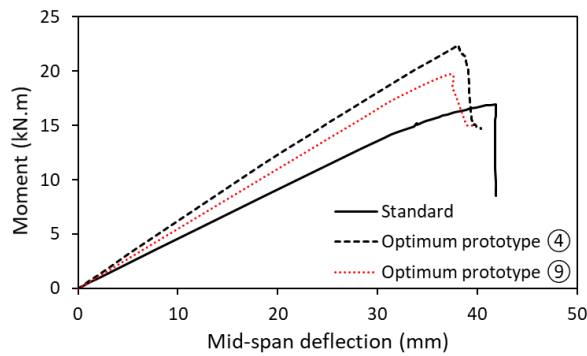
Fig. 4.6. Moment versus mid-span deflection curve for the CFS beam with standard and optimum cross-sections for prototypes ④ and ⑨
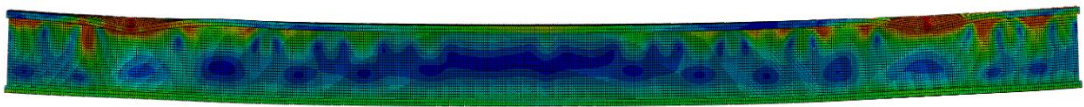
Fig. 4.7. Typical failure mode of the CFS beam at ULS

4.8. SUMMARY

Unlike Chapter 3 which was based on ultimate limit state, a new optimisation tool was presented in this chapter to develop more economical laterally braced CFS beam based on both serviceability and ultimate limit states, according to EC3 effective width method, by optimising the relative dimensions of cross-sections and allowing for the inclined single or double edge lips and triangular intermediate web and flange stiffeners. To obtain optimum solutions, Big Bang–Big Crunch (BB-BC) optimisation algorithm was adopted while design variables were determined by taking into account EC3 design constraints as well as a range of manufacturing and end-use limitations. The proposed optimisation framework was applied to twelve different prototypes and the accuracy of the results at both SLS and ULS was examined through detailed FE models.

Chapters 3 and 4 conducted optimisations to find the best design solutions for the buckling strength of CFS elements determined according to Eurocode 3. The results of these two chapters will be used in Appendix C where a coupled optimisation framework at the element and structural levels is introduced for CFS frames. In another study which is presented in Appendix A, CFS elements will be also optimised to improve their post-buckling behaviour.

4.9. CONCLUDING REMARKS

Based on the results presented in this paper, the following conclusions could be drawn:

1. For the same amount of material, the proposed optimisation framework could increase the flexural capacity and stiffness of the standard benchmark section by 58% and 44%, respectively. In general, optimised cross-sections (at both SLS and ULS) tend to use taller web and narrower flanges. The main differences between optimised shapes for ULS and SLS are the size and the angle of edge stiffeners as well as the location of the intermediate web and flange stiffeners.

2. The optimum dimensions of the plain channels for SLS are very similar to those obtained for ULS. While optimisation of plain channel sections (including those with intermediate stiffeners) at ULS did not provide efficient design solutions, using optimum plain channels at SLS could offer considerably higher stiffness compared to the benchmark lipped channel section. This implies that optimum plain channels are more adequate for SLS requirements.

3. The flexural capacity and stiffness of the benchmark lipped channel at ULS and SLS was increased by 30% and 37%, respectively, only by optimising its relative cross-sectional dimensions. While an additional 10% flexural capacity at ULS was obtained by using double edge stiffeners, a negligible improvement in flexural stiffness was observed at SLS.

4. The flexural capacity and stiffness of the optimum single and double lipped channels at ULS and SLS, respectively, were not generally enhanced by incorporating intermediate stiffeners in the web. However, adding intermediate stiffeners in the flanges could increase the flexural capacity and stiffness of the sections at ULS and SLS by up to 17% and 10%, respectively.

5. It was shown that the newly developed folded flange channel can be considered as the most desirable section owing to the fact that it is capable to provide 58% and 41% higher bending capacity and stiffness at ULS and SLS, respectively, compared to the standard lipped channel section with the same amount of material.

6. The efficiency of the optimised CFS beam sections was assessed by using detailed FE models accounting for material non-linearity and initial geometric imperfections. The results of the FE simulations in general confirm the accuracy of the mid-span deflection and flexural capacity of the sections predicted by EC3 proposed methodology (less than 12% error).

CHAPTER 5

Behaviour and Design of Cold-Formed Steel Bolted Connections

5.1. INTRODUCTION

Cold-formed steel (CFS) portal frames are gaining increased popularity around the world. The behaviour and capacity of these frames are to a large extent controlled by the rafter-to-column and column-to-base connections, which are implemented in a fundamentally different way compared to the traditional frames composed of hot-rolled sections with welded connections. In CFS portal frames the connecting members are typically bolted to a gusset plate (or 'bracket') through their webs only. However, due to the characteristic thinness of CFS members, local buckling failure of the cross-section adjacent to the bolted connection has been previously identified as an often governing failure mode. While previous chapters (i.e. Chapters 3 and 4) focused on the optimum design of CFS elements, the research work presented in this chapter aimed to conduct a detailed investigation of the flexural and compression behaviour, capacity and design of CFS bolted connections failing by local buckling. To this end, experimentally validated finite element models were used, accounting for material nonlinearity, geometric imperfections and non-linear bolt bearing behaviour. The effects of the cross-sectional shape and thickness of the beam, the bolt group configuration and the bolt group length were investigated. The results were then employed to develop design equations with a wide range of applicability. A reliability analysis was performed within the framework of both the Eurocode and the AISI standards to ensure that the proposed design equations could provide the required level of safety. Finally, the interaction of bending and shear, and bending, shear and compression were assessed, and appropriate interaction formulas were then recommended.

5.2. BACKGROUND

Cold-formed steel (CFS) structural members have several important advantages over their hot-rolled counterparts, such as a high strength-to-weight ratio, a light-weight which facilitates handling, transportation and installation, a high flexibility in manufacturing different cross-sectional shapes and a relatively straightforward manufacturing process through brake-pressing or cold-rolling. The use of CFS has therefore dramatically increased over the past decades. At the same time a significant widening of its range of application has taken place. CFS members are no longer solely used as secondary members such as purlins, girts (side rails) and cladding, but are now also frequently used to assemble the primary load-bearing structural system (Williams, 2016). An example of this evolution is the emergence of CFS portal frames, which are combined with CFS purlins, girts and cladding in a building solution provided by a single specialized CFS fabricator/contractor. These CFS systems are used in industrial and agricultural buildings, sports and leisure halls, warehouses and hangars and typically feature a pitched roof.

CFS portal frames are fundamentally different from hot-rolled frames in the way the connections are made. They are typically bolted connections and consist of steel gusset plates, usually featuring folded edge stiffeners (and in those cases sometimes referred to as 'brackets'), to which the webs of the connecting members are bolted. Fig. 5.1 shows typical arrangements for an eave and an apex connection between back-to-back channel members. CFS bolted connections under tensile loads are frequently used in trusses and lateral bracing systems (Zeynalian et al., 2016, Reda et al., 2019), while they can be also employed in CFS frames to transfer the axial compression loads of the column to the base (Fig. 5.2) (Mojtabaei et al., 2018, Phan et al., 2017b). These types of connections are economical and easy to assemble and spans of up to 25m have been achieved in the UK with these configurations. However, the fact that a connection is made through the webs of the connecting members only, leaving the flanges unconnected, has obvious repercussions for the behaviour of the connection, both in terms of stiffness (they typically act as semi-rigid connections with a stiffness governed by the bolt hole elongation characteristics) and strength. With respect to the latter, in a connection with properly sized bolts and gusset plates, failure typically takes place in the connecting member, adjacent to the connection, as a result of cross-sectional instability (Mojtabaei et al., 2018, Lim and Nethercot, 2004b, Sabbagh et al., 2010, Dubina et al., 2009). This instability is promoted by the introduction of compression, moment and shear through the web only, whereby the local stress concentrations at the bolt locations can potentially further reduce the capacity below the calculated cross-sectional values. Unfortunately, current design standards do not account for this type of failure, which was first

observed by Kirk (1986) in tests on CFS back-to-back lipped channel portal frame connections as early as 1986. It is also consistent with observations reported by Chung and Lau (1999) CFS moment-resisting bolted connections.

Several studies have been previously focused on the behaviour of CFS bolted moment connections (i.e. beam-to-column connections). Lim (2001) conducted a comprehensive study on CFS moment-resisting bolted connections, which also considered various failure modes of the bracket: overall lateral-torsional buckling and local buckling modes of the bracket components. A large part of the study, however, was devoted specifically to local web buckling of the connecting members. With this purpose an experimental program was subsequently carried out consisting of four apex connections tested in a four-point bending configuration, described in detail in (Lim and Nethercot, 2003a). The tests revealed a profound influence of the bolt group length l_b (i.e. the distance between the centre lines of the outer bolt rows) on the capacity of the connections. The authors explained this by pointing out the reduced magnitude of the bolt forces in the longer connection. While this is of course true, the change in inclination of the bolt force in the shorter connection should also be noted. While the bolt forces in the first row of the longer connection are near vertical, a comparatively much larger horizontal component is introduced into the portion of the web adjacent to the connection in the shorter bolt group. This horizontal force adds to the compression already present as a result of bending and increases the risk of local buckling in the web of the connected member just outside the bolt group.

(a)

(b)

Fig. 5.1. Typical CFS bolted moment connection: (a) eaves connection, and (b) apex connection
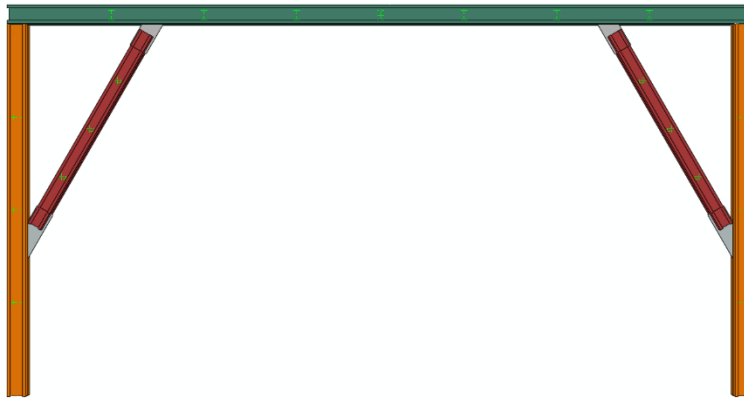
Fig. 5.2. Typical CFS frame used in CFS industries

Lim et al. (Lim et al., 2016b) dedicated a further study to the development of a design methodology for this type of connections based on the Direct Strength Method (DSM). The authors borrowed ideas from previous work by Baigent and Hancock (Baigent and Hancock, 1982), who conducted experiments on frames composed of single CFS channels with rigid connections. Baigent and Hancock drew attention to the effect of the bi-moment in the channels, which reduced their capacity below the major axis bending capacity. Lim et al. (Lim et al., 2016b) claimed that this bi-moment is also important in back-to-back channel connections where a moment is introduced eccentrically in the web of each individual channel. Consequently, they proposed to calculate the connection capacity using the DSM local buckling equations, but with an elastic buckling stress obtained from a finite strip analysis in which the stress distribution resulting from a combined bending moment and bi-moment is applied. It was concluded that this results in conservative predictions for bolt groups with reasonable lengths ($l_b/h > 1$, where h is the section depth) with the margin of safety increasing with the bolt group length l_b. In another relevant study, Dubina et al. (Dubina et al., 2009) tested a total of nine eaves joints and nine apex joints between back-to-back lipped channel members, including a limited number of specimens with additional bolts in the flanges. The specimens were tested under either monotonic or cyclic loads. The authors also investigated the applicability of the component method to predict the stiffness and strength of these connections. In addition, two tests on full-scale portal frames under monotonically increasing lateral loading (in one case combined with vertical pre-loading) were carried out.

Several studies have been also conducted on the behaviour of CFS eccentric connections (i.e. column-to-base connections). In previous studies, it was frequently reported that the non-uniform stress distribution exists in a tension member adjacent to a connection, in which all elements of the cross-section are not directly connected. In fact, this phenomenon is due to presence of the bolts, which is commonly referred to the shear lag effect. Shear lag effect was first observed by Munse and Chesson (Munse and Chesson, 1963) in the tension members

with bolted or riveted end connections and a reduction factor for the net section was also proposed. Further experimental and analytical studies were conducted on the tension members with both bolted and welded end connections and design recommendations were made by Kulak and Wu (1997) and Easterling and Gonzalez (1993). Orbison et al. (Orbison James et al., 2002) performed experimental tests on the short tension member specimens to investigate the influence of varying connection eccentricity and length on the load capacity of the members. More recently, Teh et al. (Teh Lip and Gilbert Benoit, 2013a, Teh Lip and Gilbert Benoit, 2012, Teh Lip and Gilbert Benoit, 2013b) examined experimentally the accuracy of equations specified by the North American and Australasian codes for determining the net section tension capacity of CFS angle braces bolted at one leg, flat steel sheets, and channel brace, and consequently more accurate design equations were proposed. In a follow-up study (Teh and Yazici, 2013), it was concluded that the net section is controlled by three factors: (i) the in-plane shear lag associated with stress concentration around a bolt hole, (ii) the out-of-plane shear lag which exists in a bi-symmetric I-section bolted at the flanges only, and (iii) the bending moment resulted from the connection eccentricity with respect to the neutral axis.

Despite the research conducted on CFS portal frame connections to date, a number of additional issues need to be addressed in order support and facilitate practical design:

1. The design equations previously proposed by Lim and Nethercot (Lim and Nethercot, 2003a) for CFS moment-resisting bolted connections are only valid within a certain range of design parameters. Most importantly, they were developed for back-to-back lipped channels with specific dimensions. There is an obvious need for a more universally applicable design methodology given the wide range of beam sections available in practice.

2. While comprehensive studies were conducted on the tensile capacity of the CFS members in the bolted connections, currently there is no study on the behaviour and design of CFS bolted connections subjected to axial compression load. It is worth mentioning that the formulations presented in the North American specifications (AISI S100-12, 2012) for the compression members cannot be used to accurately predict the compression capacity bolted connections due to the presence of the bolts in CFS compression members (e.g. column-to-base connections).

3. The previously developed design equations (Lim and Nethercot, 2003a) considered the influence of the relative bolt group length (l_b/h), the web slenderness (h/t) (where t is the section thickness) and the geometric arrangement of the bolts (in 2×2, 3×3 and 4×4 patterns). However, as will be shown in this paper, the connection capacity also

exhibits a major dependence on the eccentricity parameter X, which is defined as the distance between the web and the centroid of the cross-section, necessitating an update of the design equations.

4. Before applying the proposed equations in practical design a reliability study needs to be carried out in order to demonstrate that the design equations possess the required margin of safety.

This chapter aims to address all of the above issues. The scope of the current chapter will however be limited to local buckling failure in the web and excludes other failure modes such as bolt failure and failure of the gusset plate.

5.3. FINITE ELEMENT MODEL AND VALIDATION

Finite element (FE) modelling has previously been used to predict the behaviour of CFS bolted connections with gusset plates (Öztürk and Pul, 2015, Lim and Nethercot, 2003a, Lim and Nethercot, 2004c, Bagheri Sabbagh et al., 2013, Elkersh, 2010, Serror et al., 2016a, Ye et al., 2019c, Ye et al., 2019b) and good agreement between the test results and the FE predictions has generally been reported. In this study, the experimental work by Lim and Nethercot (Lim and Nethercot, 2003a) was used to validate the proposed FE model. Lim and Nethercot conducted an experimental study on apex joints using the four-point bending configuration illustrated in Fig 5.3, while varying the length l_b of the bolt group between tests. The ratio l_b/h ranged from 0.94 to 1.83 in joints A to D, respectively, as detailed in Fig. 5.3. The connected members consisted of back-to-back lipped channels with the dimensions shown in Fig. 5.3.

The software package ABAQUS (Abaqus/CAE User's Manual, 2007) was used in this study to develop a detailed FE model including geometric and material non-linearity, as well as imperfections. The model was first validated against the aforementioned tests and consequently used to conduct parametric studies in order to gain an increased understanding of the behaviour of these connections.

Gusset plate
(340×88 mm)

2.95

M16 bolts

3.98

Back-to-back channel
(336×88×20 mm)

l_b=315 mm (connection A)

l_b=390 mm (connection B)

l_b=465 mm (connection C)

l_b=615 mm (connection D)

Section A-A
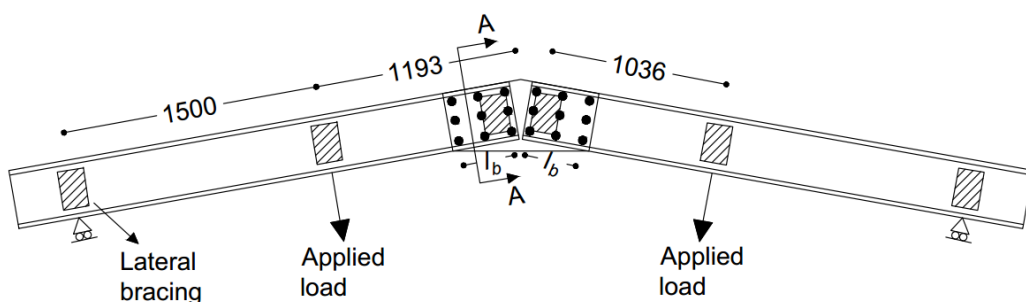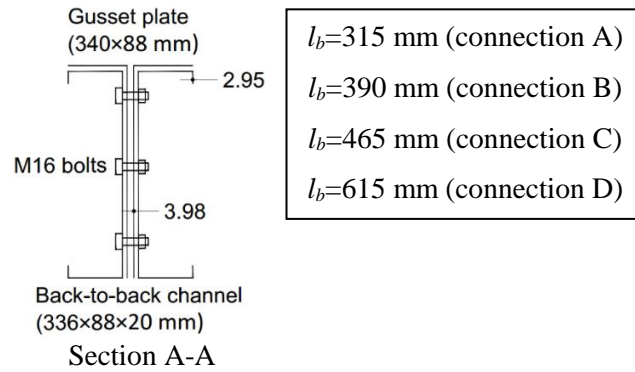
Fig. 5.3. Apex connection tested by Lim and Nethercot (Lim and Nethercot, 2003a)

5.3.1. Geometry and boundary conditions

The geometry and boundary conditions of the experimental set-up were replicated in the FE model, as shown in Fig. 5.4. To simulate pin-ended boundary conditions at the specimen ends, the nodes belonging to each end section of the back-to-back channels were first coupled to the centroid of the whole cross-section, where a reference point was defined. Simply supported boundary conditions were then applied to the reference point at both ends, as clarified in Fig. 5.3. The lateral displacements of the webs were prevented at those locations were bracing was put in place during the test, as also shown in Figs. 5.3 and 5.4. Finally, point loads were applied in a displacement controlled manner to the reference points, which were coupled to all the nodes of the cross-section at the load application points.

Z

Y

X

Lateral restraint

Lateral restraint

Z

Y

X'

Support

Support

Lateral restraint at the
location of the bolts

Lateral restraints were
applied to the web:
$U_X=0$

Nodes in the end sections
were coupled to the
reference node. Boundary
conditions were applied to
the reference node:
$U_Z'=UR_Y'=0$

Nodes in the cross-sections were
coupled to the reference node at
the load application point

Imposed
displacement

Fig. 5.4. FE model of apex connection showing loading and boundary conditions

5.3.2. Element type and material properties

Shell elements are the logical choice for thin-walled structures, where the thickness is typically considerably smaller than the other dimensions. The general-purpose S4R element, which is a 4-noded quadrilateral flat shell element with reduced integration, was selected from the ABAQUS library. The default setting of five integration points over the thickness was used. This particular element was previously shown by other researchers to yield accurate predictions when modelling cold-formed steel connections subject to bending (Bagheri Sabbagh et al., 2013, Bagheri Sabbagh et al., 2012a). To select an appropriate mesh size, a mesh sensitivity analysis was carried out using the model for connection D. The results are shown in Table 5.1 and the conclusion can be drawn that refining the mesh beyond a 20×20 mm^2 size had a negligible effect on the prediction of the connection capacity. Consequently, a mesh size of 20×20 mm^2 was selected.

The material behaviour was modelled using a bi-linear stress-strain diagram with an initial elastic modulus E=210 GPa, followed by a linear hardening range with a slope of E/100. This model was previously proposed by Haidarali, Nethercot (Haidarali and Nethercot, 2011b). The yield stress and the ultimate strength, as measured from coupon tests reported in (Lim and Nethercot, 2003a), were f_y=358 MPa and f_u=425 MPa, respectively, for the channels, and f_y=341 MPa and f_u=511 MPa for the gusset plate.

Table 5.1. Mesh sensitivity analysis on the connection D

Mesh size	Predicted capacity (M_{max}^{FE})
(mm×mm)	(kN.m)
10×10	87.69
15×15	87.80
20×20	88.02
30×30	91.91
40×40	93.06

5.3.3. Modelling of the bolts

It has previously been shown that the bearing characteristics of the bolts (i.e. the initial bearing stiffness and the inelastic bolt hole elongation stiffness) have a considerable influence on the rotational capacity of a bolted CFS connection, while only have a minor effect on its ultimate capacity (Bagheri Sabbagh et al., 2012b, Gilbert and Rasmussen, 2010). One option to model the bolt behaviour, used by several researchers in the past (Öztürk and Pul, 2015, Gutierrez et al., 2015, Liu et al., 2015), is to explicitly model the geometry of the bolts, nuts and washers

using solid elements and surface-to-surface interactions. However, this typically leads to a complex model which is computationally expensive, especially in connections with a large number of bolts. Lim and Nethercot (Lim and Nethercot, 2004b, Lim and Nethercot, 2003a) therefore employed a simplified bolt model consisting of two perpendicular linear elastic springs. They reported good agreement between the FE predicted flexural capacity of the connections and the experimental values. It should be noted, however, that all connections in (Lim and Nethercot, 2003a) failed by cross-sectional instability in the channel beams in the zone adjacent to the connection and not by failure of the actual connection. Similarly, the main focus of the study presented in this paper was to determine the capacity of the connected CFS member, as limited by cross-sectional instability, and it could therefore be argued that the modelling of the bolt behaviour was of secondary importance. However, the ability to model the actual moment-rotation behaviour of the connection zone and verify it against the experimentally recorded behaviour reported in (Lim and Nethercot, 2003a) was believed to constitute a valuable addition to the study and one thought to be relevant in light of planned further studies related to rotational capacity and associated energy dissipation under monotonic and cyclic loading. The bolts were therefore modelled using 'discrete fastener' elements from the ABAQUS library (Abaqus/CAE User's Manual), which permitted the input of the actual inelastic bolt hole elongation behaviour. The bearing behaviour of the bolts used in the tests was experimentally investigated by Lim and Nethercot (2004c) through double lap shear tests. A typical load-elongation graph is shown in Fig. 5.5. In further parametric studies, which included plate thicknesses different from those reported in (Lim and Nethercot, 2004c), the equations proposed by Fisher (1964) were adopted instead:

$$R_B = R_{ult}\left[1 - e^{-\mu(\delta_{br}/25.4)}\right]^{\lambda} \tag{5.1}$$

$$R_{ult} = 2.1 \cdot d \cdot t \cdot F_u \tag{5.2}$$

In the above equations δ_{br} is the bearing deformation (in mm), R_{ult} is the ultimate bearing strength, t is the web thickness, d is the bolt diameter and R_B is the bearing force in the bolt. F_u is the tensile strength of the web material, while $\mu = 5$ and $\lambda = 0.55$ are regression coefficients presented by Uang et al. (2010). The bolt diameter was reported to be 16 mm in (Lim and Nethercot, 2003a) and this value was maintained throughout the parametric studies. It should be noted that Equation 5.1 ignores bolt slip.

The 'discrete fastener' elements in ABAQUS use attachment lines to create connectors between selected faces of surfaces, as shown schematically in Fig. 5.6. The three surfaces in

this figure represent the two webs of the channels and the gusset plate in between. A 'radius of influence' is assigned to each connector, whereby the displacements and rotations of the surface nodes within this radius are coupled to the displacements and rotations of the fastening point. This radius was taken as 8 mm. However, a sensitivity study varying the radius of influence between 5 mm and 30 mm indicated that this variable had negligible influence, with the corresponding capacity predictions varying by only 2%.
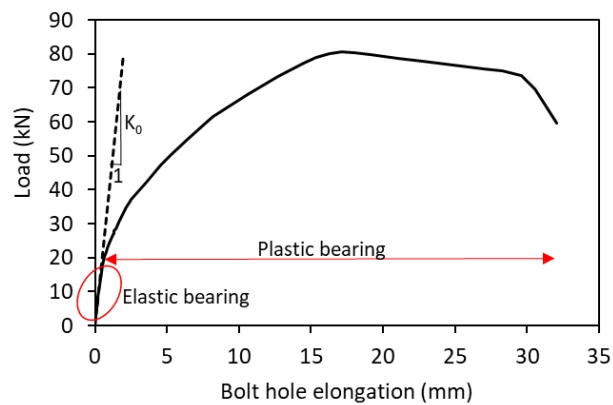
Fig. 5.5. Bearing behaviour of bolt against steel plate adopted from tests by Lim and Nethercot (Lim and Nethercot, 2004c)
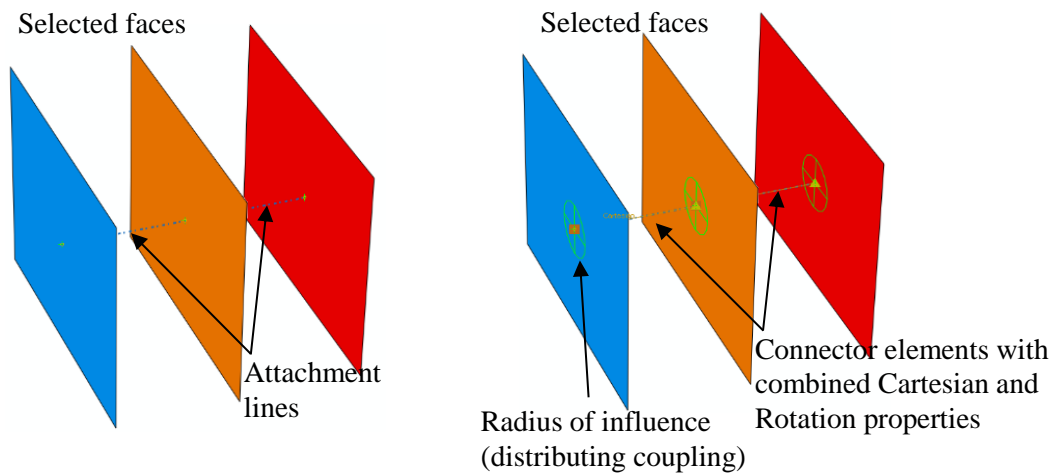
Fig. 5.6. Modelling a single bolt with a discrete fastener element

5.3.4. Imperfections

Lateral-torsional buckling of the test specimens in (Lim and Nethercot, 2003a) was prevented by the presence of a lateral bracing system and all specimens failed by cross-sectional instability in the zone adjacent to the connection. Therefore, either a local or a distortional imperfection was incorporated into the model, depending on which mode had the lower critical buckling stress. This was achieved by carrying out an elastic buckling analysis of the apex

connection in ABAQUS and using the scaled first eigenmode as the shape of the initial imperfection. The amplitude of the imperfection was determined based on the work by Schafer and Peköz (Schafer and Peköz, 1998), whereby the 50% value of the cumulative distribution function of the imperfection magnitudes was adopted. This represents the 'most likely' imperfection and amounts to a magnitude of $0.34t$ and $0.94t$ for the local and distortional imperfections, respectively. It should be noted, however, that the aforementioned work (Schafer and Peköz, 1998) was based on data pertaining to CFS sections with thicknesses below 3 mm. It therefore directly applies to the modelling of the experimental programme carried out by Lim and Nethercot (Lim and Nethercot, 2003a) in the validation study. However, further parametric studies were carried out for thicknesses (t) which in some cases exceed 3 mm (Section 3). In those models the imperfection magnitude was determined using the equation proposed by Walker (Walker, 1975):

$$\omega_d = 0.3t\sqrt{\frac{\sigma_{0.2\%}}{\sigma_{cr}}} = 0.3t\lambda_s \qquad (5.3)$$

where $\sigma_{0.2\%}$ and σ_{cr} are the 0.2% proof stress of the material and the elastic local buckling stress, respectively, and λ_s is cross-sectional slenderness. The cross-sectional slenderness for beam and column elements representing the cross-sectional shapes and thicknesses are calculated Equations 5.4 and 5.5:

$$\lambda_s = \sqrt{M_y / M_{cr}} \qquad (5.4)$$

$$\lambda_s = \sqrt{P_y / P_{cr}} \qquad (5.5)$$

where $M_y = Z_f f_y$ and $P_y = A_g f_y$ are the yield moment and compression capacities of the cross-section, respectively, and $M_{cr} = Z_f \sigma_{cr}$ and P_{cr} are the elastic local buckling moment and compression force of the cross-section, respectively. Also Z_f and A_g are the section modulus about horizontal axis and gross cross-sectional area. σ_{cr} is the elastic buckling stress of CFS section which can be computed using software such as CUFSM (Li and Schafer, 2010).

While this approach was motivated by the lack of actual imperfection measurements in the experimental programme, a sensitivity study previously carried out by Lim and Nethercot (2003a) has demonstrated that this particular failure mode can be considered to be rather insensitive to the imperfection magnitude, thus largely justifying the adopted methodology.

5.3.5. Validation of FE model

The four connections A to D, representing apex connections with different bolt group lengths, were analyzed using a "Static General" analysis. As an example, Fig. 5.7 shows the moment in the constant moment span versus the vertical apex displacement of connections A and D obtained from the experiments, as well as the corresponding curves predicted by the FE models. It should be mentioned that the initial gradual increase in the gradient of the experimental moment-deflection curve of connection A was reported to be due to imperfect alignment of the bolt holes and slack in the loading rods (Lim and Nethercot, 2003a). Hence, this experimental curve was modified by first determining the connection stiffness at a bending moment of 40 kNm, extending the curve down from this point to the horizontal axis with the same stiffness and then shifting the curve to the origin. It is seen that the FE results agree well with the experimental observations over the whole loading range up to the peak load. Concurrently, Table 5.2 also demonstrates that the proposed FE modelling predicts the maximum moment capacity (M_{max}^{FE}) of all apex connections very well compared to the experimental results (M_{max}^{exp}), with an average error of 2% and a standard deviation of 0.018.
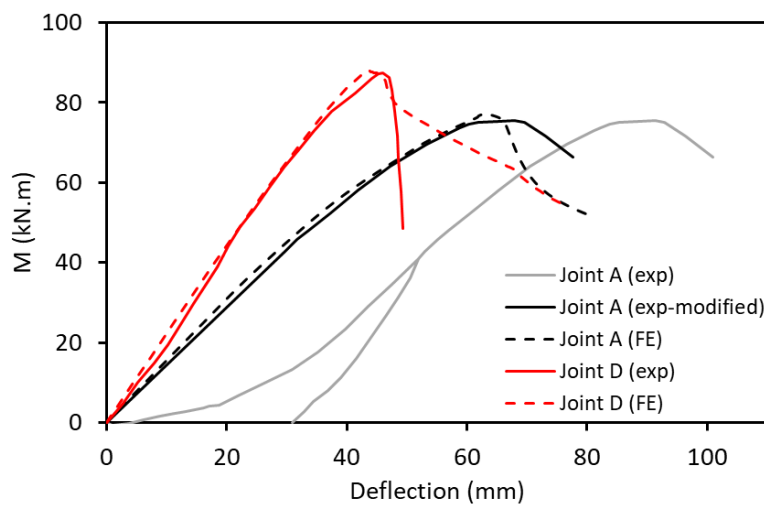
Fig. 5.7. Comparison between moment-deflection curves of apex connections obtained from tests and FE simulations

Table 5.2. Comparison between the flexural capacities of the connections obtained from tests and FE simulations

Connection	l_b (mm)	l_b/h	M_{max}^{exp} (kN.m)	M_{max}^{FE} (kN.m)	$M_{max}^{exp}/M_{max}^{FE}$	M_{max}^{ideal}	$M_{max}^{ideal}/M_{max}^{exp}$
A	315	0.94	75	76.01	1.01	75.92	1.01
B	390	1.16	77.5	80.72	1.04	80.39	1.04
C	465	1.38	82.5	82.5	1.00	81.55	0.99
D	615	1.83	87.5	88.02	1.01	85.36	0.98
Average					1.02		1.00
St. dev					0.018		0.027

5.3.6. Simplification of the connection model

In order to simplify the FE model for further investigations, the apex connection in four-point bending was idealized as a cantilever beam and column with a bolted gusset plate connection subjected to pure bending moment and axial compression force, respectively. Fig. 5.8 and Fig. 5.9 illustrate the FE models and indicate the loading and boundary conditions of the bolted moment, and bolted compression connections, respectively. The gusset plate was fixed (clamped) at its end and connected to back-to-back channels by means of the fastener elements. At the loaded end of the element, the rotational degrees of freedom about the x and y-axis of all points in the cross-section were coupled to those of the centroid and an increasing rotation/force was applied. The beam/column was supported in the out-of-plane direction along its length to prevent global buckling. A sensitivity study was carried out using connections with two different bolt group sizes ($l_b/h = 0.5$ and $l_b/h = 3$, which could be considered to constitute the practical extremities of the l_b/h spectrum) in order to determine an appropriate value of the cantilever length l_e (see Fig. 5.10), expressed as a multiple of the cross-sectional depth ($l_e = \omega h$). This study is necessary since the boundary conditions at the loaded end prevent warping of the cross-section and thus, for an insufficient length, restrain the shear lag effect which occurs at the bolted connection (as discussed in Section 5.4.2), resulting in an increased capacity. The results presented in Fig. 5.10 show that the results converged past $\omega = 6$ for both bolt group lengths. Hence, an effective length (l_e) equal to $6h$ was used in further parametric studies.
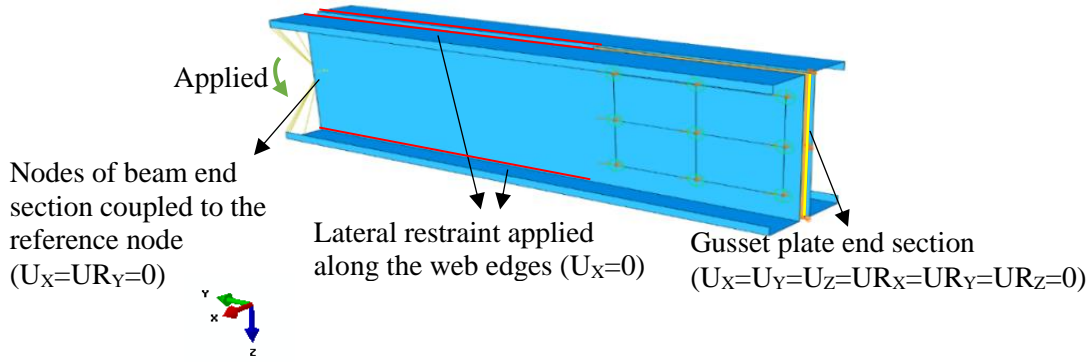
Fig. 5.8. FE modelling of idealised bolted moment connection including loading and boundary conditions
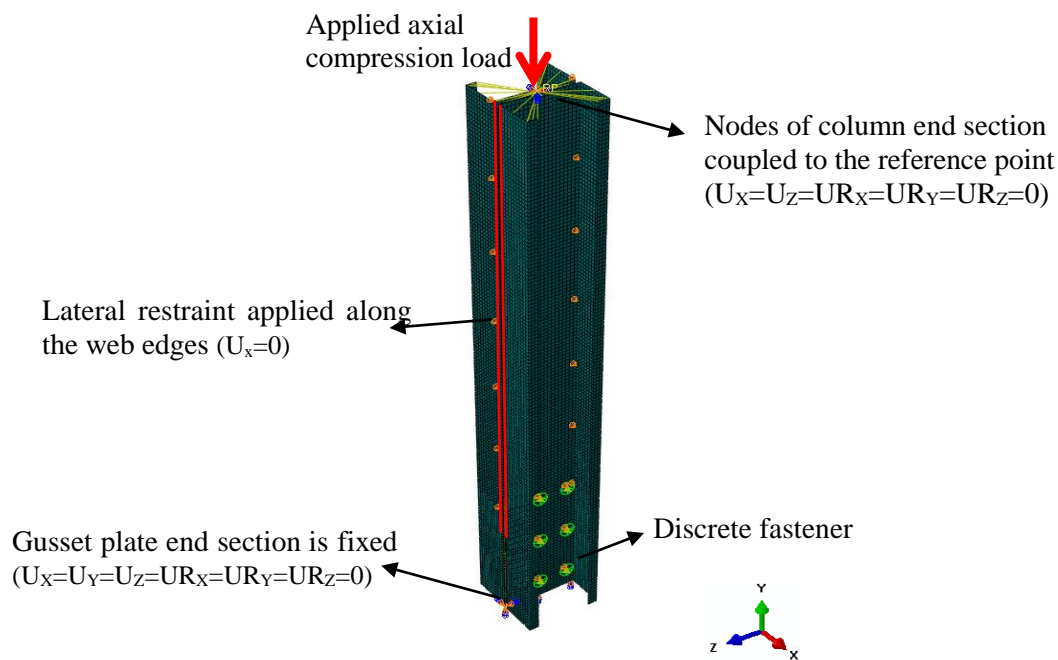
Fig. 5.9. FE modelling of idealised bolted compression connection including loading and boundary conditions
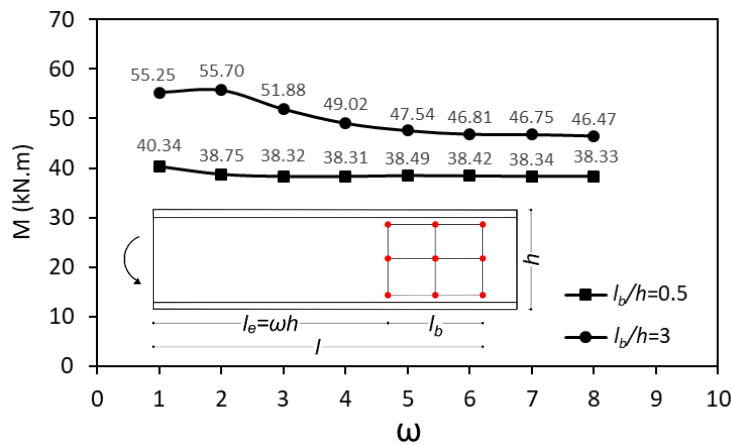
Fig. 5.10. Sensitivity study of the cantilever length for two different bolt group sizes ($l_b/h = 0.5$ and $l_b/h = 3$)

The failure mode of connections A to D predicted by the idealized FE models is local buckling of the web immediately adjacent to the first bolt line, as shown in Fig. 5.11 for connections A and D. This is consistent with the experimental observations, as well as with the more detailed FE models. The predicted moment capacities (M_{max}^{ideal}) of connections A-D also agree very well with the experimental results, as shown in Table 5.2, with a negligible average error and a standard deviation of 2.7 %. In addition, a typical failure mode mechanism of the CFS bolted compression connection is similar to that for bolted moment connection, as shown in Fig. 5.12.

(a)

(b)
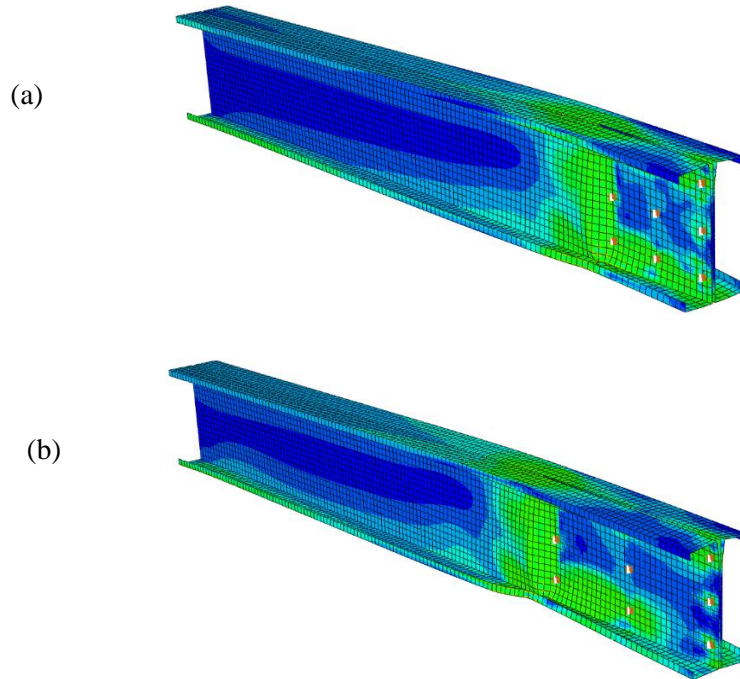
Fig. 5.11. Failure modes of idealised connections obtained from FE models: (a) connection A, (b) connection D
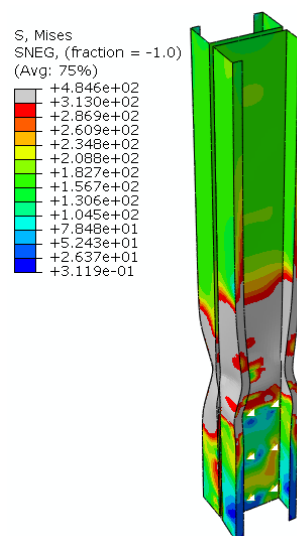
Fig. 5.12. Typical failure mode mechanism in the CFS bolted compression connections

It should be noted that, regardless of loading, the modelled compression connection resembles the moment connection. While no experimental tests under axial loads were conducted on the compression connection, as a part of this research study conducted by the authors, the detailed FE models for CFS columns under axial loads were validated against experimental tests, and very good agreement was achieved. (Ye et al., 2018c, Meza, 2018)

5.4. PARAMETRIC STUDIES

The simplified FE models described in the previous section were further used to conduct parametric studies. Three distinct bolt group arrangements were considered as a design variable, containing bolts in 2×2, 3×3 and 4×4 arrays (see Fig. 5.13). Within each configuration the ratio of the bolt group length to the section depth (l_b/h) was varied from 0.5 to 3 in intervals of 0.25. Five different cross-sectional geometries were considered. They consisted of conventional back-to-back lipped channels with progressively wider flanges and a shallower web (Fig. 5.14). The underlying aim was to vary the parameter X, which is the distance from the centroid of the channel to the centreline of the web, as listed in Table 5.3. In addition, four different section thicknesses $t = 1, 2, 4$, and 6 mm were considered for each channel geometry in order to vary the cross-sectional slenderness (λ_s), which is defined by Equations 5.4 and 5.5 for beam and column elements, respectively. The values of λ_w and λ_s corresponding to the web and whole cross-section slenderness comprised in the parametric studies are also listed in Table 5.3. The yield stress f_y, the elastic modulus E and the Poisson's ratio of the material ν were taken as 313 MPa, 210 GPa and 0.3, respectively. A total of 660 FE models for each type of connections (moment and compression connections) were needed to systematically investigate the effects of the aforementioned variables on the capacity of the connections and to achieve this the ABAQUS Scripting Interface (Abaqus/CAE User's Manual, 2007) based on the object-oriented programming language Python was used.

(a)   (b)   (c)
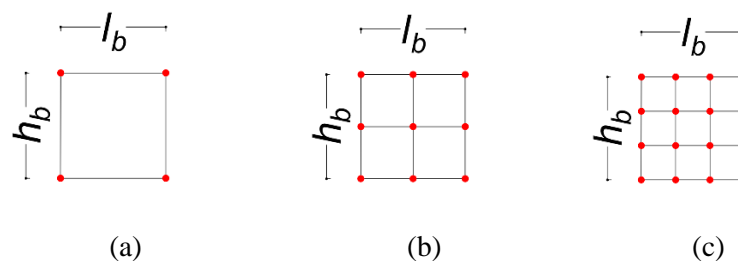
Fig. 5.13. Bolt group configurations; (a) 2×2, (b) 3×3, (c) 4×4
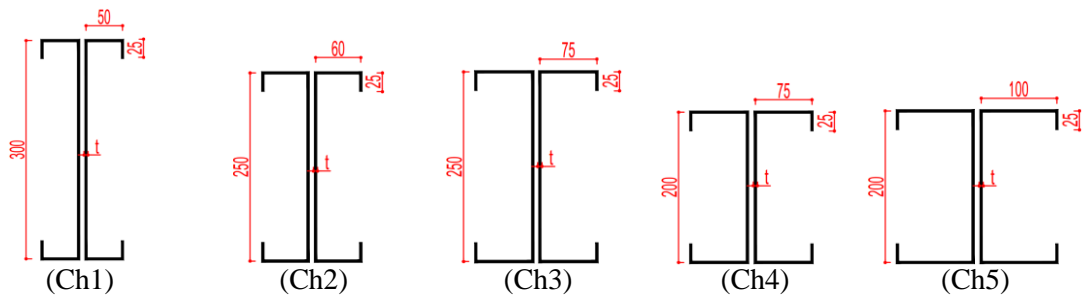
Fig. 5.14. Cross-sectional dimensions of the beams/columns used as the design variables

Table 5.3. Eccentricity, slenderness and compression capacity of the CFS back-to-back sections

Cross-sections	X (mm)	λ_w	Beam		Column	
			λ_s	M_u (kN.m)	λ_s	P_u (kN)
Ch1	11.11	300	2.047	15.26	4.892	37.89
		150	1.033	44.05	2.456	127.24
		75	0.572	107.15	1.271	343.27
		50	0.436	168.00	0.913	679.89
Ch2	15.71	250	1.724	12.97	4.145	40.12
		125	0.863	39.30	2.081	134.10
		62.5	0.524	88.59	1.056	408.16
		41.67	0.405	135.41	0.723	734.77
Ch3	20.83	250	1.752	13.08	4.193	42.61
		125	0.877	41.81	2.101	142.65
		62.5	0.575	96.13	1.060	447.38
		41.67	0.446	147.72	0.717	798.71
Ch4	23.44	200	1.521	10.63	3.266	45.75
		100	0.798	30.69	1.639	151.63
		50	0.536	70.77	0.832	454.86
		33.33	0.418	108.60	0.585	749.36
Ch5	33.33	200	1.844	10.78	3.346	50.54
		100	0.970	32.89	1.676	167.85
		50	0.658	80.86	0.845	487.33
		33.33	0.514	123.96	0.639	827.57

5.4.1. Results

The moment and compressive capacities of a CFS beam and a CFS column at the gusset plate connection (M_c and P_c) can be expressed in Equations 5.6 and 5.7, respectively:

$$M_c = RM_u \tag{5.6}$$

$$P_c = RP_u \tag{5.7}$$

where M_u and P_u are the cross-sectional moment and compressive capacities of the beam and column, respectively, and R is a reduction factor accounting for the fact that local web buckling adjacent to the connection may prevent the full cross-sectional bending strength (M_u) and compressive strength (P_u) from being reached. The reduction factor R is assumed to be a function of the previously selected variables, including the bolt group length (l_b/h), the bolt group arrangement and the channel geometry and thickness.

For the purpose of evaluating Equations 5.6 and 5.7, the cross-sectional moment and compressive capacities of a given CFS beam (M_u) and column (P_u) were obtained from FE analyses of a beam and a column segments subjected to pure bending moment and axial compressive load, respectively. The FE models shown in Figs. 5.8 and 5.9 were used for this purpose, except that the gusset plate and the connector elements were removed from the model and equal and opposite rotations and axial displacement were applied to both ends of the beam and the column, respectively. The CFS elements (i.e. beam and column), however, remained laterally restrained along the web-flange junctions. The length of the beam and the column segments was taken as three times the distortional buckling half-wave length, calculated using the CUFSM (Li and Schafer, 2010) software, as suggested by Shifferaw and Schafer (2012). The values of M_u and P_u obtained for the different cross-sections and thicknesses under consideration are listed in Table 5.4.

Figs 5.15 to 5.17 and Figs 5.18 to 5.20 present the results of the parametric studies in terms of the R values for the bolted moment and compression connections, respectively. The graphs show that, for a given cross-section and bolt group arrangement, the R values exponentially approach 1 for increasing l_b/h values. This is confirmed by plotting $ln(1 - R)$ versus l_b/h, as illustrated for the results of moment connections in Fig. 5.21. This finding dislodges earlier suggestions by Lim and Nethercot (2003a) that the trend is logarithmic rather than exponential. Moreover, the group of curves in Fig. 5.21 display a fan shape and appear to have

the tendency to pass through a single point on the vertical axis, suggesting an equation of the form:

$$1 - R = C_1 e^{[S(\frac{X}{t})](\frac{l_b}{h})} \tag{5.8}$$

where C_1 is a constant and S is a currently unknown function. Further analysis of the gradients S of the lines in Fig. 5.21 as a function of X/t revealed that the data trends can be accurately captured using an equation of the following form:

$$R = 1 - C_1 e^{-C_2(\frac{l_b}{h})(\frac{t}{X})} \tag{5.9}$$

where C_1 and C_2 are constants. The fact that R is dependent on the product of l_b/h and t/X allows the alternative interpretation that the moment capacity is instead governed by the parameters (h/t), which constitutes the slenderness of the web (and thus determines the susceptibility to local buckling) and (X/l_b), which has also been used in the AISI (AISI S100-12, 2012) guidelines as a parameter determining the severity of the effect of shear lag in a tensile connection.

MATLAB (Mathworks, 2015) was used to determine the constants C_1 and C_2 in Equation 5.9 from an optimization problem. The procedure minimized an error measure, which was taken as the standard deviation of the ratio (R_{pred}/R_{FE}). R_{pred} is the R value predicted by Equation 5.9, while R_{FE} is the corresponding R value resulting from the numerical simulations. The ensuing equations are listed in Table 5.4, together with their statistical indicators. A similar approach was also applied to the R values for the bolted compression connections, and consequently, the design equations were proposed for such connections (see Table 5.4). It is worth mentioning that, similar to the equation for the tensile connections proposed by AISI (AISI S100-12, 2012), the reduction factor for the compressive connection includes the term of X/l_b. However, the CFS connection under axial compression consists of an additional term which represents the slenderness of the web against local buckling (h/t).

Figs. 5.15 to 5.20 graphically compare the reduction factors R predicted by Equations 5.10 to 5.15, respectively, to the FE analysis results for different bolt configurations (i.e. 2×2, 3×3, and 4×4). Good agreement between the predictions and the numerical data is visually observed, confirming the favourable statistics in Table 5.4.

Table 5.4. Proposed reduction factors for different bolt group configurations

Connection type	No. Equation	Bolts configuration	Reduction factor (R)	R_{pred}/R_{FE} Average	COV
Moment	5.10	2×2	$R = 1 - 0.43\exp(-11.9(\frac{t}{X})(\frac{L_b}{h}))$	1.01	0.0008
	5.11	3×3	$R = 1 - 0.40\exp(-14.9(\frac{t}{X})(\frac{L_b}{h}))$	0.99	0.0005
	5.12	4×4	$R = 1 - 0.42\exp(-14.5(\frac{t}{X})(\frac{L_b}{h}))$	1.00	0.0009
	5.13	2×2	$R = 1.15 - 0.77(\frac{X}{L_b})^{0.34} + 6.27(\frac{h}{t})^{-1.36}$	1.03	0.001
Compression	5.14	3×3	$R = 1.06 - 0.84(\frac{X}{L_b})^{0.59} + 8.22(\frac{h}{t})^{-1.38}$	1.01	0.0009
	5.15	4×4	$R = 1.04 - 0.91(\frac{X}{L_b})^{0.68} + 6.04(\frac{h}{t})^{-1.24}$	1.02	0.0008

It is noted that the proposed equations for the 3×3 and 4×4 bolt group configurations lead to only minutely different predictions of *R*, so that Equations 5.12 and 5.15 can be adopted for both 3×3 and 4×4 bolt groups. Equations 5.10 and 5.13 for the 2×2 bolt group leads to different values of *R* compared to the equations for 3×3 and 4×4. However, the difference is relatively small, so that an attempt to unify equations for each type of connection (Equations 5.10 to 5.12 for moment connection and Equations 5.13 to 5.15 for compression connection) into a single universally valid design equation appears justified. This was achieved by applying the same optimization procedure to the full set of 660 data points, resulting in the following equation:

Bolted moment connection:
$$R = 1 - 0.42\exp(-13.8(\frac{t}{X})(\frac{L_b}{h})) \tag{5.16}$$

Bolted compression connection:
$$R = 1.05 - 0.83(\frac{X}{L_b})^{0.56} + 3.71(\frac{h}{t})^{-1.09} \tag{5.17}$$

Evaluated over all data, Equations 5.16 and 5.17 displayed an average ratio of (R_{pred}/R_{FE}) of 0.97 and 0.95 with a standard deviation of 0.02 and 0.03, respectively.
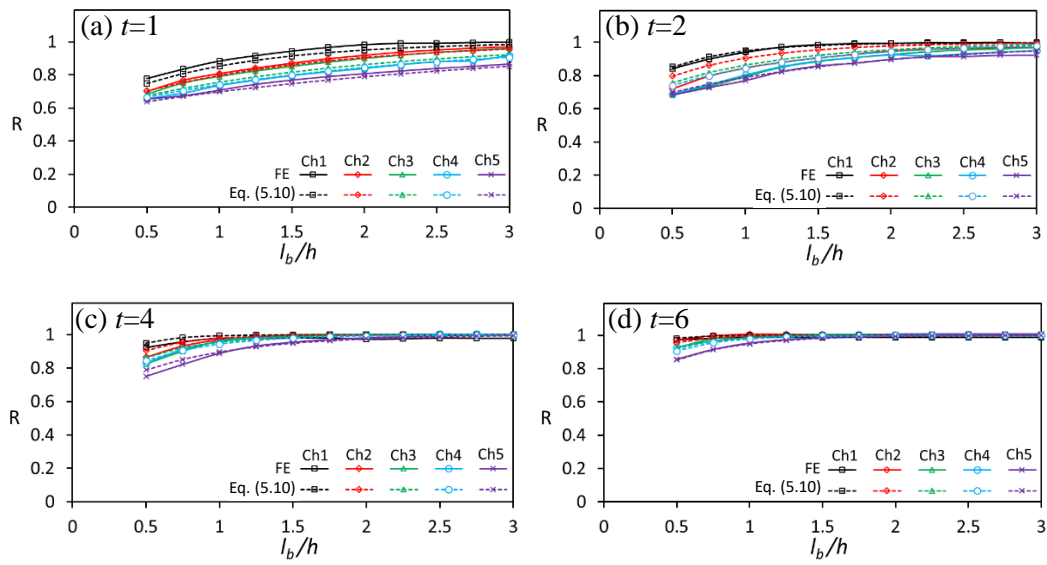
Fig. 5.15. Flexural capacity of CFS bolted moment connections with rectangular 2×2 bolt configuration and various bolt group lengths and cross-sectional eccentricities
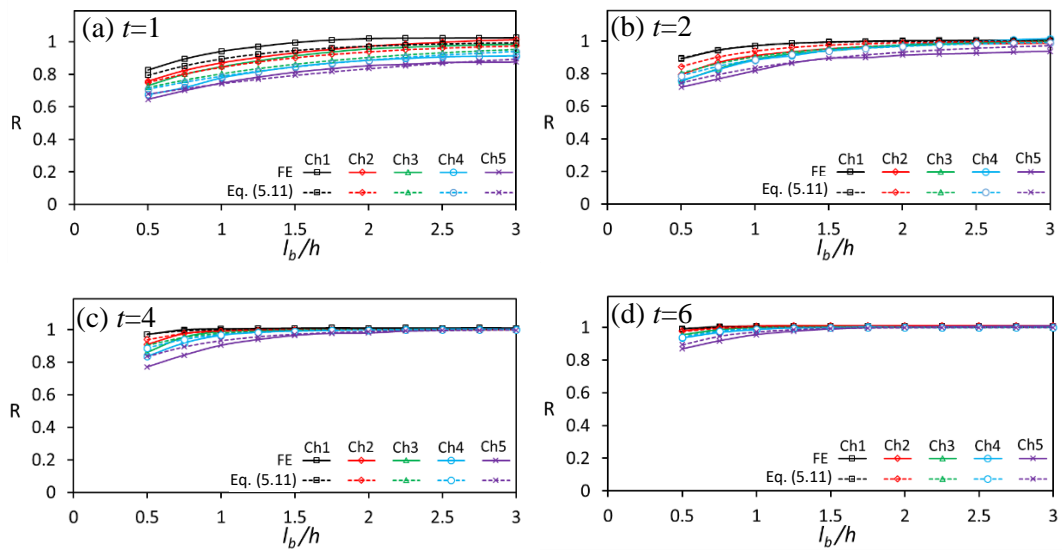
Fig. 5.16. Flexural capacity of CFS bolted moment connections with rectangular 3×3 bolt configuration and various bolt group lengths and cross-sectional eccentricities
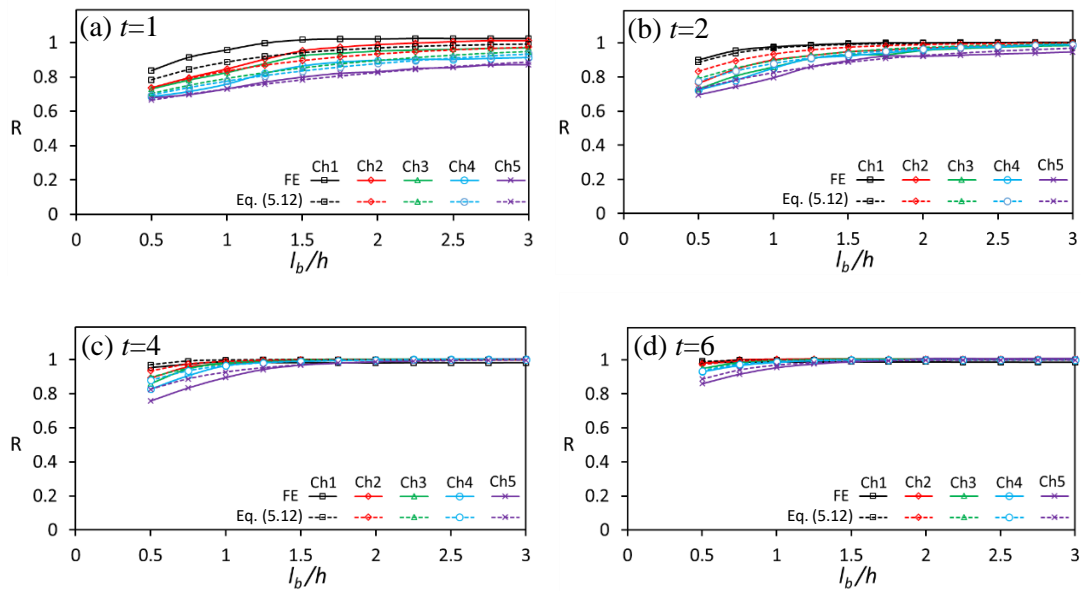
Fig. 5.17. Flexural capacity of CFS bolted moment connections with rectangular 4×4 bolt configuration and various bolt group lengths and cross-sectional eccentricities
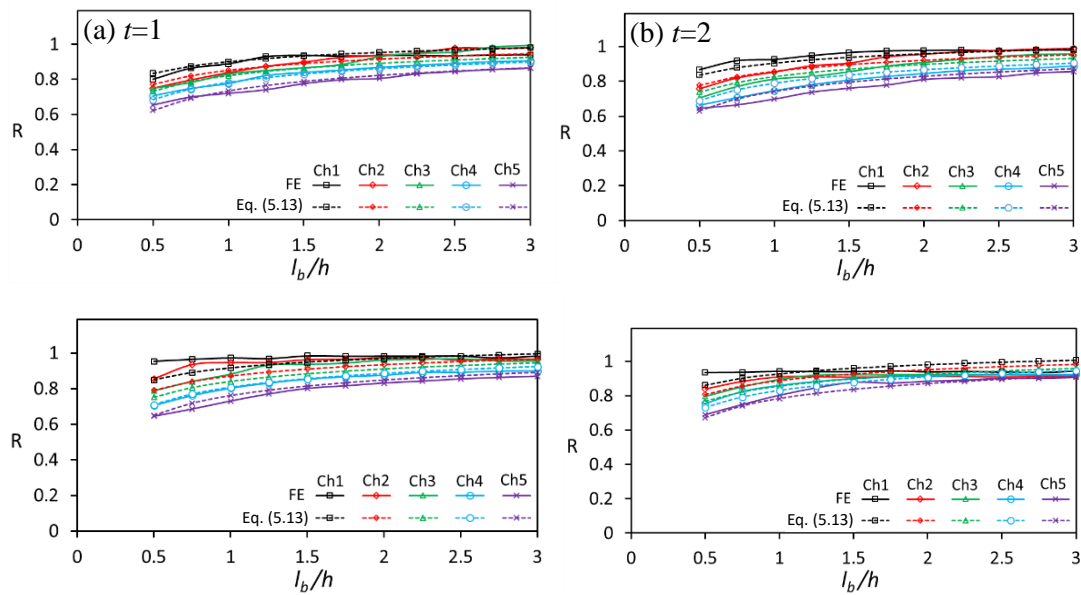
Fig. 5.18. Axial capacity of CFS bolted compression connections with rectangular 2×2 bolt configuration and various bolt group lengths and cross-sectional eccentricities
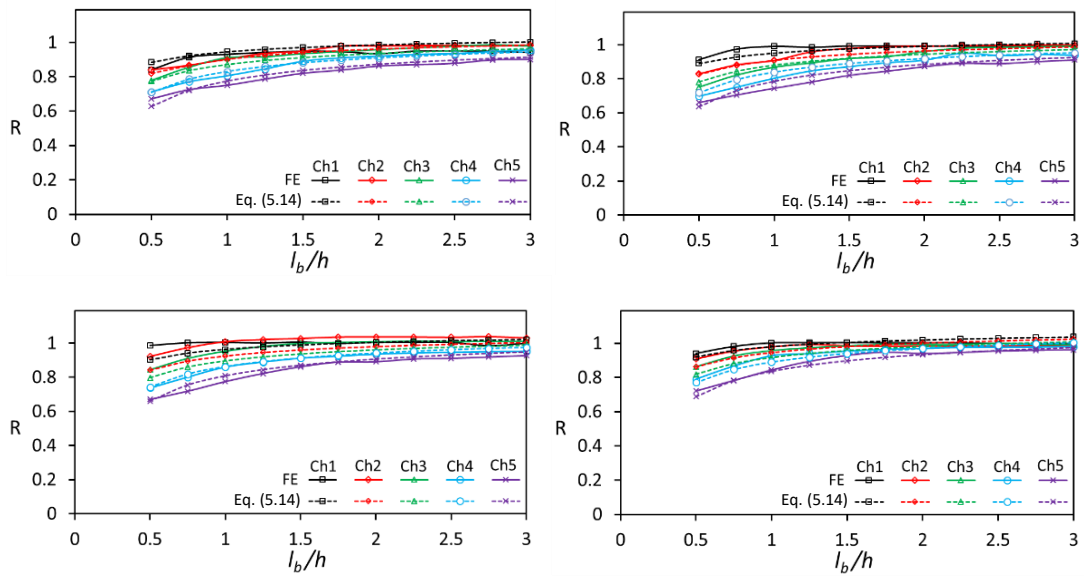
Fig. 5.19. Axial capacity of CFS bolted compression connections with rectangular 3×3 bolt configuration and various bolt group lengths and cross-sectional eccentricities
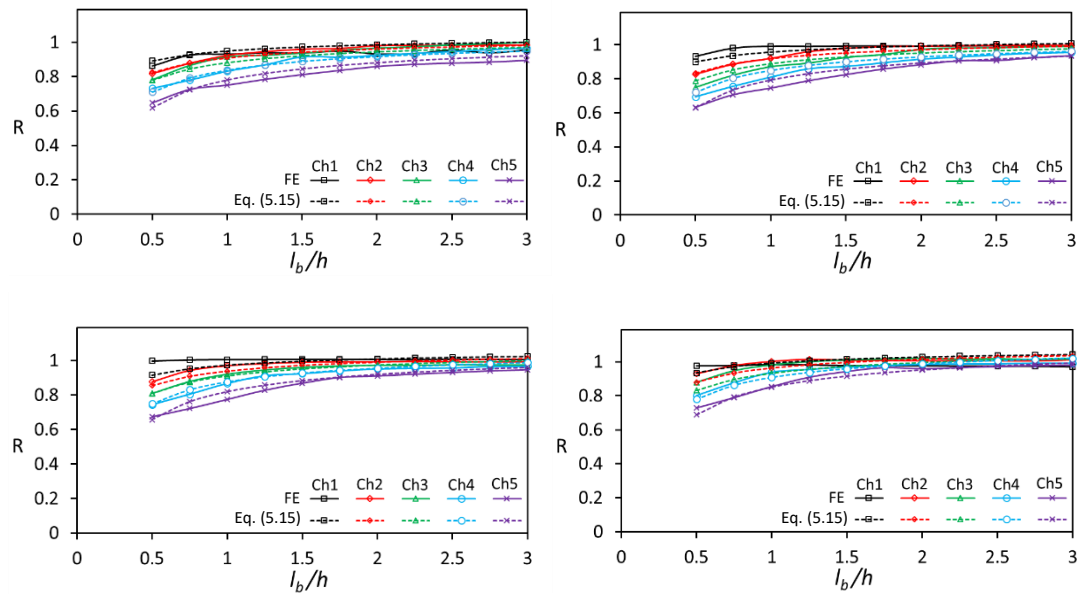
Fig. 5.20. Axial capacity of CFS bolted compression connections with rectangular 4×4 bolt configuration and various bolt group lengths and cross-sectional eccentricities
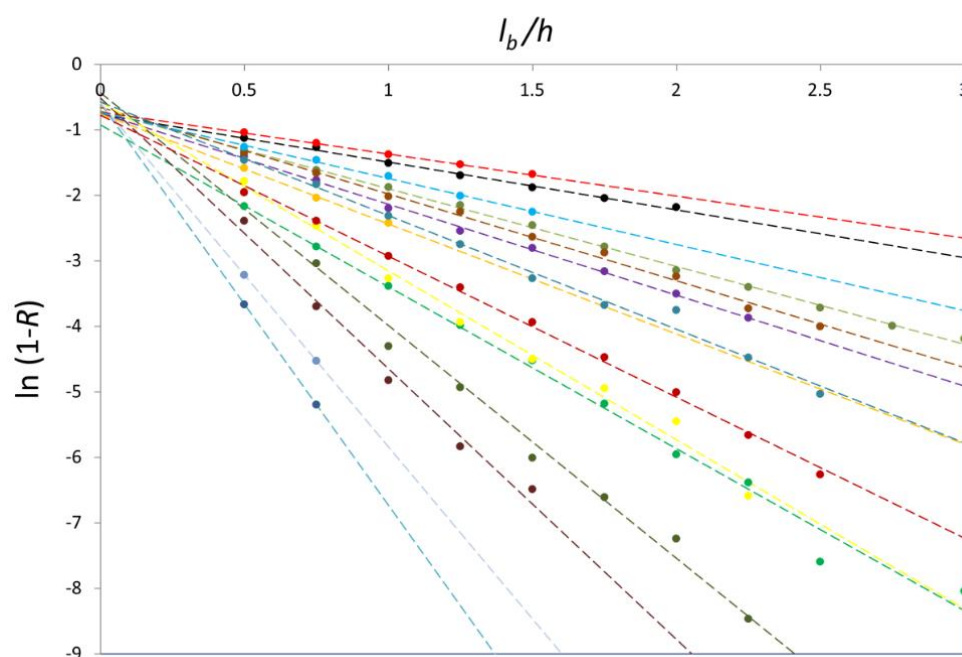
Fig. 5.21. FE data in semi-logarithmic format. The various colours indicate results for various bolt groups, channel geometries and thicknesses

5.4.2. Discussion of the results

In order to further investigate the physical phenomena which underlie the dependence of the moment capacity on the bolt group length l_b/h, thickness t and eccentricity X, Tables 5.5 and 5.6 show the various stress profiles in the beam and the column extracted from the FE models for a range of these parameters, respectively. The stresses were evaluated in the initial elastic range, before local buckling or plasticity took hold. However, a small imperfection was included in the models, as previously explained in Section 5.3.4. The profiles represent the stress state in the beam and the column sections located at the end of the gusset plate, a distance of $1.5d$ removed from the first bolt row, which is representative of the location of failure. Only the two extremes of the bolt group length spectrum considered in this study are represented in Tables 5.5 and 5.6: a first case which corresponds to a short bolt group with $l_b/h = 0.5$ and a second case which represents a much longer bolt group with $l_b/h = 3$. All results pertain to a 3×3 bolt group. However, similar observations were made for the other bolt group configurations.

It is seen that the stress profile differs significantly across these examples, mainly depending on the bolt group length, but with additional influence of the channel thickness and eccentricity. In particular, it is clear that the stress profile in the channels with the longer bolt group bears a much closer resemblance to the expected linear stress gradient over the section

height predicted by classical beam theory. On the other hand, the flanges in the channels with the shorter bolt group display a stress gradient with decreasing contribution towards the lip, while the stress profile in the web also deviates more from the expected linear trend. The difference in stress behaviour between short and long bolt groups becomes more pronounced as the eccentricity of the centroid relative to the web increases (i.e. when progressing from channel Ch1 to channel Ch5), while the thickness also has an influence. The thickest channels (t= 6 mm) show stress profiles for $l_b/h = 3$ which agree most with the predictions of beam theory, while the thinnest channel (t= 1 mm) with $l_b/h = 0.5$ and the largest eccentricity (Ch5) has the strongest varying stress profile across the flanges, with stress reversal even taking place at the flange-lip junction. A possible explanation for this phenomenon was put forward in (Lim et al., 2016b), where the researchers argued that it is caused by the presence of a bi-moment in the connection. Indeed, the bending moment is introduced in the plane of the channel web by the bolts in the connection. If this moment is resolved, for the sake of reasoning, into a couple of forces acting at the level of the flanges, then each force will cause in-plane bending in the flange, but in an opposite direction in each flange, thus producing a stress profile similar to the one observed for $l_b/h = 0.5$. Lim et al. (2016b) proposed to calculate this bi-moment as the product of the moment and the distance from the web to the shear centre. While the argument that a bi-moment is introduced cannot completely be discarded, the counterargument can be put forward that this bi-moment is largely counteracted by axial forces in the bolts, which force the web of the channel to remain in contact with the gusset plate and thus eliminate any twist in the channel necessarily associated with a bi-moment. It therefore does not seem sensible to design the cross-section of the beam just outside the connection for a full bi-moment, specified as above, in combination with the bending moment.

To strengthen this argument one can point out that a parallelism exists in the design of an eccentric tensile connection, where a tensile member is never designed for a moment equal to the product of the tensile force with the eccentricity, in addition to the actual tensile force. Rather it is assumed that the bolted connection largely counteracts any tendency of end rotation in the member. In the practical design of these connections, a reduction factor is typically applied to the tensile capacity of the member to account for the eccentricity, with which the force is introduced into the member at the connection. The accepted explanation is that this reduction factor accounts for the shear lag effect, i.e. the fact that a certain distance along the member is required for the forces introduced into the connected plate element to spread out into the other parts through longitudinal shear stresses.

In the authors' opinion, the mismatch between the stress distribution predicted by classical beam theory and those pictured in Tables 5.5 and 5.6 can equally be interpreted as the result of a shear lag effect. This effect exists because the bending moment and compressive load are introduced by the connection into the plane of the web and subsequently has to spread out into the flanges, with the flange tips initially lagging behind the web in longitudinal strains. An approach similar to the one used for eccentric tensile connections, with reduction factors applied to the cross-sectional bending and compression capacities to account for the shear lag effect, was therefore preferred.

It is clear that a larger shear lag effect will generally develop for larger values of the eccentricity X between the web and the centroid of the cross-section and this is in agreement with the observations from Tables 5.5 and 5.6. On the other hand, the length of the bolt group affects the phenomenon by influencing the direction of the bolt shear forces. For the case of bolted moment connection, the bolt shear forces are required to remain perpendicular to the line connecting each bolt to the centre of the bolt group (Fig. 5.22). Consequently, a longer bolt group will lead to the moment being introduced into the web mainly by vertical forces (which are also smaller in magnitude). However, since the web naturally carries the bulk of the shear force, these vertically introduced forces do not require any major redistribution of stresses. Horizontal components of the bolt forces, however, as significantly present in shorter bolt groups, will need to find their way into the flanges through shear lag. At the same time, the compressive part of the web adjacent to these connections needs to carry a disproportionate amount of stress relative to the predictions of beam theory, resulting in an increased susceptibility to local web buckling.

The above explanations comprehensively account for the observed differences between the various cases pictured in Tables 5.5 and 5.6, something which cannot be achieved in an entirely satisfactory way by the theory in (Lim et al., 2016b). Indeed, an identical bi-moment would be present in all cases associated with a particular cross-sectional geometry (Ch1 to Ch5), while Table 6 indicates that very different stress profiles originate within each group.

(a)   (b)
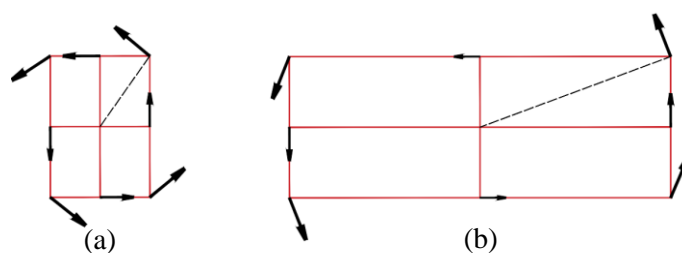
Fig. 5.22. Schematic distribution of bolt forces in a moment connection with: (a) a short bolt group, and (b) a long bolt group

Table 5.5. FE elastic stress profile in the beam for different bolt group lengths, thicknesses and eccentricities

Channel type	Bolt group length l_b/h	Thickness			
		1 (mm)	2 (mm)	4 (mm)	6 (mm)
Ch1	0.5				
	3				
Ch2	0.5				
	3				

3
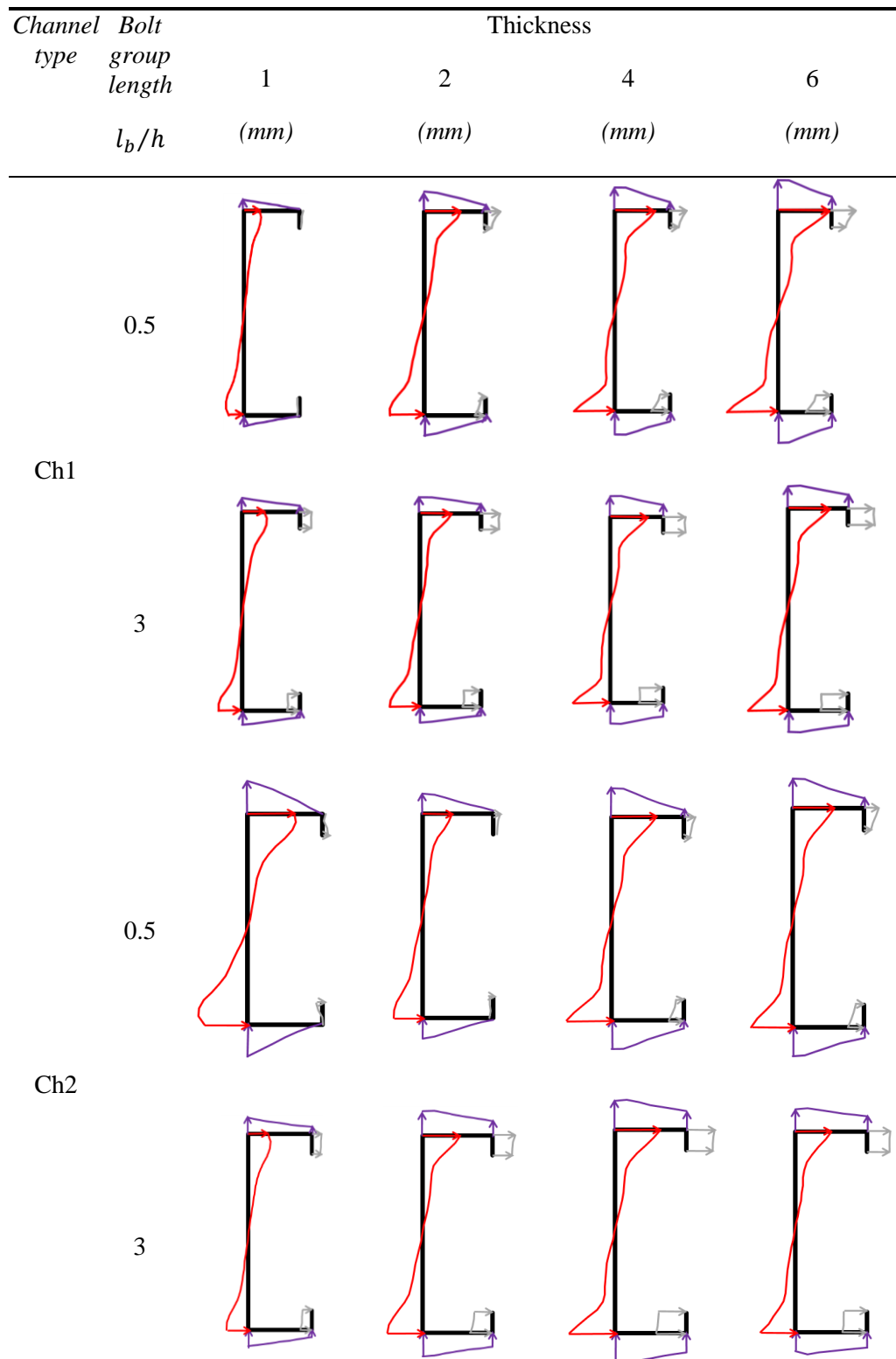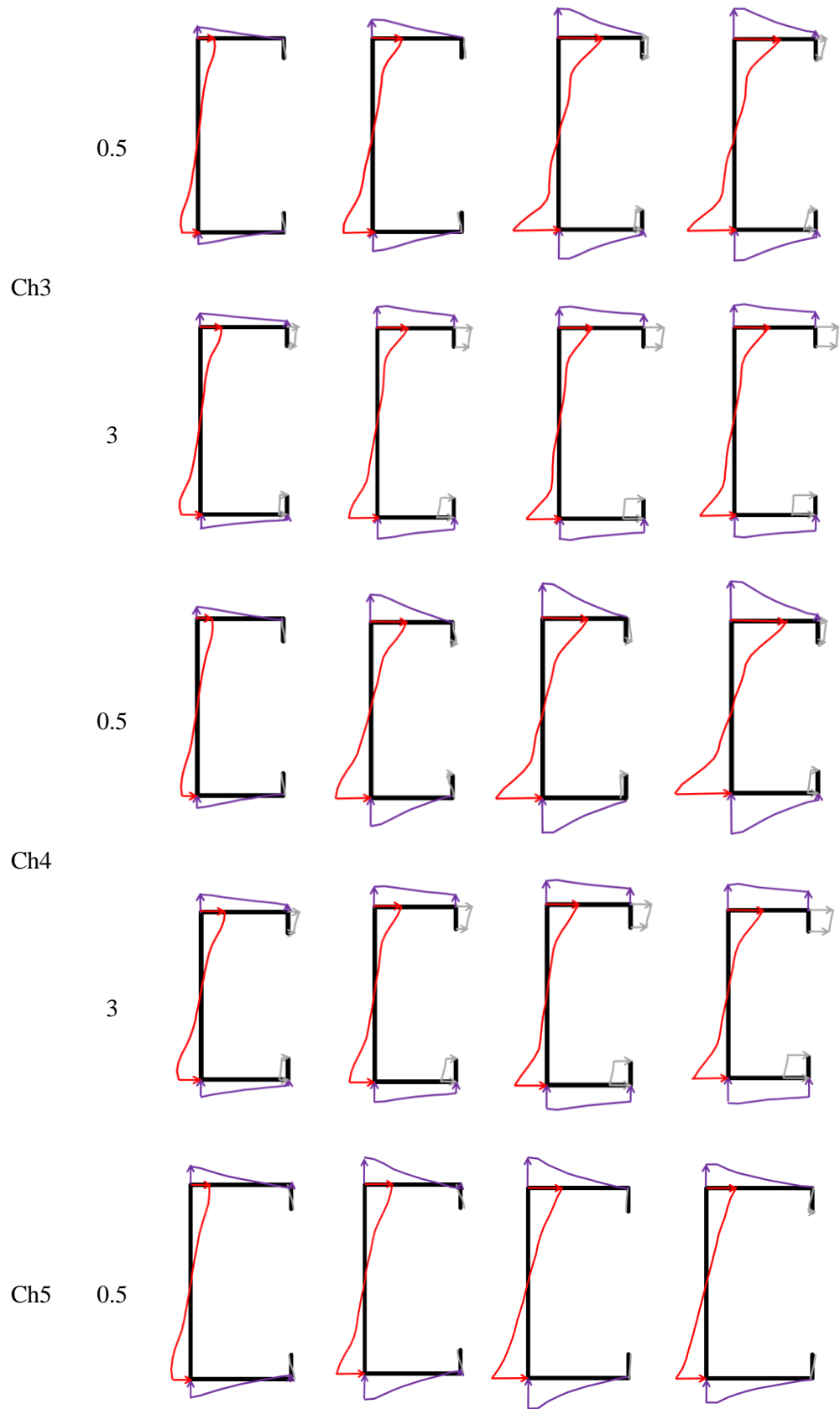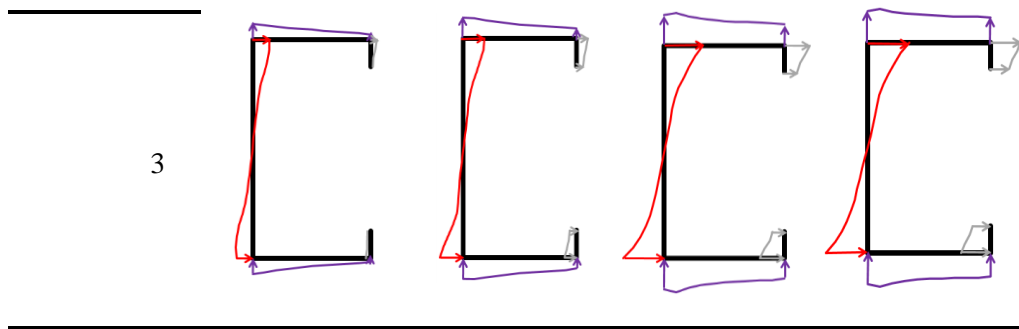
Table 5.6. FE elastic stress profile in the column for different bolt group lengths, thicknesses and eccentricities

Channel type	Bolt group length l_b/h	Thickness			
		1 (mm)	2 (mm)	4 (mm)	6 (mm)
Ch1	0.5				
	3				
Ch2	0.5				
	3				

5.5. RELIABILITY ANALYSIS

In order to ensure that the proposed design equations provide the required margin of safety, a reliability analysis was performed within the framework of both the Eurocode (CEN 2002) and the AISI specifications (Hsiao et al., 1988). To ensure that the structure has an acceptable level of safety with a sufficiently small probability of failure, the reliability index β must exceed a specific target value. For new structures with a design working life of 50 years and a consequence class rated as CC2 (moderate consequences of failure), the Eurocode prescribes a reliability index of 3.8 (CEN, 2002)(CEN, 2002)(CEN, 2002)(CEN, 2002)(CEN, 2002)(CEN, 2002)(CEN, 2002), while the AISI specifications suggest β=2.5 for CFS flexural members, β=2.89 for compression members and β=3.5 for connections (Hsiao et al., 1988). Since the failure mode under consideration was local buckling of the CFS element outside the actual bolted connection, β=2.5 and β=3.5 were considered for moment and compression connections, respectively, when the AISI framework is used. In the Eurocode for structural steel, resistances are divided by a partial safety factor γ, while in the AISI specifications they are multiplied by a resistance factor ϕ. The required nominal resistances are determined from load combinations involving the nominal values of the dead load D_n and the live load L_n , as follows:

$$\frac{R_n}{\gamma} = \gamma_D D_n + \gamma_L L_n \quad \text{(Eurocode)} \qquad \phi R_n = \gamma_D D_n + \gamma_L L_n \quad \text{(AISI)} \qquad (5.18)$$

In the Eurocode $\gamma_D = 1.35$, and $\gamma_L = 1.5$, while in the AISI code, $\gamma_D = 1.2$, and $\gamma_L = 1.6$, Both standards consider the design resistance r_d to be equal to the load $(\gamma_D D_n + \gamma_L L_n)$ in their reliability analyses, which implies a full use of the resistance, without reserve capacity.

Based on Annex D of Eurocode 0 (CEN 2002), the design resistance r_d can be determined as follows:

$$r_d = b_1.b_2.r_m.e^{-[k_{d,\infty}\alpha_{rt}Q_{rt}+k_{d,n1}\alpha_{\delta1}Q_{\delta1}+k_{d,n2}\alpha_{\delta2}Q_{\delta2}+0.5Q^2]} \qquad (5.19)$$

The factors b_1 and b_2 replace the original factor b specified in Annex D, to account for the fact that the model uncertainty in the applied methodology has two sources: b_1 accounts for the deviation of the predicted resistance from the FE model, while b_2 accounts for the FE model uncertainty relative to the experiment. r_m is the resistance determined using the mean values of all relevant variables. The assumed probabilistic distributions of the basic variables are listed in Table 5.7, based on recommendations in the literature (Young and Hancock, 2001, Meza et al., 2019). Further to Equation 5.19, $k_{d,\infty} = \alpha_R \beta$ =3.04, where α_R is a sensitivity

factor which Eurocode 0 recommends to take equal to 0.8. The factor $k_{d,n1}$ depends on the number of FE results the design equation is validated against, which is 660 in this case, and thus, according to Table D2 of Eurocode 0: $k_{d,n1} = 3.04$. The factor $k_{d,n2}$, on the other hand, depends on the number of experiments used to validate the FE model. Standing at four for bolted moment connections, this number is relatively low, which again according to Table D2 of Eurocode 0, necessitates the rather conservative assumption that $k_{d,n2} = 11.4$. However, for the case of bolted compression connections, the values of $k_{d,n2}$ and b_2 are considered to be 0 and 1, respectively, due to the lack of experimental tests.

Table 5.7. Statistical distributions used in reliability analysis

Variable	Distribution	Nominal	Mean	SD	COV	References
E	Normal	E	E	$0.03E$	0.03	Young et al. (Young and Hancock, 2001)
f_y	Lognormal	f_y	$1.1f_y$	$0.0693f_y$	0.063	Young et al. (Young and Hancock, 2001)
t	Normal	t	t	$0.005t$	0.005	Meza et al. (Meza et al., 2019)
h	Normal	h	h	$0.005h$	0.005	Meza et al. (Meza et al., 2019)
c	Normal	c	c	$0.002c$	0.002	Meza et al. (Meza et al., 2019)
d	Normal	d	d	$0.02d$	0.02	Meza et al. (Meza et al., 2019)

The correction factors b_1 and b_2 are defined as the slope of the least squares regression line in the M_{FE} versus M_c and M_{Test} versus M_{FE}, respectively:

$$b_1 = \frac{\sum (M_c M_{FE})}{\sum (M_c)^2} \tag{5.20}$$

$$b_2 = \frac{\sum (M_{Test} M_{FE})}{\sum (M_{FE})^2} \tag{5.21}$$

M_{Test} is the moment capacity measured in the experiment, M_{FE} is the moment capacity obtained from the FE models and M_c is the moment capacity predicted by the design equation. Using the available data, b_1 and b_2 were found to be equal to 1.28 and 0.99, respectively. For the case of bolted compression connections:

$$b_1 = \frac{\sum (P_c . P_{FE})}{\sum (P_c)^2} \tag{5.22}$$

where P_{FE} is the compressive capacity obtained from the FE models and P_c is the compressive capacity predicted by the design equation. Using the available data, b_1 was calculated to be equal to 1.34.

Eurocode 0 also requires the calculation of the error terms δ_1 and δ_2, corresponding to b_1 and b_2, which are determined by:

$$\text{(Moment connection) } \delta_1 = \frac{M_{FE}}{b_1 M_c} \qquad \text{(Compression connection) } \delta_1 = \frac{P_{FE}}{b_1 P_c} \tag{5.23}$$

$$\delta_2 = \frac{M_{Test}}{b_2 M_{FE}} \tag{5.24}$$

The variables Q_{rt}, $Q_{\delta 1}$, $Q_{\delta 2}$ and Q featured in Equation 5.19 represent the standard deviation of the resistance calculated using the proposed design equation, the standard deviation of the error terms δ_1 and δ_2, and the overall standard deviation of the resistance, respectively. These standard deviations were calculated based on the assumption of lognormal distributions as follows:

$$Q_{rt} = \sqrt{\ln(V_{rt}^2 + 1)} \tag{5.25}$$

$$Q_{\delta 1} = \sqrt{\ln(V_{\delta 1}^2 + 1)} \tag{5.26}$$

$$Q_{\delta 2} = \sqrt{\ln(V_{\delta 2}^2 + 1)} \tag{5.27}$$

$$V_r^2 = V_{\delta 1}^2 + V_{\delta 2}^2 + V_{rt}^2 \tag{5.28}$$

$$Q = \sqrt{\ln(V_r^2 + 1)} \tag{5.29}$$

In the above equations V_{rt}, $V_{\delta 1}$ and $V_{\delta 2}$ are the coefficients of variation (COVs) of the calculated resistance and the error terms δ_1 and δ_2, respectively. $V_{\delta 1} = 0.071$ and $V_{\delta 2} = 0.018$ were obtained using the respective data sets of 660 and 4 points for the moment connections, while $V_{\delta 1} = 0.079$ was calculated based on the results of 660 compression connections. To determine V_{rt} a Taylor series approximation was used (in accordance with Eurocode 0 guidance) and the first term in each basic variable κ_i was maintained. The variables κ_i included the thickness t, the web depth h, the flange width c, the lip length d, the elastic

modulus E and the yield stress f_y. Consequently, V_{rt} was determined for moment and compression connections by Equations 5.30 and 5.31, respectively:

$$
\begin{aligned}
V_{rt}^2 &= \frac{1}{r_m^2}(\sum_{i=1}^{j} \frac{\partial r}{\partial \kappa_i} \sigma_i)^2 \\
&= \frac{1}{r_m^2}[(\frac{\partial M_c}{\partial t} \sigma_t)^2 + (\frac{\partial M_c}{\partial h} \sigma_h)^2 + (\frac{\partial M_c}{\partial c} \sigma_c)^2 + (\frac{\partial M_c}{\partial d} \sigma_d)^2 + (\frac{\partial M_c}{\partial E} \sigma_E)^2 + (\frac{\partial M_c}{\partial f_y} \sigma_{f_y})^2]
\end{aligned}
\tag{5.30}
$$

$$
\begin{aligned}
V_{rt}^2 &= \frac{1}{r_m^2}(\sum_{i=1}^{j} \frac{\partial r}{\partial \kappa_i} \sigma_i)^2 \\
&= \frac{1}{r_m^2}[(\frac{\partial P_c}{\partial t} \sigma_t)^2 + (\frac{\partial P_c}{\partial h} \sigma_h)^2 + (\frac{\partial P_c}{\partial c} \sigma_c)^2 + (\frac{\partial P_c}{\partial d} \sigma_d)^2 + (\frac{\partial P_c}{\partial E} \sigma_E)^2 + (\frac{\partial P_c}{\partial f_y} \sigma_{f_y})^2]
\end{aligned}
\tag{5.31}
$$

In the above equations, the σ_i are the standard deviations of the basic variables κ_i. Representative values were obtained from Young et al. (Young and Hancock, 2001) and Meza et al. (Meza et al., 2019) as listed in Table 5.7. The partial derivatives in Equations 5.30 and 5.31 were numerically calculated by replacing them by finite differences:

$$
\frac{\partial M_c}{\partial \kappa_i} = \frac{\Delta M_c}{\Delta \kappa_i} \qquad \text{and} \qquad \frac{\partial P_c}{\partial \kappa_i} = \frac{\Delta P_c}{\Delta \kappa_i}
\tag{5.32}
$$

The parameters α_{rt}, $\alpha_{\delta 1}$ and $\alpha_{\delta 2}$ in Equation 5.19 are weighting factors for Q_{rt}, $Q_{\delta 1}$ and $Q_{\delta 2}$ respectively, obtained as:

$$
\alpha_{rt} = \frac{Q_{rt}}{Q}
\tag{5.33}
$$

$$
\alpha_{\delta 1} = \frac{Q_{\delta 1}}{Q}
\tag{5.34}
$$

$$
\alpha_{\delta 2} = \frac{Q_{\delta 2}}{Q}
\tag{5.35}
$$

Based on Equation 5.19 the partial safety factors γ were calculated for two distinct cases: (i) the case where the individual equations (Equations 5.10-5.15) were used, depending on the bolt group configuration, and (ii) the case where the general equations (Equations 5.16 and 5.17) were applied to all data points. In both cases, an average partial safety factor γ of 1.01 was obtained. This is very close to the (lowest possible) γ value of 1.00, recommended by Eurocode 3 and adopted by most EU member states. It can thus be concluded that the proposed equations (Equations 5.10-5.15) are safe for use in conjunction with the Eurocode standards.

On the other hand, according to the North-American AISI (Hsiao et al., 1988) standard the resistance factor ϕ is calculated as:

$$\phi = C_\phi (M_m F_m P_{m1} P_{m2}) e^{-\beta_0 \sqrt{V_M^2 + V_F^2 + C_{P1} V_{P1}^2 + C_{P2} V_{P2}^2 + V_Q^2}} \qquad (5.36)$$

In the above equation C_ϕ =1.52 (AISI S100-12, 2012). M_m (= 1.1) and F_m (= 1.0) are the mean values of the material and fabrication factors, and V_M=0.1 and V_F=0.05 are the corresponding COVs, respectively (Hsiao et al., 1988, C.H Pham and Hancock, 2012). The professional factor P_m in the original AISI equation was replaced by the product of and P_{m1} and P_{m2}. P_{m1} is the mean ratio of the FE predicted capacity to the capacity calculated with the proposed design equation (M_{FE}/M_c or P_{FE}/P_c), and P_{m2} is the mean ratio of the experimentally measured capacity to the corresponding FE prediction (M_{Test}/M_{FE}) (note that P_{m2} is equal to 1 for the compression connection due to lack of tests). V_{p1} and V_{p2} are the corresponding COVs (equivalent to $V_{\delta 1}$ and $V_{\delta 2}$ in the Eurocode procedure). V_Q is the COV of the loading and can be taken as 0.21 for CFS structures (Hsiao et al., 1988). The C_p factors account for the samples sizes are defined by:

$$C_p = \frac{n+1}{n} \frac{n-1}{n-3} \qquad (5.37)$$

With respective sample sizes of 660 and 4, C_{p1}=1.005 and C_{p2} =3.75 are obtained using the above equation.

With the cross-sectional bending capacity (M_u) and compressive capacity (P_u) in Equations 5.6 and 5.7, respectively, calculated according to the AISI effective width provisions, resistance factors ϕ=0.94 for bolted moment and ϕ=0.9 for bolted compression connections were obtained. Both of these factors exceed the values of 0.9 and 0.85 prescribed by the AISI design rules for CFS flexural and compression members, respectively, demonstrating that the proposed design rules can safely be used within this context. The AISI rules also allow the option of determining M_u and P_u using the Direct Strength Method (AISI S100-12, 2012) and when this option was used, resistance factors ϕ= 0.98 and ϕ= 0.95 were obtained for bolted moment and compression connections, respectively. These values again exceed the specified values of 0.9 and 0.85, indicating a safe design procedure.

5.6. DESIGN CONSIDERATIONS FOR THE EFFECTS OF SHEAR

The effect of shear in CFS bolted connection has to be taken into account simultaneously with the bending moment. Since all selected cross-sections used in this study (Fig. 5.14) were relatively deep, the shear capacity was controlled by shear buckling of the web. The AISI equations for the shear strength of web were employed to assess the shear capacity of CFS bolted connections.

5.6.1. DSM design rules for pure shear

In the AISI provisions, the nominal shear capacity of a section is expressed in terms of a nominal shear stress (F_V). However, in this study the equations have been written as a function of the shear capacity (V_n):

$$\text{For} \qquad \frac{h}{t} \leq \sqrt{\frac{EK_V}{f_y}} : V_n = 0.6 f_y A_w \tag{5.38}$$

$$\text{For} \qquad \sqrt{\frac{EK_V}{f_y}} < \frac{h}{t} \leq 1.51 \sqrt{\frac{EK_V}{f_y}} : V_n = \frac{0.6\sqrt{EK_V f_y}}{h/t} A_w \tag{5.39}$$

$$\text{For} \qquad \frac{h}{t} > 1.51 \sqrt{\frac{EK_V}{f_y}} : V_n = \frac{0.904 EK_V}{(h/t)^2} A_w \tag{5.40}$$

where K_V is the shear buckling coefficient of the channel web. Based on the AISI rules for unreinforced webs: K_V=5.34. It is worth mentioning that the effect of the flanges on the shear buckling coefficient (K_V), and consequently on V_n, can be ignored (C.H Pham and Hancock, 2012) due to the comparatively large web. A_w, h, and t are area of web element, the depth of the flat portion of web measured along the plane of the web, and the web thickness.

5.6.2. Assessment of bending and shear interaction

To evaluate the interaction of bending and shear, different connections subjected to a concentrated load (V) at the cantilever tip were modelled by FE in ABAQUS. The model geometry was identical to the one shown in Fig. 5.8. The studied connections were determined by variables similar to those mentioned in Section 5.4, namely such as different beam cross-sectional dimensions and thicknesses, bolt group configurations and lengths. However, only the boundaries of bolt-group length values were selected: l_b/h=0.5 and l_b/h=3. The interaction of bending moment and shear for the connection is assessed similar to the AISI approach for beams subjected to combined bending and shear in limit state design. The required flexural strength of connection (M_n) and required shear strength (V_n) should satisfy:

$$\left(\frac{M}{M_n}\right)^2 + \left(\frac{V}{V_n}\right)^2 = 1 \tag{5.41}$$

where V is the shear action equal to the applied load at the beam end section, M is the bending action due to the end load calculated at the location of failure ($1.5d$ away from the first bolt line), M_n is the flexural capacity of the connection in pure bending, which is equal to M_c determined according to Equation 5.6, and V_n is the capacity of the connection in pure shear (Equations 5.38 to 5.40). Since the shear force is almost entirely carried out by the beam web, shear knuckling of the web is assumed to be equal to the shear capacity of the cross-section and is deemed unaffected by the fact that the flanges of the beam are left unconnected. In Fig. 5.23, the specified markers indicate the interaction between (M/M_n) and (V/V_n) for different CFS bolted connections obtained from ABAQUS models, where M and V are the applied moment and shear at failure, respectively. As shown in Fig. 5.23, all markers are situated beyond the circular domain, which demonstrates that the AISI interaction equation for CFS members (Equation 5.41) can be used to assess CFS bolted connections as well.

Alternatively, since the results are scattered at a level higher than $M/M_n=0.9$ in Fig. 5.21, and the dominant failure mode always seems to be always flexural failure, a simple linear interaction equation can be proposed (Pham et al., 2014):

$$\begin{cases} \left(\dfrac{M}{M_n}\right) = 0.9 \\[3mm] \left(\dfrac{V}{V_n}\right) = 1 \end{cases} \tag{5.42}$$
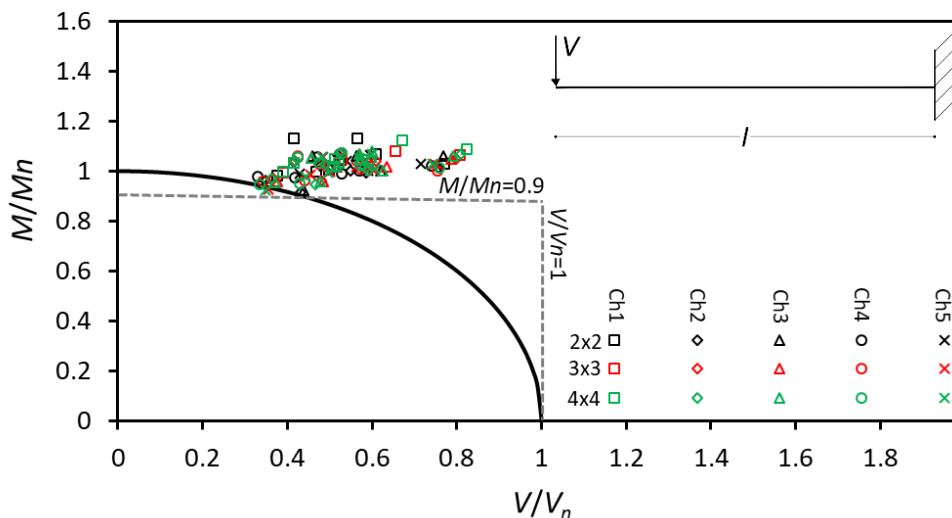
Fig. 5.23. Interaction between M/M_n and V/V_n for the assessment of proposed nominal flexural equation (M_n)

5.7.   DESIGN CONSIDERATIONS FOR THE COMBINED EFFECTS OF COMPRESSION, BENDING AND SHEAR

This section aims to expand the applicability of the proposed design equations by evaluating CFS bolted connections in beam-column members subjected to compression, bending moment and shear force simultaneously. To assess the interaction curves, FE models of various CFS bolted connections were developed, while considering an axial compressive load (P) and a transverse load (V) at the end section of the beam-column member, as shown in Fig. 5.24. The selected design variables were: (I) three different levels of compressive load: P/P_c=0.25, 0.5, and 0.75; (II) three different beam-column cross-sections: Ch1, Ch2, and Ch3; (III) four different cross-sectional thicknesses t=1, 2, 4, and 6 mm, and (IV) three different bolt group lengths: l_b/h =0.5, 1.5, and 3. The FE analysis was carried out using three consecutive analysis steps in the ABAQUS software (Abaqus/CAE User's Manual): (I) an Elastic Buckling analysis to the provide general shape of the imperfection, (II) a Static General analysis to apply the axial compressive load, (III) a Static General analysis to apply the transverse tip load.
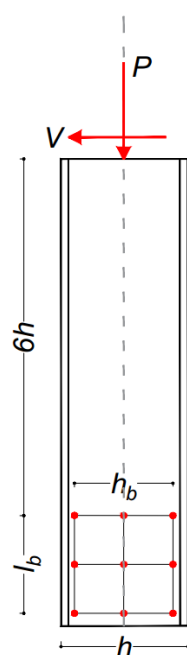
Fig. 5.24. Column-to-base bolted connection subjected to compression, bending and shear

While interaction of axial compression, bending moment and shear force in beam-column elements has not been considered in the AISI provisions, a complex equation is provided by the Eurocode3 part 1-5 (CEN, 2006a) based on the plastic moment resistance of the cross-section. This may not be useful to assess the interaction behaviour of CFS members with thin-walled elements due to the fact that premature buckling prevents the plastic capacity from being reached. Therefore, a simple quadratic interaction equation, similar to the equation

proposed for the interaction of moment and shear force in CFS bolted moment connections in the previous Section 5.6 (Mojtabaei et al., 2019a), is proposed to assess the interaction of CFS bolted connections in beam-columns:

$$\left(\frac{P}{P_n}\right)^2 + \left(\frac{M}{M_n}\right)^2 + \left(\frac{V}{V_n}\right)^2 \leq 1 \qquad (5.43)$$

where P, M and V are the applied compressive force, moment, and shear force, respectively. It should be noted that the bending moment (M) is calculated based on the end tip load and the distance from the end section to the location of failure ($1.5d$ away from the first bolt line). M_n and P_n are the nominal flexural strength and the axial compressive capacity of the CFS bolted connections, which are equal to M_c and P_c determined according to Equations 5.6 and 5.7, respectively. V_n is the nominal shear capacity of the connection.

The specified markers in Fig. 5.25 show the interaction between (P/P_n), (M/M_n) and (V/V_n) for the selected CFS beam-column bolted connections obtained from the FE analyses. As shown in Fig. 5.25, most of the markers are located inside the spherical domain, which implies that the proposed quadratic interaction equation (Equation 5.43) is unsafe to assess the interaction of loads in CFS beam-column bolted connections. Therefore, a linear interaction curve is proposed as an alternative to provide a safe design interaction equation for such connections:

$$\left(\frac{P}{P_n}\right) + \left(\frac{M}{M_n}\right) + \left(\frac{V}{V_n}\right) \leq 1 \qquad (5.44)$$
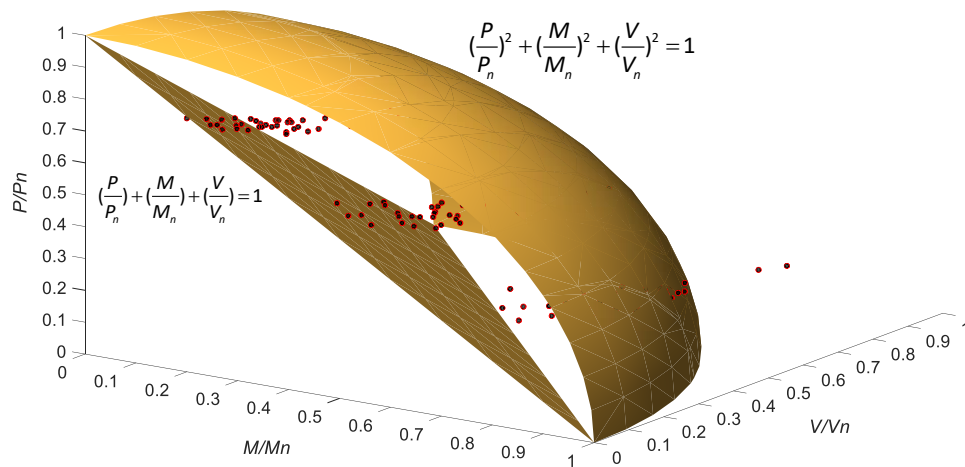
Fig. 5.25. Interaction between P/P_n, M/M_n, and V/V_n for CFS bolted connections subjected to compression, bending and shear force.

5.8.   SUMMARY

This chapter presented a numerical study on the structural behaviour of CFS bolted connections in order to propose a design procedure. Experimental results of CFS apex connections under four-point bending were used to validate GMNIA FE models. It was shown that models of an idealised cantilever CFS bolted moment connection can adequately represent the flexural capacity of the corresponding CFS apex connection. The flexural and compressive capacities of connections with different variables, including the beam cross-sectional dimensions and slenderness, the bolt configuration and the bolt-group length were obtained to investigate the effects of bi-moment/shear lag. General equations for the nominal flexural and compressive capacities of CFS bolted connections were proposed using a best fit of the FE results with an average error of less than 3%. A reliability analysis was also carried out, both within the framework of the Eurocode and the AISI specifications, and appropriate safety factors for design purposes were presented. The capacities of connections under bending and shear interaction and combined bending, shear and compression were also investigated.

It should be noted that while this chapter focused on the static behaviour of CFS bolted connections, the seismic characteristics of such connections are optimised in the next chapter (i.e. Chapter 6) by improving their post-buckling behaviour. Furthermore, efficient seismic design of this type of connections is presented in Appendix B by conducting a comprehensive parametric study on their key design parameters (e.g. bolt slip resistance, bolt configurations, cross-sectional thickness and shape and etc.).

5.9.   CONCLUDING REMARKS

-   The results indicated that the ultimate bending moment and compressive capacities of the CFS back-to-back sections may be reduced by up to 40% due to presence of the bolts, depending on the eccentricity and the thickness of the channel and the bolt group size.

-   The predicted capacities of connections under an imposed tip displacement at the beam end section showed that the bending and shear interaction equation proposed by the AISI for CFS members is safe to use for CFS beam-to-column bolted connections.

-   The results showed that a quadratic equation was not safe for the interaction of compression, bending, and shear in CFS bolted connections, therefore, a linear interaction was alternatively proposed.

CHAPTER 6

Development of Cold-Formed Steel Bolted Moment Connections for Maximum Ductility and Energy Dissipation

6.1. INTRODUCTION

Thin-walled cold-formed steel (CFS) elements and connections are not generally suitable for moment-resisting frames in high seismic regions due to their low ductility and energy dissipation capacity and inherited susceptibility to local/global instabilities. The static behaviour and design of CFS bolted connections were already investigated in Chapter 5. However, this chapter aims to improve the seismic performance of CFS moment-resisting frames by developing more efficient bolted moment connections using optimised CFS beams with enhanced non-linear post-buckling behaviour. By taking into account material non-linearity and geometrical imperfection effects, the detailed Finite Element (FE) models of a typical CFS bolted moment connection is developed using ABAQUS software, and then validated based on experimental cyclic test results. Particle Swarm Optimisation (PSO) algorithm is linked to GMNIA ABAQUS FE analysis to optimise CFS bolted moment connections with respect to their energy dissipation capacity and ductility. Establishing a link between three different softwares, including ABAQUS, PYTHON, MATLAB, is considered as a main novelty of this chapter. To show the efficiency of the method, connections with five different beam cross-sectional shapes are optimised, and the results are compared with a standard channel section used as a benchmark. The relative dimensions of the cross-sections, the location of triangular intermediate stiffeners, and the inclination of the lip stiffeners are considered to be the main design variables. To provide practical beam cross-sections, the plate

slenderness limit values defined by Eurocode 3 (EC3) along with a range of manufacturing limitations are also imposed as design constraints in the optimisation process. It is shown that, for the same amount of material, the proposed optimisation framework results in a considerable (up to 160%) improvement in the ductility and energy dissipation capacity of the CFS bolted moment connections.

6.2. BACKGROUND

Cold-formed steel (CFS) members are manufactured by bending or press-breaking thin-walled steel coils at ambient temperature to the desired cross-sectional shapes. The light-weight CFS structural elements can provide a high strength-to-weight ratio, more flexible member profiles compared to hot-rolled sections, and also facilitate onsite manufacturing and installation (Hancock, Ye et al., 2016b). Previous studies on the structural performance of moment-resisting frames with CFS members in general indicate that they can provide more efficient design solutions compared to conventional CFS shear wall panel systems (Bagheri Sabbagh et al., 2012b, Pan and Shan, 2011). Currently, the applications of CFS moment-resisting systems are mainly limited to portal frames and industrial platforms where higher mobility and space-planning flexibility is required. However, CFS elements and connections are not considered to be suitable for moment-resisting frames in high seismic regions due to their susceptibility to local and global instabilities which reduces their ductility and energy dissipation capacity.

In general, beam-to-column connections play a key role in the global behaviour, strength, and seismic characteristics of moment-resisting frames under seismic excitations (McCrum et al., 2019, Mojtabaei et al., 2018, Blum and Rasmussen, 2019b). Several studies have experimentally and analytically investigated the structural performance of apex and eaves CFS connections under monotonic loads (e.g. (Lim and Nethercot, 2003a, Elkersh, 2010, Tshuma and Dundu, 2017, Öztürk and Pul, 2015)). It was concluded that the local buckling of CFS beam close to connection zone was normally identified as a dominant failure mode, while it was shown that bolt-group size can have a significant effect on the flexural strength of the connections. In another relevant study, Bučmys et al. (2015b) presented an analytical approach to determine the rotational stiffness of CFS bolted moment connections based on the component method stipulated in Eurocode 3 (CEN, 2005f). The results of experimental cyclic tests on CFS bolted moment connections indicate that a rigid behaviour (based on Eurocode (CEN, 2005e) definition) can be obtained if the connections are designed properly ((Bagheri Sabbagh et al., 2012b, Serror et al., 2016a)).

While using multiple plate stiffeners in the connection zone can postpone the failure of the CFS beam and ultimately lead to a considerable increase in the ductility of the connection (Bagheri Sabbagh et al., 2012a), this may not be a practical solution due to complexity of the required detailing. More recent studies by Ye et al. (2019c) demonstrated that beam cross-sectional shapes and slenderness, gusset plate thicknesses, and bolt distribution can also significantly (up to 250%) improve the seismic performance of bolted moment connections. In a follow-up study, it was shown that incorporating bolting friction slip mechanism can result in up to 200% higher ductility, energy dissipation capacity and damping coefficient of the connections especially for CFS beams with thinner plates (Eurocode classes 3 and 4) (Ye et al., 2019b). Sato and Uang (2009) also demonstrated that the ductility of CFS special bolted moment frames defined by AISI S110 standard (2012) can be enhanced through bearing action and slippage of the bolts.

There are several studies on the optimum design of CFS beam elements to maximise their ultimate capacity (Ye et al., 2018d, Wang et al., 2016a), energy dissipation capacity (Ye et al., 2018a) and flexural stiffness (Mojtabaei et al., 2019). However, the presence of the bolts in CFS bolted moment connections can change the flexural performance of the system due to the effects of bi-moment and bolt-web interactions (Lim and Nethercot, 2003a). Currently, there is no study on the optimisation of CFS bolted moment connections incorporating the bolt effects.

This paper aims to develop a framework for shape optimisation of CFS bolted moment connections to maximise their seismic characteristics including energy dissipation capacity and ductility. Detailed FE models of bolted moment connections are developed in ABAQUS (2014) by taking into account material nonlinearity and geometrical imperfections, while the adopted modelling technique is validated against available experimental test results. Five different CFS beam cross-sectional shapes are selected and their relative dimensions, location of intermediate stiffeners, and the inclination of the lip stiffeners are considered as key design variables. Optimisation process is done by using a MATLAB code (Mathworks, 2015) which is developed to link Particle Swarm Optimisation (PSO) (Kennedy J and Eberhart R) to the validated FE models in ABAQUS (2014).

The efficiency of the obtained optimum design solutions compared to standard sections is demonstrated under cyclic loading condition. The results are then used to investigate the effect of hysteretic loops on the seismic performance of the optimum and conventional bolted moment connections.

6.3. MODELLING OF TESTED BOLTED MOMENT CONNECTION

Typical bolted moment connections aimed in this research consist of a column and a beam with back-to-back CFS channel sections connected by bolts, gusset plate, and column stiffeners as shown in Fig. 6.1. The column stiffeners are used to prevent premature failure modes in the column in accordance with weak-beam strong-column philosophy. The gusset plate passed through the back-to-back beam and column can transfer bending moment and shear force from the CFS beam to the column. Sabbagh et al. (2012b) conducted several experimental tests on this type of CFS bolted moment connections at The University of Sheffield. The results of those tests are used as a benchmark to validate the FE models in this study.
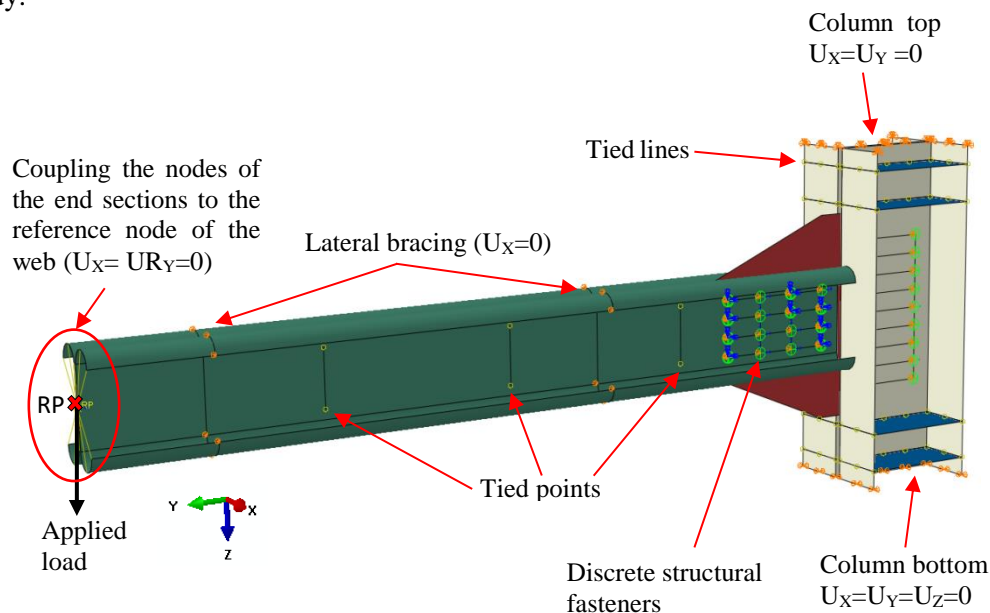
Fig. 6.1. Boundary conditions of the FE model for typical bolted moment connections

6.3.1. Material properties and element type

The measured stress-strain curves of the CFS elements obtained from average of two coupon tests (Bagheri Sabbagh, 2011b) are incorporated in the FE models (see Fig. 6.2). Since it was reported that the analysis of post-failure of CFS bolted moment connections involves large inelastic strains (Bagheri Sabbagh et al., 2012b), the nominal (engineering) static stress-strain curve is converted to a true stress and logarithmic plastic strain curve. The true stress σ_{true} and plastic true strain ε_{true}^{pl} required by ABAQUS (2014) are defined as:

$$\sigma_{true} = \sigma(1+\varepsilon)$$

$$\varepsilon_{true}^{pl} = \ln(1+\varepsilon) - \frac{\sigma_{true}}{E} \tag{6.1}$$

where σ and ε represent the engineering stress and strain, respectively, and E is the module of elasticity of the material.

The CFS connection is modelled using 8-node quadrilateral shell elements with reduced integration and four nodal degrees of freedom (S8R). These elements can provide an accurate solution to most applications by allowing for transverse shear deformation which is especially important for the simulation of thicker CFS elements (Abaqus/CAE User's Manual, 2014). Following a sensitivity analysis, the mesh size providing adequate accuracy with minimum computational time is selected to be 20 mm.
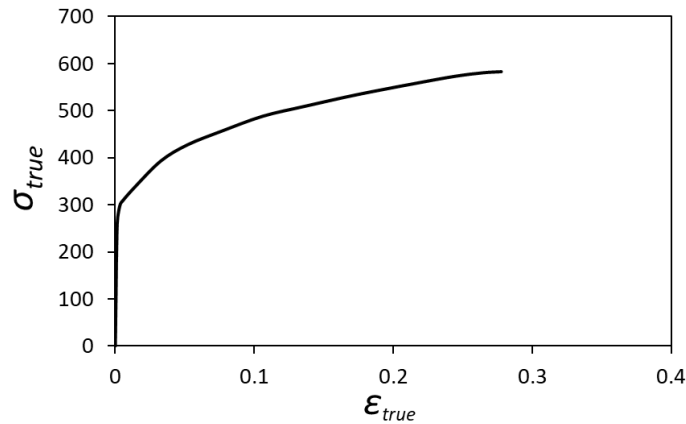
Fig. 6.2. Stress-strain curve used in the FE model

6.3.2. Bolt modelling

To model the bolt-group, the discrete structural "fastener" available in ABAQUS (2014) is adopted. The discrete fasteners make use of attachment lines to create connectors for coupling between the selected faces. The displacement and rotation of each fastening point were coupled to the average displacement and rotation of the surface nodes within the radius of influence (r). It should be noted that modelling of the fastener with the radius of influence can reduce the stress concentration around the node at the bolt position. In this study, r is assumed to be half of the bolt shank.

6.3.3. Imperfection

As can be seen in Fig. 6.1, to prevent global buckling of the beam specimens, lateral displacements were restrained in the x-direction in the experimental tests (Bagheri Sabbagh et al., 2012b). Therefore, either a distortional or a local geometrical imperfection was

incorporated into the FE models, depending on which mode had the lower critical buckling resistance. The imperfection amplitude for the steel sheets with the plate thickness (t) less than 3 mm was defined as $0.34t$ and $0.94t$ for the local and distortional imperfection, respectively, as recommended by Schafer and Peköz (1998). For the elements with higher plate thicknesses, the imperfect magnitude was determined based on the work by Walker (1975):

$$\omega_d = 0.3t\sqrt{\frac{\sigma_{0.2\%}}{\sigma_{cr}}} = 0.3t\lambda_s \tag{6.2}$$

where $\sigma_{0.2\%}$ and σ_{cr} are 0.2% proof stress of the material and elastic local buckling stress, respectively; and λ_s is cross-sectional slenderness. The general shapes of beam cross-sections after incorporating geometrical imperfections were generated by using an eigenvalue elastic buckling analysis in ABAQUS (2014) and were then scaled based on the calculated imperfection magnitudes.

6.3.4. Loading and boundary conditions

The boundary conditions in the FE models were imposed based on the test set-up used in the experiments (Bagheri Sabbagh et al., 2012b) (see Fig. 6.1). The translational degrees of freedom U_X, U_Y and U_Z on the bottom, and U_X and U_Y on the top surface of the back-to-back channel column were restrained. The nodes at the location of the interconnections along the length of the CFS beam were tied in the U_X, U_Y and U_Z directions by using "Tie" constraint in ABAQUS (2014). The column stiffeners were also tied to the column surfaces to be consistent with the experimental test set-up.

Both monotonic and cyclic loads were applied incrementally by using the "STATIC GENERAL" method in the ABAQUS library, which can take into account the non-linear behaviour of the material and the stiffness degradation due to buckling. The static concentrated load was applied through a displacement at the beam end nodes, which were coupled to the centroid of the cross-section as shown in Fig. 6.1. The effects of large displacements were taken into account by using the nonlinear geometry parameter "NLGEOM". For cyclic analyses, the ANSI/AISC 341-16 (2016) proposed loading regime shown in Fig. 6.3 was adopted.
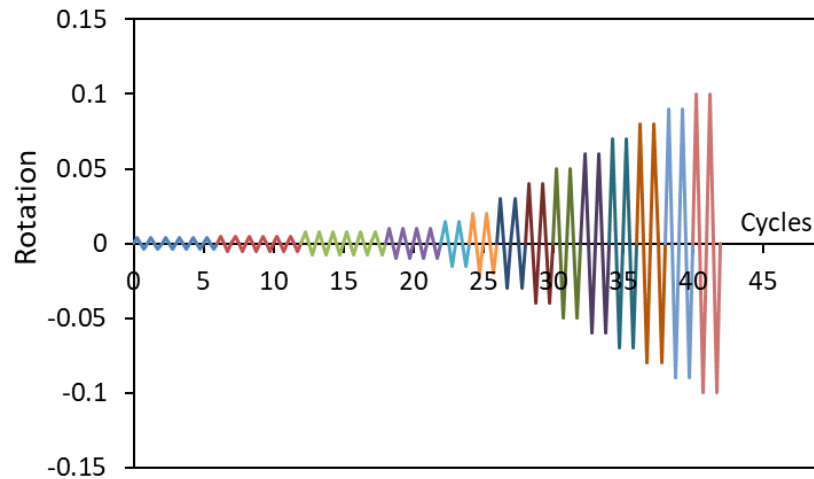
Fig. 6.3. Cyclic loading protocol in accordance with ANSI/AISC 341-16 (2016)

6.3.5. FE modelling validation

Fig. 6.4 shows the ratio of the applied bending moment to the CFS beam plastic moment (M/M_p) versus the rotations obtained from the experimental tests and the detailed FE models for both cyclic and monotonic loading. The rotation of the connection was determined according to the ratio of beam tip displacement to the length of the beam up to the gusset plate. In general, it is shown that the FE models could simulate the behaviour of the connections with a good level of accuracy over the whole loading range. Comparison between the FE cyclic and monotonic results indicates that the initial stiffness and the maximum strength values are coincident. However, the results of the monotonic analyses slightly underestimated the stiffness degradation rate. The dominant failure of the CFS bolted moment connection under both monotonic and cyclic loads generally started with the local buckling at beam webs followed by buckling of the compression flange, as shown in Fig. 6.5.
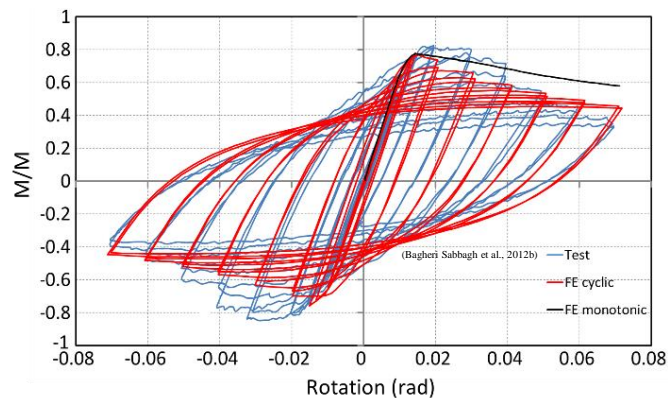
Fig. 6.4. Comparison between the results of tests and FE analysis

<div align="center">(a)   (b)</div>
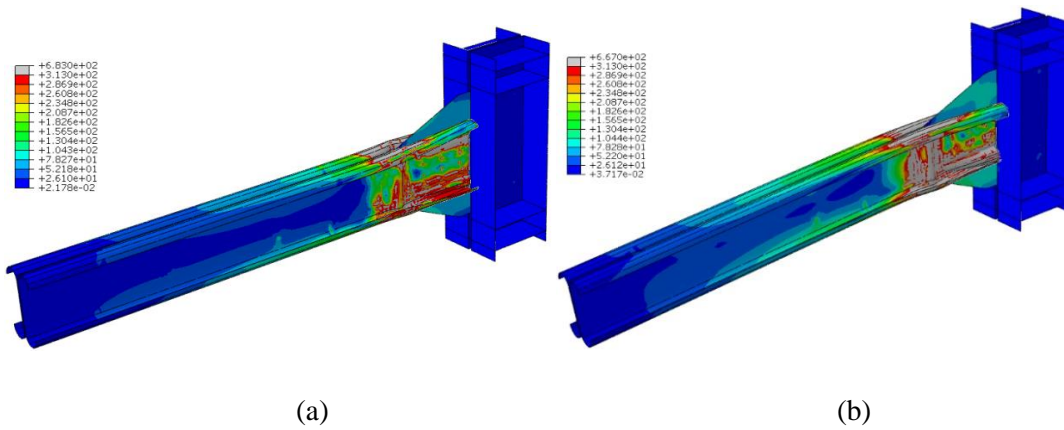
Fig. 6.5. Typical failure mode of CFS bolted moment connection subjected to (a): cyclic and (b): monotonic loads

6.4. DEFINITION OF SEISMIC CHARACTERISTICS

Ductility and energy dissipation capacity are considered as key performance parameters for the seismic design of moment-resisting frames, where the structural components are expected to exceed their elastic limits in severe Earthquakes. Therefore, in this study, these parameters are used as optimisation target to improve the seismic performance of CFS connections.

6.4.1. Energy dissipation

In general, energy in bolted moment connection is dissipated through (i) bearing behaviour of the bolts and steel plate, (ii) plasticity of the cross-sections and (iii) slippage of the bolts. The earthquake-induced energy in CFS moment-resisting frames is mainly dissipated by their bolted moment connections through plastic deformation of the beam elements as well as bearing deformation of bolts against a steel plate. To estimate the plastic energy dissipation of the connections in ABAQUS, the following integration is used through the beam volume (V) and loading history (t):

$$E = \int_V \int_0^t \sigma_{ij}(\tau)\dot{\varepsilon}_{ij}^p(\tau)d\tau dV \tag{6.3}$$

where $\sigma_{ij}(\tau)$ is the plastic stress tensor and $\dot{\varepsilon}_{ij}^p(\tau)$ is the first derivative of plastic strain tensor with respect to time. In this study, the energy dissipation of CFS bolted moment connection is determined up to 4% (rad) inter-story drift ratio, which is in accordance with the AISC 341-16 (2016) requirements for the Special Moment Frame (SMF).

6.4.2. Ductility ratio

The ductility ratio (μ) for the connections can be determined using the ratio of target rotation (θ_t) to yield rotation (θ_y) of an idealised bi-linear moment-rotation curve as the representative of the actual structural response of the system:

$$\mu = \frac{\theta_t}{\theta_y} \tag{6.4}$$

In this study, the idealised moment-rotation curve is determined using ASCE 41-17 (ASCE/SEI 41-17, 2017) proposed method, in which an iterative graphical procedure is adopted to balance the areas below the actual and idealised curves up to the target rotation (θ_t). The yield rotation (θ_y) is obtained based on the condition that the first line segment intersects the actual envelope curve at 60% of the nominal yield moment (M_y), as shown in Fig. 6.6. The target rotation (θ_t) depends mainly on the expected performance from the connections. Generally, it is assumed that the target rotation is the maximum rotation prior to a considerable fall in the strength of the system (Uang, 1991, Park, 1989, Gad et al., 1999). In this study, the target rotation is considered as the rotation at which the flexural capacity of the connection is reduced by 20% as also recommended by ANSI/AISC 341-16 (2016).
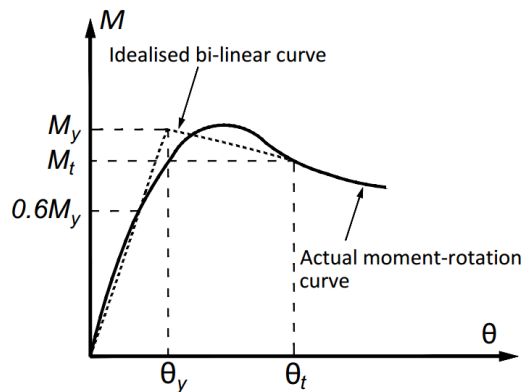
Fig. 6.6. Calculation of ductility based on ASCE's method (ASCE/SEI 41-17, 2017)

6.5. CONNECTION OPTIMISATION

This section is aimed to find best design solutions for the bolted moment connections in terms of energy dissipation capacity and ductility, as key seismic performance parameters, by optimising the cross-sectional shapes of the CFS beam element. The experimentally validated FE models of CFS bolted moment connections subjected to monotonic loading (discussed in section 6.3) are used to simulate the non-linear response of the connections. A standard commercially available back-to-back lipped channel section is taken as a benchmark to assess

the efficiency of the optimised sections. Five different cross-sectional shapes are selected for the CFS beam element, including channel sections with inclined lips, rolled-in intermediate stiffeners in flange and web, and folded flanges. Design constraints are imposed on plate slenderness and relative dimensions of the cross-sections according to Eurocode 3 (CEN, 2005c, CEN, 2006a), while a range of manufacturing limitations are also considered as suggested by the industrial partner of this project (see Table 6.1). It should be noted that optimisation of the connections under cyclic loading will be too computationally expensive to be practical, and therefore in this study, the connections are optimised under monotonic loading condition. However, it will be discussed in Section 6.8 that using monotonic or cyclic loading in the optimisation process leads to the same optimum design solution.

6.5.1. Problem formulation

Similar to the reference experimental test, a cantilever beam-to-column bolted connection loaded concentrically is selected for the optimisation, as shown in Fig. 6.7. The length of CFS beam element $L=2000$ mm is considered to represent a mid-length contraflexure point in a typical moment-resisting frame with 4000 mm span subjected to lateral loading. The bolt-group size of 170×170 mm arrayed 3×3 is selected and kept constant during optimisation process. To avoid global buckling of the CFS beam, lateral restraints are placed at 500 mm spacing along the length of the beam. Other parameters and modelling techniques such as material properties, loading, element types, mesh size and bolt modelling are taken the same as the experimentally validated connection discussed in Section 6.3. To find the best design solution for the CFS beam cross-sections, bolted moment connections loaded monotonically in a displacement control manner are analysed in each iteration of the optimisation process. The moment-rotation (M-θ) response of each connection is then calculated from the centre of failure (i.e. plastic hinge region), which is assumed to be located at the end of the gusset plate.
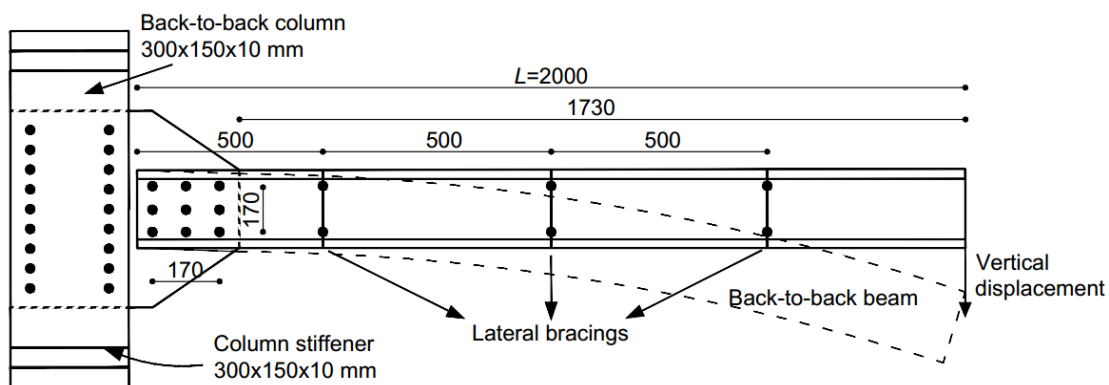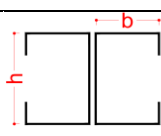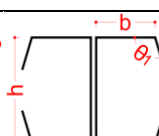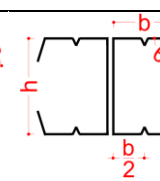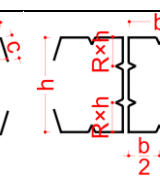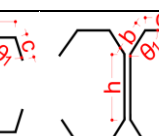
Fig. 6.7. Schematic view of bolted moment connection for optimisation process

Table 6.1 shows cross-sectional shapes of beam prototypes, Eurocode 3 design constraints, manufacturing limitations, and design variables including relative dimensions of the cross-sections, location of intermediate stiffeners, and angles of inclined lips. It should be mentioned that the manufacturing constraints were determined following consultation with the industrial advisor of this project.

The CFS beam with standard commercially available lipped channel section (depth=260 mm, flange=79 mm, lip=16 mm, and plate thickness t=4 mm) is taken as a benchmark to assess the efficiency of the optimum solutions. In this study, five different beam cross-sectional shapes are selected; Beam ①: (back-to-back conventional lipped channels); Beam ②: (beam ① with inclined lip); Beam ③: (beam ② + intermediate flange stiffeners); Beam ④: (beam ③+intermediate web stiffeners); and Beam ⑤: (back-to-back channels with folded flanges). The triangular intermediate web stiffeners consist of two 15 mm legs with an intersecting angle of 60°, and their locations are varied during the optimisation process. The flange stiffeners are placed at the middle mainly for practicality reasons. The width of the flanges is also assumed to be at least 50 mm in order to connect trapezoidal decking or plywood boards to the beam by means of screws. The minimum feasible lip length for rolling or press-braking process is considered $c \geq 15$ mm. The web depth limit of $h \geq 200$ mm is also imposed to appropriately fit the selected bolt-group (170×170 mm) in the connection zone. In the adopted optimisation process, the plate thickness and the total coil width remain similar to the benchmark section to keep the material use of the cross-sections invariable. For the sections with web and flange stiffeners, their developed length is considered in the calculation of the total coil width.

Table 6.1. Selected beam cross-sections, design variables and constraints

Prototypes	①	②	③	④	⑤
Cross-section					
Design variables(X_i)	$X_1=c/b$ $X_2=b/L$	$X_1=c/b$ $X_2=b/L$ $X_3=\theta_1$	$X_1=c/b$ $X_2=b/L$ $X_3=\theta_1$	$X_1=c/b$ $X_2=b/L$ $X_3=R$ $X_4=\theta_1$	$X_1=\theta_1$ $X_2=\theta_2$ $X_3=b$ $X_4=c$ $X_5=d$
EC3 design constraints	$0.2 \leq c/b \leq 0.6$ $b/t \leq 60$ $c/t \leq 50$ $h/t \leq 500$	$0.2 \leq c/b \leq 0.6$ $b/t \leq 60$ $c/t \leq 50$ $h/t \leq 500$	$0.2 \leq c/b \leq 0.6$ $b/t \leq 60$ $c/t \leq 50$ $h/t \leq 500$	$0.2 \leq c/b \leq 0.6$ $b/t \leq 60$ $c/t \leq 50$ $h/t \leq 500$	$h/t \leq 500$

		$\pi/4 \leq \theta_l \leq 3/4\pi$	$\pi/4 \leq \theta_l \leq 3/4\pi$	$\pi/4 \leq \theta_l \leq 3/4\pi$ $0.1 \leq R \leq 0.4$	
Practical limitations (mm)	$c \geq 15$ $b \geq 50$ $h \geq 200$	$c \geq 15$ $b \geq 50$ $h \geq 200$	$c \geq 15$ $b \geq 50$ $h \geq 200$	$c \geq 15$ $b \geq 50$ $h \geq 200$	$7/12\pi \leq \theta_l \leq 5/6\pi$ $\pi/4 \leq \theta_2 \leq 3/4\pi$ $b \leq 50$ $c \geq 50$ $d \geq 15$

In this study, optimisation process is carried out on the CFS bolted moment connection based on two seismic performance indices: (I) energy dissipation capacity determined within the loading history up to drift ratio of 4% (i.e. SMF limit), and (II) ductility ratio calculated based on ASCE 41-17 (ASCE/SEI 41-17, 2017) with the target rotation corresponding to 80% of peak moment in softening branch. The optimisation formulations are as follows:

Optimisation for energy dissipation capacity *E(X)*:

$$\text{max} \quad E(X) \tag{6.5}$$

$$X_i^L \leq X_i \leq X_i^U, \qquad (i = 1, \cdots, n) \tag{6.6}$$

Optimisation for ductility ratio *μ(X)*:

$$\text{max} \quad \mu(X) \tag{6.7}$$

$$X_i^L \leq X_i \leq X_i^U, \qquad (i = 1, \cdots, n) \tag{6.8}$$

In the above equations, *X* indicates a vector including cross-sectional design variables X_i listed in Table 6.1 with the lower bound X_i^L and upper bound X_i^U.

6.5.2. Optimisation technique

A population-based stochastic optimisation technique, based on Particle Swarm Optimisation (PSO), was used to find the global optimum design solutions. An initial population of potential solutions (defined as a swarm of particles) is randomly selected. The particles then move in the problem space based on their own and neighbours' best performances. Unlike most conventional evolutionary optimisation techniques such as Genetic Algorithms (GA) (Kennedy J and Eberhart R, Ye et al., 2016b), PSO method does not require crossover or mutation operators. This usually results in a better computational efficiency especially for highly nonlinear optimisation problems (Hassan et al., 2005, Jeong et al., 2009).

According to PSO algorithm, a swarm contains N particles which possess different position $\rho_i = (\rho_{i1}, \rho_{i2}, \dots, \rho_{ij}, \dots, \rho_{iD})$ and velocity $V_i = (v_{i1}, v_{i2}, \dots, v_{ij}, \dots, v_{iD})$ in a D-dimensional search space. The initial position and velocity of particles are randomly generated to form a swarm, which is then spread out within the range of selected design variables ($X_i^L \leq X_i \leq X_i^U$, $i=1,\dots,n$):

$$\rho_{ij}^0 = X_j^L + r_{ij}(X_j^U - X_j^L) \tag{6.9}$$

$$V_{ij}^0 = \frac{s_{ij}(X_j^U - X_j^L)}{\Delta t} \tag{6.10}$$

where matrices of r_{ij} and s_{ij} possess the components between 0 and 1. Subsequently, the particles fly through the search space to find the optimal solution. The velocity and position of the ith particle at kth iteration are updated mathematically according to the following formulas:

$$V_i^{k+1} = w \cdot V_i^k + c_1 \cdot r_1 \cdot \left(P_{best,\,i}^k - \rho_i^k\right) + c_2 \cdot r_2 \cdot \left(G_{best}^k - \rho_i^k\right) \tag{6.11}$$

$$\rho_i^{k+1} = \rho_i^k + V_i^{k+1} \cdot \Delta t \tag{6.12}$$

where t is the selected time increment, and w is an inertial weight factor. The vectors $P_{best,i}^k = (p_{i1}, p_{i2}, \dots, p_{ij}, \dots, p_{iD})$ and $G_{best}^k = (g_1, g_2, \dots, g_D)$ are, respectively, the best position of the ith particle over its history up to iteration k, and the position of the best particle in the swarm in iteration k. The cognitive parameter c_1 represents the level of confidence in the best position of the particle ($P_{best,i}$). The social parameter c_2 indicates the degree of confidence in the favourable position of the swarm. r_1 and r_2 are independent coefficients selected randomly between 0 and 1. Finally, w is the inertial weight factor applied to preserve a part of the particles' previous velocity. To improve the convergence of the problem, the following recommendations made by Perez and Behdinan (2007) were used:

$$0 < c_1 + c_2 < 4 \tag{6.13}$$

$$\frac{c_1 + c_2}{2} - 1 < w < 1 \tag{6.14}$$

In this study, the developed PSO algorithm was linked to GMNIA ABAQUS through scripting option which combines the functionality of the Graphical User Interface (GUI) of ABAQUS

and the power of the Python object-oriented scripting language. The adopted optimisation process followed the following steps as also illustrated in the flowchart of Fig. 6.8:

(1) The experimentally validated FE model of a connection with the beam cross-sectional dimensions generated by PSO was built using Python script. A vertical displacement was applied at the beam tip, while the material properties, boundary conditions, and bolt modelling were taken the same as the validated model described in Section 6.3.

(2) The initial geometric imperfections of the CFS beam was generated by conducting an eigenvalue elastic linear BUCKLE analysis in ABAQUS and subsequently scaling the first buckling mode shape. The scale factor was determined based on the 50% cumulative distribution values for the measured local or distortional imperfections as reported by Schafer and Pekoz (1998). It should be noted that the local buckling was identified as the dominant failure mode in this type of connection (Bagheri Sabbagh et al., 2012b, Lim and Nethercot, 2003a), hence imperfections magnitude was scaled to 0.34t (see Section 6.3).

(2) An eigenvalue elastic linear BUCKLE analysis is performed in ABAQUS, and the normalized displacements of each node in the first buckling mode are extracted to be used as initial geometrical imperfections. The displacement field is then scaled and applied to the initial meshed geometry to form the initially imperfect model for Standard Static analysis. It should be mentioned that the local buckling is always dominant in this type of connection, hence imperfections magnitude is scaled by 0.34t (as discussed in section 6.3).

(3) The standard "Static-General" analysis available in ABAQUS was performed and the required output data including the resisting moment, applied rotation, and dissipated energy (($E(X)$)) were then extracted using the post-processing scripting in Python.

(4) The extracted moment-rotation output data were transferred to a MATLAB code for the calculation of ductility based on ASCE 41-17 (ASCE/SEI 41-17, 2017).

(5) The values of energy dissipation capacity and ductility calculated in previous steps were imported to the PSO algorithm and a new particle was produced using Equations 6.11 and 6.12.

(6) This loop was repeated by starting a new iteration from step 1 until convergence was achieved or the maximum number of iteration was reached.

It should be noted that the optimised sections obtained from Python programming were modelled once again in Abaqus GUI (i.e. visualisation) to ensure that the results from scripting

are reliable. The population of the swarm was taken as 15 particles for beam prototypes ① to
③, while 20 particles were used for beam prototypes ④ and ⑤ due to their more complex
shape (i.e. more design variables). The minimum and maximum inertial weight factors were
selected as 0.4 and 0.95, respectively. To ensure all possible solutions were taken into account
during the optimisation process, 250 iterations were considered as the maximum number of
iterations. The whole optimisation procedure was conducted on the University of Sheffield's
High-Performance Computing (HPC) cluster due to an extensive number of computations.
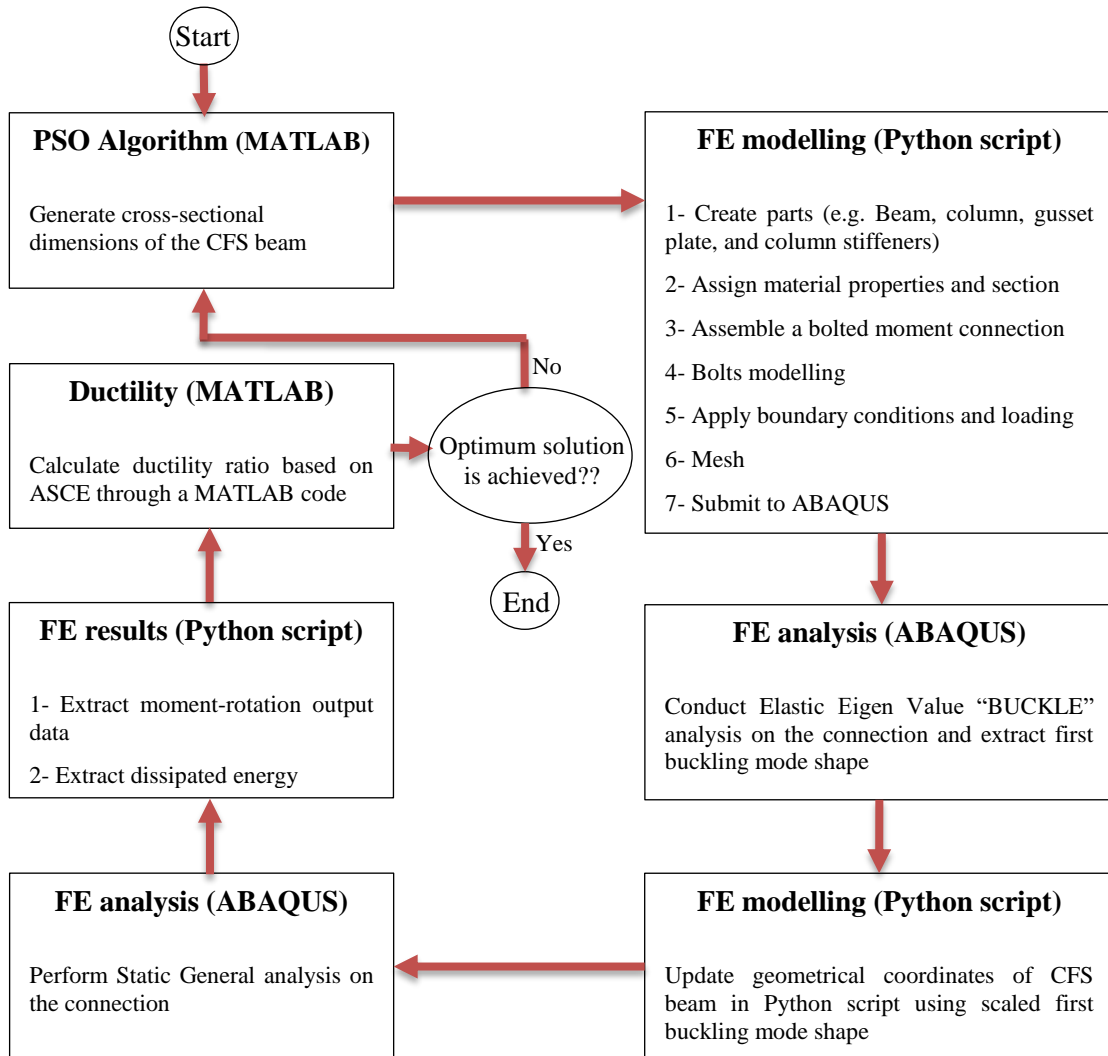
Fig. 6.8. Flowchart of optimisation process for maximum dissipated energy and ductility

6.6. OPTIMISATION RESULTS BASED ON ENERGY DISSIPATION

The iteration history of optimisation process for the maximum energy dissipation of
connections is shown in Fig. 6.9. It can be seen that the optimisation process for the

connections with beam cross-sections ①, ②, and ③ converged to the best solution after around 60 iterations. For the more complex beam cross-sections ④ and ⑤, however, the convergence was achieved after only around 100 iterations due to more design variables leading to higher nonlinearity of the optimisation problem. These results confirm the adequacy of using 250 iterations for the optimisation process as mentioned before.
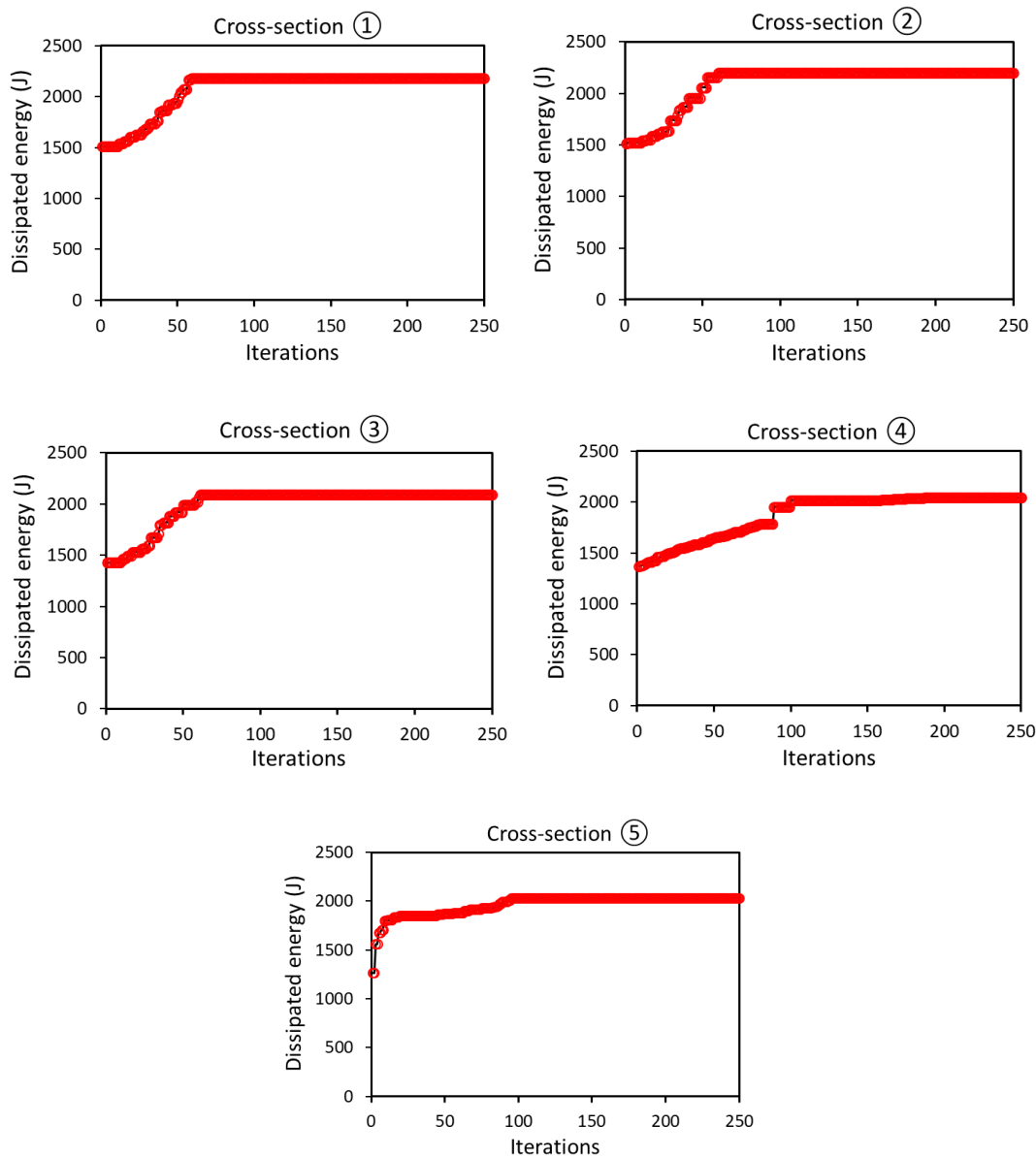
Fig. 6.9. Iteration history of optimisation process based on maximum dissipated energy for the connections with different beam cross-sections

The cross-sectional dimensions of the optimum beams for maximum energy dissipation capacity are listed in Table 6.2. The results are compared with the energy dissipation and flexural strength of the benchmark connection (E_{ben}, $M_{u,ben}$) with the same amount of material (see Section 6.3). In general, it can be seen that the optimum connections with the highest

energy dissipation capacity tend to provide a beam with minimum flanges width (herein 50 mm) and large web height (note that the total length of cross-section is kept constant). This increase in the energy dissipation capacity of the connections is mainly attributed to (a) the delay in flanges buckling due to smaller width to thickness ratio, and (b) development of plastic zone in the beam web for a given drift ratio (4%) leading to higher peak moments.

Table 6.2. Dimensions, energy dissipation and moment capacity of optimum CFS bolted moment connections with different beam cross-sections

Beam section	h (mm)	b (mm)	c (mm)	d (mm)	R	θ_1°	θ_2°	E (kJ)	$\dfrac{E}{E_{ben}}$	M_u (kN.m)	$\dfrac{M_u}{M_{u,ben}}$
Benchmark	260	79	16					1.91	1.00	74.33	1
①	320	50	15					2.18	1.14	88.21	1.19
②	320	50	15			120		2.2	1.15	88.60	1.19
③	290	50	15			112		2.09	1.10	83.57	1.12
④	260	50	15		0.1	108		2.02	1.06	80.46	1.08
⑤	224	38	60	15		150	135	2.03	1.06	79.04	1.06

Fig. 6.10 compares the efficiency of different optimum beam shapes (①, ②, ③, ④, ⑤) used in the CFS bolted moment connection. Based on the results, the following considerations can be drawn:

- The energy dissipation of the connection with the benchmark beam (E_{ben}) can be increased up to 14% by changing its relative dimensions (beam ①). Consequently, the flexural strength of the connection with benchmark beam section ($M_{u,ben}$) is also improved by 19%. It should be noted that a parametric study will be conducted in Appendix A considering the effect of thickness on the percentage of improvement in energy dissipation capacity.

- While the optimum lips' angle is calculated to be 120° in the connection with beam cross-section ②, generally releasing the lips' angle as an optimisation variable leads to a negligible increase in energy dissipation capacity and strength of the connection.

- Incorporating intermediate stiffeners in the flanges (beam section ③) reduces the energy dissipation capacity and flexural strength of the connection by 4% and 5%, respectively,

compared to optimum beam section ①. These reductions are exacerbated to 8% and 10% by adding combined intermediate stiffeners in the flanges and webs (beam section ④)), as a result of the reduction in the cross-sectional web height. It should be noted that the stiffeners' legs are accounted for the total length of the cross-section, and therefore, the web height of the optimum beams ③ and ④ is less than that of optimum beam section ①.

- A CFS connection with folded-flange beam section (⑤) provides approximately as much energy and strength as a connection with flange and web stiffeners beam section (④). The main reason is that the folded-flange beam section in this study had lower web slenderness compared to the other beam sections due to the imposed constraints for its constituent elements (listed in table 6.1). This is consistent with the results of previous studies, where folded-flange beam sections with thicker plate provided lower energy dissipation capacity compared to other standard shapes (Ye et al., 2016b). It should be noted that, in general, folded flange sections benefit from easer forming process (e.g. do not require press braking) and connection to typical floor systems. This demonstrates the efficiency of the beam with folded flange section compared to those with intermediate stiffeners (sections ③ and ④).
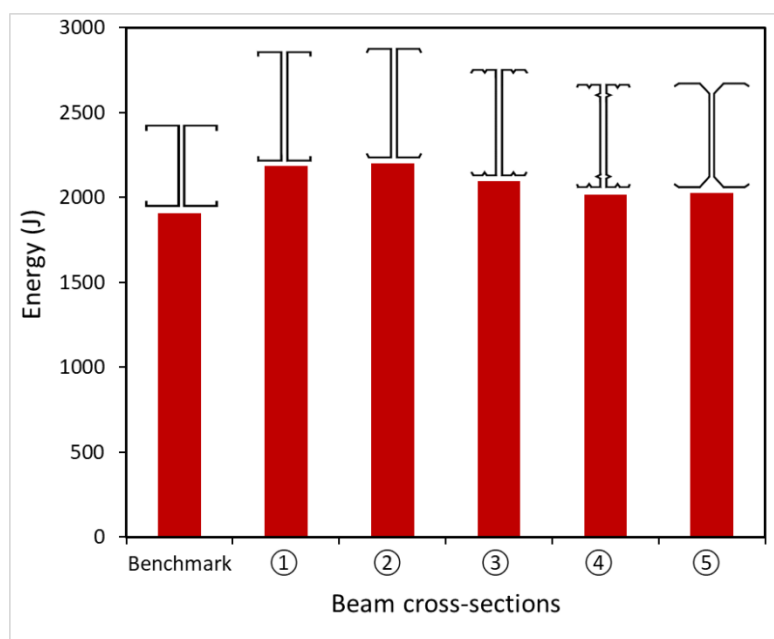
Fig. 6.10. Maximum energy dissipation provided by connections with optimum beams

The optimum connections in terms of energy dissipation capacity and their distribution of von Mises stresses are provided in Fig. 6.11. Von Mises stress values larger than yield stress f_y=313 MPa are highlighted by the dark grey color. It is seen that the connections with beam cross-sections ①, ② fail locally in the beam close to the first bolt line. However, interaction of

local and distortional buckling is dominant for the connections with beam cross-sections ③,
④, and ⑤. It is shown that the plastic zone in the connection with beam section ① is
significantly more extended by simply optimising the relative dimensions of the benchmark
beam, leading to higher energy dissipation capacity and flexural strength of the connection.
While, optimising the lips' angle in beam section ② does not considerably affect the plastic
zone, using connections with beam sections ③, ④, and ⑤ generally provides less plasticity
compared to the connection with beam section ①. These observations made from Fig. 6.11
are in agreement with the results presented in Table 6.2.

(a): Benchmark   (b): ①   (c): ②

(d): ③   (e): ④   (f): ⑤
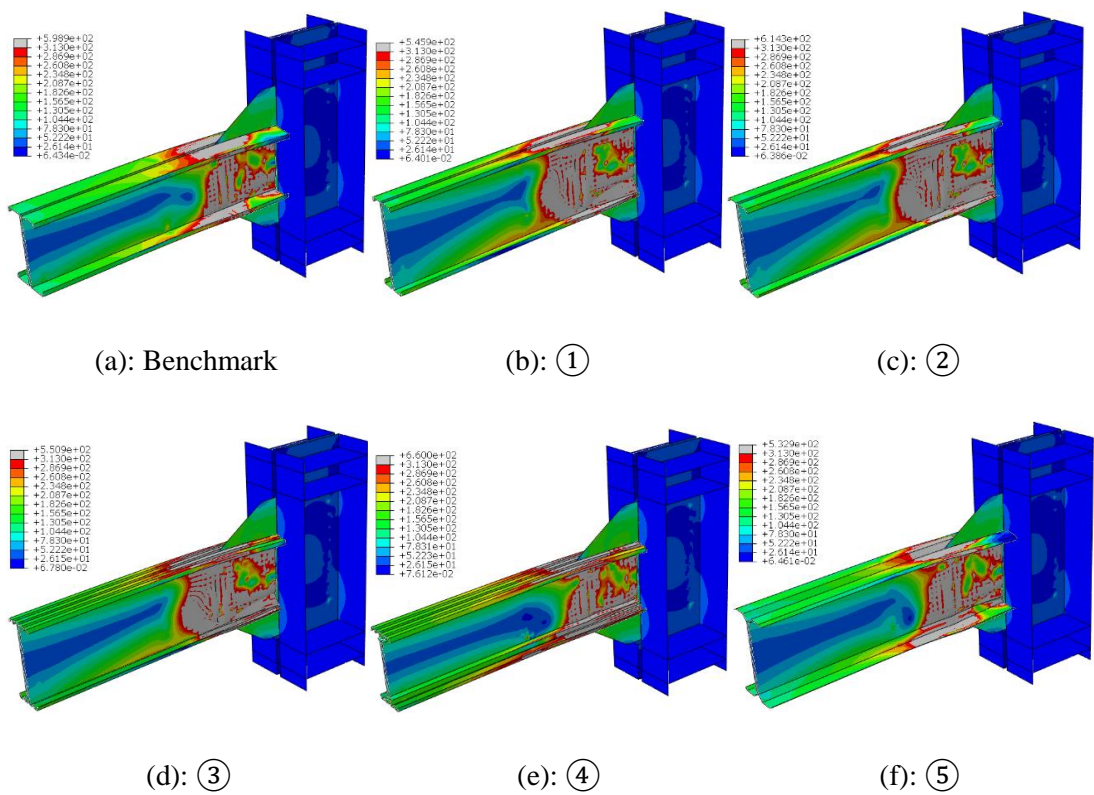
Fig. 6.11. Von Mises stress contour of CFS bolted moment connection with standard and
optimised beams based on maximum energy dissipation at 0.04 rad rotation

6.7. OPTIMISATION RESULTS BASED ON DUCTILITY

Based on the results history provided in Fig. 6.12, optimisation process based on ductility in
general requires a higher number of iterations to converge to the optimum solution compared
to the energy-based optimisation. It is shown that convergence is obtained after 80 iterations
for the connections with beam sections ①, ②, and ③, while 150 iterations are needed for

the connections with beam sections ④, and ⑤. Therefore, the selected maximum 250 iterations used in the optimisation process is sufficient in the case as well.
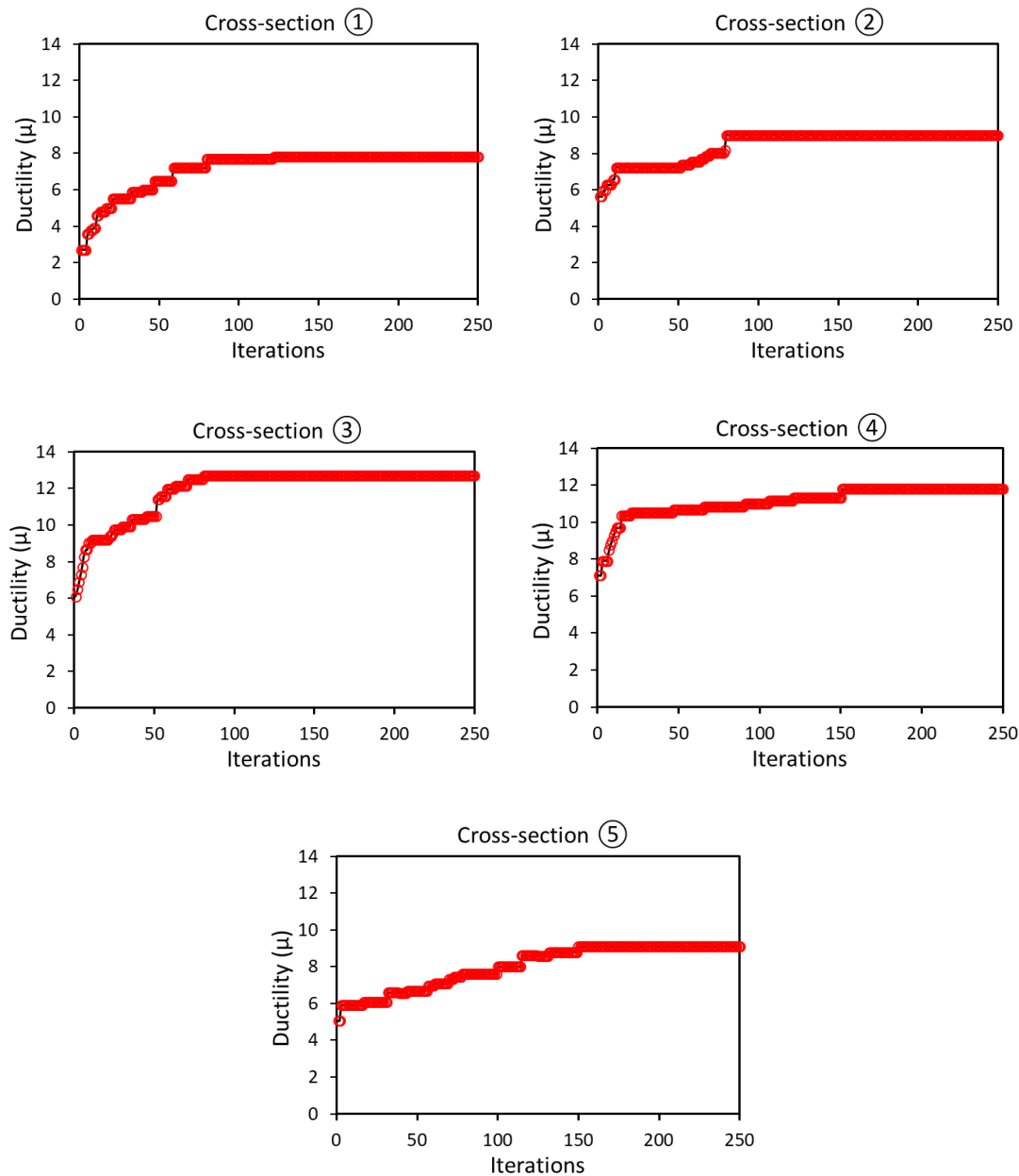
Fig. 6.12. Iteration history of optimisation process based on maximum ductility for the connections with different beam cross-sections

Table 6.3 lists the dimensions of optimised beam sections with the same steel coil width (450 mm) obtained from optimisation based on maximum ductility. The ductility and flexural strength of the benchmark connection (μ_{ben}, $M_{u,ben}$) are also considered as a measure to investigate the efficiency of the optimum sections. As a general trend shown in Table 6.3, the adopted optimisation process enhances the ductility of the connections by reducing the height

of the beam web (minimum 200 mm) and subsequently increasing the flange width and lip length. In this case, the local failure occurs in the flanges, which leads to a gradual drop in moment-rotation curve.

Table 6.3. Dimensions, ductility and moment capacity of optimum CFS bolted moment connections with different beam cross-sections

Beam section	h (mm)	b (mm)	c (mm)	d (mm)	R	θ_1°	θ_2°	μ	$\dfrac{\mu}{\mu_{ben}}$	M_u (kN.m)	$\dfrac{M_u}{M_{u,ben}}$
Benchmark	260	79	16					4.3	1	74.33	1
①	200	78	47					7.6	1.77	58.60	0.79
②	200	78	47			104		9	2.09	58.39	0.79
③	200	69	41			104		12.7	2.95	60.47	0.81
④	200	59	36		0.4	95		11.8	2.74	63.44	0.85
⑤	200	30	65	30		110	68	9.1	2.12	60.25	0.81

Based on Table 6.3 and Fig. 6.13, the following remarks can be made:

- Ductility of the connection with the benchmark beam can be increased up to 77% by simply changing cross-sectional relative dimensions (section ①), however, its flexural capacity is reduced by 21%.

- By optimising the cross-sectional lips angle to 104° (section ②), the ductility ratio of the connection is increased up to 18%. However, the maximum moment capacity of the connection is not considerably affected.

- Unlike optimisation based on energy dissipation discussed in section 6.6, placing intermediate stiffeners in the flanges (section ③) or combined stiffeners in the flanges and web (section ④) can improve the ductility of the connection with optimised conventional beam (section ①) by 67% and 55%, respectively. Using intermediate stiffeners also slightly increases the flexural strength of the connection, mainly by delaying the stiffness degradation due to buckling.

- Using the optimised folded flange beam (section ⑤), the ductility of the connection is increased by 20% compared to the connection with optimised conventional section (section ①), while no reduction is observed in the flexural strength of the connection.
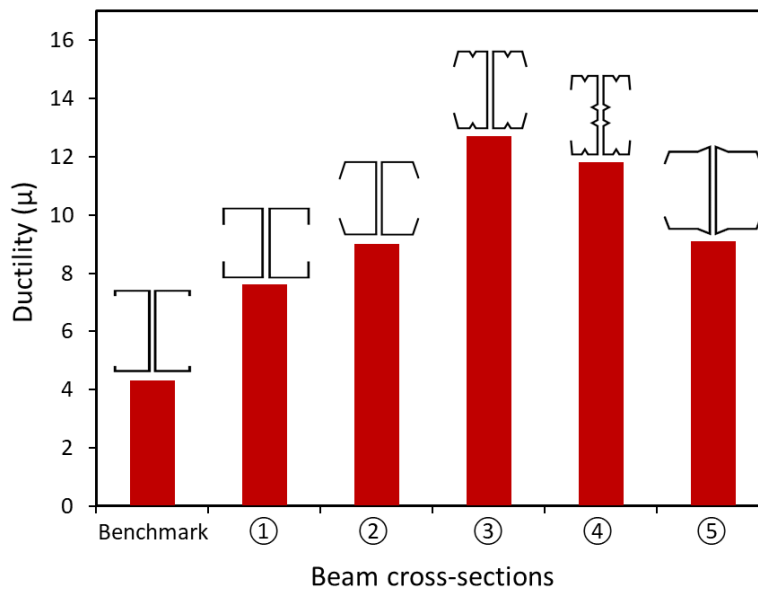
Fig. 6.13. Maximum ductility provided by connections with optimum beams

Fig. 6.14 shows the von Mises stress contour of the bolted moment connections with standard
and optimised beams based on maximum ductility. In this figure, the regions with dark grey
colour represent the stress values larger than yield stress. It can be seen that, compared to the
optimised connections based on energy dissipation, the plasticity is developed in a larger zone
(especially in the flanges and lips) to maximise the ductility of the connection. Hence,
optimised CFS bolted moment connections for ductility are capable to accommodate
significant damage in the beam up to their ultimate point (i.e. rotation corresponding to 20%
drop from the peak moment).

As shown in Fig. 6.14, the failure of the benchmark connection with the standard beam is
localised in the beam web mainly due to its large web slenderness; however, optimised
connections with the lesser beam depth (200 mm) can develop plasticity and failure in both
flanges and web. By optimising cross-sectional lips angle (section ②), plasticity is more
distributed along the length of the CFS beam. Using intermediate stiffeners in the beam flanges
(sections ③) results in a connection with the highest ductility due to a more gradual local
failure in the flanges as well as the global buckling of the lips (distortional buckling of the
section). Although the flanges of cross-section ④ are smaller than cross-sections ①, ②, and
⑤, this cross-section is still able to provide more ductility due to the presence of intermediate
flange stiffeners.

(a): Benchmark   (b): ①   (c): ②

(d): ③   (e): ④   (f): ⑤
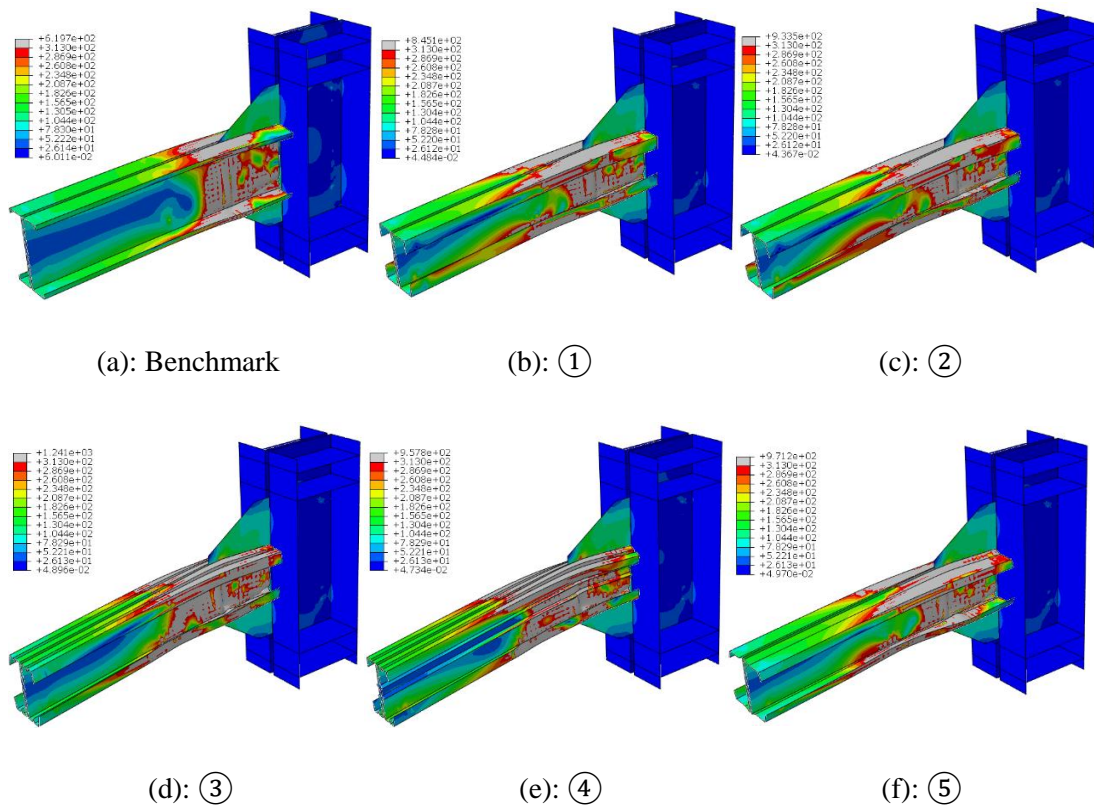
Fig. 6.14. Von Mises stress contour of bolted moment connection with standard and optimised beams based on maximum ductility at a 20% drop from maximum moment

6.8. EFFECTS OF CYCLIC LOAD ON THE OPTIMUM SOLUTION

As discussed in section 6.5, performing optimisation on the detailed connection models (with nonlinear shell and fasteners elements) under cyclic load is highly computationally expensive, and therefore is not suitable for practical applications. In this section, the accuracy of using monotonic loading in the optimisation process as a more practical approach is assessed by investigating the effects of cyclic loading on the optimum solution. To this end, the connection with beam cross-section ① is optimised under the ANSI/AISC 341-16 (2016) proposed cyclic loading (see Fig. 6.3). The University of Sheffield's High-Performance Computing (HPC) cluster was used to solve this optimisation problem. The results showed that optimisation of the connections based on cyclic loading regime results in the same beam cross-sectional dimensions as those under monotonic loading (see Table 6.4). The hysteretic behaviour of the optimum connections under cyclic loading optimised based on energy dissipation and ductility is also shown in Fig. 6.15.

Table 6.4. Optimum dimensions of the CFS beam section ① in bolted moment connections under cyclic loading condition

Optimisation target	h	b	c
	mm	mm	mm
Energy dissipations	320	50	15
Ductility	200	78	47
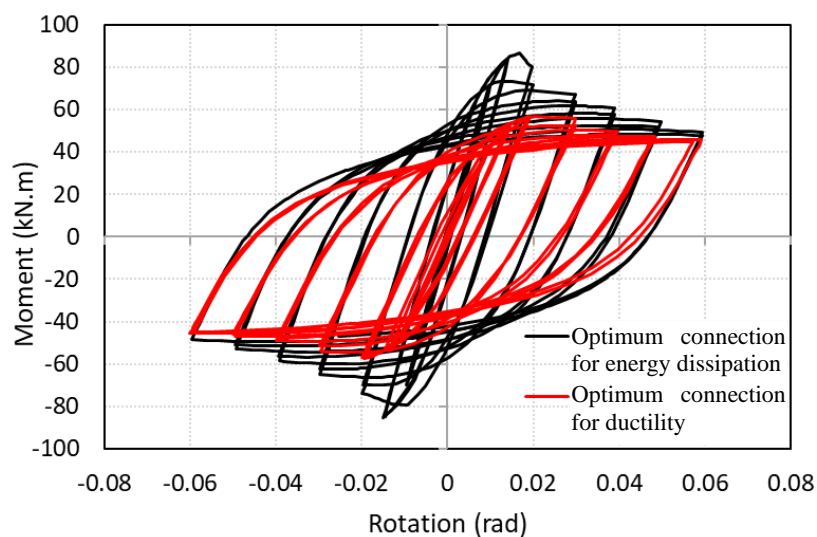
Fig. 6.15. Hysteretic behaviour of optimum connections for energy dissipation and ductility with beam cross-section ①

6.9. EFFICIENCY OF THE OPTIMUM DESIGN SOLUTIONS UNDER CYCLIC LOAD

One of the main issues associated with the use of CFS bolted moment connections in high seismic regions is their ability to develop the plastic hinge (i.e. moment hinge) and subsequently maintain the moment resistance under repeated rotations. This was shown in section 6.3 that the post-peak behaviour and consequently the seismic characteristics of the CFS bolted moment connections can be very different under monotonic and cyclic load conditions. Therefore, in this section the efficiency of the connections optimised under monotonic load (Sections 6.6 and 6.7) is investigated under cyclic load condition.

As shown in Table 6.5, energy dissipation (E_{cyc}) and ductility (μ_{cyc}) of the connections with optimised beam sections are increased by up to 20% and 164%, respectively, compared to

those with standard beam sections. Therefore, optimisation results based on monotonic and cyclic loads can both confirm the efficiency of the proposed method to find the best seismic design solutions for the CFS bolted moment connections. These observations are consistent with the general trend of the optimum results under monotonic load (see Sections 6.6 and 6.7). This demonstrates again the efficiency of the proposed optimisation method, when the connections are subjected to cyclic load.

Table 6.5. Comparison between seismic characteristics of optimum connections under cyclic load

Beam section	Optimum connections for energy dissipation		Optimum connections for ductility	
	E_{cyc}	$(E/E_{ben})_{cyc}$	μ_{cyc}	$(\mu/\mu_{ben})_{cyc}$
	kJ			
Benchmark	22660.2	1	2.8	1
①	26726.3	1.18	4.6	1.64
②	27258.4	1.20	4.6	1.64
③	25758.3	1.14	7.2	2.61
④	26124.4	1.15	6.2	2.21
⑤	26973.5	1.19	4.9	1.75

6.10. SUMMARY

This chapter presented an optimisation framework to develop CFS bolted moment connections with enhanced energy dissipation capacity and ductility. To achieve this, Particle Swarm Optimisation (PSO) algorithm was linked to GMNIA ABAQUS FE analysis using experimentally validated Finite Element (FE) models of the connections by taking into account material non-linearity and geometrical imperfections. Five different CFS beam cross-sectional shapes were selected and their relative dimensions, location of intermediate stiffeners, and the inclination of the lip stiffeners were considered as key design variables.

It should be noted that efficient seismic design of CFS bolted moment connections is presented in Appendix B by conducting a comprehensive parametric study on their key design parameters (e.g. bolt slip resistance, bolt configurations, cross-sectional thickness and shape and etc.).

6.11. CONCLUDING REMARKS

Based on the results, following conclusions can be drawn:

- By simply changing the relative dimensions of the lipped-channel beam section, the flexural strength, energy dissipation capacity, and ductility of the connection with the conventional lipped-channel beam section can be increased up to 19%, 14% and 77%, respectively. It was also shown that optimising the lips' angle only results in a negligible improvement in the structural performance of the connection.

- The adopted optimisation process enhanced the energy dissipation of the connections generally by reducing the width of the beam flanges and subsequently increasing the web height. However, CFS beam elements in the optimum connections with the highest ductility tend to have minimum specified web height and larger flanges.

- It was shown that using intermediate stiffeners in the beam section can improve both flexural strength and ductility of the connections by up to 67%. However, incorporating intermediate stiffeners in the beam section slightly (up to 8%) reduced the energy dissipation capacity of the connections compared to that with optimised lipped-channel beam section.

- Compared to the connection with optimised lipped-channel beam section, using optimised folded-flange beam section provided a more efficient connection in terms of ductility (up to 20%). However, optimised folded-flange beam section could not provide the same level of energy dissipation capacity. This can be due to the lower web slenderness of the folded-flange beam section in this study imposed by the selected design constraints.

- For both energy dissipation and ductility, the optimisation of the CFS bolted moment connections under cyclic load leads to the same optimum sections obtained under monotonic load. It was also shown that the energy dissipation and ductility of the optimised connections under cyclic load follow the same general trend obtained for the optimised connections under monotonic load. This indicates that, to reduce the computational costs of the optimisation process, CFS connections can be efficiently optimised under monotonic load as suggested in this study.

CHAPTER 7

Summary and Conclusions, and Recommendations for Future Work

7.1. SUMMARY AND CONCLUSIONS

The main purpose of this research was to develop more efficient CFS structural components, and to investigate the behaviour and design of CFS bolted connections subjected to both static and seismic loads. At the element level, the capacity of CFS elements at serviceability and ultimate limit states, determined in accordance with the Eurocode 3 effective width method, was first optimised, and the efficiency of the optimised elements was then assessed at the structural level by incorporating them into CFS frames. At the connection level, the behaviour of various CFS bolted connections under both monotonic and cyclic loading conditions was investigated using experimentally validated FE models. Extensive parametric studies were also conducted using the validated FE models by considering a wide range of design variables in order to eventually propose general design equations for the capacity of CFS bolted connections and identify the most efficient design solutions which considerably improve their seismic performance. Based on the results of this study the following general conclusions can be drawn at different levels of CFS structures:

7.1.1. Element Level (objectives 1 and 2)

The following conclusions regarding objectives 1 and 2 were drawn:

(1) When increasing the level of the applied bending moment in the beam-column member, the optimisation process tends to generate a section with larger vertical internal elements (webs). However, optimum beam-column members under pure compression (columns)

can be achieved by minimising the web height and subsequently increasing the horizontal internal and outstand elements of the cross-section (e.g. the flange and flange stiffener).

(2)   The proposed optimisation process is more efficient for CFS members with larger wall thickness and larger length. It is also shown that, while the highest gains through optimisation can be obtained for members subjected to pure compression, the least improvement is obtained for the beam-column members under negligible compressive load.

(3)   By simply changing the relative cross-sectional dimensions of the standard single and back-to-back lipped channel sections, the capacity of the CFS beam-column member can be increased by up to 193%, and 158% when it performs as a column, and 13% and 12% when it acts as a beam, respectively.

(4)   The optimised beam-column member with a diamond shape is able to carry more compressive load compared to back-to-back channels and RHS sections. However, it would be less efficient when combined compression and major axis bending moment are applied.

(5)   For the same amount of material, the proposed optimisation framework was able to increase the flexural capacity and stiffness of the standard benchmark section by 58% and 44%, respectively. In general, optimised cross-sections (at both SLS and ULS) tend to use deeper web and narrower flanges. The main differences between optimised shapes for ULS and SLS are the size and the angle of the edge stiffeners, as well as the location of the intermediate web and flange stiffeners.

(6)   The optimum dimensions of the plain channels for SLS are very similar to those obtained for ULS. While optimisation of plain channel sections (including those with intermediate stiffeners) at ULS did not provide efficient design solutions, using optimum plain channels at SLS could offer considerably higher stiffness compared to the benchmark lipped channel section. This implies that optimum plain channels are more adequate for SLS requirements.

(7)   The flexural capacity and stiffness of the benchmark lipped channel at ULS and SLS were increased by 30% and 37%, respectively, only by optimising its relative cross-sectional dimensions. While an additional 10% flexural capacity at ULS was obtained by using double edge stiffeners, a negligible improvement in flexural stiffness was observed at SLS.

(8) The flexural capacity and stiffness of the optimum single and double lipped channels at ULS and SLS, respectively, were not generally enhanced by incorporating intermediate stiffeners in the web. However, adding intermediate stiffeners in the flanges could increase the flexural capacity and stiffness of the sections at ULS and SLS by up to 17% and 10%, respectively.

(9) It was shown that the newly developed folded flange channel can be considered as the most desirable section, owing to the fact that it is capable to provide 58% and 41% higher bending capacity and stiffness at ULS and SLS, respectively, compared to the standard lipped channel section with the same amount of material.

(10) The efficiency of the optimised CFS beam sections was assessed by using detailed FE models accounting for material non-linearity and initial geometric imperfections. The results of the FE simulations in general confirm the accuracy of the mid-span deflection and flexural capacity of the sections predicted by the proposed methodology in EC3 (less than 12% error).

7.1.2. Connection Level (objectives 3, 4, and 5)

The following conclusions regarding objective 3 were drawn:

(1) The results indicated that the ultimate bending moment capacity of the CFS back-to-back sections may be reduced by up to 40% due to presence of the bolts, depending on the eccentricity and the thickness of the channel and the bolt group size.

(2) The predicted capacities of connections under an imposed tip displacement at the beam end section showed that the bending and shear interaction equation proposed by the AISI for CFS members is safe to use for CFS beam-to-column bolted connections.

(3) It was shown that, depending on the cross-sectional thickness and eccentricity and the bolt group length, the shear lag effect can considerably reduce the axial compressive capacity of the connected compressive member. Using CFS channels with large eccentricity results in a noticeable change in the compressive capacity of the connection, regardless of the bolt group length. It was also demonstrated that, for channels with small eccentricity, the effect of shear lag was significantly mitigated by increasing the bolt group length.

(4) Similar to the equation proposed by the AISI specification for the tensile connections, the capacity is directly related to the ratio of the eccentricity to the connection length

(X/l_b). However, the proposed equation representing the capacity of CFS connections under axial compression features an additional term containing the web slenderness (h/t).

The following conclusions regarding objective 4 were drawn:

(5)   The simplified method adopted for modelling slip in bolted moment connections using fastener elements in parallel with stop elements in ABAQUS provides an efficient and reliable tool to simulate the experimental moment-rotation behaviour and dominant failure mode of connections with a friction-slip mechanism.

(6)   Incorporating a friction-slip mechanism causes a horizontal shift in the hysteretic moment-rotation response of the connections, while it also reduces the stress concentrations in the connection zone and postpones failure of the CFS beam element. The effect of the pretension force is generally negligible on the flexural capacity of the connections, while the bolt configuration and the CFS beam cross-sectional shape and classification play the main roles. Generally, using a bent flange cross-section and a square bolt configuration provides a higher flexural capacity in the connections (by up to 40%), which is more evident in the case of a larger plate thickness.

(7)   Using a bolt friction-slip mechanism can significantly improve the energy dissipation capacity of the connections (by up to 200%), especially when class 3 and 4 beams are used. Stiffened-flange and folded-flange sections generally provide the highest energy dissipation capacity, while using a diamond shaped bolt configuration can also increase the energy dissipation capacity of the connections with class 1 and 2 beams by up to 70%.

(8)   The proposed friction-slip mechanism can significantly increase the equivalent damping coefficient of connections with class 3 and 4 beam sections (by up to 6 times), while it may cause a small reduction in the damping coefficient when cross-sections of class 1 and 2 are used. This problem can be addressed by adjusting the slip resistance to be activated in the inelastic stage of the moment-rotation curve. It was also observed that the effect of the cross-sectional class on the damping coefficient of the connections is practically negligible.

(9)   The ductility of CFS bolted moment connections can be significantly increased by using a friction-slip mechanism (up to 100%), which is particularly beneficial for CFS sections with smaller plate thickness (class 3 and 4). Folded-flange sections generally exhibited the highest ductility ratios, while diamond shaped and circular bolt configurations provided larger ductility ratios for connections with cross-section class 1 and 2, and class 3 and 4, respectively. It was shown that conventional bolted moment connections with

class 3 and 4 CFS beam sections do not generally satisfy the AISC regulations for IMF and SMF systems. However, accommodating a bolt friction-slip mechanism can improve their seismic performance to be suitable for moment-resisting frames in high seismic regions.

(10) Using gusset plates with the same or lower thickness as the CFS beam may lead to a premature failure mode in the gusset plate and considerably reduce the moment capacity of the connection. However, this failure mode can be effectively prevented by increasing the gusset plate thickness slightly above the thickness of the CFS beam.

The following conclusions regarding objective 5 were drawn:

(11) By simply changing the relative dimensions of the lipped-channel beam section, the flexural strength, energy dissipation capacity, and ductility of the connection with the conventional lipped-channel beam section can be increased up to 19%, 14% and 77%, respectively. It was also shown that optimising the lips' angle only results in a negligible improvement in the structural performance of the connection.

(12) The adopted optimisation process enhanced the energy dissipation of the connections generally by reducing the width of the beam flanges and subsequently increasing the web height. However, CFS beam elements in the optimum connections with the highest ductility tend to have minimum specified web height and larger flanges.

(13) It was shown that using intermediate stiffeners in the beam section can improve both flexural strength and ductility of the connections by up to 67%. However, incorporating intermediate stiffeners in the beam section slightly (up to 8%) reduced the energy dissipation capacity of the connections compared to that with optimised lipped-channel beam section.

(14) Compared to the connection with optimised lipped-channel beam section, using optimised folded-flange beam section provided a more efficient connection in terms of ductility (up to 20%). However, optimised folded-flange beam section could not provide the same level of energy dissipation capacity. This can be due to the lower web slenderness of the folded-flange beam section in this study imposed by the selected design constraints.

(15) For both energy dissipation and ductility, the optimisation of the CFS bolted moment connections under cyclic load leads to the same optimum sections obtained under monotonic load. It was also shown that the energy dissipation and ductility of the optimised connections under cyclic load follow the same general trend obtained for the

optimised connections under monotonic load. This indicates that, to reduce the computational costs of the optimisation process, CFS connections can be efficiently optimised under monotonic load as suggested in this study.

7.1.3. Frame Level (objective 6)

The following conclusions regarding objective 6 were drawn:

(1) It was shown that, while using the same amount of material, the ultimate flexural capacity of the optimum CFS members was significantly higher (by up to 84%) than their standard counterparts.

(2) The results indicated that the proposed coupled framework can considerably reduce (by up to 20%) the required structural weight of the CFS frame system by using the CFS sections optimised for generic applications.

(3) It was also shown that optimising the frame geometry and knee brace configuration could further reduce the structural weight (by up to 17%), especially under combined ULS and SLS design conditions.

7.2. RECOMMENDATIONS FOR FUTURE WORK

This research can be further developed to cover the following subjects:

- There is a need to conduct experimental studies on some of the CFS sections proposed in this thesis as a result of the optimisation studies (especially the folded flange sections) to obtain more knowledge of their structural behaviour and failure modes.

- An analytical approach can be developed to calculate the effects of bi-moment on the capacity of CFS bolted connections using classical structural analysis theories. The calculated capacities can be then compared with the results of experiments and the equation proposed in this research. In addition, to evaluate the efficiency of the optimised connections at the frame level, the seismic characteristics of CFS moment-resisting frames with optimised connections can be calculated and compared with the results of the optimum connections proposed in this study.

- Experiments on CFS beam-column assemblies with different configurations (e.g. where the flanges are connected in addition to the web), boundary conditions, and beam and column cross-sections can be performed to investigate the flexural and deformation capacities and failure modes in more depth.

- Experiments on CFS bolted connections subjected to different combinations of axial compression/tension, bending and shear can be conducted to investigate their performance and failure modes.

- Apart from the design equations developed in this thesis for the ultimate capacities of CFS bolted connections, parametric studies can be performed to propose design equations for the initial stiffness, deformation capacity, ductility and energy dissipation capacity of CFS bolted connections.

- It was shown in this work that the dominant failure mode of CFS bolted connections is a local buckling failure close to the connection zone. Hence, the seismic performance of CFS moment-resisting frames can be accurately investigated by developing beam-column elements with lumped plasticity at both ends, which take into account the hysteretic behaviour of CFS connections. A similar approach has been previously employed in the form of the Ibara-Krawinkler model in the FE OpenSees software to investigate the seismic performance of hot-rolled steel moment-resisting frames.

- Innovative seismic resistant structural systems, such as braced frames and dual frames, can be proposed based on the conducted research, and subsequently, detailed nonlinear FE models can be developed by taking into account imperfections and material nonlinearity to analyse the behaviour of such structural systems.

- Currently, there is no generic performance-based optimisation framework for the optimum design of CFS structures at the frame level, while taking into account the post-buckling behaviour of CFS elements and connections. The majority of the existing optimisation techniques are not adequate for such complex optimisation with a large number of non-linear structural elements and connections due to high computational costs. Hence, a new optimisation tool should be developed to provide optimum design solutions for the design of complex CFS structures considering multiple performance levels.

APPENDIX A

Development of Optimum Cold-Formed Steel Sections for Maximum Energy Dissipation in Uniaxial Bending

A.1. INTRODUCTION

Cold-formed steel (CFS) elements are increasingly used as load-bearing members in construction, including in seismic regions. More conventional hot-rolled steel and concrete building structures are typically allowed by the design standards to exceed their elastic limits in severe earthquakes, rendering parameters indicating ductility and energy dissipation of primordial importance. However, insufficient research has yet been conducted on the energy dissipation of CFS structures. In the majority of previous optimisation research on CFS sections the ultimate capacity, as typically controlled by local, distortional and/or global buckling modes, is considered to be the sole optimisation criterion. While Chapters 3 and 4 optimised buckling strength of CFS elements at different limit states, this appendix aims to improve the seismic performance of CFS elements by optimising their geometric and material highly non-linear post-buckling behaviour to achieve maximum energy dissipation. A novel shape optimisation framework is presented using the Particle Swarm Optimisation (PSO) algorithm, linked to GMNIA ABAQUS finite element analyses. The relative dimensions of the cross-section, the location and number of intermediate stiffeners and the inclination of the lip stiffeners are considered to be the main design variables. All plate slenderness limit values and limits on the relative dimensions of the cross-sectional components as defined by Eurocode 3, as well as a number of practical manufacturing and construction limitations, are taken into account as constraints in the optimisation problem. It is demonstrated that a substantial improvement in energy dissipation capacity and ductility can be achieved through

the proposed optimisation framework. Optimised cross-sectional shapes are presented which dissipate up to 60% more energy through plastic deformations than a comparable commercially available lipped channel.

A.2. BACKGROUND

Cold-formed steel (CFS) sections are produced by rolling or brake-pressing relatively thin metal sheets into cross-sectional shapes at ambient temperature. Structural systems composed of CFS members provide a wide range of advantages. They typically offer a high strength-to-weight ratio, making efficient use of the material. Moreover, they are lightweight and consequently easy to handle, transport and install. Practical limitations on the sheet thicknesses, however, result in CFS members being susceptible to instabilities such as local, distortional and global buckling. The large width-to-thickness ratios of CFS members also leave them typically outside the limits prescribed by seismic design codes (e.g. AISC 341-16 2016, EN1998-1 2005) for high seismic regions.

It has been shown that optimisation of CFS elements based on their maximum strength under bending or compression can lead to significant material savings. Relevant work has been carried out by, among others, Liu et al. (2004), Tian and Lu (2004), Leng et al. (2014) and Ma et al. (2015).

While research has previously been conducted on the seismic behaviour of CFS stud wall systems (Nithyardan and Kalyanaraman 2012), research into the energy dissipation capacity of individual CFS load-bearing elements is very limited. Calderoni et al. (2009) conducted monotonic and cyclic tests to study the seismic behaviour of CFS channel beams. The results of their study showed a substantial ductility and energy dissipation capacity. The cyclic behaviour of typical CFS wall studs was investigated by Padilla-Llano et al. (2014). The experimental results showed that the amount of energy dissipated by the studs varied with the dimensions and the shape of the profile, but typically decreased with increasing cross-sectional slenderness.

Other research on the development of members for CFS moment-resisting frames has shown that the ductility and energy dissipation of the sections can be significantly improved by curving the flanges into a semi-circular shape (Sabbagh et al. 2012). However, such curved flanges are difficult to manufacture and provide challenges when connecting them to floor elements. More practical shapes can be developed by taking into account manufacturing and construction constraints, as demonstrated by Ye et al. (2016a) and Ye et al. (2016b).

In other relevant research Pan et al. (2007) developed an optimisation method to obtain hot-rolled H-beams with optimal flange shapes which maximize the energy dissipation capacity of the members under monotonic and cyclic loads. To achieve this, they combined a Simulated Annealing optimisation algorithm with detailed nonlinear finite element analyses.

The fact that the production process of CFS members is relatively straightforward and versatile offers great scope for the development of new, innovative and optimised cross-sections. A novel framework is therefore proposed in this paper to optimise CFS sections with respect to their energy dissipation capacity under monotonic loading. The relative dimensions of the cross-sections, the location and the number of intermediate stiffeners and the inclination of the lip stiffeners were thereby considered as the main design variables. To obtain the global optimum solution a Particle Swarm Optimisation (PSO) algorithm was combined with the general purpose finite element program ABAQUS v6.14 (2014), which was used to carry out geometric and material non-linear analyses including the effects of initial imperfections (GMNIA).

A.3. SCOPE AND RANGE OF PROTOTYPE SECTIONS

In the design of hot-rolled steel members for high seismic regions, the width-to-thickness ratios of compressive elements are limited by codes of practice (AISC 341-16 2016, EN1998-1 2005) to allow for the development of sufficient plastic deformations. As expected, CFS members generally do not satisfy these limits. However, unlike hot-rolled steel members, intermediate stiffeners and lips can be rolled into CFS members to suppress cross-sectional instabilities (Fig. A.1). Adding a lip stiffener is a very effective way to stabilize the top flange of cross-sections subjected to bending (Fig. A.1(a)), while an additional intermediate stiffener in the flange (Fig. A.1(b)) is useful for wide flanges. For slender webs with high width-to-thickness ratios local buckling may be initiated in the web and an intermediate web stiffener may therefore increase the flexural performance (Fig. A.1(c)).

(a)　　　　(b)　　　　(c)　　　　(d)
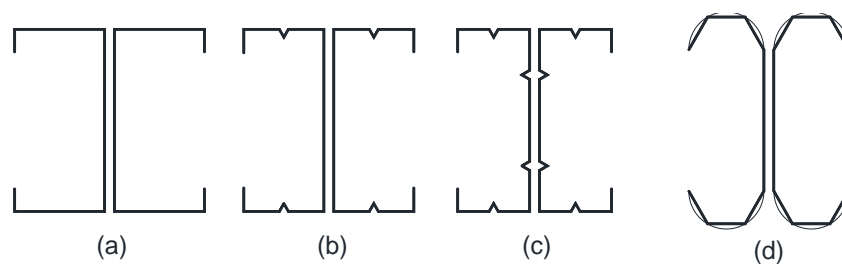
Fig. A.1. Cross-section prototypes

In addition to sections (a)-(c) in Fig. A.1, the 'folded flange' section pictured in Fig. A.1(d) was also considered as a prototype in the proposed optimisation procedure. This cross-section was previously developed and studied by Ye et al. (2016b) and originated from a practical approximation of a curved flange section. The study provided additional design guidance to determine the bending capacity of this section to EN1993-1-3 (2005), accounting for the possible occurrence of multiple distortional buckling modes. Furthermore, the paper reports on an optimisation study where the Particle Swarm Optimisation (PSO) algorithm was employed to maximise the flexural strength of various prototypes, including the sections shown in Fig. A.1(a)-(c), as well as the folded flange section. The results showed that, for the same amount of material, the folded flange section provided a bending capacity which was up to 57% higher than other optimised shapes, as illustrated in Fig. A.2. Consequently, it is an obvious candidate to be considered in the current optimisation study.
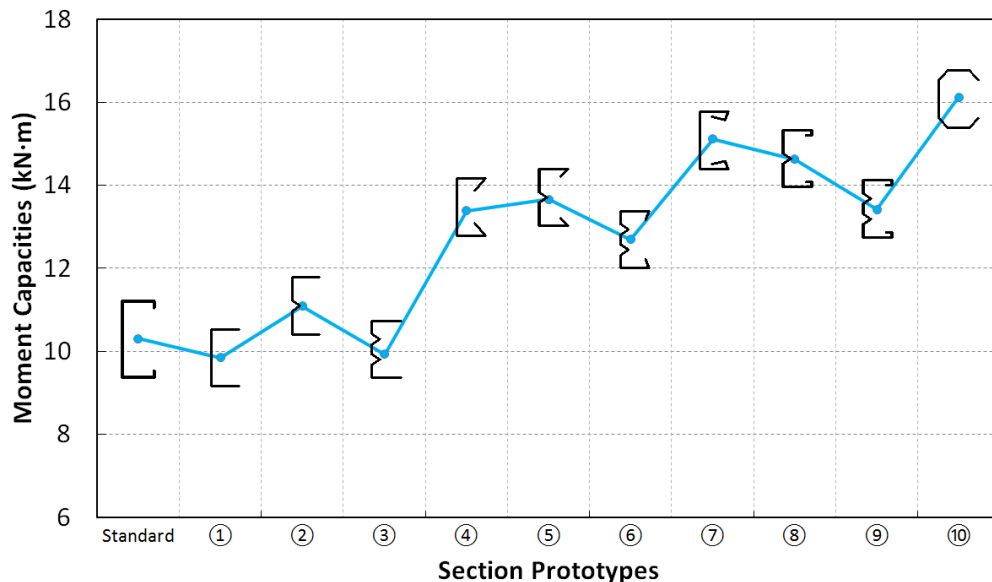
Fig. A.2. Comparison of the flexural capacities of optimum CFS prototypes (Ye et al. 2016b)

A.4.   FE ANALYSES OF CFS BEAMS

Previous research studies have shown that finite element (FE) models can be used to accurately predict the load carrying capacity and post-buckling behaviour of CFS sections, provided that the appropriate element type, material parameters and imperfection profiles are selected (Haidarali and Nethercot 2011, Yu and Schafer 2007, Becque and Rasmussen 2009a 2009b). In this paper, the general purpose FE package ABAQUS v6.14 (2014) was used, after validation, to predict the deformation behaviour of the prototype beams and to search for the optimum cross-sectional shapes which maximize the energy dissipation.

A.4.1.   FE Model and Validation

The modelling techniques used in the FE models were first verified against a series of tests on CFS back-to-back channels described by Ye (2016). Six specimens were tested in four-point bending and failed by interaction of local and distortional buckling in the constant moment region. The specimens were laterally supported near the loading points to prevent global instability due to lateral-torsional buckling. The test set-up is schematically shown in Fig. A.3. All specimens had a span length of 3100 mm, while the constant moment span was 1200 mm long. Three different cross-sections were considered (Fig. A.4) and two specimens of each cross-section were tested. The wall thickness of all specimens was 1.5 mm. The channels were connected above the end supports and under the loading points by M12 bolts, but the constant moment span did not feature any connectors. The material properties and the specimen imperfections were accurately measured and details of the measuring procedure, as well as full results, can be found in Ye (2016). The average measured yield stress was 422 MPa.
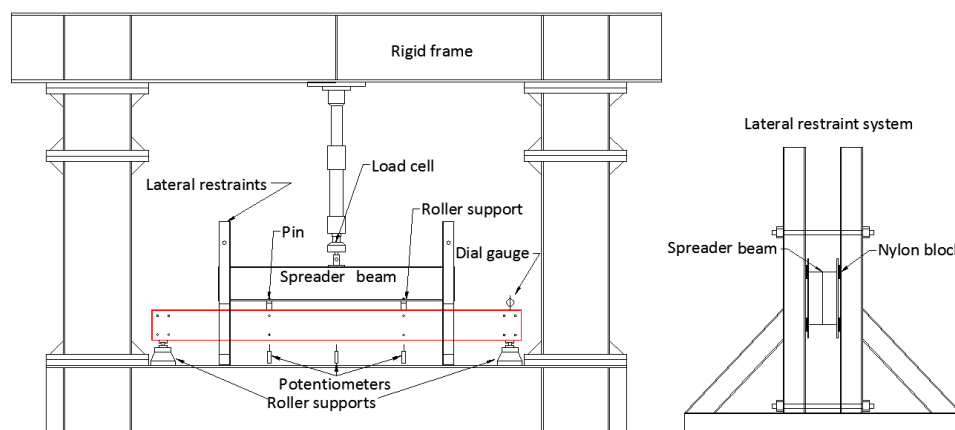
Fig. A.3. Test set-up (Ye, 2016)
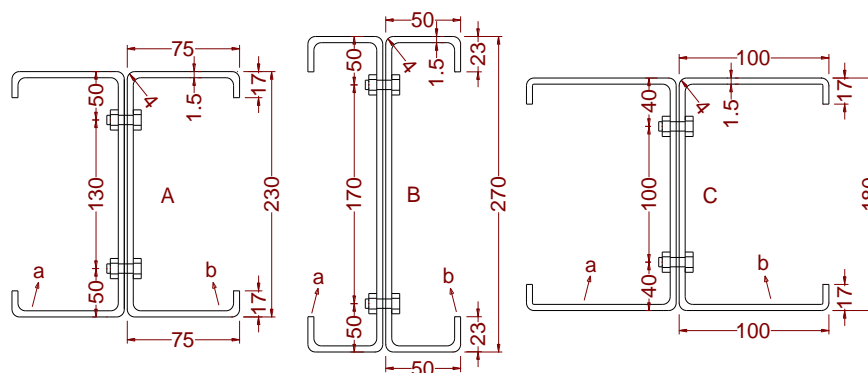
Fig. A.4. Cross-sectional dimensions (Ye, 2016)
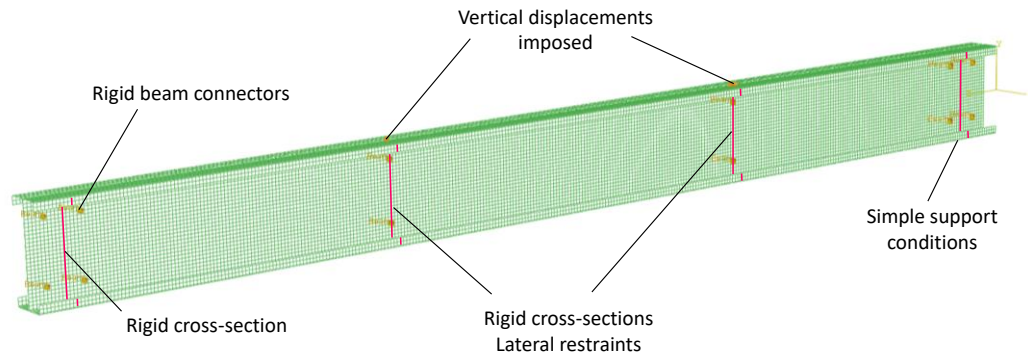
Fig. A.5. FE model
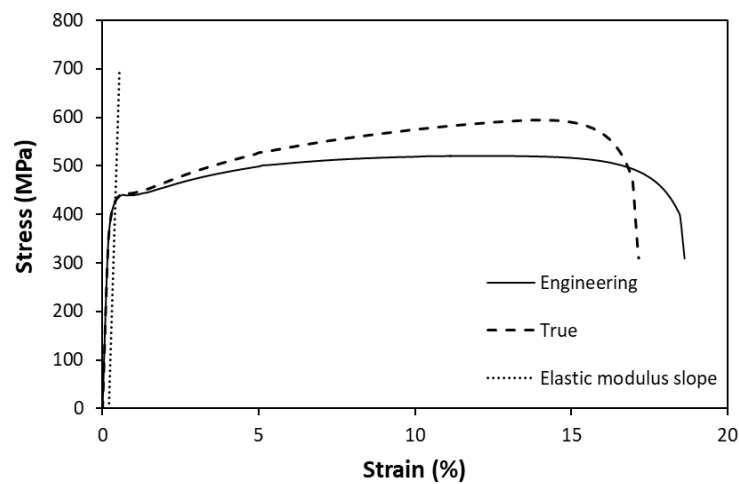
Fig. A.6. Material stress-strain curve

The FE models of the CFS beams were developed using 8-node quadrilateral shear-flexible shell elements with reduced integration and five nodal degrees of freedom (S8R5). Fig. A.5 illustrates the features of the FE model. Rigid cross-sections were defined over the end supports and under the loading points to simulate the wooden blocking used in the test to prevent localized failure by web crippling. The out-of-plane deformations of the beam were restrained at the supports and at the loading points. Surface-to-surface contact was modelled between the webs of the channels. The bolts were modelled using rigid BEAM connector elements. The measured imperfection profile was transferred into the model by adjusting the initial nodal coordinates. The material was modelled using the measured stress-strain curve, converted from engineering stress and strain to true stress and strain, as shown in Fig. A.6. The measured material properties were: elastic modulus E = 200 GPa, yield stress fy = 427

MPa and tensile strength fu = 593 MPa. A geometrically non-linear 'static general' analysis was carried out.

Residual stresses and the effects of work hardening as a result of the rolling process were not included in the model, based on the observation that they have to some extent opposite effects and based on the recommendation by Schafer et al. (2010) that both phenomena are not independent and that they should therefore either be modelled together or ignored together. Moreover, all sections considered in the study were open sections, in which residual stresses are typically limited.

A mesh sensitivity study was performed using the 180 mm deep specimen indicated in Ye (2016) as C180-1. Four different meshes were considered, containing square elements with 40 mm, 30 mm, 20 mm and 10 mm sides. The results are presented in Fig. A.7 in the form of mid-span moment vs. deflection diagrams. The experimentally obtained curve is also shown. It is seen that a mesh refinement to at least 20×20 mm^2 elements is required in order to obtain a good correspondence with the experiment in terms of peak load and overall behaviour.
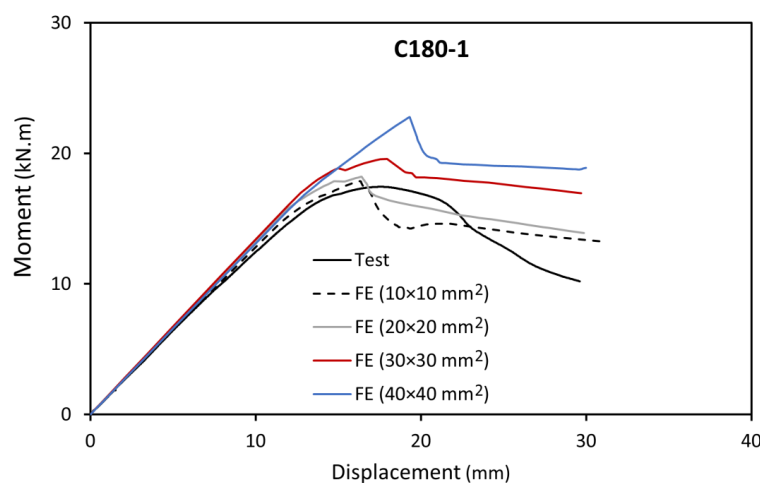
Fig. A.7. Results of FE mesh sensitivity study

FE models of all six specimens were constructed and their predictions are compared to the experimentally recorded behaviour in Fig. A.8. The specimen labels refer to the cross-section type (A, B or C, with reference to Fig. A.4), the cross-section depth (in mm) and the test number (twin specimens were tested).
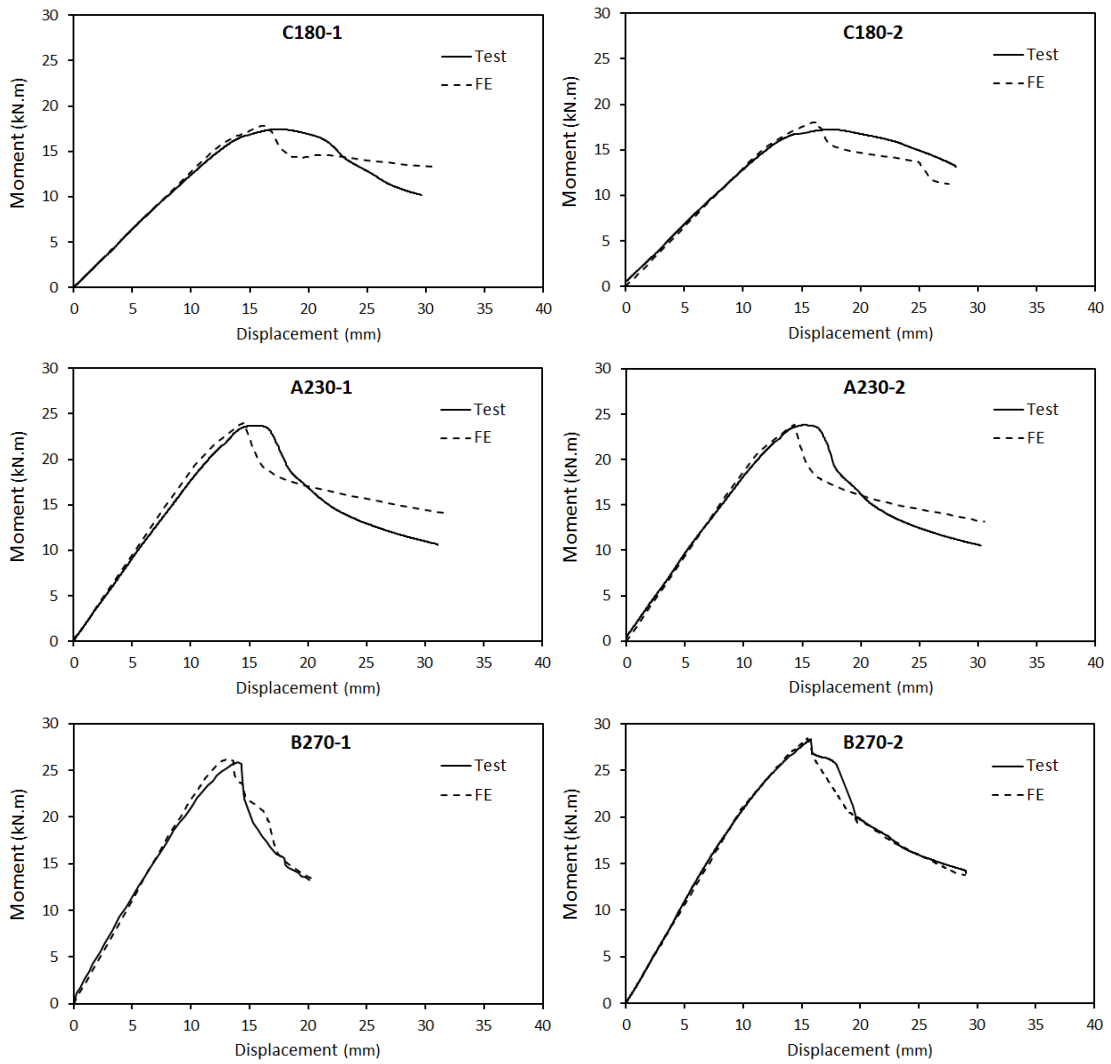
Fig. A.8. Comparison of FE results with experimental behaviour

Table A.1. Comparison of FE predicted and experimentally recorded peak moment

Specimen	*Moment capacity*		*Ratio*
	(kN.m)		
	Test	*FE*	*FE/Test*
C180-1	17.43	17.86	1.024
C180-2	17.24	18.02	1.045
C230-1	23.72	23.97	1.010
C230-2	23.79	23.87	1.003
C270-1	25.83	26.17	1.013
C270-2	28.34	28.47	1.005
		Average	1.017
		Standard Dev.	0.016

Table A.1 compares the FE predicted moment capacity to the experimentally obtained results. It is seen that very good agreement was achieved: the average ratio of the predicted to the measured moment capacity was 1.017 with a standard deviation of less than 2%. However, given that the aim of this paper is to optimise CFS structural members with respect to their energy dissipation capacity, the ability of the FE models to capture the post-peak behaviour with sufficient accuracy is also of primordial importance. This presents a significant challenge because CFS members quite often display interaction between various buckling modes. In the experimental programme here used for validation this pertains to local-distortional interaction. Buckling interaction typically results in a highly unstable post-peak behaviour which displays very high imperfection sensitivity (van der Neut 1969, Becque 2014). This is also observable in Fig. A.8, where twin specimens (e.g. C180-1 and C180-2) display a somewhat different post-peak behaviour as a result of the difference in initial imperfections (although the overall trend is similar). Nevertheless, it is seen from Fig. A.8 that the FE models predict the overall post-peak behaviour of the test specimens with reasonable accuracy. In the case of the 270 mm deep channels (B270-1 and B270-2) the agreement is excellent with the predicted load-displacement curve following the experimental curve very closely. The area under the curve, which can be deemed an approximate proportional measure of the dissipated energy, is also well represented by the FE models, with an average difference with the experiment over the six specimens of 3% and a maximum difference of 9% (A230-1). For the purpose of the optimisation process comparative behaviour is important, e.g. the fact that the 270 mm deep channels display a much steeper post-peak behaviour than the 180 mm deep channels, and in this context it can be concluded that the developed FE techniques provide a sufficiently accurate tool set.

A.4.2. Flexural Strength and Post-Buckling Behaviour of Prototypes

A preliminary numerical study was carried out using six different prototype cross-sections (Fig. A.9) with the aim of investigating the effect of different cross-section geometries (and in particular the effect of adding intermediate stiffeners) on the general buckling and post-peak behaviour of the section. Fig. A.9 shows the dimensions of the six CFS prototype beams, which include two conventional back-to-back lipped channel configurations (C1 and C2), one back-to-back lipped channel configuration with intermediate flange stiffeners (C3), one back-to-back lipped channel configuration with both intermediate web and flange stiffeners (C4), one back-to-back configuration with curved flanges (C5) and one back-to-back configuration with folded flanges (C6).

To allow some measure of comparison, all cross-sections used the same amount of material (i.e. they had the same thickness of 3 mm and total developed length of 450 mm) and they all had a 200 mm deep web (with the exception of cross-section C2 which was meant to be compared to C1 to reveal the effect of increasing the web height and narrowing the flanges). All six cross-sections were modelled in back-to-back configurations, in part because this is the arrangement typically encountered in CFS moment-resisting frames, and in part to avoid torsion in the sections resulting from the load being applied eccentrically with respect to the shear centre. The webs of both sections were connected along discrete lines at the ends and at the mid-section of the beam using 'tie'-constraints (Fig. A.10).
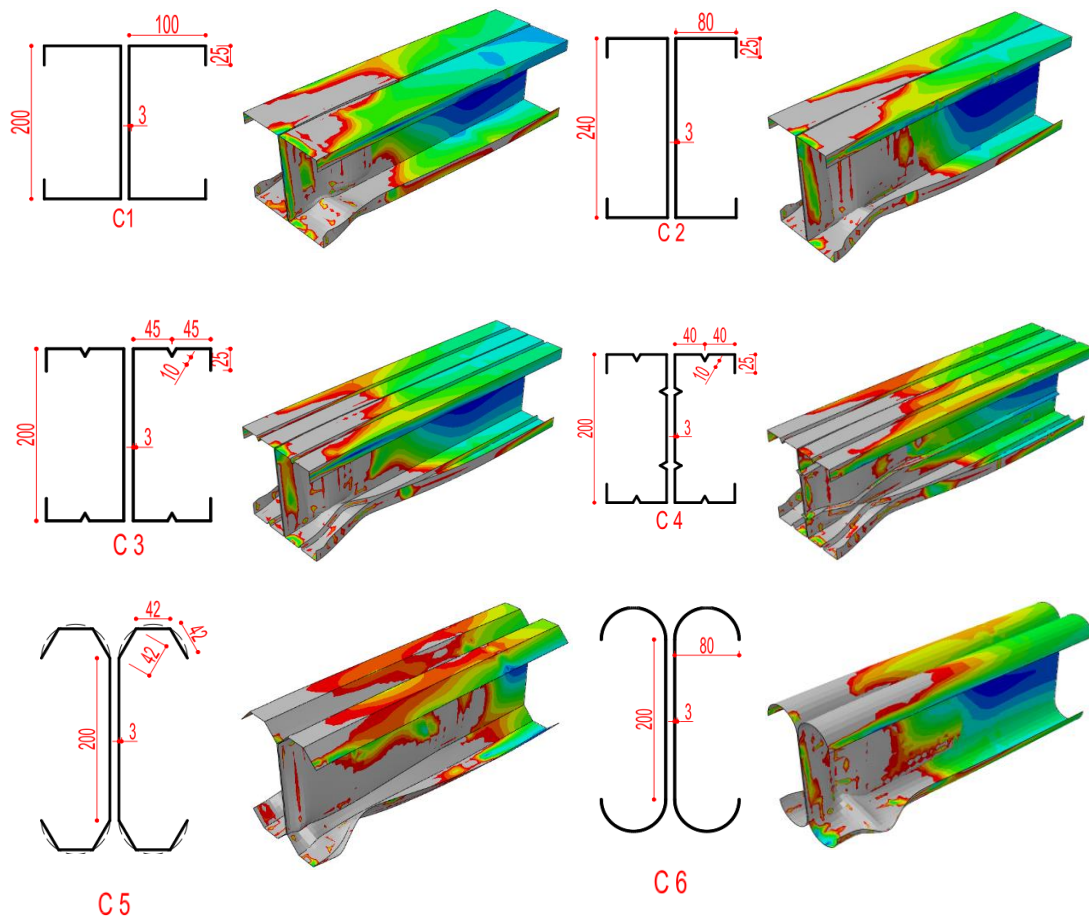
Fig. A.9. Cross-sectional shapes and their deformations at a drift angle of 0.04 rad (SMF limit)

A two meter long cantilever beam was modelled, as this was judged to be more representative of the portion of an actual member in a laterally loaded moment-resisting frame between the point of inflection and the beam-to-column connection than a four-point bending arrangement. The beam was laterally restrained to avoid lateral-torsional instability. Fig. A.10 illustrates the

details of the FE model, including the mesh, boundary conditions and lateral restraints. A $20{\times}20$ mm^2 mesh was used.
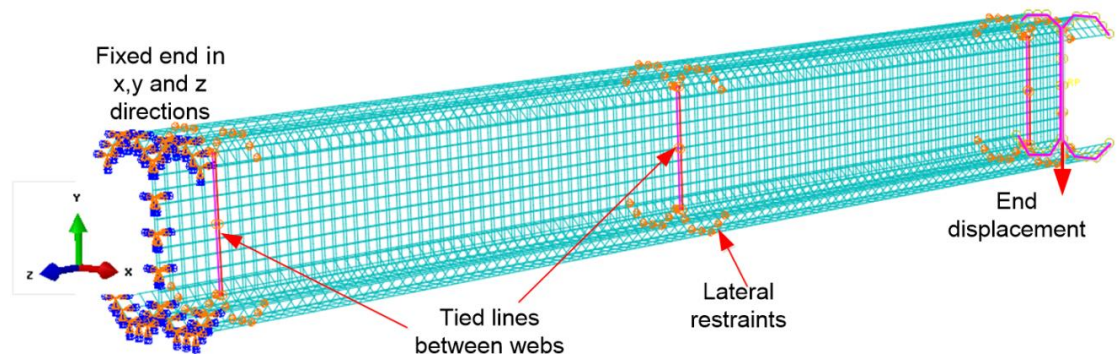
Fig. A.10. Mesh, boundary conditions and loading of the beam model

The measured material stress-strain curve shown in Fig. A.6 was used in the simulations.

Geometric imperfections were also included in the FE model, using the lowest eigenmode from a buckling (linear perturbation) analysis. The amplitudes of the local and distortional imperfections were taken from Schafer and Pekoz (1998) and were $0.34t$ and $0.94t$, respectively, where t is the wall thickness of the section. These are the 50% values in the cumulative distribution function of measured imperfection amplitudes.

The AISC Seismic Provisions (2016) make a distinction between Intermediate Moment Frames (IMF) and Special Moment Frames (SMF), in part depending on whether they can sustain at least 80% of their peak load carrying capacity at inter-storey drift angles of 0.02 and 0.04 rad, respectively. To determine whether the CFS beam sections under consideration could potentially qualify for either designation, GMNIA modelling was carried out where a vertical displacement of 150 mm (equivalent to a drift angle of 0.075 rad) was imposed at the tip of the cantilever beam (see Fig. A.10). Fig. A.9 shows the deformations of all six CFS beams at a drift angle of 0.04, while Fig. A.11 shows the moment-rotation curves of the beams. It is seen that there is a sudden loss in flexural capacity for the lipped channel C1 well before a rotation of 0.02 rad is achieved due to distortional buckling of the flanges, followed by local buckling. By reducing the width of the flanges and increasing the height of the section in C2, the flexural strength was improved by 25%. However, this did not substantially improve the general post-buckling behaviour of the section. Fig. A.11 also shows that the CFS section with an intermediate stiffener in the flanges (C3) had a slightly higher flexural capacity (by about 10%) compared to the corresponding section without stiffeners (C1), but exhibited considerably less post-buckling strength degradation. A comparison of sections C3 and C4 shows that adding intermediate web stiffeners further improved the post-buckling behaviour

of the CFS section, while it had a negligible effect on the flexural strength. The results also demonstrate that, for the same amount of material (i.e. the same thickness and coil width), the curved flange and folded flange sections provided the highest flexural capacity compared to other sections, confirming the results of Ye et al. (2016b).
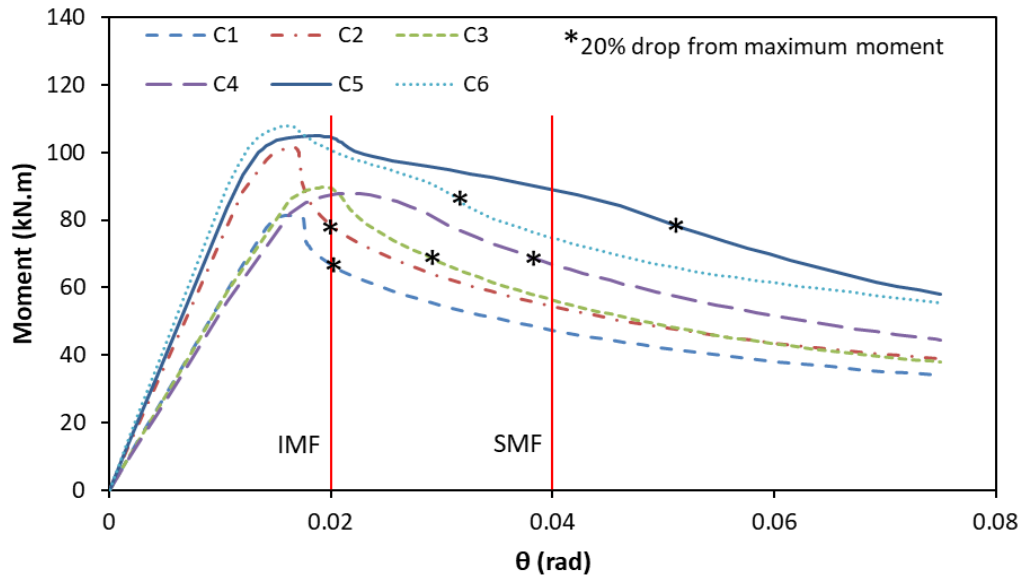
Fig. A.11. Moment-rotation curves of beams with dimensions shown in Fig. A.9

It can be concluded from Fig. A.11 that, while sections C1 and C2 satisfied the drift requirement of an IMF, they did not satisfy the SMF drift limits. When adding intermediate stiffeners in the flange, section C3 still did not satisfy the SMF drift requirement due to premature buckling of the web. However, when using intermediate stiffeners in both the flanges and webs (C4), the CFS section came close to satisfying the SMF inter-storey drift angle requirement. Only the folded flange section (C5) was able to reach a rotation in excess of 0.04 rad without any significant drop in strength. The curved flange section (C6) did not meet the SMF requirement, although its overall moment-rotation behaviour, in qualitative terms, was close to that of C5.

A.4.3.   Cross-Section Ductility

In accordance with ASTM E2126-09 (2009), the ductility of the six selected sections was evaluated using the equivalent energy elastic-plastic (EEEP) bi-linear model, as shown in Fig. A.12. This model idealizes the moment-rotation behaviour of the cross-section into an elastic-perfectly plastic response. The idealized bi-linear curve is obtained by equating the areas A1 and A2 included between the idealized and the actual curves and located below and above the actual curve, respectively. The elastic part of the EEEP curve is defined using an initial secant

stiffness (K_e) determined by the moment equal to 40% of the idealised yield moment of the cross-section. The ultimate rotation θ_u is then determined by the point on the softening branch of the actual curve corresponding to a 20% drop in moment carrying capacity relative to the peak moment.
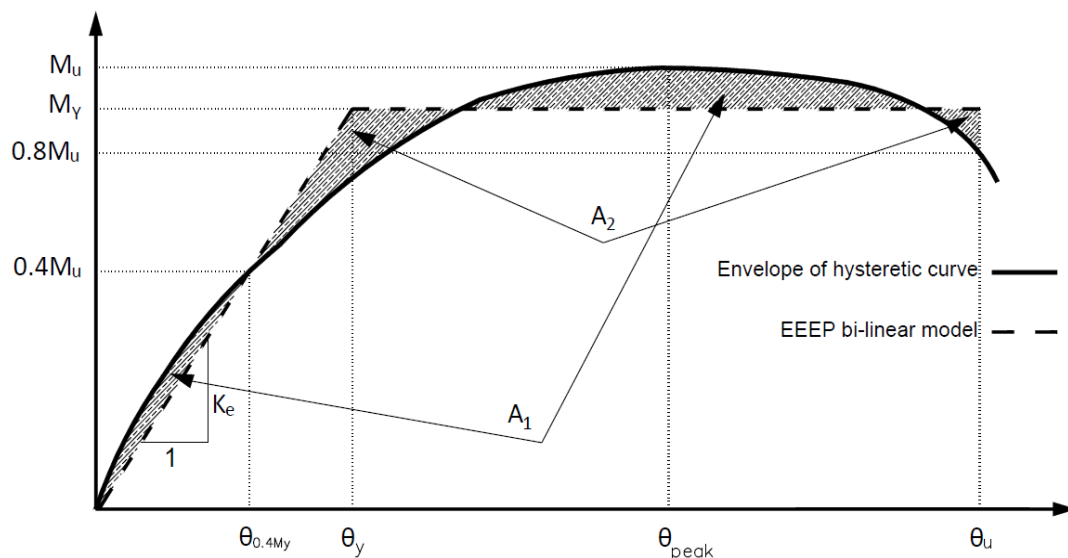
Fig. A.12. Equivalent energy elastic-plastic (EEEP) bi-linear model

To investigate the effect of the cross-sectional shape on the ductility of CFS beams, the bi-linear moment-rotation curves were used to calculate the ductility of the CFS sections using the following equation:

$$\mu = \frac{\theta_u}{\theta_y} \tag{A.1}$$

where θ_y is the yield rotation in the equivalent bi-linear diagram, as shown in Fig. A.12. The ductility of the six selected beam sections (with the specifications shown in Fig. A.9) is compared in Fig. A.13. The results indicate that, in this case, adding intermediate stiffeners in the flange (C3) increased the ductility of the CFS beam sections by 18% compared to the standard section (C1). By comparison, using intermediate stiffeners in both the web and the flanges (C4) increased the ductility by 51% relative to C1. It can also be seen that, for the same amount of material, the folded flange (C5) and curved flange (C6) sections exhibited much better ductility than the standard channel sections. It should also be noted that the folded flange section C5 offers a more practical solution from the manufacturing and construction point of view than C6. In particular, it is much easier to connect steel decking to the flat flanges of C5 than to the curved flanges of C6.
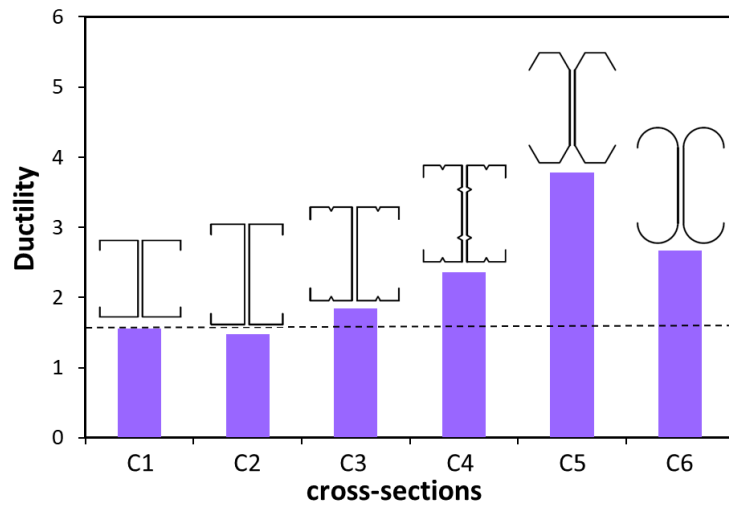
Fig. A.13. Ductility of CFS beams with dimensions shown in Fig. A.9

A.4.4.   Energy Dissipation Capacity

The total energy dissipation through plastic deformations can be obtained from the ABAQUS output and is based on the following equation:

$$E = \int_V \int_0^t \sigma_{ij}(\tau)\dot{\varepsilon}_{ij}^p(\tau)d\tau dV$$

(A.2)

where V is the total volume of the beam, t is the duration of loading, σ_{ij} are the components of the stress tensor and $\dot{\varepsilon}_{ij}^p$ are the incremental plastic strains. Fig. A.14 presents the dissipated energy calculated according to Equation A.2 at a drift ratio of 4% (i.e. the SMF limit) for all six CFS prototypes.
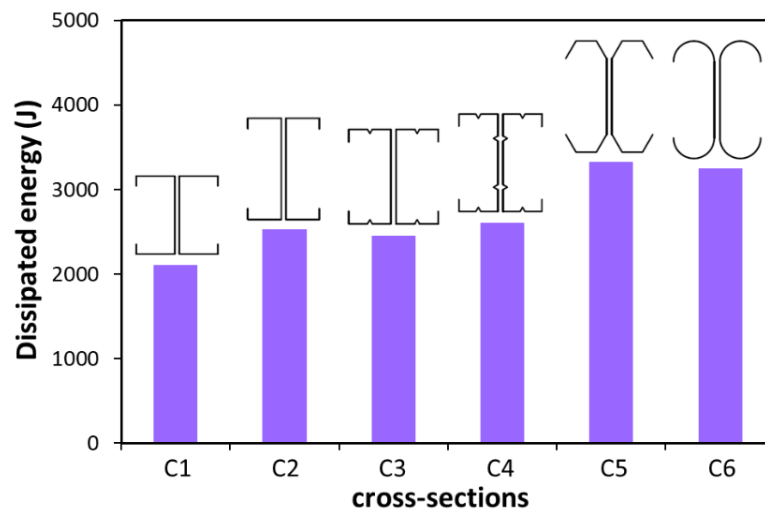
Fig. A.14. Comparison of dissipated energies for cross-sections shown in Fig. A.9

Fig. A.14 indicates that the deeper sections are able to dissipate considerably more energy (due to their higher moment capacity), while the addition of flange and/or web stiffeners in the 200 mm deep sections also has a beneficial effect on the energy dissipation capacity (mainly due to their beneficial influence on the post-peak behaviour). The curved and folded flange sections were able to dissipate the most energy.

A.5.   PROPOSED OPTIMISATION FRAMEWORK

The optimisation procedure aimed to develop cross-sectional shapes for CFS beams which, for a constant developed length (coil width) and given thickness, maximize the energy dissipation capacity. A commercially available lipped channel section, shown in Fig. A.15, was taken as the starting point, with the optimisation process allowing for the addition of inclined lips and rolled-in intermediate stiffeners in the flanges and the web to form more complex cross-sections. The position of the web stiffeners was also made variable in the optimisation process. In addition, the folded flange prototype was considered, based on its favourable performance in Section A.4, showing that it has the potential to dissipate high levels of energy. In the optimisation process the energy dissipation capacity was determined based on the results from detailed GMNIA FE models.
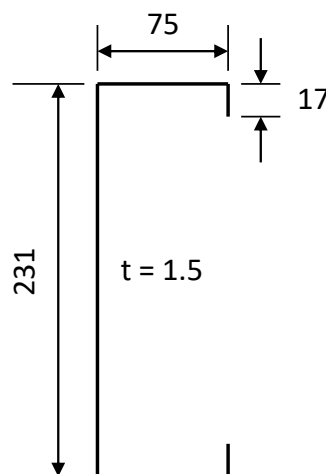
Fig. A.15. Dimensions (in mm) of commercial CFS channel

A.5.1.   Problem Formulation

Given that the optimisation work presented in this paper required several tens of thousands of FE analyses, the cantilever model in Fig. A.10 was further simplified. The cantilever length was reduced to 1400 mm and a single channel was modelled. The cantilever was still loaded by applying a vertical displacement to the end section, while twisting of the end section was

also restrained (Fig. A.10). As previously explained, the cantilever setup was devised to be representative of the portion of a beam between the connection and the point of inflection in a typical moment-resisting frame. The mesh size was maintained at 20×20 mm^2. Eight-noded shell elements with reduced integration and five nodal degrees of freedom (S8R5) were again used.

Five different prototype sections, listed in Table A.2, were considered and independently optimised. The same amount of material as used in the 'standard' commercial channel was used for all cross-sections (i.e. the same total developed plate width L=415 mm and the same thickness t=1.5 mm). The independent design variables are listed in Table A.2 and consisted of cross-sectional dimensions, stiffener locations and the angles included between various plate segments. The intermediate stiffeners were always comprised of two 10 mm legs with an intersecting angle of 60°. It is noted that, for each prototype in Table A.2, one of the independent variables has already been eliminated by using the constraint of a constant developed length. All cross-sections were required to meet the dimensional restrictions determining the range of validity of the EN1993-1-3 specifications. These restrictions, also listed in Table A.2, pertain to plate slenderness limits as well as limit values on the relative dimensions of the cross-section and were included as constraints on the optimisation problem. These restrictions were imposed in order to obtain cross-section which can be validly designed using EC3. They are not considered very stringent and in most cases were not critical to the optimisation process. However, an important practical constraint was also imposed on all cross-sections: in order to allow the section to support the roof or floor diaphragm above and be screw-connected to it, a minimum flat flange width (indicated by the symbol 'b' for prototypes 1-4 and 'c' for prototype 5) of 50 mm was specified. This value was obtained after consultation with the industrial partner on the project. For the purpose of manufacturing the section, the lip stiffener also needed to have a minimum length, since a very short lip cannot be rolled or brake-pressed. For prototypes 1-4 the EC3 requirement that $c/b \geq 0.2$ (EN1993-1-3 Clause 5.2), combined with a minimum flange width of 50 mm, automatically resulted in a minimum lip length of 10 mm, which is acceptable as an absolute minimum. For prototype 5, however, the requirement of a minimum lip length ($d \geq 15$ mm) needed to be explicitly enforced. Finally, a maximum length $b \leq 50$ mm was imposed on prototype 5 in order to leave enough flat web width to accommodate a bolted or screwed connection at the member ends.

After optimising the cross-sections for a thickness of 1.5 mm, two additional optimisation studies were carried out, where the wall thickness of the channel was increased to 3 mm and 5 mm, respectively, in order to be able to draw conclusions over a wider range of wall slenderness values.

The measured material stress-strain curve shown in Fig. A.6 was used in the optimisation process. The corresponding yield stress f_y, elastic modulus E and Poisson's ratio υ were 427 MPa, 200 GPa and 0.3, respectively.

The optimisation procedure aimed to optimise each CFS cross-section prototype with respect to its energy dissipation $E(X)$ over the load history up to a drift ratio of 4%. This is the rotation capacity required for Special Moment Frames (SMF) according to AISC Seismic Provisions (2016) and allows a consistent comparison.
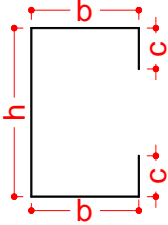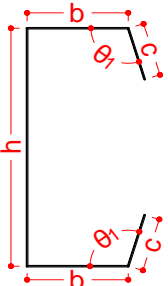
The optimisation problem was formulated mathematically as follows:

$$\text{Max} \qquad E\left(X\right) \tag{A.3}$$

$$x^L \leq x_i \leq x^U, \qquad (i = 1, \cdots, n) \tag{A.4}$$

where X denotes the vector containing the independent cross-sectional variables X_i listed in Table A.2. X^U and X^L indicate the upper and lower bounds, respectively, of the design variables which are subject to constraints.

Table A.2. Selected prototypes, design variables and constraints

Prototype	Prototype section	Design variables	Constraints	Comment
①		$X_1 = c/b$ $X_2 = b/L$	$0.2 \leq c/b \leq 0.6$ $b/t \leq 60$ $c/t \leq 50$ $h/t \leq 500$ $b \geq 50$	EN1993-1-3, Clause 5.2 Practical
②		$X_1 = c/b$ $X_2 = b/L$ $X_3 = \theta_1$	$0.2 \leq c/b \leq 0.6$ $b/t \leq 60$ $c/t \leq 50$ $h/t \leq 500$ $\pi/4 \leq \theta_1 \leq 3/4\pi$ $b \geq 50$	EN1993-1-3, Clause 5.2 Practical

③	$X_1=c/b$	$0.2 \leq c/b \leq 0.6$	EN1993-1-3, Clause 5.2
	$X_2=b/L$	$b/t \leq 60$	Practical
	$X_3= \theta_1$	$c/t \leq 50$	
		$h/t \leq 500$	
		$\pi/4 \leq \theta_1 \leq 3/4\pi$	
		$b \geq 50$	

④	$X_1=c/b$	$0.2 \leq c/b \leq 0.6$	EN1993-1-3, Clause 5.2
	$X_2=b/L$	$b/t \leq 60$	Practical
	$X_3=R$	$c/t \leq 50$	Practical
	$X_4= \theta_1$	$h/t \leq 500$	
		$\pi/4 \leq \theta_1 \leq 3/4\pi$	
		$0.1 \leq R \leq 0.4$	
		$b \geq 50$	

⑤	$X_1= \theta_1$	$h/t \leq 500$	EN1993-1-3
	$X_2= \theta_2$	$7/12\pi \leq \theta_1 \leq 5/6\pi$	Practical
	$X_3=b$	$\pi/4 \leq \theta_2 \leq 3/4\pi$	Practical
	$X_4=c$	$b \leq 50;$	Practical
	$X_5=d$	$d \geq 15$	
		$c \geq 50$	

A.5.1.   Optimisation Techniques

The optimisation framework made use of the Particle Swarm Optimisation (PSO) method. This global optimisation algorithm is population-based and does not need any gradient information, which makes it suitable for solving complex problems with high non-linearity. PSO generally possesses better computational efficiency in terms of both speed and memory requirements compared to conventional Genetic Algorithm (GA) techniques (Hassan et al. 2005, Jeong et al. 2009).

PSO is inspired by the swarming behaviour of biological populations such as flocks of birds or schools of fish. An initial population of solutions is randomly selected and the solutions are then optimised by updating subsequent generations, but unlike GA this is done without using any evolution operators such as crossover or mutation. The potential solutions in PSO, called particles, move in the problem space by following the current optimum particles to search for the global optimal solution. A swarm is thus comprised of N particles moving around a D-dimensional search space. The position and velocity vectors of the ith particle are $\rho_i=(\rho_{i1},\rho_{i2},...,\rho_{ij},...,\rho_{iD})$ and $V_i=(v_{i1},v_{i2},...,v_{ij},...,v_{iD})$, respectively, where $i=1,2,3,...N$. In each

iteration, the ith particle updates its position and velocity based on a combination of its personal best position over its history and the position of the particle within the swarm with the best position in the previous iteration. This can mathematically be described as:

$$V_i^{k+1} = w \cdot V_i^k + c_1 \cdot r_1 \cdot \left(P_{best,i}^k - \rho_i^k\right) / \Delta t + c_2 \cdot r_2 \cdot \left(G_{best}^k - \rho_i^k\right) / \Delta t \qquad (A.5)$$

$$\rho_i^{k+1} = \rho_i^k + V_i^{k+1} \cdot \Delta t \qquad (A.6)$$

where the subscripts i and k denote the particle and the iteration number, respectively, and Δt is the time increment. $P_{best,i}^k = (p_{i1}^k, p_{i2}^k, \dots, p_{iD}^k)$ represents the best position of the ith particle over its history up to iteration k, while $G_{best}^k = (g_1^k, g_2^k, \dots, g_D^k)$ indicates the position of the best particle in the swarm in iteration k. The cognitive parameter c_1 indicates the degree of confidence in the solution $P_{best,i}$ obtained from each individual particle. The parameter c_2 is a social parameter to reflect the confidence level that the swarm as a whole has reached a favourable position. In addition, the factors r_1 and r_2 are independent random numbers uniformly distributed between 0 and 1, adding a random search aspect to the algorithm. Finally, w is an inertial weight factor used to preserve part of the previous velocity of the particles, in order to improve the convergence of the optimisation process. PSO has the added advantage that the optimisation constraints (Equation A.4) can easily be accommodated by restricting the search space and defining appropriate boundaries.

The initial position and velocity of each particle were randomly generated to obtain a swarm which was initially distributed throughout the whole design space. Given a number of design variables $X_j=(j=1,\dots,D)$, each with a lower bound X_j^L and an upper bound X_j^U, the following equations were used to obtain the initial position and velocity vectors of the ith particle:

$$\rho_{ij}^0 = X_j^L + r_{ij}(X_j^U - X_j^L) \qquad (A.7)$$

$$V_{ij}^0 = s_{ij}(X_j^U - X_j^L) / \Delta t \qquad (A.8)$$

where r_{ij} and s_{ij} are matrices containing random numbers between 0 and 1.

If, during the search, the position ρ_i^{k+1} (Equation A.6) of a particle ends up outside the design domain defined by X^L and X^U, the particle is placed back on the boundary by equating the component of the position vector violating the constraint to the upper or lower bound ($\rho_{ij}^{k+1} = X_j^L$ or $\rho_{ij}^{k+1} = X_j^U$).

Fig. A.16 illustrates the flowchart of the proposed optimisation method, which had to overcome the difficulty of linking the detailed FE simulations in (ABAQUS-v6.14 2014) to the PSO algorithm in Matlab (2011). In each iteration the PSO algorithm generated new input data, i.e. new position vectors ρ_i containing values of the basic variables which determine the cross-sectional geometry (as listed in Table A.2). This data was then transmitted to the ABAQUS pre-processing module to create the cantilever beam model. The entire FE analysis was controlled using a Python script which consisted of the following steps:

(1) The FE model of a 1400 mm long cantilever beam was generated using the cross-sectional dimensions generated by the PSO algorithm. The material stress-strain curve shown in Fig. A.6 was used. Boundary conditions as previously described in Section A.4.2 and illustrated in Fig. A.10 were applied to the FE model and a vertical displacement was imposed at the cantilever tip.

(2) A linear elastic buckling analysis was conducted in ABAQUS. The normalized nodal displacements of the most critical buckling mode were extracted and used as the shape of the initial geometric imperfection. This shape was then scaled to obtain an imperfection amplitude of 0.94 times the thickness of the cross-section, which is the 50% cumulative distribution value for the distortional imperfection as measured by Schafer and Pekoz (1998). In order to automate the optimisation process this amplitude was chosen irrespective of whether the local mode or the distortional mode was critical, in the knowledge that this value might be slightly conservative for the local mode.

(3) The Standard solver of ABAQUS was used to carry out a GMNIA FE analysis for each PSO particle. The dissipated energy $E(X)$ of each particle was then extracted from the ABAQUS output files using its post-processing module.

(4) The data extracted in the previous step were returned to the PSO algorithm and a new particle swarm was generated based on Equations A.5 and A.6. Subsequently, a new iteration was started from step 1 above.

The number of iterations was taken as 100 for all prototype sections. To obtain good convergence the population of the swarm was set to 10 particles for prototypes ① to ③ and 15 particles for prototypes ④ and ⑤, to accommodate the fact that these latter prototypes contained more design variables. The maximum and minimum inertial weight factors were chosen as 0.95 and 0.4, respectively. Larger values of the weight factor were used in the initial stages of the optimisation, as this promotes global searching over a large area of the parameter domain. Conversely, a small value of the weight factor tends to localize the search pattern, a

technique which can be used to accelerate the convergence in the later stages. The weight factor was varied linearly over the iterations between the above values. These choices for the PSO parameters were based on previous experience by the authors (Ye et al. 2016a) and on recommendations by Perez and Behdinan (2007). Fig. A.17 shows a typical convergence diagram and illustrates that there was no obvious increase of the objective value (i.e. the energy dissipation capacity) after about 60 iterations. This confirms that the number of iterations used in this study was adequate. Due to the substantial computational effort required, the non-linear FE analyses were conducted on the High-Performance Computing system Iceberg at the University of Sheffield.
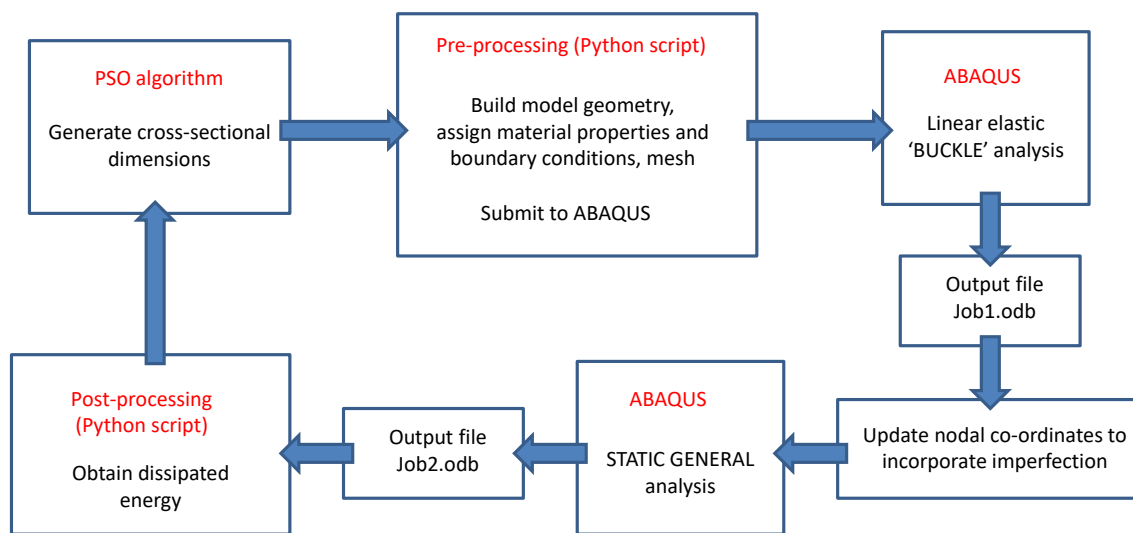
Fig. A.16. Flowchart of the proposed optimisation framework for maximum dissipated energy
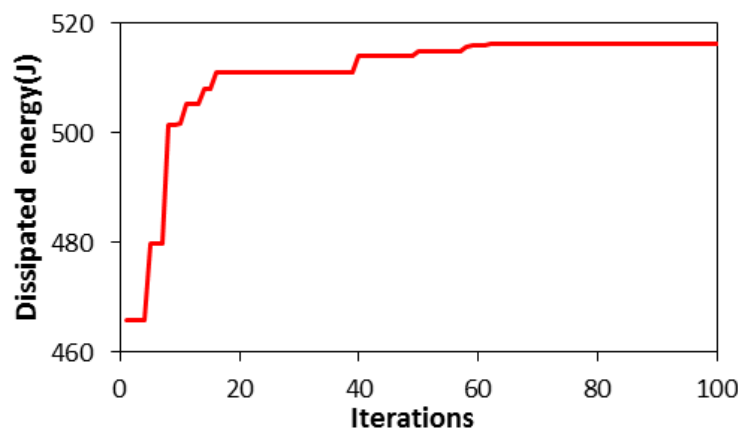
Fig. A.17. Typical iteration history

A.6. OPTIMISATION RESULTS AND DISCUSSIONS

Table A.3 summarizes the dimensions of the cross-sectional shapes obtained from the optimisation process (with reference to Table A.2 for the symbols used) and compares them with the standard lipped channel section with the same amount of material taken as a starting point.

Table A.3. Dimensions, energy dissipation and moment capacity of optimum CFS cross-sections of different prototypes and thicknesses

Plate thickness (mm)	Prototypes	a (mm)	b (mm)	c (mm)	d (mm)	R	θ_1°	θ_2°	E (J)	M_{max} (kN.m)	$\dfrac{E}{E_{standard}}$	$\dfrac{M_{max}}{M_{max,standard}}$
1.5	Standard	231	75	17					329	16.6	1.00	1.00
	Type ①	255	50	30					407	18.3	1.24	1.10
	Type ②	255	50	30			82		413	18.3	1.26	1.10
	Type ③	249	50	18			89		441	18.6	1.34	1.12
	Type ④	205	50	25		0.2	45		512	19.4	1.56	1.17
	Type ⑤	183	41	50	25		126	135	508	20.1	1.55	1.21
3	Standard	231	75	17					963	45.0	1.00	1.00
	Type ①	255	50	30					1199	47.5	1.25	1.05
	Type ②	366	50	30			90		1199	47.5	1.25	1.05
	Type ③	265	50	10			92		1181	47.8	1.23	1.06
	Type ④	235	50	10		0.1	77		1199	45.2	1.24	1.00
	Type ⑤	189	48	50	15		105	135	1343	48.6	1.39	1.08
5	Standard	231	75	17					2189	78.6	1.00	1.00
	Type ①	276	50	20					2467	87.3	1.13	1.11
	Type ②	278	50	19			87		2474	87.0	1.13	1.11
	Type ③	265	50	10			78		2430	86.1	1.11	1.10
	Type ④	235	50	10		0.1	45		2237	79.8	1.02	1.02
	Type ⑤	169	48	60	15		105	135	2252	79.4	1.03	1.01

The resulting cross-sectional geometries are also graphically presented in Fig. A.18, while Fig. A.19 presents a comparison between the dissipated energies of the various optimised prototypes.
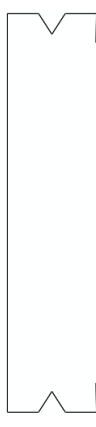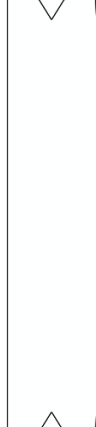
Thickness (mm)	Prototypes				
	①	②	③	④	⑤
1.5					
3					
5					

Fig. A.18. Optimised cross-sections (to scale)
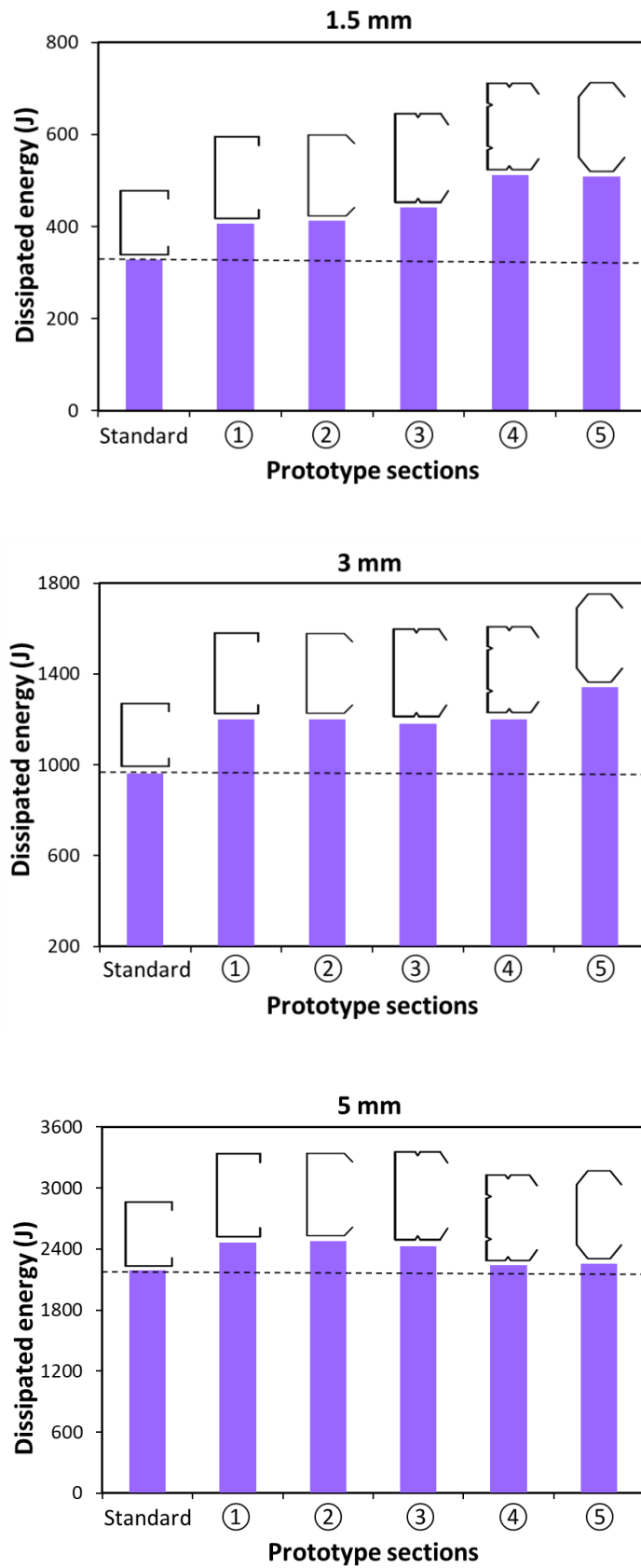
Fig. A.19. Maximum dissipated energy of prototypes at 4% drift ratio

A number of interesting observations can be made from Figs. A.18-19:

- By simply changing the relative dimensions of the standard commercial channel an optimised section could be obtained (prototype 1) with noticeably better energy dissipation characteristics. The gains for thicknesses of 1.5 mm, 3 mm and 5 mm were 24%, 25% and 13%, respectively. At the same time, the peak moment capacity was also improved by 5-11%.

- For all thicknesses, the lipped channel without any intermediate flange or web stiffeners strived to increase its energy dissipation capacity by increasing the depth of the web, while at the same time shortening the flange (note that the total developed length of the cross-section needed to remain constant). This has the combined effect of (1) increasing the peak moment, and (2) delaying the distortional buckling mode until larger deformations have taken place. For all thicknesses considered and over the range of prototypes 1-4, the flanges took on the minimum value of 50 mm, which was set as the minimum required width to allow for connections to the floor or roof diaphragm.

- Allowing the angle between the lip stiffener and the web to vary in prototype 2 did not result in a noticeable effect on either the ultimate moment capacity or the energy dissipation capacity of the optimised section. The optimum angles resulting from the process were all close to 90º.

- For a thickness of 1.5 mm, the addition of flange stiffeners or combined flange and web stiffeners significantly improved the energy dissipation capacity. Prototype 3 had an 8% higher energy dissipation capacity than prototype 1, while this number was 26% for prototype 4. The stiffeners are effective in suppressing cross-sectional instability, resulting in a slightly increased peak moment (as indicated in Table A.3). At the same time these cross-sections also exhibited an increased ductility (as indicated in Fig. A.13 and defined on the basis of a 20% drop in capacity), which is a direct result of the stiffeners delaying and mitigating the stiffness degradation due to buckling. It is noted that the stiffeners were accounted for in the total developed length of the cross-section and that, therefore, the depth of the optimised prototypes 3 and 4 is less than that of prototype 1. Nevertheless, prototype 3 has a 2% higher ultimate moment capacity than prototype 1, while this number is 6% for prototype 4.

- For a thickness of 3 mm, adding intermediate stiffeners to the section did not have a significant effect on the ultimate moment capacity of prototype 3 compared to

prototype 1, while it actually slightly reduced the ultimate moment capacity in prototype 4 (by 5%). This is a result of the reduction in section depth needed to accommodate the stiffeners, while the stiffeners become less effective as the width-to-thickness ratios of the web and flange are reduced. However, the stiffeners still played a beneficial role in the post-peak behaviour of the cross-section by mitigating the loss in stiffness due to buckling. Interestingly, the net result of these two opposing effects is zero and no significant loss or gain in energy dissipation was obtained by adding intermediate stiffeners.

- For a thickness of 5 mm, adding intermediate stiffeners to the section resulted in a slight reduction in energy dissipation capacity. Prototype 3 dissipated 1.5% less energy than prototype 1, while prototype 4 dissipated 9% less energy than prototype 1. This is mainly due to the fact that sacrificing some of the depth of the section in order to accommodate the stiffeners led to a slight reduction in peak moment capacity of 1.4% for prototype 3 and 9% for prototype 4. In this context it is noted that EN1993-1-1 (2005) classifies the optimised prototype 1 section with a thickness of 5 mm as a Class 2 cross-section. While this classification does not account for distortional instability, it provides an indication of the limited effectiveness of intermediate stiffeners in increasing the ultimate moment capacity.

- The folded flange section (prototype 5) in general performed well in terms of energy dissipation. For a thickness of 1.5 mm prototype 5 provided a slightly less efficient solution than the prototype with flange and web stiffeners (prototype 4). For a thickness of 3 mm it provided the overall optimum solution, as it combines a beneficial section depth with a defence against local and distortional buckling due to the segmental shape. For a thickness of 5 mm, however, prototype 5 did not dissipate as much energy as most of the other optimum prototypes, although the differences were marginal.

Fig. A.20 illustrates the deformed shapes of all optimum prototypes with thickness t = 1.5 mm at a drift ratio of 4% (i.e. the SMF limit). The von Mises stress distribution is also shown with grey areas indicating yielding. It is seen that the cross-sections all fail in either a predominantly local (prototypes 1 and 2) or predominantly distortional mode (prototypes 3, 4 and 5) and exhibit significant localized yielding near the fixed end support. The beam rotations therefore become localized in a hinge-like zone near the support.
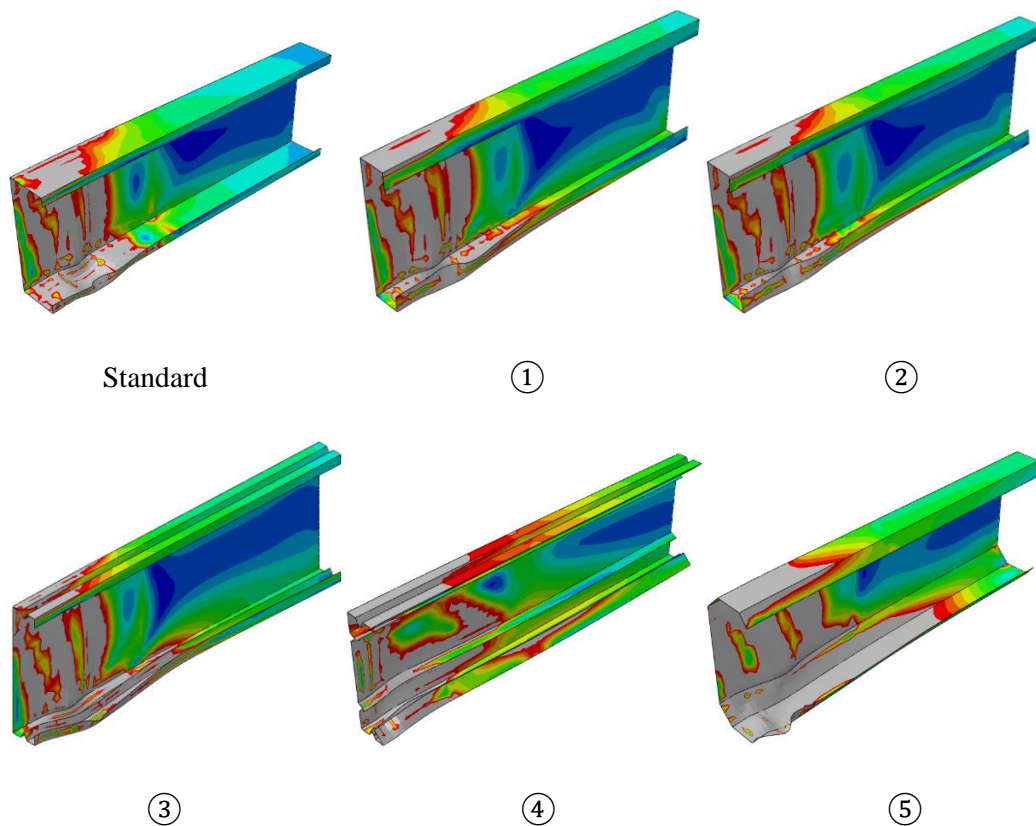
Fig. A.20. Deformed shape and distribution of von Mises stress at a drift ratio of 4% for t = 1.5 mm

A.7. SUMMARY

While Chapters 2 and 3 optimised the buckling strength of CFS elements determined according to Eurocode 3, this appendix presents a study to improve post-buckling behaviour of CFS beam elements which led to increase their ductility and energy dissipation capacity. These parameters are of the utmost importance in seismic applications, while comparatively no attention has been devoted to them in previous work.

An optimisation framework is presented which integrates a PSO algorithm with detailed GMNIA finite element analyses in order to develop CFS cross-sections with optimum energy dissipation characteristics. A number of practical construction and manufacturing constraints were also considered. Five different prototypes were considered in order to study the effect of adding intermediate flange and web stiffeners and allowing inclined lip stiffeners.

A.8.   CONCLUDING REMARKS

It was found that for the slender cross-sections with a thickness of 1.5 mm, corresponding to a web slenderness (i.e. width-to-thickness ratio) of 185 and a flange slenderness of 33, a substantial increase in energy dissipation (of up to 26%) could be obtained by adding intermediate web and flange stiffeners. This was a result of the stiffeners both increasing the ultimate capacity and mitigating the post-peak stiffness degradation. For web and flange slenderness values of 93 and 17, respectively, a turning point was reached where adding intermediate stiffeners slightly reduced the peak moment, while marginally improving the post-peak behaviour, resulting in no net gain in dissipated energy. For stockier sections, the addition of intermediate stiffeners is not expected to result in a more optimum solution. Instead, maximizing the depth of the cross-section and minimizing the flange width leads to better energy dissipation behaviour.

The 'folded flange' section performed well in the high-to-medium slenderness range, where it provided the overall optimum or slightly below-optimum solution.

APPENDIX B

Efficient Design of Cold-Formed Steel Bolted Moment Connections for Earthquake Resistant Frames

B.1. INTRODUCTION

Cold-formed steel (CFS) sections can be designed in many configurations and, compared to hot-rolled steel elements, can lead to more efficient and economic design solutions. While CFS moment-resisting frames can be used as an alternative to conventional CFS shear-wall systems to create more flexible space plans, their performance under strong earthquakes is questionable due to the inherited low local/distortional buckling of thin-walled CFS elements and limited ductility and energy dissipation capacity of typical CFS bolted moment connections. In Chapters 5 and 6, the behaviour and design of CFS bolted moment connections were investigated and their seismic characteristics were optimised by improving their post-buckling behaviour, respectively. This appendix presents a comprehensive parametric study on the structural behaviour of CFS bolted beam-to-column connections with gusset plates under cyclic loading aiming to develop efficient design solutions for earthquake resistant frames. To simulate the hysteretic moment–rotation behaviour and failure modes of selected CFS connections, an experimentally validated finite element model using ABAQUS is developed, which accounts for both nonlinear material properties and geometrical imperfections. Connection behaviour is modelled using a connector element, simulating the mechanical characteristics of a bolt bearing against a steel plate and slippage of the bolt. The model is used to investigate the effects of bolt arrangement, bolt slip resistance, cross-sectional shape, gusset plate thickness and cross-sectional slenderness on the seismic performance of CFS connections under cyclic loading. The results indicate that, for the same amount of

material, folded flange beam sections with diamond or circle bolt arrangements can provide up to 100% and 250% higher ductility and energy dissipation capacity, respectively, compared to conventional flat-flange sections with square bolt arrangement. Using gusset plates with the same or lower thickness as the CFS beam may result in a premature failure mode in the gusset plate, which can considerably reduce the moment capacity of the connection. It is also shown that, by activating bolting friction-slip mechanism, the ductility, energy dissipation capacity and damping coefficient of the connections can significantly increase (up to 200%) especially for CFS beams with thinner plates (class 3 and 4). While conventional bolted moment connections with class 3 and 4 beam cross-sections generally do not satisfy the AISC requirements for intermediate and special moment frames, it is shown that optimum designed connections with bolting friction-slip mechanism can be efficiently used in high seismic regions.

B.2. BACKGROUND

Compared to hot-rolled steel elements, cold-formed steel (CFS) thin-walled elements are easier to manufacture with a far greater range of section configurations. Having a high strength to weight ratio, they are easy to transport and erect and can lead to more efficient and economic design solutions. However, CFS sections are more prone to local/distortional buckling due to the large width-to-thickness ratio of their thin-walled elements. As a result, CFS cross-sections have traditionally been employed mainly as secondary load-carrying members such as roof purlins and wall girts. However, in the modern construction industry, CFS members are increasingly used as primary structural elements, especially in modular systems (Fiorino et al., 2014a). Conventional CFS structures usually comprise shear walls made of vertical studs, diagonal braces and top and bottom tracks. The performance of shear walls with different bracing systems such as straps, steel sheets, and K-bracing was evaluated experimentally on full-scale specimens under cyclic and monotonic loadings (Moghimi and Ronagh, 2009, Lin et al., 2014, Zeynalian et al., 2012). The results indicate that most of the shear wall systems tested can maintain their lateral and vertical load bearing capabilities up to the drift limits specified by most seismic codes. However, CFS shear walls may exhibit poor ductility due to the distortion buckling of the stud elements and the resulting rapid decrease in their load-bearing capacity (Xu et al., 2018). Fiorino et al. (2016) conducted shake table tests on a full-scale two-storey sheathing-braced CFS building, where the results demonstrated the acceptable seismic lateral resistance of these structures under seismic loads. However, monotonic and cyclic tests on full-scale strap-braced CFS walls showed that stud wall systems

may exhibit a non-ductile seismic performance (e.g. due to gusset-to-track connection failure) (Fiorino et al., 2016).

CFS members have also been used as primary structural elements in low- to mid-rise multi-storey buildings (Fiorino et al., 2014b) and CFS portal frames with bolted moment connections (Lim and Nethercot, 2004b, Lim and Nethercot, 2003a). Experimental and numerical investigations on bolted moment connections using CFS sections in general demonstrated their good strength and stiffness, and adequate deformation capacity for seismic applications (Lim et al., 2016a, Lim and Nethercot, 2003a). However, the typical CFS bolted moment connections may exhibit very low ductility and energy dissipation capacity, especially when the width-to-thickness ratio of the CFS elements increases (Mojtabaei et al., 2018). This highlights the need to develop more efficient CFS connections suitable for moment-resisting frames in seismic regions. The global moment-rotation behaviour of CFS bolted connections is mainly governed by bolt distribution configuration, bolt tightening and bearing behaviour (Bagheri Sabbagh et al., 2012b, Gilbert and Rasmussen, 2010). The behaviour of CFS bolted moment connection is presented schematically in Fig B.1 in which bolt slippage in CFS bolted connections is prevented by appropriate tightening. It should be noted that seismic design of structures normally relies on inelastic deformations through hysteretic behaviour, leading to damage and permanent deformation of structural elements, and hence high repair costs, following a strong earthquake event. In steel construction, using friction-slip mechanism is known as an alternative seismic design approach, implemented to absorb the energy of the earthquake and consequently reduce and control the damage to the structural elements (Sabbagh et al., 2012) . In general, development of plasticity in the connection zone of CFS moment-resisting frames cannot be easily achieved due to the higher vulnerability of thin-walled elements (i.e. with large width-to-thickness ratio) to local/distortional buckling compared to their hot-rolled counterparts (Mojtabaei et al., 2018). Therefore, accommodating friction-slip mechanism in the CFS bolted moment connections to dissipate the earthquake input energy can provide a practical solution to improve the seismic performance of CFS moment-resisting frames. In practice, friction-slip mechanism can be easily activated in bolted moment connection by providing appropriate bolt tightening and detailing (Sabbagh et al., 2012), which is presented schematically in Fig. B.2.

The behaviour of beam-to-column CFS bolted moment-resisting connections with gusset plates has been investigated experimentally and numerically under monotonic and cyclic loading conditions (Uang et al., 2010, Serror et al., 2016b, Bučmys and Daniūnas, 2015a, Lim and Nethercot, 2003b, Wong and Chung, 2002, Bagheri Sabbagh et al., 2012b). It was found that, though they usually exhibit a semi-rigid behaviour, they can generally provide enough

stiffness and moment resistance for low to medium rise moment frames (Wong and Chung, 2002). In another study, Lim et al. (2003a) examined experimentally the ultimate strength of bolted moment-connections between CFS channel-sections. The tested specimens included apex and eaves connections, and it was concluded that the connections exhibit a semi-rigid behaviour due to bolt-hole elongation in the thin-walled steel sheet. Analytical work by Lim et al. (2016a) indicated that bolt-group sizes in CFS connections can also have a significant impact on the bending capacity of connected sections. Bagheri Sabbagh et al. (2013) investigated analytically the cyclic behaviour of CFS bolted moment connections by considering bolt slip effects. The results of their study showed that the proposed FE model could reasonably capture the hysteretic behaviour of the connections. However, the results were limited to the connections with curved-flange beam sections and rectangular bolt configuration. More recently, Shahini et al. (2018) used experimentally validated FE models to estimate the hysteretic energy dissipation capacity of the CFS connections with circular bolting arrangement designed to slip at a specific value. It was concluded that the bolting friction-slip mechanism can effectively delay the local buckling and yielding in the CFS beams.
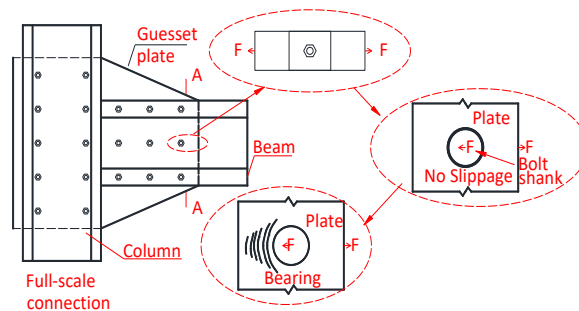
Fig. B.1. Bearing behaviour of a single bolt against steel plate used in CFS bolted moment connection
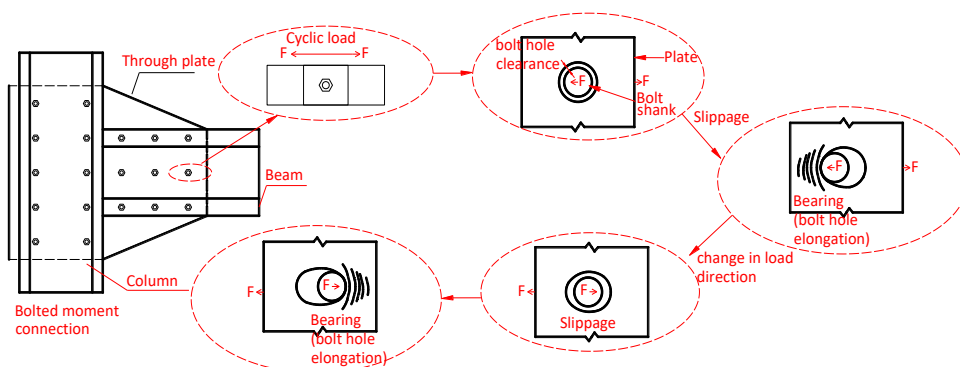
Fig. B.2. Slippage and bearing behaviour of a CFS bolted moment connection with friction-slip mechanism

Unlike the common misconception that slender CFS structural elements are not ductile, previous studies showed that by using an appropriate design CFS sections can offer significant ductility and energy dissipation capacity even when subjected to local/distortional buckling (Calderoni et al., 2009b, Padilla-Llano et al., 2014, Padilla-Llano et al., 2016). Experimental and analytical research on CFS moment-resisting frames (Bagheri Sabbagh et al., 2012a) at the University of Sheffield, UK, has also demonstrated that increasing the number of flange bends in CFS channel sections can delay the buckling behaviour. Follow-up studies proved that the optimised folded flange sections can provide up to 57% higher bending capacity (Ye et al., 2016b) and dissipate up to 60% more energy through plastic deformations (Ye et al., 2018a) compared to commercially available lipped channels. Consequently, higher strength, stiffness, and ductility can be potentially developed in CFS beams with an infinite number of bends (curved flange shown in Fig. B.3 (a)). Nevertheless, this type of cross-section is hard to manufacture and difficult to connect to typical floor systems. Considering the construction and manufacture constraints, the curved flange can be substituted with a folded flange cross-section (Fig. B.3 (b)). Both of these sections are examined in this study.
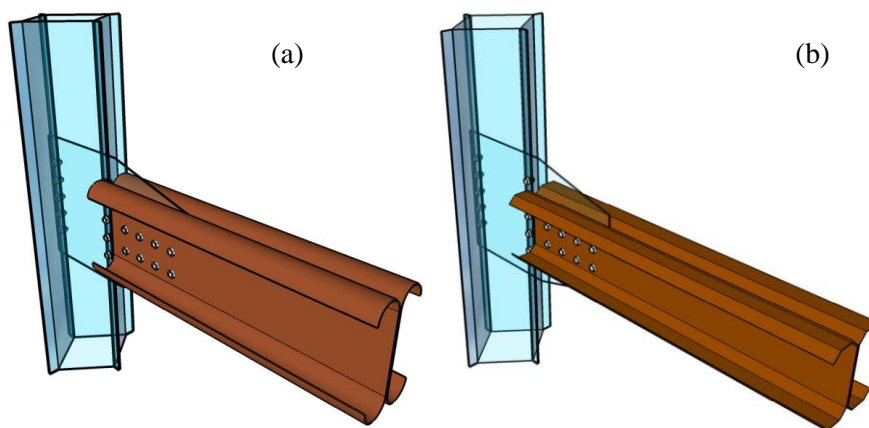
Fig. B.3. Configuration of CFS moment-resisting connections using gusset plate with (a) curved flange beam adopted from (Bagheri Sabbagh et al., 2012a) and (b) folded flange beam adopted from (Ye et al., 2016b)

Based on the outcomes of the above mentioned-studies, it can be concluded that the seismic performance of CFS moment-resisting connections depends on the following design parameters: (a) bolt distribution and bolt tightening (bolt slippage); (b) material yielding and bearing around the bolt holes; (c) yield lines developed in the buckled CFS plates; and (d) shape and dimensions of the beam cross-section. The effects of these factors will be investigated in this study and will be used to obtain more efficient design configurations for CFS bolted moment connections with bolting friction-slip mechanism with higher energy dissipation capacity and ductility. Detailed nonlinear FE models are developed by considering

the effects of initial geometrical imperfections. To model the friction-slip mechanism, equivalent connector elements are used to represent the bearing behaviour of a single bolt against CFS plate as well as the slip action of the bolts. The developed models are then verified against the results of an experimental programme on the cyclic behaviour of CFS bolted connections (Sabbagh et al., 2012). Subsequently, based on a comprehensive parametric study, the influences of different design parameters such as cross-sectional shape, member classification, gusset plate thickness, slip load resistance, and bolt configuration are investigated on the seismic performance of the connections. Finally, the results are used to identify the most efficient design solutions to considerably improve the seismic performance of CFS bolted moment connections.

B.3. FINITE ELEMENT MODEL

B.3.1. Element Type, Loading and Boundary Conditions

Detailed Finite Element (FE) models have been shown to be efficient in predicting the monotonic (Lim and Nethercot, 2004a, Öztürk and Pul, 2015) and cyclic (Bagheri Sabbagh et al., 2013) behaviour of CFS connections. In this study, the general-purpose S8R element in ABAQUS (2007) is used to model the CFS connection components. By conducting a mesh sensitivity analyses, the mesh size 20×20 mm was found to provide a balance between computational efficiency and accuracy. Fig. B.4 shows the adopted boundary conditions, which are similar to the reference experimental test set-up (Sabbagh et al., 2012). The back-to-back channel column is connected to the base by using pinned support, while the translational degrees of freedom on top face of the column are restrained. Since the back-to-back beam was assembled with bolts and filler plates in the experimental tests, the web lines are connected together in the U_X, U_Y and U_Z direction using the "Tie" constraint in ABAQUS (2007). Lateral bracing in the X direction is imposed at the locations of lateral frames used in the experiments to prevent lateral-torsional buckling of the beam element (Sabbagh et al., 2012) (see Fig. B.4). Previous studies showed that the panel zone deformation can also affect the rotation of the connections (D'Aniello et al., 2017b, Tartaglia et al., 2018). Due to the use of column stiffeners in the reference tests, it is assumed that the connection panel zone remains elastic.
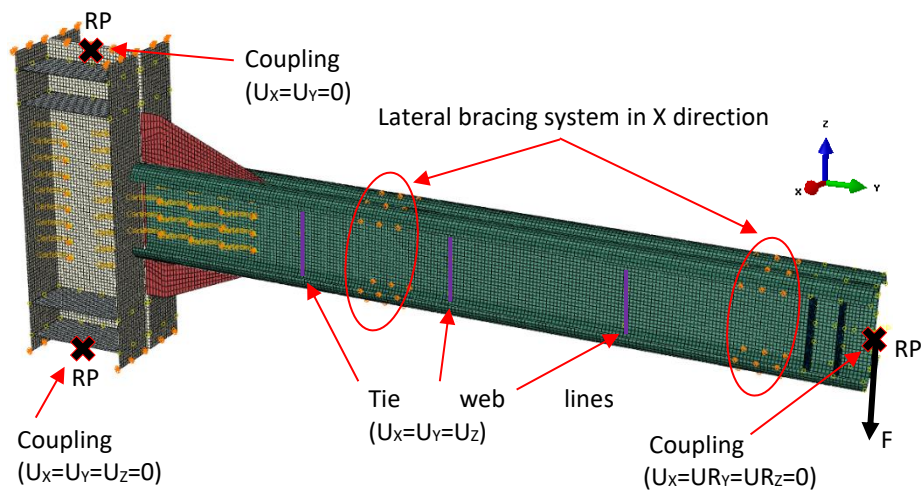
Fig. B.4. FE model of the beam-column connection

A tip displacement corresponding to rotation of the connection is applied at the Reference Point (RP) on the cross-sectional centroid of the beam end section. The cyclic loading regime suggested by AISC 341-16 (ANSI/AISC 341-16, 2016) is used as shown in Fig. B.5 (similar to the reference experimental tests (Sabbagh et al., 2012)). To obtain the response of the connections, displacement control nonlinear analyses are conducted in ABAQUS (2007).
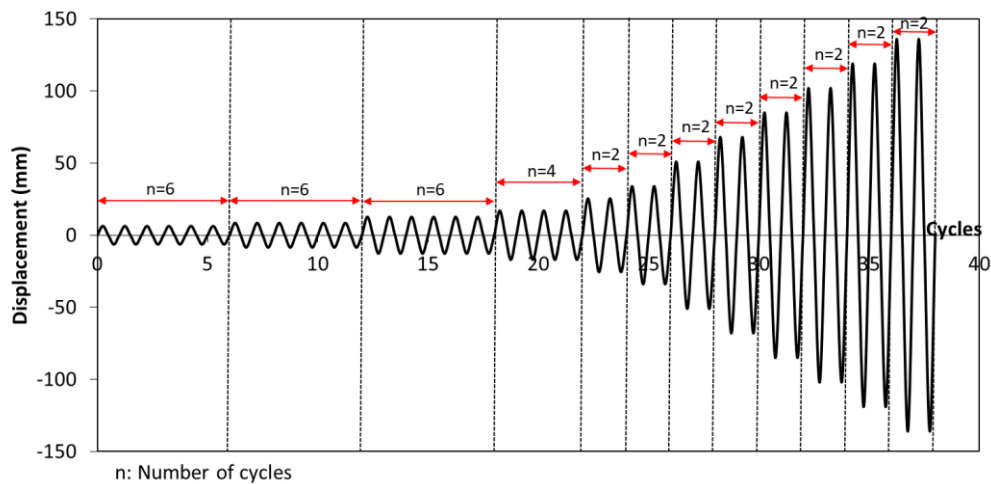
Fig. B.5. FE model of the Cyclic loading regime used for the reference test (Sabbagh et al., 2012) and analytical studies

B.3.2.   Material Properties

The stress-strain behaviour of the CFS plate is simulated using the constitutive model suggested by Haidarali and Nethercot (2011a). The stress-strain relationship consists of a Ramberg-Osgood equation up to the 0.2% proof stress, followed by a straight line with a slope of $E/100$ (where E is the elastic modulus taken as 210 GPa). This slope is obtained according to the coupon tests results reported by Sabbagh et al. (2012b), as shown in Fig. B.6. The ultimate strain used here is 0.08. Mathematically, the stress-strain model is expressed as:

$$\varepsilon = \frac{\sigma}{E} + 0.002 \left(\frac{\sigma}{\sigma_{0.2}} \right)^{n} \qquad for \ \sigma \leq \sigma_{0.2}$$
$$\varepsilon = \varepsilon_{0.2} + \frac{100(\sigma - \sigma_{0.2})}{E} \qquad for \ \sigma \geq \sigma_{0.2} \tag{B.1}$$

where $\sigma_{0.2}$ is the 0.2% proof stress ($\sigma_{0.2}$=310 MPa), $\varepsilon_{0.2}$ is the strain corresponding to the 0.2% proof stress and n is a parameter determining the roundness of the stress-strain curve. The parameter n is taken as 10 to have the best agreement with the coupon test results. Fig. B.6 compares the stress-strain curve from the coupon tests (Bagheri Sabbagh et al., 2012b) with the material model used in this study.

Since the reference bolted moment connection exhibited plastic deformations with strain reversals under the applied cyclic loading, the effect of cyclic strain hardening was taken into account in this study. The combined hardening law in ABAQUS (2007) was adopted based on the linear kinematic hardening modulus, C, determined as follows:

$$C = \frac{\sigma_u - \sigma_{0.2}}{\varepsilon_{pl}} \tag{B.2}$$

where $\sigma_{0.2}$ is the yield stress at the zero plastic strain and σ_u is a yield stress at ultimate plastic strain, ε_{pl}, all obtained from the monotonic coupon test results shown in Fig. B.6. The adopted method is capable to take into account the Bauschinger effect (Wang et al., 2012, Boger) and has been shown to be efficient at simulating the cyclic behaviour of steel material with isotropic/kinematic hardening (Bagheri Sabbagh et al., 2013, Jia et al., 2013).
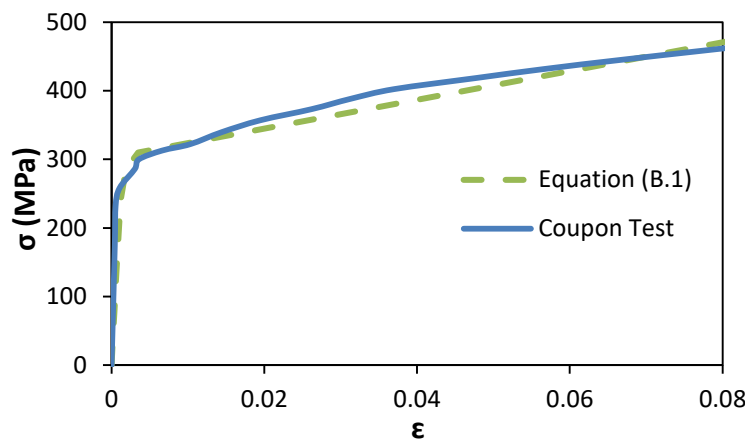
Fig. B.6. Stress-strain curve used in the FE model

B.3.3.   Imperfections

As mentioned before, the lateral-torsional buckling was prevented in the reference tests by using a lateral bracing system in the experimental test setup (Sabbagh et al., 2012). Therefore, only local and distortional geometrical imperfections (the one with the lower critical buckling resistance) are incorporated into the FE model. The imperfection magnitude for the thickness of steel sheet (t) less than 3mm is considered to be $0.94t$ and $0.34t$ for distortional and local imperfections, respectively, as suggested by Schafer and Peköz (1998). For plate thicknesses (t) greater than 3mm, the imperfection magnitude is assumed to be $0.3t\lambda_s$ as recommended by Walker (1975), where λ_s is the cross-sectional slenderness. The general shape of the local and distortional imperfections is generated based on the first buckling mode of the CFS connection obtained by an eigenvalue buckling analysis in ABAQUS. It should be noted that to include geometrical imperfection under monotonic load, the eigenvalue buckling analysis is conducted by applying a tip displacement in the Z, which leads to an unsymmetrical mode as shown in Fig. B.7 (a). However, in the case of cyclic loading, a symmetrical imperfection mode is generated by performing two eigenvalue buckling analyses on +Z and -Z direction and then combining the results of the first buckling mode shapes as shown in Fig. B.7 (b).
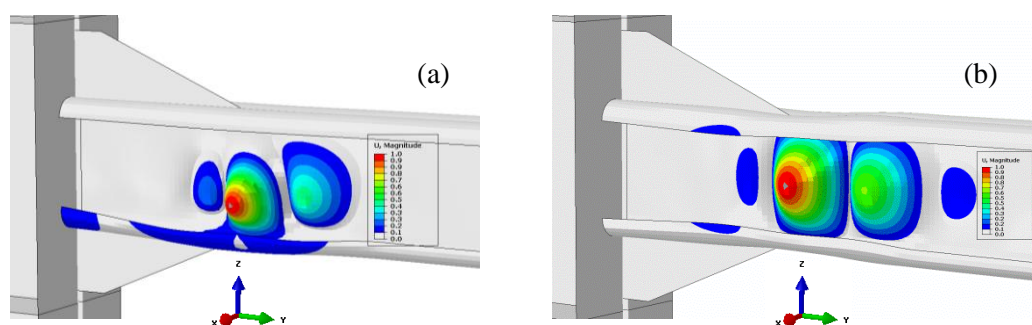
Fig. B.7. Geometrical imperfection in the cases of (a) monotonic and (b) cyclic load

B.3.4.   Bolt Modelling

Lim and Nethercot (2003b, 2004a) developed a simplified bolt model comprising of two perpendicular linear springs to model the bearing behaviour of a single bolt, and reported good agreement with experimental results of full-scale CFS joints subjected to monotonic loading. However, the linear spring elements used are not suitable for modelling the bearing behaviour of bolts under cyclic loads, due to nonlinearities in the bearing plate. Sabbagh et al. (2013) used the connector element in ABAQUS (2007) to model the behaviour of bolts under both monotonic and cyclic loading and achieved good agreement with experimental tests. Nonetheless, this approach induces stress concentrations around the two connector nodes. This issue can be overcome if the bolt behaviour is modelled explicitly using solid elements and surface-to-surface contact interactions (Öztürk and Pul, 2015, Gutierrez et al., 2015, Liu et al., 2015). The disadvantage of this is that it makes the model more complex and computationally expensive for cyclic modelling, especially when a large number of bolts is needed. Furthermore, convergence becomes an issue in the presence of bolt rigid body movement and slippage (Liu et al., 2015). In this study, a simplified connection element which is similar to the concept of "component method" adopted by Eurocode 3 (CEN, 2005e) is used to simulate the CFS full-scale connection behaviour. It is anticipated that the proposed model can provide accurate results with considerably lower computational costs compared to the complex FE models.

In this study, the bolt slip resistance F_{slip} is considered to be a function of bolt pretension force P_b (corresponding to the applied torque) and friction coefficient μ of the contact surfaces (Wong and Chung, 2002) :

$$F_{slip} = \mu \cdot P_b \cdot n_b \qquad \text{(B.3)}$$

where n_b is the number of slip planes. In this study, based on the mean frictional coefficient for galvanised steel surfaces, μ is assumed to be 0.19 (Bučmys and Daniūnas, 2015b).

The point-based "Fastener" using a two-layer fastener configuration found in ABAQUS library (2007) is employed to model the rigid and friction-slip behaviour of the bolts shown in Figs. B.8 and B.9, respectively. Each layer is connected to the CFS beam and gusset plate using the connector element to define the interaction properties between the layers. To model the connector element, a "physical radius" r is defined to represent the bolt shank radius and simulate the interaction between the bolt and the nodes at the bolt hole perimeter. The adopted method can accurately capture the stress concentrations around the nodes at the bolt positions

and help to simulate more accurately the bearing work of the bolts. As shown in Figs. B.8 (a) and B.9 (a), each fastener point is connected to the CFS steel plates using a connector element that couples the displacement and rotation of each fastener point to the average displacement and rotation of the nearby nodes. To prevent bolt slippage, rigid behaviour is therefore assigned to the local coordinate system corresponding to the shear deformation of the bolts (see Fig. B.8 (b)). Also to simulate the slippage of the bolts, the friction-slip behaviour is assigned to the connector element using "Cartesian" with three parallel translational degrees of freedom representing "Elasticity", "Friction" and "Stop" behaviours, as shown in Fig. 9 (b). To model "Elasticity" characteristic, a rigid behaviour is assigned to the local coordinate system corresponding to the shear deformation of the bolts. The friction coefficient μ and internal contact force P_b in Equation B.3 are used to model "Friction" behaviour. The "Stop" behaviour is also used to limit the bolt slip movement within the bolt-hole clearance. The connector behaviour is schematically presented in Fig. B.9 (c).

Based on the above discussion, the connector behaviour for friction-slip mechanism is characterised as follows:

(a) The connector is reasonably assumed to be rigid before activation of the bolt slippage (i.e. up to the slip resistance F_{slip}).

(b) Connector shear force is gradually developed and overcomes frictional resistance (F_{slip}), and subsequently relative slippage between the two plates in each layer of the CFS connection starts to happen (see Fig. B.9 (a)). The slippage will stop when the bolt shank is in contact with the hole perimeter surface.

(c) When the relative displacement between two fastener points exceeds Δ_{slip}, the bearing stiffness is considered to be practically infinite.
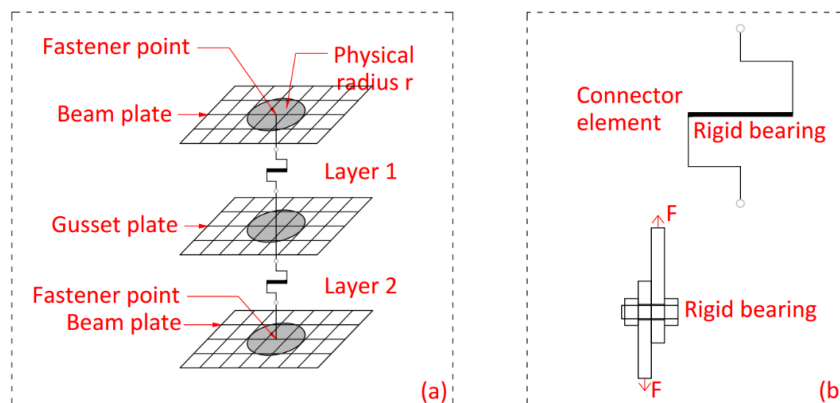
Fig. B.8. Single bolt modelling in ABAQUS: (a) definition of fastener; (b) components defined in a connector section
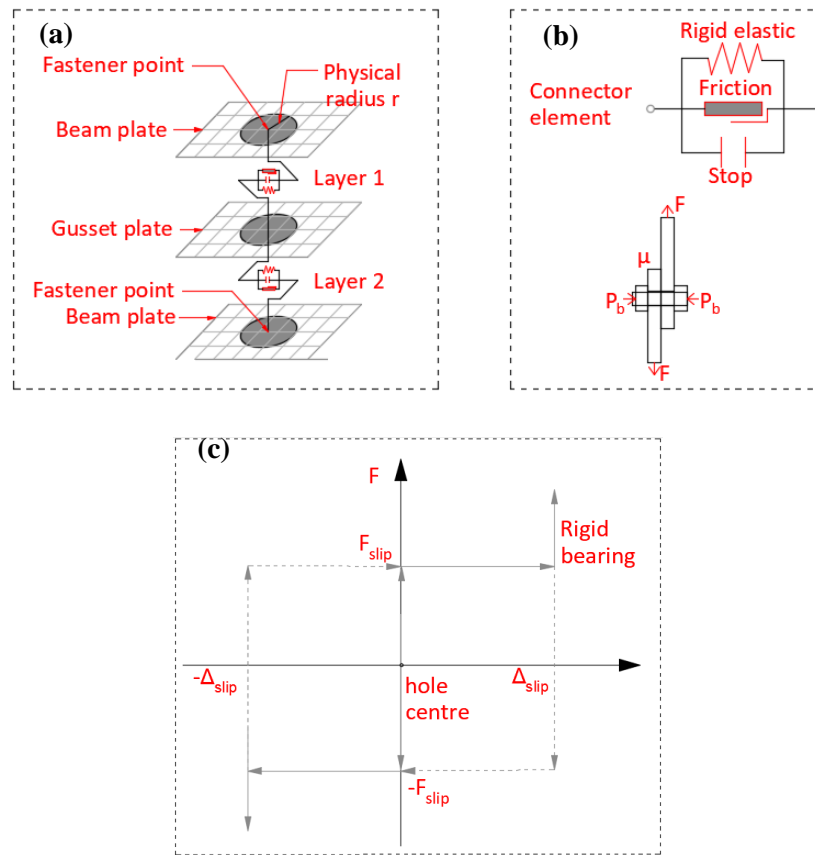
Fig. B.9. Modelling of the single bolts: (a) fastener; (b) connector components; and (c) slip-bearing behaviour

Fig. B.10 shows the fasteners with connector elements modelled in a typical CFS bolted moment connection. It should be mentioned that previous studies by D'Aniello et al. (2016, 2017a) highlighted the importance of accounting for the non-linear response of the bolts (e.g. due to shank necking or nut stripping) in the modelling of preloadable bolt assemblies. However, no bolt damage was observed in the reference experimental tests, and therefore, the failure modes of the bolts were not considered in this study.
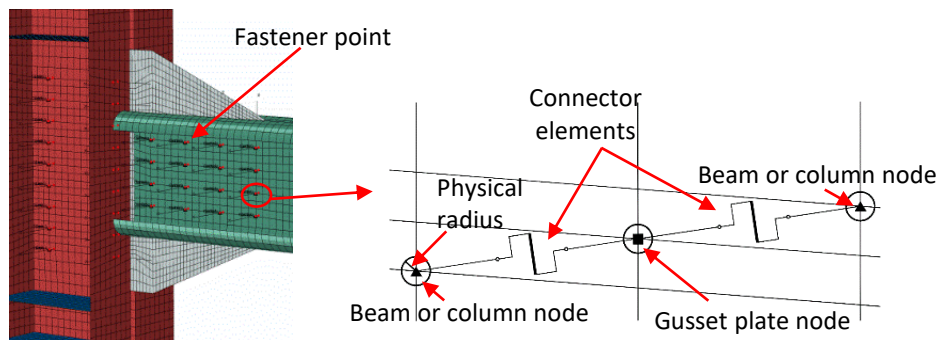
Fig. B.10. FE model of the beam-column connection with fastener definition

B.3.5.   Validation of Adopted FE Modelling Approach

Based on Equation B.3, the pretension force in the bolts is directly related to the applied torque. In the reference experimental test for both types of the connections (with and without slippage of the bolts), the friction force was provided by pre-tensioning the connection bolts using 240 N·m torque controlled by a torque wrench (Bagheri Sabbagh, 2011a).

The physical radius used to model the bolts (see Fig. B.9) is defined in accordance with the bolt shank radius equal to 9 mm (Bagheri Sabbagh, 2011a). To partially account for the effect of bolt elongation of the plate holes, the range of slippage of the stop element in Fig. B.9 is increased from $\pm 1 \, mm$ to $\pm 2 \, mm$ in the first lines of the bolts (Sabbagh et al., 2012). The experimental measurements and FE responses for the connections with rigid and slip-friction mechanism subjected to both monotonic and cyclic loading are presented in terms of moment-rotation (M-θ) hysteretic curves in Figs. B.11 and B.12, respectively. Generally, the results of numerical simulations under cyclic load compare very well with the corresponding experimental observations. However, compared to the cyclic load condition, slightly lower strength degradation is observed in the M-θ curve under the monotonic load. This behaviour can be attributed to the fact that the cyclic deterioration effects cannot be accurately captured under monotonic loading condition. For better comparison, Figs. B13 and B.14 compare the failure shape of the modelled connections with rigid and friction-slip mechanism under cyclic loads with the experimental observations. It is shown that the developed numerical model captures successfully the shape and the position of local/distortional buckling in the CFS beam.

It should be mentioned that, after a number of cycles, the slip resistance was reduced in the reference experimental test (Sabbagh et al., 2012). This can be justified since the high torque applied in the assembling process affects the contact surface between the plates after a number of loading cycles and the new slippage force will be then stabilised. The slippage resistance corresponding to the normal surface contact condition defined in Equation B.3 proved to be reasonable in the numerical validation of FE modelling against tested results in this study.

(a)   (b)
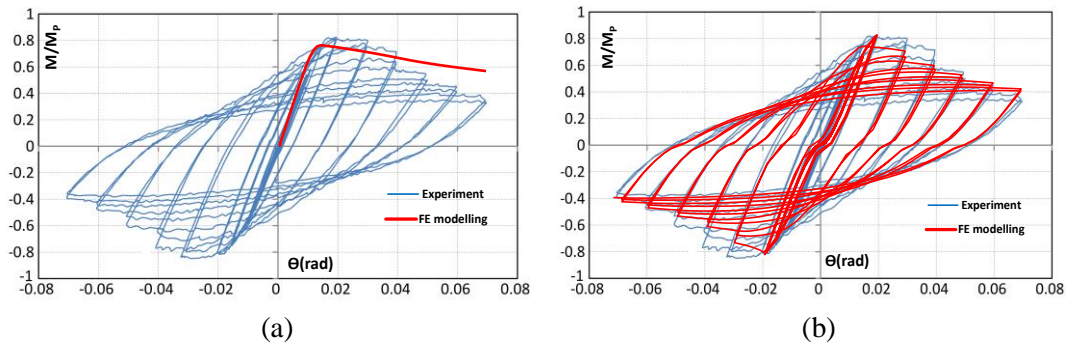
Fig. B.11. Comparison between experimental (tested by Bagheri et al. (Sabbagh et al., 2012)) and FE moment-rotation results of the connection without friction-slip mechanism under: (a) monotonic load and (b) cyclic load

(a)   (b)
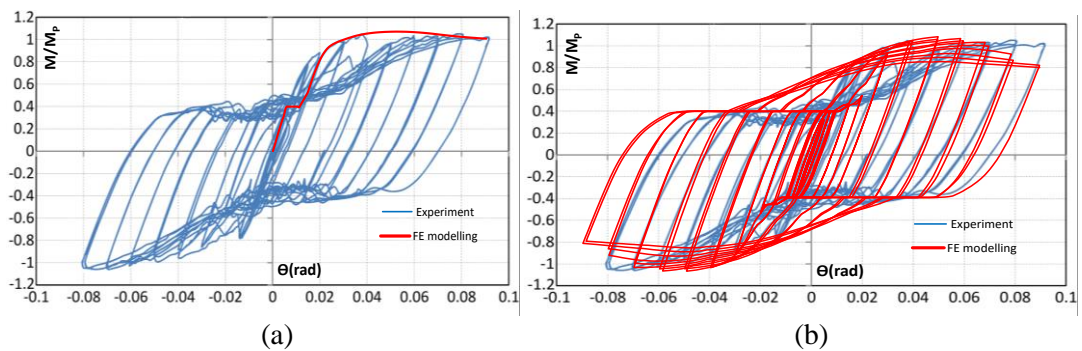
Fig. B.12. Comparison between experimental (tested by Bagheri et al. (Sabbagh et al., 2012)) and FE moment-rotation results of the connection with friction-slip mechanism under: (a) monotonic load and (b) cyclic load
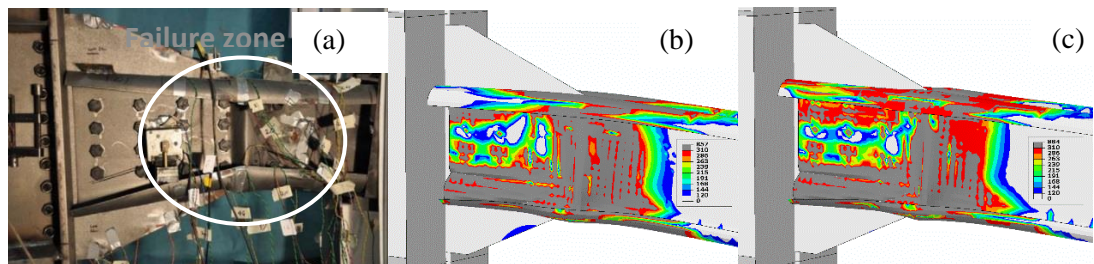
Fig. B.13. Comparison between experimental observations and analytical results of the connection without friction-slip mechanism: (a) experimental cyclic load (adopted from (Sabbagh et al., 2012), (b) FE under monotonic load, and (c) FE under cyclic load
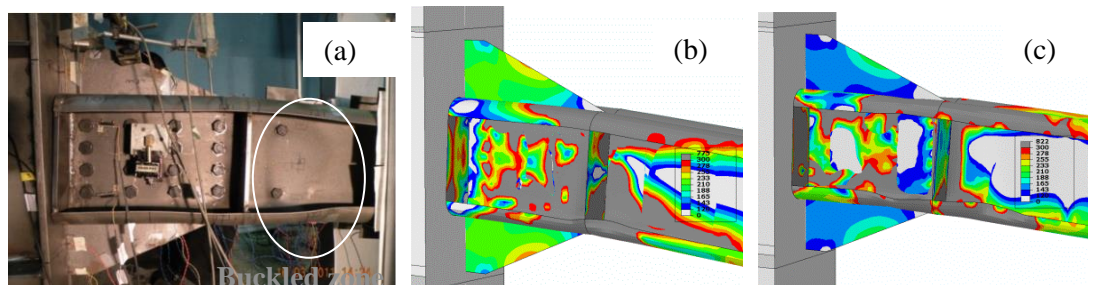
Fig. B.14. Comparison between experimental observations and analytical results of the connection with friction-slip mechanism: (a) experimental cyclic load (adopted from (Sabbagh et al., 2012), (b) FE under monotonic load, and (c) FE under cyclic load

B.4. DISCUSSIONS ON THE GENERAL RESPONSE OF CONNECTIONS WITH AND WITHOUT FRICTION-SLIP MECHANISM

CFS bolted moment connections with bolting friction-slip mechanism can reduce damage in structural elements by absorbing a part of earthquake input energy and also decrease maximum stresses in connection zones through slippage of the bolts. To show the efficiency of the proposed system, the flexural deformation and the von-Mises stress distribution of the connections with and without bolting friction-slip mechanism are extracted from FE analysis and compared in Fig. B.15. While the details of the FE models for both types of connections are similar (see Section B.3), bolt slippage is prevented in the connections with no friction-slip mechanism by using very high pretension force values (Ye, 2016). The results in Fig. B15 confirm that using the proposed friction-slip mechanism can significantly reduce the stress concentrations in the connection zone.

In general, the flexural behaviours of a typical CFS bolted moment connection and the one which friction-slip mechanism is mobilised through slippage of the bolts can be distinguished in different phases as shown in Fig. B.16. The first phase (O-A) occurs during initial loading of the connection corresponding to the elastic performance of the connection. During this phase, the bearing action of the bolts occurs for both types of connection. However, in the connection with friction-slip the bearing action is interrupted at slip moment M_{slip} (point A), which corresponds to the beginning of bolts slippage phase. The total slippage (θ_b) in the connection can be determined based on the summation of bolt holes clearance and elongation. It will be discussed in section B.5 that the slip moment (M_{slip}) and bolt clearance are the key parameters which affect the energy absorbing capability of friction-slip systems.

As can be seen in Fig. B.16, point B corresponds to the position that the bearing action of the bolts is re-activated. Points C and C' show the peak moments (M_p) of the CFS bolted moment connections with and without bolting friction-slip mechanism, respectively. In the final stage, there is a sudden loss of strength for both connections due to local buckling of the beam element. In this study, it was assumed that the ultimate moment of both connections (M_u) is reached at 20% drop from peak moment (points D and D' for connections with and without friction-slip mechanism, respectively).
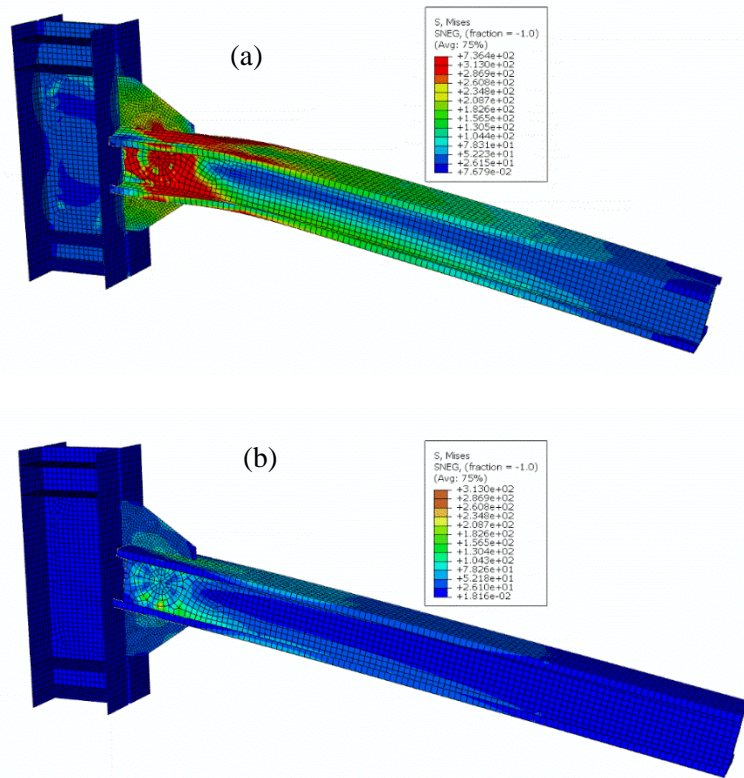
Fig. B.15. Von-Mises stress distribution and corresponding damage in the (a) normal, and (b) mobilised friction-slip connections with flat-flange beam section and circular bolt configuration
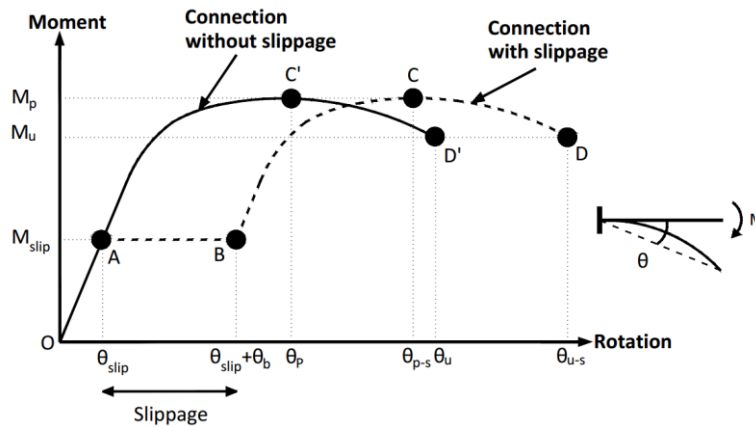
Fig. B.16. Moment-rotation relationships of CFS connections with and without bolting friction-slip mechanism

Fig. B.17 compares the cyclic hysteretic performance of the CFS bolted moment connection without and with friction-slip mechanism under cyclic loading regime shown in Fig. B.5. The results indicate that, similar to monotonic behaviour, using friction-slip mechanism provides a horizontal shift in each cycle of hysteretic moment-rotation curve while the peak and

ultimate moments are not considerably affected. This will be discussed in more detail in the following sections.
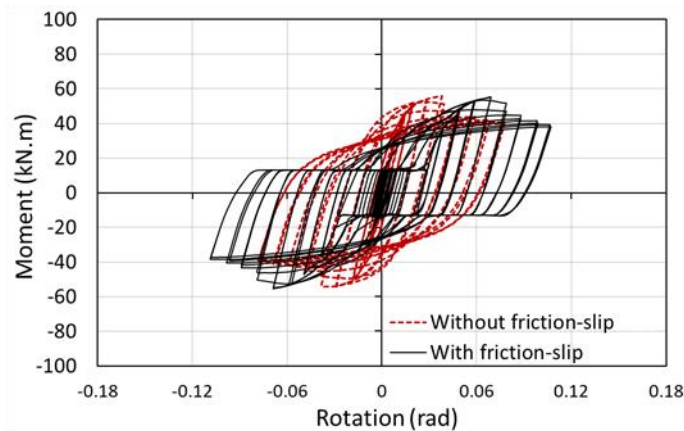
Fig. B.17. Example of comparison between cyclic hysteretic performance of the CFS bolted moment connection without and with friction-slip mechanism

B.5. KEY DESIGN PARAMETERS

The main design parameters examined are beam cross-sectional shape, plate thickness (or cross-sectional slenderness), bolt configuration, bolt slip load resistance, and gusset plate thickness. Considering the capabilities of the cold-rolling and press-braking processes to provide cross-sections with intermediate stiffeners or folded plates, four different geometries including flat, stiffened flat, folded and curved shaped channel cross-sections are selected for the parametric study, as listed in Table B.1. For each cross-section, four different plate thicknesses of 1, 2, 4, 6 mm are used. The selected cross-sections have the same total plate width, and therefore, use the same amount of structural material. Moreover, to investigate the effect of different flange shapes, all cross-sections are designed to have a similar web slenderness ratio. It should be mentioned that the curved flange cross-section in this study is less practical and is mainly used for comparison purposes and verification of analytical models with experimental results (Bagheri Sabbagh et al., 2012b). Also thin-walled sections with curved or folded flange cross-sections may be sensitive to crippling due to support transverse actions from joints and purlins, which should be considered in the design process of these elements.
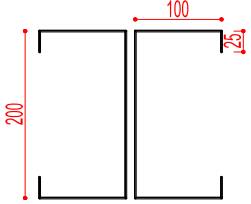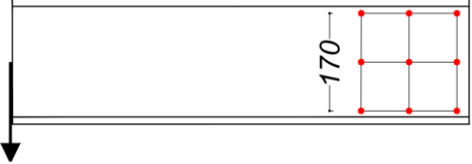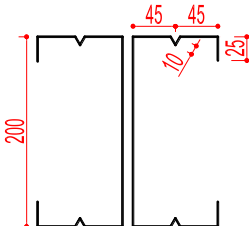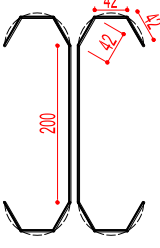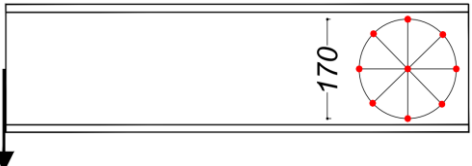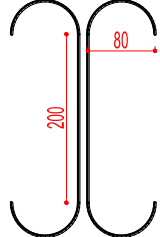
Since bolt distribution can also affect the stress field distribution of bolted moment connections (Lim et al., 2016a), three types of bolt distributions including circle, diamond and square shapes are selected, as shown in Table B.1. To increase the efficiency of the proposed connection, the number of bolts and their arrangement were also optimised in this study. As a

result, the number of required bolts was reduced from 16 in the reference experimental tests (Bagheri Sabbagh et al., 2012b) to 9 bolts. It is worth mentioning that circular bolt arrangement may be less practical compared to square and diamond in real constructional practice, however, in this study it is investigated for comparison purposes. The effect of gusset plate thicknesses on the cyclic behaviour of the bolted CFS connections is also investigated in the parametric study. It should be noted that, for better comparison, the performance parameters of the sections with different shapes and plate thicknesses are presented as a function of their slenderness ratio calculated as:

$$\lambda_s = \sqrt{\frac{f_y}{\sigma_{cr}}} \tag{B.4}$$

where σ_{cr} and f_y are the critical buckling stress and yield stress, respectively.

Table B.1. Definitions and values of the design assumptions

Channel type	Bolt configuration
Flat-flange	Square
Stiffened-flange	Diamond
Folded-flange	
Curved-flange	Circle

B.5.1. Cross-Sectional Classification of CFS beams

B.5.1.1 Eurocode regulations

To design CFS beams for bending, Eurocode 3 (CEN, 2005e, BS EN, 1993) divides the cross-section of CFS beam elements into individual plates subjected to either compression, bending or combined bending and compression. Each plate is identified as internal or outstand element according to the edge boundary conditions. Based on their susceptibility to local buckling, sections are categorized into four different classes (1, 2, 3 and 4). This classification is based on the slenderness of the constituent flat elements (width to thickness ratio), yield stress, edge boundary conditions and applied stress gradient. The overall classification of a cross-section is obtained using the highest (most unfavourable) class of its compression parts. Table B.2 lists the Eurocode 3 classifications obtained for channels with flat, stiffened flat and folded flanges used in this study. It should be noted that the Eurocode classification cannot be applied directly to sections with round elements (e.g. curved-flange channel).

As shown in Fig. B.18, the concept of the Eurocode cross-sectional classification is based on the moment-rotation (M-θ) curves of the elements, where M_y, M_p and M_u represent yield moment, plastic moment and peak moment capacity, respectively. Class 1 cross-sections can form a plastic hinge with the rotation capacity obtained from plastic analysis without reduction of their resistance ($M_p < M_u$). Class 2 cross-sections are capable of developing their full plastic moment resistance, but have limited rotation capacity due to local buckling ($M_p < M_u$). In class 3 cross-sections, the stress in the extreme compression fibre reaches the yield strength, but local buckling prevents the development of the plastic moment resistance ($M_y < M_u < M_p$). In class 4 cross-sections, local buckling occurs before the attainment of yield stress in one or more parts of the cross-section ($M_u < M_y$). Since the moment-rotation response of class 1 and class 2 sections follow a similar trend ($M_p < M_u$), the two classes can be distinguished based on the pure plastic rotation capacity factor (R) in EN 1993-1-1(CEN, 2005d):

$$R = \frac{\theta_u - \theta_p}{\theta_p} \tag{B.5}$$

where θ_u is the ultimate rotation corresponding to the drop in the moment-rotation curve in the softening branch, and θ_p is the rotation corresponding to the plastic moment at the hardening branch, as shown in Fig. B.18.
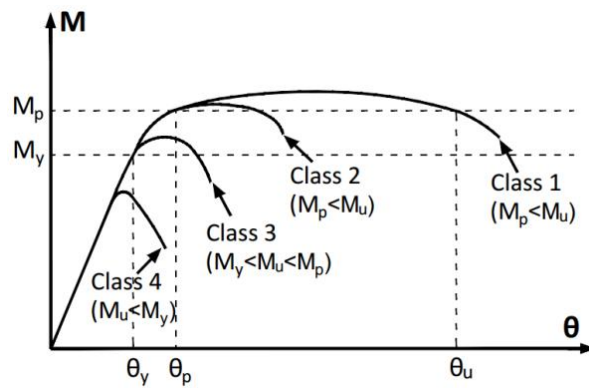
Fig. B.18. Cross-sectional classification based on moment-rotation curves

B.5.1.2 *Classification based on moment-rotation behaviour*

The Eurocode 3 cross-sectional classification concept is assessed here by examining the predicted moment-rotation behaviour under monotonic load. Non-linear inelastic post-buckling analyses (Static Riks) are performed on 2 m long CFS cantilevers, using single channel cross-sections, as shown in Fig. B.19. The CFS members are fully fixed at one end and are subjected to a tip load at the centroid of the other end. The centroid is coupled to the beam end cross-section and boundary conditions are applied to prevent the lateral movement of the flanges at 1/3 length intervals (see Fig. B.19). Other FE modelling parameters (e.g. mesh size, material properties and geometric imperfections) are as described in Section 2.

Fig. B.20 illustrates how the cross-section classification is applied based on normalised moment and pure plastic rotation capacity factor (R). As shown in Table B.2, all of the sections with 1, 2, 4, and 6 mm plate thickness are identified as class 4, 3, 2 and 1, respectively. The Eurocode slenderness limits for class 1 and 4 channel sections are found to be in general sufficient, but they are not very accurate for class 2 and 3 channel sections.
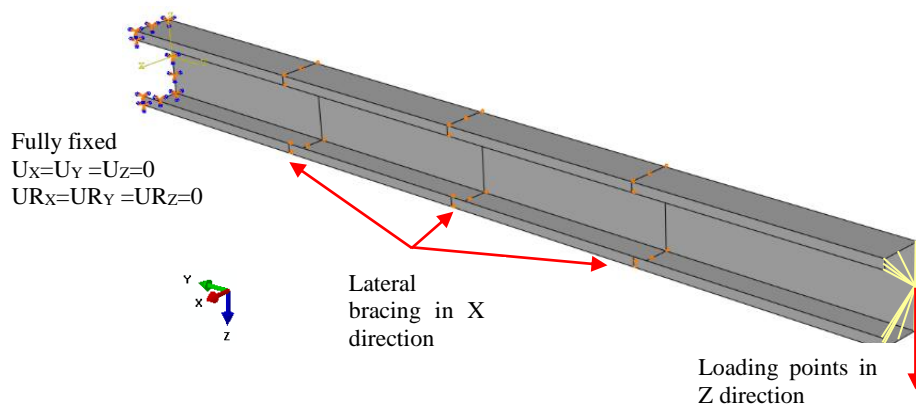
Fig. B.19. Typical boundary conditions, constrains and loading point of cantilever channels

Table B.2. Cross-sectional classification of the CFS cross-sections

| Section | Plate Thickness (mm) | Eurocode classification based on slenderness limits | | | | | Eurocode concept | Finite Strip Method |
| | | Flanges | | Lips | Web | Overall | | |
		Internal	Outstand					
Flat	1	4	-	4	4	4	4	σ_l=0.2794f_y Local
	2	4	-	3	3	4	3	σ_d=1.0633f_y Distortional
	4	1	-	1	1	1	2	σ_d=2.3122f_y Distortional
	6	1	-	1	1	1	1	σ_d=3.7827f_y Distortional
Stiffened Flat	1	4	-	4	4	4	4	σ_l=0.5029f_y Local
	2	1	-	3	3	3	3	σ_d=1.1994f_y Distortional
	4	1	-	1	1	1	2	σ_d=2.6401f_y Distortional
	6	1	-	1	1	1	1	σ_d=4.3095f_y Distortional
Folded	1	4	4	-	4	4	4	σ_l=0.3995f_y Local
	2	1	4	-	3	4	3	σ_d=1.4895f_y Distortional
	4	1	3	-	1	3	2	σ_d=3.2351f_y Distortional
	6	1	1	-	1	1	1	σ_d=5.2191f_y Distortional
Curved	1	-	-	-	4	-	4	σ_l=0.5808f_y Local
	2	-	-	-	3	-	3	σ_d=1.6887f_y Distortional
	4	-	-	-	1	-	2	σ_d=3.6603f_y Distortional
	6	-	-	-	1	-	1	σ_d=5.896f_y Distortional
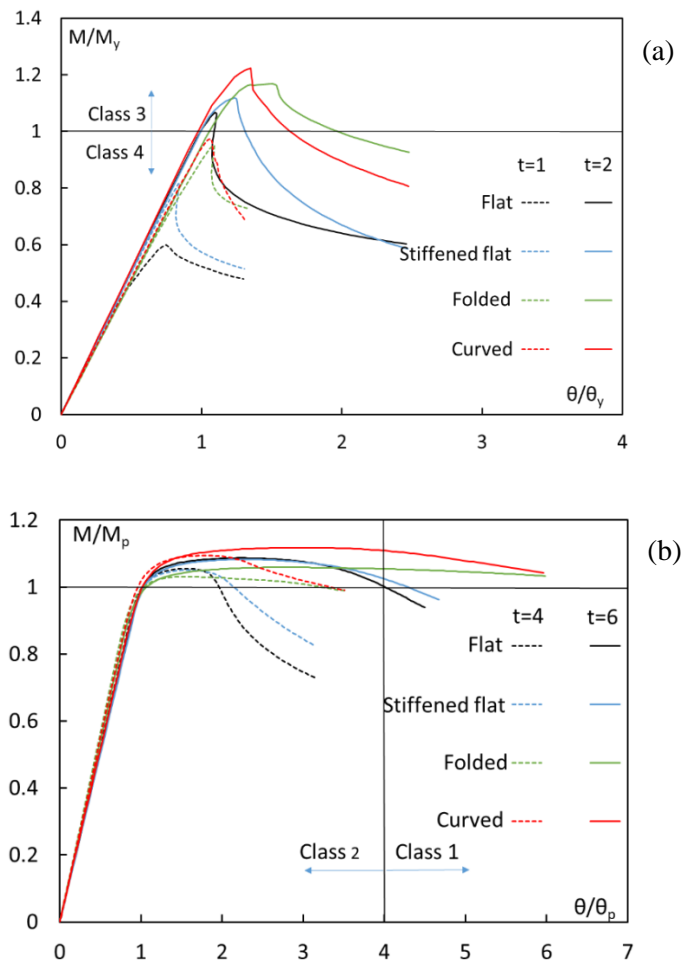
Fig. B.20. Normalised moment–rotation responses for cross-section classification: (a) $t=1$ mm and 2 mm and (b) $t=4$ mm and 6 mm

Cross-sectional classifications may also be determined using the classical finite strip method (Ádány and Schafer, 2006a, Ádány and Schafer, 2014), which estimates the buckling capacity of thin-walled members by taking into account local, distortional and global buckling elastic modes. The critical elastic buckling stresses of the cross-sectional shapes used in this study (subjected to bending) are determined based on the minimum of the local buckling (σ_l) and the distortional buckling (σ_d) stresses obtained from constrained finite strip software CUFSM (Li and Schafer, 2010). Due to the presence of the lateral supports, the global buckling mode is not considered to be dominant in this study (see Fig. B.19). The critical buckling stresses obtained for the different cross-sections are presented in Table B.2. It is shown that the ratio of the critical stress to the yield stress is in the range of 3-6, 2-3 and 1-1.5 for class 1, 2 and 3 sections, respectively. For class 4 sections, local buckling is always identified as the dominant buckling mode and the critical buckling stress is generally smaller than the yield stress. This

indicates that the critical buckling stress can be also used as a simple measure to identify the cross-sectional classification based on Eurocode 3.

B.5.2.   Effect of Various Bolt Slip Resistance

To assess the influence of using different bolt slip resistance on the overall moment-rotation behaviour of the studied connections, a range of bolt pretensions are applied on the connections with the beam flat-flange class 1 (t=6 mm). The slip resistance design values are calculated based on the allowable slip resistance suggested by ASTM A325 (2014) using the following equation:

$$R_n = 1.13 \mu N_b T_m \qquad \text{(B.6)}$$

Where R_n is slip resistance of the connection, μ is the frictional coefficient, N_b is the number of bolts, and T_m is minimum bolt pretension. Monotonic analyses are then carried out on the connections with three different bolts pretensions. Bolt pretensions are selected to be: T_m =90 kN which activates the bolt slippage while the CFS beam is still in the elastic behaviour range, T_m =270 kN which activates the slippage of the bolts when CFS is in its inelastic behaviour range, and fully clamped beam (no friction-slip). As shown in Fig. B.21, the adopted friction-slip mechanism generally generates a horizontal shift in the moment-rotation response while the global behaviour of the connection is very similar to the no slippage connection. It should be noted that, depending on bolt configuration, the behaviour of the connection with friction-slip mechanism in inelastic range (especially after buckling) may be slightly different compared to the connection with no friction-slip mechanism. It can be also seen in Fig. B.21 that changing the value of the bolt pretension force can shift the starting point of slippage in moment-rotation curve while performance of the connection in both elastic and inelastic stages remains unchanged. It is worth noting that while the dominant failure mode in CFS bolted moment connection is local buckling of the beam close to bolt-group, accommodating bolting friction-slip mechanism in the connection using different bolt-pretension force and bolt configurations did not change the failure mode. Consequently, activation of friction-slip action in CFS bolted moment connections provides a means to adjust the global behaviour of the connection, especially when higher class beam sections (thicker elements) are utilised. Friction-slip mechanism and its effects on maximum moment capacity, energy dissipation and damping coefficient will be discussed in Section 5 by using the results of cyclic analyses on the connections.
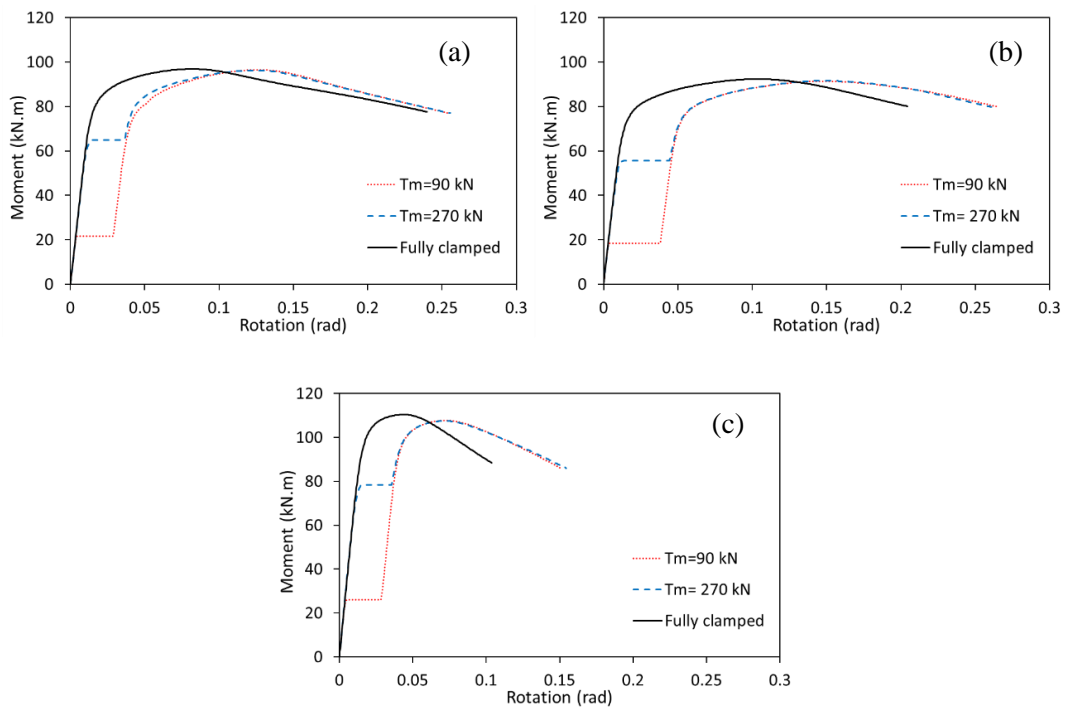
Fig. B.21. The moment-rotation behaviour of class 1 connections using different bolt configurations and pretension forces: (a) Circle, (b) Diamond, (c) Square

B.6.   EFFICIENCY OF CFS BOLTED MOMENT CONNECTIONS

In this section, the results of the parametric study are used to identify efficient design solutions for CFS bolted-moment connections.

B.6.1.   Moment Rotation Behaviour

Figs. B.22 and B.23 compare the cyclic response and the cyclic moment-rotation envelope of the connections without and with friction-slip mechanism. The results are shown for the flat flange channels with circle bolt arrangement and various plate thicknesses (1, 2, 4 and 6 mm). The cyclic moment-rotation envelope is specified in both positive and negative rotations by plotting the locus of peak moment points at the first cycle of each load amplitude. It should be noted that, unlike a monotonic moment rotation backbone curve, the cyclic moment-rotation envelope can take into account the strength degradation due to cyclic loading as observations in the experimental results conducted by Padilla-Llano et al. (2014, 2016). The rotation of the connection was quantified as the ratio of beam tip displacement to the length of the beam up to the gusset plate. The moment-rotation results are used to determine different performance parameters such as moment capacity, yield moment, ductility, energy dissipation capacity and equivalent viscous damping coefficient in the following sections. The initial stiffness of a CFS

bolted-moment connection, $S_{j,ini}$, can be used to classify the rigidity of the connection based on Eurocode 3 part 1–8. The connections with $S_{j,ini} \times (\frac{L_b}{EI_b})$ less than 0.5, between 0.5 and 25 and over 25 are classified as "simple", "semi-rigid" and "rigid", respectively, where L_b is the beam length and EI_b is the flexural rigidity of the beam. Table B.3 lists the rigidity of the different connections used in this study. The results indicate that connections with cross-sectional classes 1 and 2 are always classified as "rigid", while those with cross-sectional classes 3 and 4 should be treated as "semi-rigid".
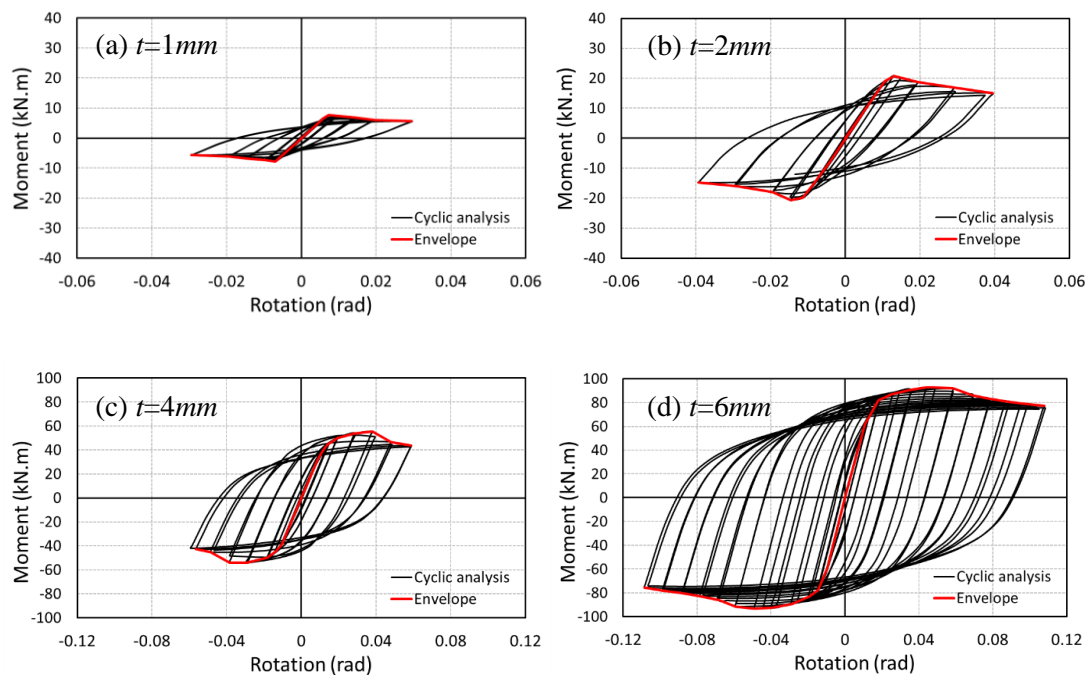
Fig. B.22. Cyclic moment-rotation relationship and envelope curves of the connections without friction slip mechanism and with flat flange beam section and circular bolt arrangement

(a) t=1 mm   (b) t=2 mm

(c) t=4 mm   (d) t=6 mm
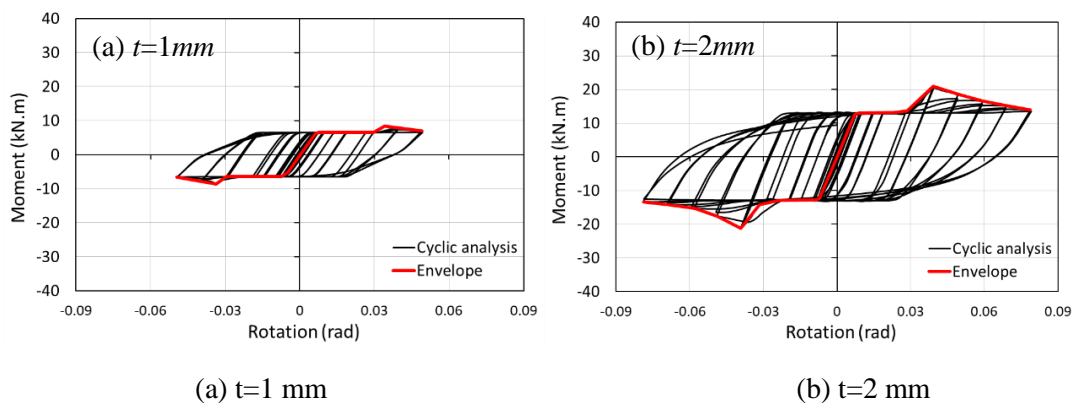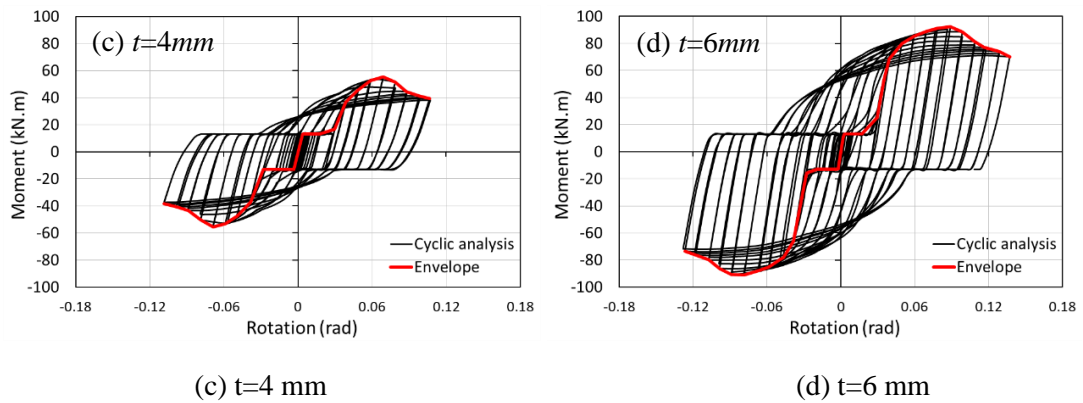
Fig. B.23. Cyclic moment-rotation relationship and envelope curves of the connections with friction slip mechanism and with flat flange beam section and circular bolt arrangement

B.6.2. Failure Mode

The failure modes of the bolted-moment CFS connections obtained from the detailed FE models are identified in Table B.3. It is shown that, in general, the dominant mode is local buckling of the CFS beam section close to the first row of the bolts. This can be attributed to the effect of bolt group on the stress distribution at the connection zone. It should be noted that mobilising friction-slip mechanism into the connection cannot change the dominant failure mode of the CFS beam. The results indicate that for flat and stiffened flat channels, local buckling occurs at both web and flange of the CFS section. But using curved and folded flange channels can postpone the local buckling of the flange by creating an in-plane stiffness through arching action and shifting the local buckling failure to the web. Fig. B.24 shows the typical failure mode of the beams with flat and bent flange channel sections.
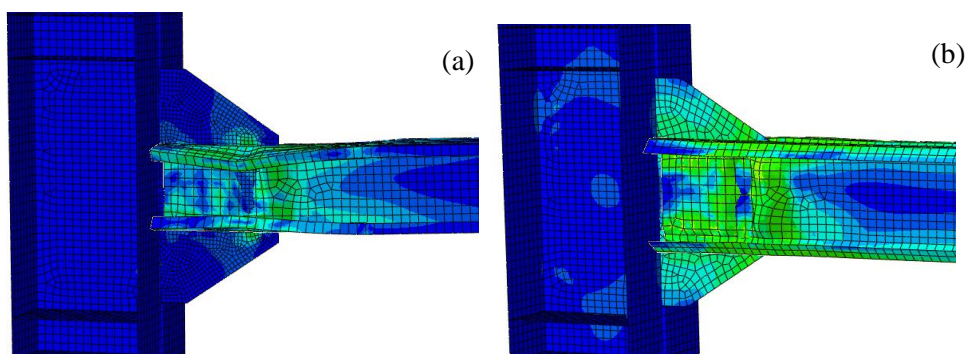
Fig. B.24. Typical failure modes: (a) flat flange channel, (b) bent flange channel

B.6.3. Moment Capacity of the Connection

Fig. B.25 shows the maximum moment capacity of both connections with and without bolting friction-slip system, indicating the effect of bolt slippage is generally negligible on the flexural strength of the connections regardless of the beam cross-sectional class. The minor differences

can be attributed to the fact that after bolt slippage the centre of rotation shifts from the centre of the bolts, leading to a small change in the maximum flexural capacity of the connections. The results in Fig. B.25 indicate that the beam cross-sectional class and the bolt configuration are the most influential parameters on the flexural capacity of the CFS connections. Compared to other bolt configurations, using a conventional square bolt configuration generally resulted in a higher (up to 32%) flexural capacity in the connections, especially where class 1 and 2 beam sections were used. While it was previously shown that bent flange sections can generally provide noticeably higher flexural capacity compared to their standard flat-flange counterparts (Sabbagh et al., 2012, Ye et al., 2016b), the results of this study indicate that using bent flange sections can improve the capacity of the connections by less than 10%. This is referred to two main reasons: (i) effect of bi-moment generated due to presence of bolts (Lim et al., 2016a), and (ii) The effect of flange shape on the moment capacity of the connection is reduced when channel sections with a deep web are utilised.
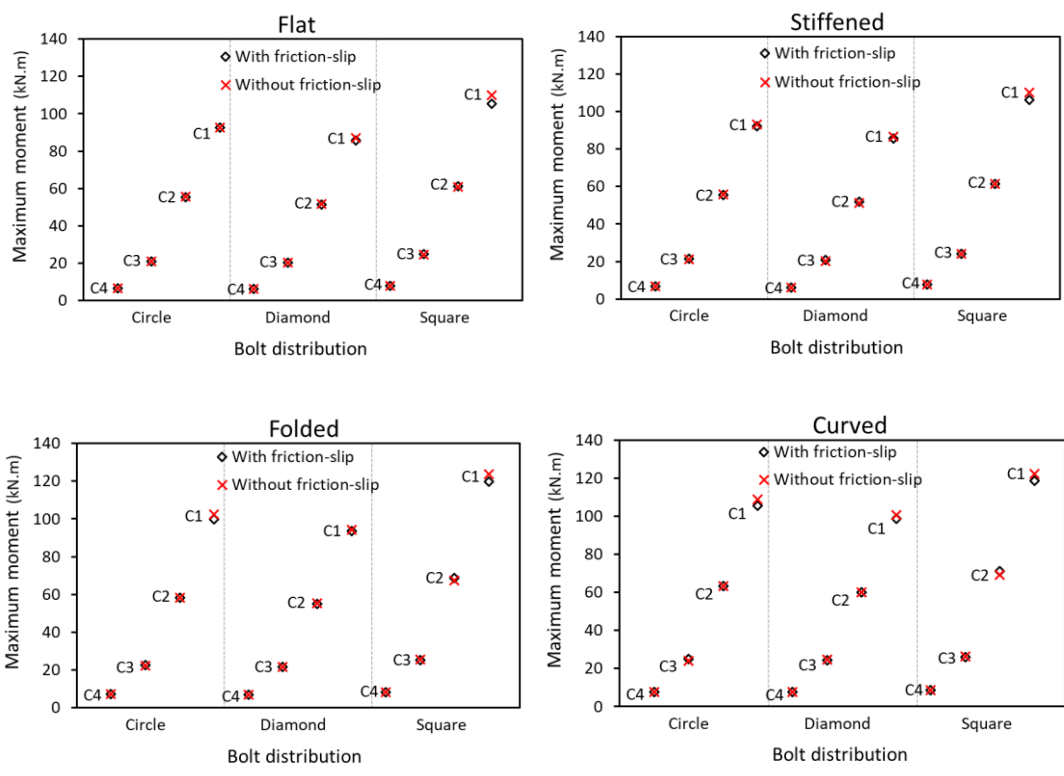
Fig. B.25. Moment capacity of CFS connections with different bolt configurations and cross-section classes (C1, C2, C3, and C4 are cross-section classes 1, 2, 3 and 4, respectively)

B.6.4. FEMA Bilinear Idealisation

To characterize the cyclic behaviour of the selected bolted-moment connections, FEMA model (2000) is developed based on the cyclic moment-rotation envelope, which is capable to take into account both positive and negative post-yield slopes. As shown in Fig. B.26, FEMA

model uses an ideal bi-linear elastic plastic response to represent the non-linear behaviour of an assembly by incorporating an energy balance approach. The area below the cyclic moment-rotation envelope curve is assumed to be equivalent to the area under the idealised bilinear FEMA curve.

The yield rotation (θ_{y1}) is determined on the condition that the secant slope intersects the actual envelope curve at 60% of the nominal yield moment (M_{y1}), while the area enclosed by the bilinear curve is equal to that enclosed by the original curve bounded by the target displacement (θ_t). The target rotation was assumed to be corresponding to the rotation at which the flexural capacity of the system dropped by 20% (i.e. $\theta_t = \theta_u$), also recommended by AISC (ANSI/AISC 341-16, 2016). The characteristic parameter values of the FEMA models corresponding to the different bolted-moment CFS connections are presented in Table B.3. For better comparison between the behaviour of different types of connections, Table B.3 also presents the yield moment results calculated based on the FEMA idealised bi-linear curve up to the rotation at the maximum moment capacity (M_{y2}).
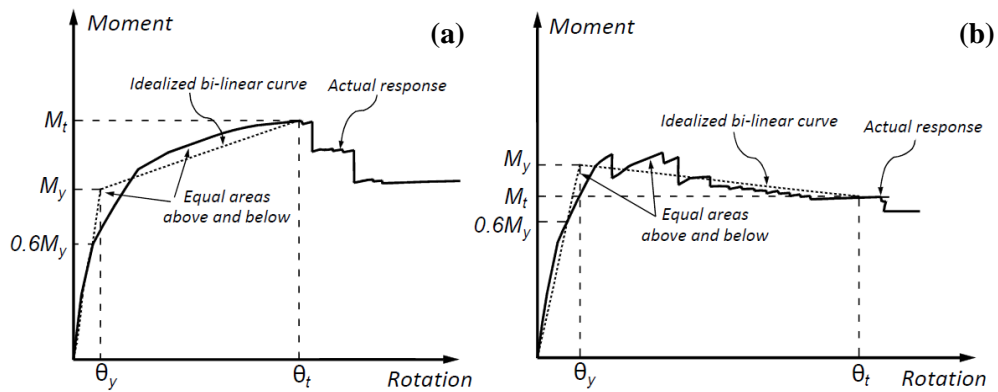
Fig. B.26. FEMA bi-linear idealisation model: (a) Positive post-yield slope, (b) Negative post-yield slop

Table B.3. Characteristic parameters of the CFS connections using FEMA models

Bolt Configuration	Plate Thickness (mm)	Beam type	Yield moment M_{y2} (kN·m)	Yield moment M_{y1} (kN·m)	Yield rotation θ_{y1} (rad)	Ultimate rotation (rad)	Buckling mode *	Connection Rigidity (EN 1993-1-8)
Circle	1	Flat	6.9	5.8	0.006	0.013	LW-LF	Semi-Rigid
		Stiffened flat	6.9	6	0.006	0.018	LW-LF	
		Folded	7.6	6.4	0.006	0.014	LW	
		Curved	7.9	7	0.006	0.010	LW	
	2	Flat	20.8	20.1	0.011	0.029	LW-LF	Semi-Rigid
		Stiffened flat	20.9	21.8	0.012	0.049	LW-LF	
		Folded	21.6	23.1	0.011	0.039	LW	

		Curved	24.0	23.3	0.010	0.030	LW	
		Flat	48.3	55.3	0.015	0.059	LW-LF	
	4	Stiffened flat	48.7	54.6	0.015	0.066	LW-LF	Rigid
		Folded	51.7	60.0	0.014	0.057	LW	
		Curved	59.6	65.8	0.014	0.049	LW	
		Flat	82.9	93.4	0.015	0.118	LW-LF	
	6	Stiffened flat	83.4	94.6	0.016	0.125	LW-LF	Rigid
		Folded	95.3	103.6	0.015	0.116	LW	
		Curved	98.5	111.1	0.014	0.079	LW	
		Flat	7.1	5.7	0.007	0.010	LW-LF	
	1	Stiffened flat	7.1	5.9	0.007	0.015	LW-LF	Semi-Rigid
		Folded	7.8	6.2	0.007	0.015	LW	
		Curved	8.0	7.4	0.007	0.009	LW	
		Flat	18.7	19.9	0.012	0.029	LW-LF	
	2	Stiffened flat	19.6	20.6	0.012	0.038	LW-LF	Semi-Rigid
		Folded	20.8	22.1	0.011	0.039	LW	
Diamond		Curved	24.5	24.6	0.011	0.019	LW	
		Flat	46.4	53.1	0.016	0.059	LW-LF	
	4	Stiffened flat	46.9	51.1	0.015	0.068	LW-LF	Rigid
		Folded	49.0	56.3	0.014	0.066	LW	
		Curved	52.1	62.1	0.015	0.059	LW	
		Flat	76.4	87.3	0.015	0.108	LW-LF	
	6	Stiffened flat	76.8	87.6	0.015	0.117	LW-LF	Rigid
		Folded	84.3	94.5	0.015	0.147	LW	
		Curved	92.9	105.2	0.015	0.097	LW	
		Flat	7.6	6.8	0.006	0.007	LW-LF	
	1	Stiffened flat	7.7	6.6	0.006	0.020	LW-LF	Semi-Rigid
		Folded	7.9	7.3	0.005	0.018	LW	
		Curved	8.2	7.8	0.005	0.011	LW	
		Flat	23.6	23.4	0.011	0.020	LW-LF	
	2	Stiffened flat	23.8	23.7	0.011	0.040	LW-LF	Semi-Rigid
		Folded	24.2	26.0	0.010	0.038	LW	
Square		Curved	26.3	26.3	0.010	0.019	LW	
		Flat	54.5	62.5	0.015	0.041	LW-LF	
	4	Stiffened flat	55.0	60.8	0.015	0.058	LW-LF	Rigid
		Folded	59.6	69.5	0.014	0.059	LW	
		Curved	62.1	69.8	0.013	0.040	LW	
		Flat	101.0	118.4	0.017	0.058	LW-LF	
	6	Stiffened flat	104.4	118.7	0.018	0.069	LW-LF	Rigid
		Folded	112.9	133.6	0.015	0.088	LW	
		Curved	115.2	123.7	0.014	0.069	LW	

* LF: Local buckling in flange;   LW: Local buckling in web

B.6.5. Energy Dissipation

In this study, the area under the FEMA idealised bilinear curves (see Section 5.3) is used to calculate the energy dissipation capacity of the different CFS connections. Table B.4 lists the energy dissipation capacity results without and with bolting friction-slip mechanism (stand for (E) and (E_f), respectively). It can be seen that the energy dissipation capacity of connections with beam cross-section class 3 and 4 (2 mm and 1 mm thickness) is almost negligible due to premature buckling of the CFS beams at early stage of loading. However, class 1 and 2 elements (6 mm and 4 mm thickness) with the same cross-sectional shapes can develop their full plastic moment capacity (see section 4.1), and therefore, they result in significantly higher (up to 40 times) energy dissipation capacity in the connections.

It is shown that using bolting friction-slip mechanism can increase the energy dissipation capacity of the connections by approximately up to 200% and 50% for cross-sections class 3-4 and class 1-2, respectively. This is especially evident when diamond configuration of the bolts is used. The results indicate that in general stiffened-flange and folded-flange sections provide the highest energy dissipation capacity in the connections compared to other cross-sectional types in both connections with and without bolting friction-slip mechanism. It is also shown that the bolt distribution can play an important role in increasing the energy dissipation capacity of the connections. Using conventional square bolt configuration generally leads to higher energy dissipation capacity (up to 25%) in the connections with beam cross-section class 3 and 4, while diamond bolt configuration usually provides higher (up to 70%) energy dissipation capacity when class 1 and 2 elements are used.

It should be noted that CFS connection with bolting friction-slip mechanism can be designed to provide higher energy dissipation by adjusting bolt pretension force in beam cross-section class 1 and 2, so slippage of the bolts is activated in the plastic stage of the moment-rotation curve. The results of this study showed that reasonable increasing of bolt holes clearance can also slightly increase the energy dissipation capacity of the connections.

Table B.4. Comparison between energy dissipation capacity of the CFS bolted moment connections without (E) and with friction-slip mechanism (E_f)

Plate thickness (mm)	Beam type	Energy dissipation capacity (J)								
		Circle distribution			Diamond distribution			Square distribution		
		E	E_f	E_f/E	E	E_f	E_f/E	E	E_f	E_f/E
1	Flat	210	613	2.92	197	501	2.55	147	547	3.72
	Stiffened	407	719	1.76	308	641	2.08	371	700	1.89
	Folded	334	670	2.00	307	661	2.16	355	760	2.14
	Curved	220	559	2.54	199	564	2.83	196	610	3.11
2	Flat	478	876	1.83	393	715	1.82	294	782	2.66
	Stiffened	815	1170	1.44	615	915	1.49	741	1144	1.54
	Folded	669	1010	1.51	613	944	1.54	709	1170	1.65
	Curved	440	799	1.82	398	805	2.02	392	872	2.22
4	Flat	2441	3059	1.25	2257	2794	1.24	1930	2281	1.18
	Stiffened	3081	3812	1.24	2767	3928	1.42	2846	3474	1.22
	Folded	2686	3349	1.25	3049	3770	1.24	2998	3271	1.09
	Curved	2263	2884	1.27	2702	4094	1.52	2131	2419	1.14
6	Flat	9178	9229	1.01	7724	8776	1.14	5653	7097	1.26
	Stiffened	10298	10460	1.02	8837	10094	1.14	6517	7889	1.21
	Folded	10525	10681	1.01	11720	13278	1.13	9149	10223	1.12
	Curved	7141	7578	1.06	8256	9814	1.19	7499	7993	1.07

B.6.6. Damping Coefficient

Damping coefficient is considered as an important indicator to evaluate the energy dissipation capability of structures (Chopra, Wijesundara et al., Bezabeh et al., 2016). In this study, the following equivalent viscous damping coefficient, h_e, is adopted (Bolong, 1989, Yang et al., 2014, Yin et al., 2016):

$$h_e = \frac{1}{2\pi} \frac{S_{ABC} + S_{CDA}}{S_{OBE} + S_{ODF}} \tag{B.7}$$

where the area of $S_{\Delta ABC} + S_{\Delta CDA}$ represents the energy dissipated in one cycle at the expected rotation (hatched area in Fig. B.27). $S_{\Delta OBE} + S_{\Delta ODF}$ shows the total strain energy of the connection at the expected rotation by assuming the connection behaves elastically (double hatched area in Fig. B.27). Points B and D denote, respectively, the maximum positive and

negative moment capacities of a hysteresis loop. The h_e damping coefficient can demonstrate the plumpness of the hysteresis loops in non-linear systems.
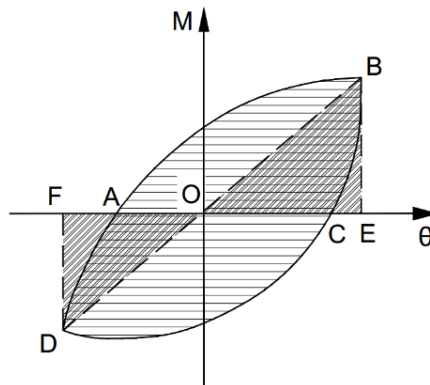
Fig. B.27. Definition of the equivalent viscous damping coefficient

In this study, the equivalent viscous damping coefficients are calculated for the following two scenarios: (i) peak moment loops, in which the hysteresis loop reaches the maximum flexural capacity; (ii) ultimate moment (near-failure) loops, when the hysteresis loop reaches the ultimate point (corresponding to 20% drop from peak moment). Figs. B.28 and B.29 show the equivalent viscous damping coefficients at peak and ultimate moment loops, respectively, for the CFS bolted moment connections using conventional square bolt configuration with and without friction-slip mechanism. It can be seen that the damping coefficients calculated based on the peak moment loops are smaller (up to 20 %) compared to those calculated based on the ultimate moment loops. However, in general, the results are consistent and follow a very similar trend.

It is shown in Figs. B.28 and B.29 that using friction-slip system in the connections with cross-sectional class 3 and 4 can significantly increase (up to 6 times) the equivalent damping coefficient of the connections, while it may cause a small reduction in the damping coefficient when cross-sections class 1 and 2 are used. The main reason for this behaviour is that the plastic moment play a more dominant role in the damping of the connection with class 1 and 2 elements, and therefore, to improve the equivalent viscous damping coefficient the activation of slip resistance has to be postponed from elastic to inelastic stage of moment-rotation curve through adjusting bolt pretension forces. The results imply that connections with class 3 and 4 beam elements (2 mm and 1 mm thickness) without friction-slip mechanism provide very low viscous damping coefficients and, hence, may not be suitable for seismic applications. This problem can be sufficiently addressed by increasing the damping of the connections through a friction-slip mechanism (see Figs. B.18 and B.19). It can be also noticed

that, for each type of connection, the effect of cross-sectional class on the damping coefficient is practically negligible.
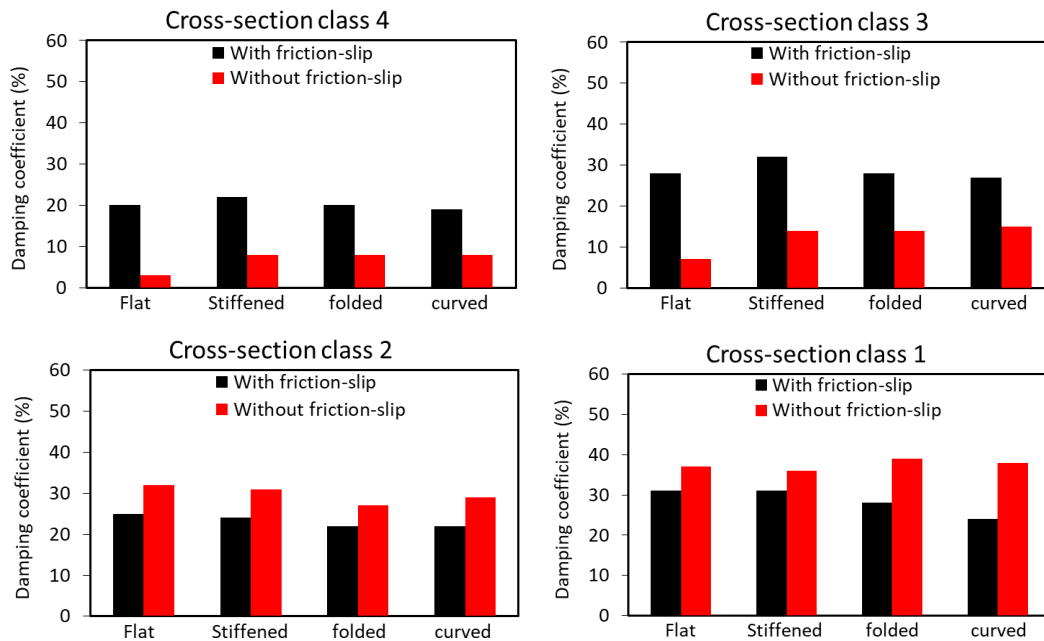
Fig. B.28. Equivalent viscous damping coefficients calculated based peak moment loops
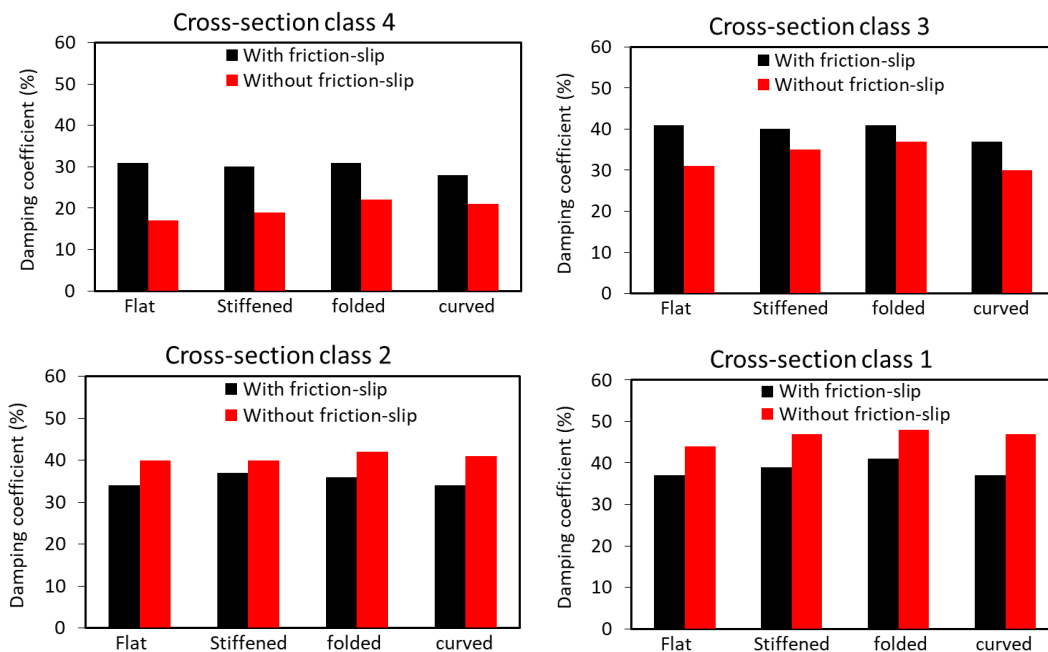
Fig. B.29. Equivalent viscous damping coefficients calculated based on ultimate moment loops

B.6.7.   Ductility Ratio

Moment-resisting connections in seismic resisting systems should provide enough ductility to withstand and redistribute the seismic loads. The fundamental definition of ductility ratio (μ) is the ratio of the ultimate rotation (θ_u) to the yield rotation (θ_y), as follows:

$$\mu = \theta_u / \theta_y > 1 \tag{B.8}$$

The ductility ratio of the CFS connections in this study is calculated based on the results of the FEMA bi-linear idealisation models by using the rotation at 80% of the post-ultimate moment as the ultimate rotation (see Fig. B.26). It should be noted that since yield rotation (θ_y) of the connections with friction-slip mechanism cannot be reasonably obtained by using FEMA idealisation model, the yield rotation is assumed to be the same as those calculated for the similar connections without friction-slip mechanism (Ye, 2016). The ductility ratios of the CFS connections with and without friction- slip mechanism are compared in Fig. B.30 by considering different design parameters including beam cross-sections, bolt configurations and CFS plate thicknesses. The results indicate that using bolting friction-slip mechanism is particularly more efficient for the cross-sections with lower plate thickness (i.e. class 3 and 4), where they can lead to up to 100% higher ductility ratios compared to standard bolted moment connections. This can significantly improve the seismic performance of the connections with class 3 and 4 beam sections and make them suitable for seismic applications similar to those with beam classes 1 and 2.

It can be observed from Fig. B.30 that, in general, the ductility ratio of the connections is considerably influenced by the cross-sectional shape and classification of the CFS beam and the selected bolt configuration. Connections with lower beam cross-sectional class always exhibit higher ductility ratios. It can be also seen that, for the same beam cross-sectional class and bolt configuration, the highest ductility ratio is observed for folded-flange sections. For the connections with class 1 and 2 folded-flange and curved-flange sections, diamond bolt configuration leads to the highest ductility ratios. However, by using class 3 and 4 beam channels, the circle bolt configuration generally provides to highest ductility ratios. While circle and diamond bolt configurations can significantly improve (up to 85%) the ductility of the CFS moment connections with conventional square bolt configuration, they may not be very practical for the connections with a large number of bolts.
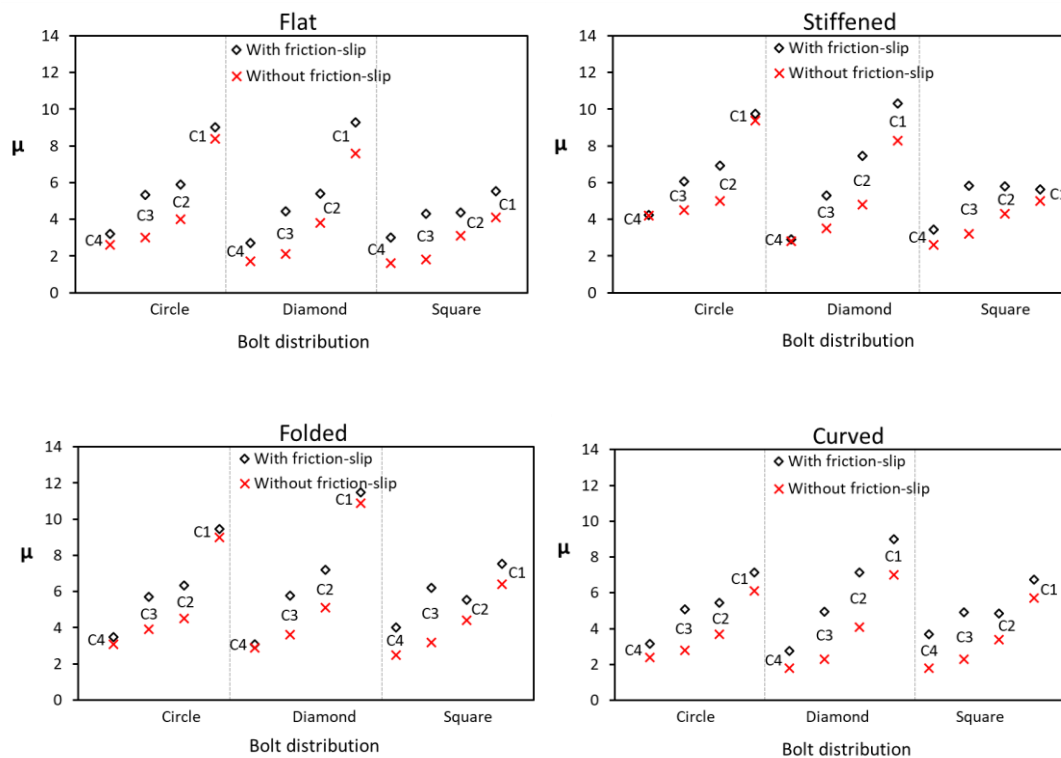
Fig. B.30. Ductility ratio of CFS connections as a function of bolt configuration and beam cross-section class (C1, C2, C3, and C4 are cross-section classes 1, 2, 3 and 4, respectively)

B.6.8.   Code Requirement

Most current seismic design guidelines (e.g. AISC 341-16 (2016) and Eurocode 8) categorise steel moment-resisting frames into Special Moment Frames (SMFs), Intermediate Moment Frames (IMFs), and Ordinary Moment Frames (OMFs) based on their ductility capacity. AISC 341-16 (2016) suggests that SMFs, IMFs and OMFs should be capable of, respectively, exhibiting over 4%, between 2% and 4%, and less than 2% inter-storey drift with less than 20% strength degradation. In the absence of clear criteria for CFS systems, the same definitions are used in this study to assess the suitability of moment CFS connections for seismic applications. Based on the results of the cyclic moment-rotation envelope curves (see Section B.6.1), Table B.5 lists the AISC structural performance category of each type of connections. It is shown that some connections with beam cross-sections class 4 and 3 do not satisfy SMF and IMF requirements, and therefore, cannot be used in seismic regions. However, accommodating bolting friction-slip system in these CFS bolted moment connections can considerably improve their ductility capacity to satisfy IMF and even SMF design requirements. This conclusion is in complete agreement with the results in previous sections and highlights the efficiency of the proposed friction-slip system for CFS moment-resisting frames in seismic regions. It should be noted that in this study the effects of low cycle

fatigue and fracture of steel plate under cyclic loading have not been taken into account, which can be a topic for further research in this area.

Table B.5. Comparison between the structural performance of the CFS bolted moment connections with and without friction-slip mechanism according to AISC requirements

Plate thickness (mm)	Beam type	AISC requirements					
		Circle distribution		Diamond distribution		Square distribution	
		Without friction-slip	With friction-slip	Without friction-slip	With friction-slip	Without friction-slip	With friction-slip
1	Flat	OMF	IMF	OMF	IMF	OMF	IMF
	Stiffened	IMF	SMF	IMF	SMF	OMF	IMF
	Folded	IMF	SMF	IMF	SMF	OMF	SMF
	Curved	OMF	SMF	IMF	SMF	OMF	IMF
2	Flat	IMF	SMF	IMF	SMF	OMF	SMF
	Stiffened	SMF	SMF	IMF	SMF	SMF	SMF
	Folded	IMF	SMF	IMF	SMF	IMF	SMF
	Curved	IMF	SMF	IMF	SMF	IMF	SMF
4	Flat	SMF	SMF	SMF	SMF	SMF	SMF
	Stiffened	SMF	SMF	SMF	SMF	SMF	SMF
	Folded	SMF	SMF	SMF	SMF	SMF	SMF
	Curved	SMF	SMF	SMF	SMF	SMF	SMF
6	Flat	SMF	SMF	SMF	SMF	SMF	SMF
	Stiffened	SMF	SMF	SMF	SMF	SMF	SMF
	Folded	SMF	SMF	SMF	SMF	SMF	SMF
	Curved	SMF	SMF	SMF	SMF	SMF	SMF

B.6.9.   Effect of Gusset Plate Thickness

In general, previous studies indicated that the design of gusset plate in the stiffened end-plate bolted joints can influence the transfer mechanism of the forces and affect the cyclic rotational behaviour of the connections (D'Aniello et al., 2017b, Tartaglia et al., 2018). Therefore, in this section the effect of gusset plate thickness on the cyclic behaviour of the bolted-moment connection is investigated. Fig. B.31 compares the moment-rotation curves of the connections

with class 1 to 4 flat channel beam sections (see Table B.1) using the square bolt configuration and various gusset plate thicknesses. In general, using gusset plates with the same or lower thickness as the CFS beam (1, 2, 4 and 6 mm thickness for class 4, 3, 2 and 1 sections, respectively) shifts the local buckling from the CFS beam to the gusset plate. As shown in Fig. B.31, this premature failure mode can significantly reduce the moment capacity of the connections and lead to higher post-buckling strength degradations. This undesirable failure mode can be prevented by increasing the gusset plate thickness slightly above the thickness of the CFS beam.
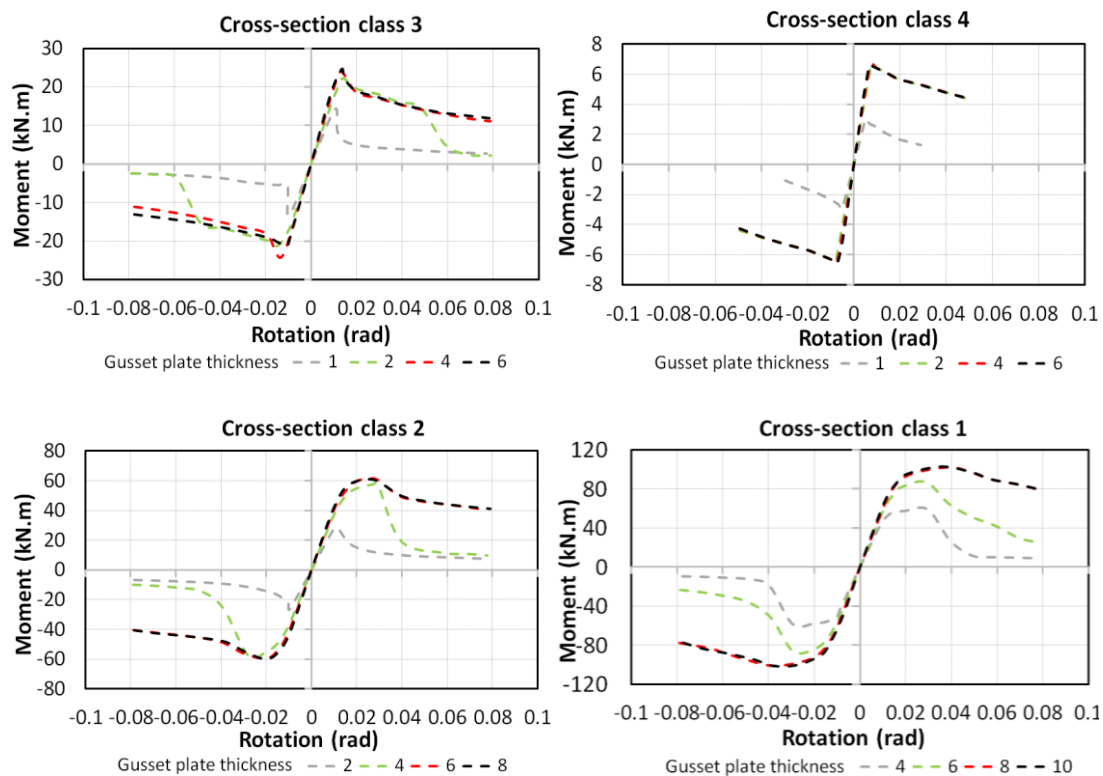
Fig. B.31. Effect of gusset plate thickness on the moment-rotation behaviour of CFS connections

B.7. SUMMARY

Previous studies at the connection level (i.e. Chapters 5 and 6) investigated the static behaviour and design of CFS bolted moment-resisting connections and optimised their seismic characteristics based on post-buckling behaviour, respectively. This study aimed to investigate the efficiency of such connections with and without bolting friction-slip mechanism and to provide more efficient design solutions for CFS frames in seismic regions. Experimentally validated FE models were developed by incorporating geometrical imperfections, material nonlinearity and detailed characteristics of the bolting friction-slip system. A comprehensive

analytical study was conducted to assess the influence of CFS beam cross-sectional shape and classification, bolt configuration, and slip resistance on the moment capacity, energy dissipation capacity, equivalent damping coefficient and ductility of the connections.

B.8. CONCLUDING REMARKS

Based on the results, the following conclusions can be drawn:

- The dominant failure mode of the CFS bolted-moment connections is due to the local buckling of the CFS beam sections close to the first row of the bolts. Curved and folded flange channels can postpone the local buckling of the flange by creating an in-plane stiffness through arching action and shifting the local buckling failure to the web. However, using bent flange channels (folded and curved) can only increase the moment capacity of the connections by up to 10%.

- The simplified method adopted for modelling slippage in bolted moment connection using fastener elements parallel with stop elements in ABAQUS provides an efficient and reliable tool to simulate the experimental moment-rotation behaviour and dominant failure mode of connections with friction-slip mechanism.

- Accommodating friction-slip mechanism provides a horizontal shift in the hysteretic moment-rotation response of the connections, which reduces the stress concentrations in the connection zone and postpones the failure of the CFS beam element. The effect of pretension force is generally negligible on the flexural capacity of the connections, while the bolt configuration and CFS beam cross-sectional shape and classification play the main roles. Generally using bent flange cross-section and square bolt configuration provides higher (up to 40%) flexural capacity in the connections, which is more evident in the case of higher plate thickness.

- Using bolting friction-slip mechanism can significantly improve (up to 200%) the energy dissipation capacity of the connections, especially when class 3 and 4 beams are used. Stiffened-flange and folded-flange sections generally provide the highest energy dissipation capacity, while using diamond bolt configuration can increase the energy dissipation capacity of the connections with class 1 and 2 beams by up to 70%.

- The proposed friction-slip mechanism can significantly increase (up to 6 times) the equivalent damping coefficient of the connections with class 3 and 4 beam sections, while it may cause a small reduction in the damping coefficient when cross-sections class 1 and

2 are used. This problem can be addressed by adjusting the slip resistance to be activated in the inelastic stage of moment-rotation curve. It was also observed that the effect of cross-sectional class on the damping coefficient of the connections is practically negligible.

- The ductility of the CFS bolted moment connections can be significantly (up to 100%) increased by using friction-slip mechanism, which is particularly beneficial for cold-formed steel sections with lower plate thickness (class 3 and 4). Folded-flange sections generally resulted in the highest ductility ratios, while diamond and circle bolt configurations provided larger ductility ratios for the connections with cross-section class 1 and 2 and class 3 and 4, respectively. It was shown that conventional bolted moment connections with class 3 and 4 CFS beam sections do not generally satisfy the AISC regulations for IMF and SMF systems; however, accommodating the bolting friction-slip mechanism can improve their seismic performance to be suitable for moment-resisting frames in high seismic regions.

- Using gusset plates with the same or lower thickness as the CFS beam may lead to a premature failure mode in the gusset plate and considerably reduce the moment capacity of the connection. However, this failure mode can be efficiently prevented by increasing the gusset plate thickness slightly above the thickness of the CFS beam.

APPENDIX C

Coupled Element and Structural Level Optimisation Framework for Cold-Formed Steel Frames

C.1. INTRODUCTION

Optimisation of cold-formed steel (CFS) structures can be challenging due to the complex behaviour of thin-walled CFS sections affected by different buckling modes. Chapters 3 and 4 investigated the best design solutions for the buckling strength of CFS elements determined according to Eurocode 3. The results of these two chapters are now used in this appendix where a coupled framework is presented for element and structural level optimisation of CFS portal frames, under serviceability limit state (SLS) and ultimate limit state (ULS) conditions, using Genetic Algorithm. First, CFS lipped-channel beam sections are optimised with respect to their flexural capacity determined in accordance with the effective width method specified in Eurocode 3 (EC3). The relative dimensions of the cross-section are considered as the main design variables, while the EC3 plate dimensions and slenderness limits and a number of manufacturing and end-use constraints are taken into account in the optimisation process. The results show that the optimum CFS sections exhibit significantly higher (up to 84%) ultimate capacity compared to the standard lipped channel sections with the same plate width and thickness. The structural level optimisation is then carried out to obtain the optimal design solution for a long-span CFS portal frame with knee braces under SLS and ULS conditions. Compared to conventional optimisation using standard cross-sections, it is shown that the proposed coupled framework leads to more cost-effective solutions (up to 20% less structural material) by using the more efficient CFS cross-sectional shapes optimised for generic applications. The results also indicate that optimising the frame geometry and knee brace

configuration can noticeably improve the structural performance and reduce the required structural weight, especially when both ULS and SLS conditions are considered.

C.2. BACKGROUND

Cold-formed steel (CFS) sections are increasingly used in construction practice due to their advantages such as a relatively high strength-to-weight ratio, greater flexibility in manufacturing, and ease of handling, transportation and installation. The flexibility of CFS cross-sectional shapes, through determining optimum relative dimensions of channel sections (i.e. size optimisation), provides an excellent opportunity to enhance the load-carrying capacity of available standard sections. This enhancement of capacity at the element level may subsequently improve the capacity of the CFS frame system, especially for medium to long-span CFS portal frame buildings.

Optimisation of CFS sections can be a challenging task due to typical manufacturing and end-use design constraints and complex behaviour of CFS elements controlled by combinations of local, global and distortional buckling modes. Several investigations have previously been conducted to optimise predefined standard CFS profiles such as C channels, and I and Z shape beams (Adeli and Karim, 1997, Karim and Adeli, 1999). The results demonstrated that optimising the cross-sectional geometry of simply-supported CFS beams subjected to uniformly distributed vertical or transverse load can substantially improve their flexural capacity, as compared with standard sections. Ye et al. (Ye et al., 2016b) showed that by simply changing the relative dimensions of standard commercial channels, optimised sections could be obtained with considerably (up to 30%) higher flexural capacities. Based on their study, Fig. C.1 compares the dimensions of a standard CFS lipped-channel beam section and the section with the same coil width and plate thickness optimised for maximum flexural capacity. In a follow-up study, Ye et al. (Ye et al., 2016a) concluded that the optimisation on unbraced CFS beams with different length could offer up to 75% higher flexural strength compared to using standard sections. Gilbert et al. (Gilbert et al., 2012a) and Wang et al. (Wang et al., 2016a) adopted Genetic Algorithm (GA) and Augmented Lagrangian methods to minimised the required material to achieve the same level of strength in CFS column and beam-column members, respectively. Leng et al. (Leng et al., 2011, Leng et al., 2014) optimised the shape of CFS columns for maximum compressive capacity using and unconstraint optimisation methods. It was demonstrated that by restricting the cross-sectional shape to pre-determined elements, the capacity of the optimised designs may drop significantly compared to unconstrained optimum solutions. In another relevant study, Tran

et al. (Tran and Li, 2006) presented a global optimisation technique using the trust-region method (TRM) for designing the cross-section of channel beams subjected to uniformly distributed transverse loading based on the yielding strength, deflection limitation, and different instability modes.

| (a) Standard section | (b) Optimised section |
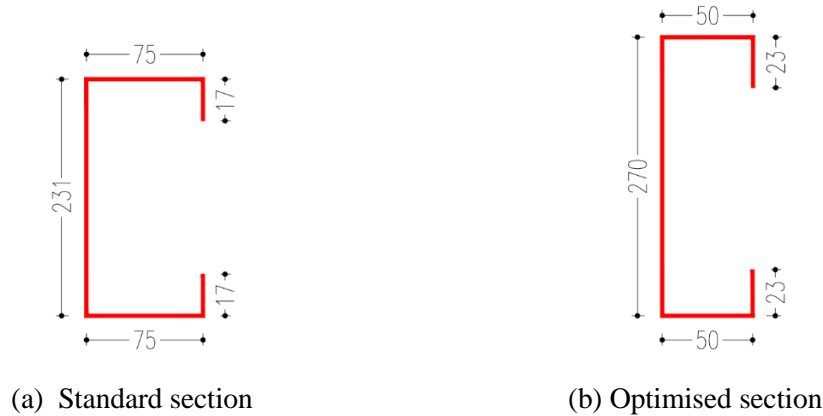
Fig. C.1. An example of optimised vs standard CFS lipped-channel beam sections with 1.5 mm plate thickness proposed by Ye et al. (2016b)

More recently, Mojtabaei et al. (Mojtabaei et al., 2019b) adopted Big Bang-Big Crunch (BB-BC) algorithm to obtain optimum CFS beam sections at serviceability limit state (SLS) and ultimate limit state (ULS) conditions. They showed that, for the same amount of material, the flexural capacity and stiffness of optimum CFS beams could be increased by up to 58% and 44%, respectively, compared to their standard counterparts. Using GA optimisation method, Parastesh et al. (Parastesh et al., 2019) optimised symmetrical CFS beam-column members by considering practical and manufacturing constraints. It was observed that increasing the eccentricity of the axial load generally leads to more spread sections especially in shorter members. Ye et al. (Ye et al., 2018a) also proposed an advanced shape optimisation framework to achieve maximum energy dissipation of CFS sections in uniaxial bending by providing a link between detailed nonlinear Finite Element (FE) analyses and Particle Swarm Optimisation (PSO) algorithm.

It should be noted that all of the above-mentioned studies were limited to the element level optimisation, and therefore, the effect of using optimised sections on the overall structural behaviour of a building has not been investigated in CFS. While optimum design of CFS elements has been extensively investigated in the past, considerably less research has been conducted on optimisation of CFS structural systems. In one of the few studies available in this area, Phan et al. (Phan et al., 2013c, Phan et al., 2013a) used Genetic Algorithm (GA) to optimise CFS portal frames with small to medium spans and reported a variation of optimal geometry in terms of pitch and frame spacing for a range of typical column heights. In a

follow-up study, it was shown that by taking into account the effects of stressed-skin action (owing to the stiffening effect of roof diaphragm) in the optimisation process, the material cost of the CFS portal frame structural system can be noticeably (up to 53%) reduced (Phan et al., 2015). Similar studies on hot-rolled steel portal frames reached a similar conclusion and demonstrated that such frame systems were controlled by serviceability limits (McKinstray et al., 2015, Phan et al., 2013b).

As mentioned above, several studies have been conducted either on the optimisation of cross-sectional dimensions of CFS sections or on the geometry of the CFS frames. However, currently there is no study available to couple these two optimisation levels. It should be noted that for practical applications the simultaneous optimisation of cross-sectional dimensions and the geometry of the structural system is too computationally expensive. To address this issue, a novel methodology is proposed to simplify this complex optimisation process by coupling the element and structural level optimisations. The CFS elements are first optimised for a range of element length, plate thickness and coil width under different uniform distributed load (UDL) levels (continues optimisation). The optimised elements are then used as structural components of the frame to obtain the best design solution under different serviceability limit state (SLS) and ultimate limit state (ULS) conditions (discrete optimisation), while the optimisation solver simultaneously searches through a practical range of values for the roof pitch, frame spacing, and knee brace configuration (i.e. knee depth and knee angle). It is shown that using this innovative approach can significantly reduce the computational cost required for simultaneous optimisation of CFS elements and geometry of the structural systems.

At element level, a practical procedure is presented for development of conventional CFS back-to-back lipped-channel beam sections with maximum flexural strength by taking into account local, distortional and global buckling modes. To provide a comprehensive range of optimum sections suitable for CFS portal frames, CFS beam members with different span lengths subjected to various levels of uniformly distributed loads (UDLs) are considered in this study. A Genetic Algorithm (GA) program is developed in MATLAB (Mathworks, 2011) to find the optimum shape of CFS beam members designed according to European design guidelines (CEN, 2005e, CEN, 2005c, CEN, 2006a) by considering the relative cross-sectional dimensions as main design variables. The EC3 geometrical requirements, as well as a number of practical and manufacturing constraints, are also included in the optimisation process. The efficiency of the proposed optimum CFS cross-sections is then investigated compared to standard commercially available back-to-back sections. At structural level, a long span CFS portal frame with knee braces subjected to different serviceability limit state (SLS) and ultimate limit state (ULS) design load combinations is first analysed using Finite Element (FE)

ANSYS software (ANSYS Inc., 2009) to determine elements' internal forces and lateral displacement of the joints. Subsequently, the GA program is adopted to find the best design solution (i.e. with minimum structural weight) by using standard and optimum CFS sections and considering a set of predefined structural design constraints. The results are then used to assess the efficiency of the proposed coupled framework and to investigate the influence of knee brace configuration on the structure performance of the optimised frame.

C.3. DESIGN OF CFS ELEMENTS

The structural elements of CFS portal frames are designed in accordance with EC3, taking into account ultimate limit state (ULS) and serviceability limit state (SLS) conditions. This section first presents a brief description of effective width method, used to calculate the buckling resistance of the CFS sections at ULS, following the provisions of EC3 Part 1-3 (CEN, 2005c) and EC3 Part 1-5 (CEN, 2006a). The design procedure of CFS members at ULS is then provided to take into account the effect of length based on the provisions of EC3 Part 1-1 (CEN, 2005e). Finally, SLS checks, which are used to control the deflection of the designed CFS members, are briefly described. While it is more accurate to consider the column and beam elements as built-up members (Meza et al., 2019), the interactions between the back-to-back channels were neglected in this study for the sake of simplicity and providing more conservative design solutions.

C.3.1. Ultimate Limit State (ULS) Design

C.3.1.1 *Buckling resistance of the cross-section*

C.3.1.1.1 Local buckling

In Eurocode 3 (EC3), the effect of local buckling is considered through the effective width concept. It is based on the observation that local buckling causes a loss of compressive stiffness in the centre of a plate supported along both longitudinal edges (labelled an 'internal' plate element), or along the free edge of a plate supported along one longitudinal edge (an 'outstand' element) as a result of non-linear effects. The corner zones of the cross-section consequently become the main load-bearing areas. This implied that the local buckling causes the centroid of the effective cross-section to shift over a distance e_N relative to the original centroid of the gross cross-section. As an instance, the effective area of a sample cross-section under major axis pure bending moment are shown in Fig. C.2 highlighted in solid black lines. According to EC3 Part 1-5 (CEN, 2006a), the effective widths of internal and outstand compression elements are given by:

$$\rho=\frac{b_e}{b} = \begin{cases} \dfrac{1}{\lambda_l}\left(1-\dfrac{0.055(3+\psi)}{\lambda_l}\right) & \text{for interal compression element} \\[2ex] \dfrac{1}{\lambda_l}\left(1-\dfrac{0.188}{\lambda_l}\right) & \text{for outstand compression element} \end{cases} \tag{C.1}$$

where:

$$\lambda_l = \sqrt{\frac{f_y}{\sigma_{cr}}} \tag{C.2}$$

In Equation C.1, ρ is the reduction factor on the plate width, while b and b_e are the total and the effective width of the plate, respectively. The slenderness ratio λ_l relates the material yield stress f_y to the elastic local buckling stress of the plate σ_{cr} and ψ is the ratio of the end stresses in the plate. It should be noted that EC3 Part 1-3 (CEN, 2005c) stipulates an iterative process to calculate the effective width of the cross-section since the neutral axis of the effective cross-section shifts over a distance. This affects the stress distribution due to loss of effective section in the flanges and the web. Although not required by EC3 Part 1-3 (CEN, 2005c) guidelines, full iterations to convergence are carried out in this study.
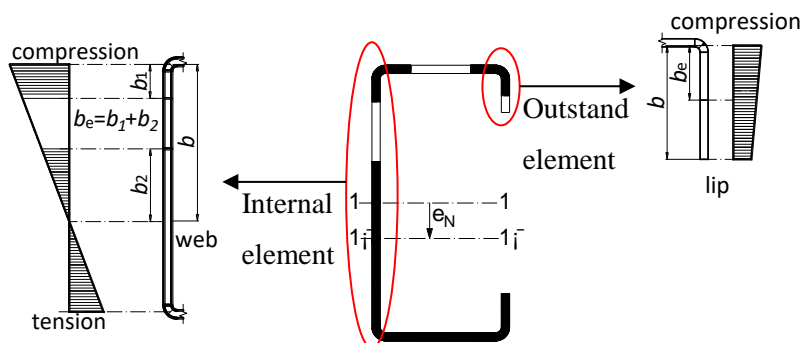
Fig. C.2. Effective width of the lipped-channel section based on EC3 (CEN, 2005c)

C.3.1.1.2 Distortional buckling

Distortional buckling describes the distortion of the cross-section with rotation and translation at interior elements, leading to both in-plane and out-of-plane displacements of constituent plates. EC3 takes into account the local buckling and distortional buckling of CFS sections by reducing the effective width and the effective thickness of the constituent plates, respectively. The distortional slenderness, λ_d, can be calculated based on a simplified model, in which the restraining effects of the adjacent plates in the cross-section are taken into account by using equivalent elastic springs as shown in Fig. C.3:

$$\lambda_d = \sqrt{f_y / \sigma_{cr,s}} \tag{C.3}$$

Where $\sigma_{cr,s}$ is the elastic buckling stress of the plate-stiffener assembly given by:

$$\sigma_{cr,s} = \frac{2\sqrt{KEI_s}}{A_s} \tag{C.4}$$

In the above equation, K and A_s are the stiffness of the spring (per unit length) and the effective cross-sectional area of the stiffener, respectively. E is the Young's modulus and I_s is the moment of inertia of the stiffener about the centroid parallel to the plate element. K is a function of the flexural stiffness of the adjacent plates and can be calculated based on the deflection of the stiffener assembly under a unit load $u=1$ (per unit length).
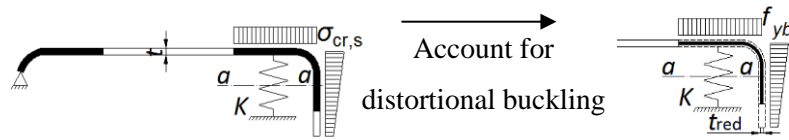
Fig. C.3. Simplified models for distortional buckling of flange for CFS lipped-channel section (CEN, 2006a)

EC3 also recommends using an iterative process to update the local slenderness ratio of the plates, λ_l, by replacing $\lambda_{l,red} = \lambda_l\sqrt{\chi_d}$. χ_d is the reduction factor corresponding to the distortional buckling resistance and can be calculated by using the relative slenderness λ_d. For the calculation of λ_d, fy should be substituted by $\sigma_{com} = \chi_d f_y$ in each iteration. This optional iteration loop was considered in this study until $\chi_{d,n} \approx \chi_{d,(n-1)}$.

C.3.1.1.3   Cross-section check

   Based on EC3 part 1-3 (CEN, 2005c), CFS cross-sections subjected to combined axial compression N_{Ed} and bending moments $M_{y,Ed}$ should satisfy the following criterion:

$$\frac{N_{Ed}}{N_{c,Rd}} + \frac{M_{y,Ed} + \Delta M_{y,Ed}}{M_{cy,Rd,com}} \leq 1 \tag{C.5}$$

In the above equation, $N_{c,Rd} = \frac{A_{eff}f_{yb}}{\gamma_{M_0}}$ is the design capacity resistance of the cross-section. A_{eff} is the effective area of the cross-section obtained by assuming a uniform compressive

stress $\sigma_{com,Ed} = \frac{f_{yb}}{\gamma_{M_0}}$, and f_{yb} is the basic yield strength. Additional moment $\Delta M_{y,Ed}$ due to the shift of the effective centroidal axes can be calculated as:

$$\Delta M_{y,Ed} = N_{Ed}.e_N \tag{C.6}$$

C.3.1.2 *Buckling resistance of the member*

C.3.1.2.1 Knee brace member

The design buckling resistance of a compression member with Class 4 cross-section is given by EC3:

$$N_{b,Rd} = \frac{\chi A_{eff} f_y}{\gamma_{M_1}} \tag{C.7}$$

where A_{eff} is the effective area of the cross-section and χ is the reduction factor for the relevant buckling mode (CEN, 2005e). Reduction factor (χ) is determined using a minimum of reduction factors for flexural buckling, torsion buckling, and flexural-torsional buckling modes.

C.3.1.2.2 Beam-column member

According to EC3, the design of CFS beam-column members requires the calculation of slenderness for various global buckling modes, defined as:

$$\begin{cases} \lambda = \sqrt{\dfrac{A_{eff} f_y}{N_{cr}}} & \text{slenderness for flexural, torsional, and flexural torsional} \\[4mm] \lambda_{LT} = \sqrt{\dfrac{W_{eff} f_y}{M_{cr}}} & \text{slenderness for lateral-torsional} \end{cases} \tag{C.8}$$

Where N_{cr} is the elastic axial critical compressive load, W_{eff} is the effective section modulus, and M_{cr} is the elastic lateral-torsional buckling moment based on the gross cross-section. It is worth noting that EC3 Part 1.1 (CEN, 2005e) implicitly considers the effects of uniform distributed load on the lateral-torsional buckling resistance. For slenderness $\lambda_{LT} \leq$ 0.4 or for $M_{y,Ed}/M_{cr} \leq 0.16$, lateral-torsional buckling effects may be ignored and only cross-sectional checks are required.

C.3.1.2.3   Capacity check

The capacity of the frame members in pure axial compression and pure bending moment should be verified using the Equations C.9 and C.10, respectively:

$$\frac{N_{Ed}}{N_{b,Rd}} \leq 1 \tag{C.9}$$

$$\frac{M_{y,Ed}}{M_{b,Rd}} \leq 1 \tag{C.10}$$

Where $M_{b,Rd} = \chi_{LT} W_{eff} f_y / \gamma_{M1}$ is the design lateral-torsional buckling resistance moment. χ_{LT} is the reduction factor to take into account lateral-torsional buckling effects. The Clause 6.2.5(2) of EN1993-1-3 (CEN, 2005c) recommends to use the following interaction formula to consider the interaction between axial force and bending moment in beam-column elements:

$$\left(\frac{N_{Ed}}{N_{b,Rd}}\right)^{0.8} + \left(\frac{M_{y,Ed}}{M_{b,Rd}}\right)^{0.8} \leq 1 \tag{C.11}$$

C.3.2.   Serviceability Limit State (SLS) Design

EC3 part 1-3 (CEN, 2005c) stipulates that the properties of the effective cross-section explained in previous sections must be used in all SLS checks for CFS members. The second moment of area of CFS sections can be also estimated by an interpolation between effective and gross cross-sections for the design load combination using the following expression:

$$I_{fic} = I_{gr} - \frac{\sigma_{gr}}{\sigma} (I_{gr} - I(\sigma)_{eff}) \tag{C.12}$$

where I_{gr} is the second moment of area of the gross cross-section, σ_{gr} is the maximum compressive bending stress based on the gross cross-section at serviceability limit state (SLS), and $I(\sigma)_{eff}$ is the second moment of area of the effective cross-section by considering local buckling estimated based on maximum stress $\sigma \geq \sigma_{gr}$.

C.4.   DESIGN OF CFS PORTAL FRAME

The characteristic values of the gravity actions applied on the proposed CFS portal frame are determined following the provisions of Eurocode 1 (BS EN 1991-1-1, 2002, Koschmidder and

Brown, 2012) by assuming that the frame is located at Belfast, Northern Ireland. The permanent load (G) and variable loads (Q), including imposed load and snow load, are considered as below:

- Permanent load: 0.15 kN/m^2 + self-weight of primary steel members
- Snow load: 0.4 kN/m^2
- Imposed load: 0.6 kN/m^2

The wind load is laterally applied to the CFS frame at both transverse and longitudinal directions in accordance with Eurocode 1, Part 1-4 (2005). The design wind pressures (*w*) is calculated using the following expression:

$$w = q_p(C_{pe} - C_{pi})$$ (C.13)

where q_p is the peak velocity pressure taken equal to 1.0 kN/m^2, and C_{pe} and C_{pi} are the external and internal pressure coefficients, respectively. It is assumed that the proposed frame is under normal permeability condition without dominant openings, hence C_{pi} possesses the minimum values of -0.3 and +0.2 for negative and positive pressure, respectively. In total, six wind load cases are taken into account in this study (Phan et al., 2015).

The load combinations at ultimate limit state (ULS) design is adopted from Eurocode 0 , Equation 6.10 (2002):

$$\sum_{j\geq1}\gamma_{G,j}G_{k,j} + \gamma_{Q,1}Q_{k,1} + \sum_{i\geq1}\gamma_{Q,i}\psi_{0,i}Q_{k,i}$$ (C.14)

For the serviceability limit state (SLS) design, Equation 6.14b extracted from Eurocode 0 (2002) is used:

$$\sum_{j\geq1}G_{k,j} + P + Q_{k,1} + \sum_{i\geq1}\psi_{0,i}Q_{k,i}$$ (C.15)

The design load combinations used in this study, including the partial factors and combination factors, are listed in Table C.1. It is worth mentioning that the load combinations including imposed action of roofs and either wind or snow load are not considered, since it is expected that the permanent action with imposed load or the permanent action with snow load and wind load provide the critical load combinations for ultimate and serviceability limit state designs (Koschmidder and Brown, 2012). In this study, the serviceability checks of the CFS portal frame such as vertical deflection at apex and horizontal displacement at eaves joints are determined based on SCI recommendations (SCI Advisory Desk, 2010), in which the lateral

displacement of the eaves joint is limited to 1% of column height and the apex vertical deflection limit is considered to be span/200. The serviceability checks are carried out following the SLS load combinations as listed in Table C.1.

Table C.1. Frame loadings and typical load combinations

Load combinations (LCs)	Permanent actions	Variable actions				
	Partial factor (γ_G)	Leading action		Accompanying action		
		Action	Partial factor (γ_Q)	Action	Partial factor (γ_Q)	Combination factor ψ_0
LC1: Permanent & imposed (ULS)	1.35	Imposed	1.5			
LC2: Permanent, snow & wind (ULS)	1.35	Snow	1.5	Wind	1.5	0.5
LC3: Permanent, wind & snow (ULS)	1.35	Wind	1.5	Snow	1.5	0.5
LC4: SLS 1	1.0	Imposed	1.0			
LC5: SLS 2	1.0	Wind	1.0	Snow	1.0	0.5
LC6: SLS 3	1.0	Snow	1.0	Wind	1.0	0.5

C.5. FRAME MODELLING AND ANALYSES

The CFS long-span portal frame considered in this study is based on the full-scale experimental tests conducted by Blum (Blum, 2016, Blum and Rasmussen, 2019b). The main structural components of the CFS portal frame include CFS columns and rafters consisted of back-to-back lipped-channel sections (BBC). In this study, the geometry of the CFS portal frame is expressed in terms of the following design parameters: span length L_f, column height h_f, pitch of frame θ_f, frame spacing (bay) b_f, knee brace length L_k, knee depth d_k, and knee angle θ_k (see Fig. C.4). The design parameters for the CFS frame used in the reference experimental tests (Blum, 2016, Blum and Rasmussen, 2019b) are: L_f=13.6 m, h_f=5.4 m, θ_f=10º, b_f=3.6 m, L_k=2.68 m, d_k=1.36 m, and θ_k=50º. It is worth noting that more efficient framing system with a given span and column height could be obtained through varying the pitch of frame, frame spacing, and knee brace configuration.
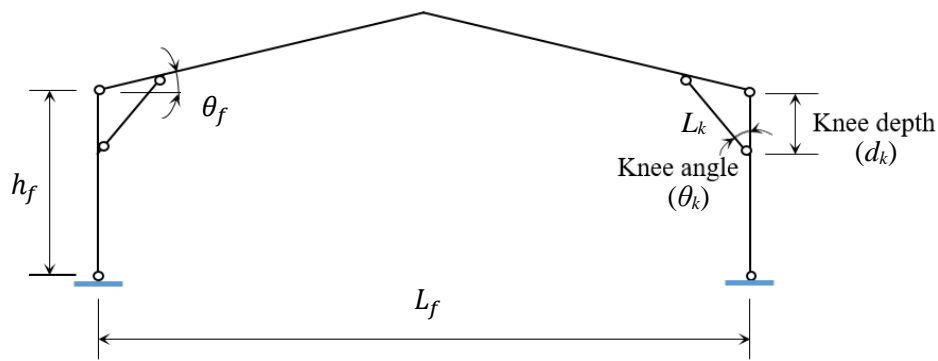
Fig. C.4. Geometry of long-span CFS portal frame with knee braces used in this study

In the reference experimental test, all frame members (i.e. columns and rafters) were laterally restrained by using secondary members such as purlins and side rails. Therefore, in this study out-of-plane restraints were applied at 1.3 m intervals along the length of the elements to prevent lateral displacements. The column-to-base connection was assumed to be pinned to the foundation. While the column base connections in the CFS portal frames are generally semi-rigid, the results of the reference experimental frame (Blum, 2016, Blum and Rasmussen, 2019b) showed a relatively small bending moment at the column base (around 20% of the moment for fix base columns). This indicates that the responses of the column base connections were closer to the pined connections. It should be also noted that assuming pin column base connections leads to more conservative results especially when serviceability limit state governs the design. Column-to-rafter connections and rafter-to-rafter connections were assembled using eaves and apex joints, respectively, formed through plane brackets bolted between the webs of the channel-sections (Fig. C.5). It should be noted that the thickness and depth of the CFS rafter can significantly affect the connection stiffness and strength, leading to a change in the distribution of internal actions and deflections of a portal frame (Peng et al., 2018).
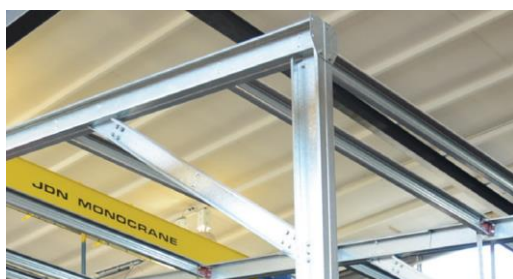
(a) Eaves joint (Blum, 2016)   (b) Apex joint
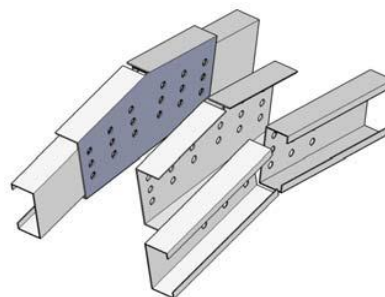
Fig. C.5. Details of frame connections at eaves and apex

Based on the results obtained from the reference experimental tests, column-to-rafter connections, knee-to-column and knee-to-rafter connections can be reasonably considered as pinned joints (Blum, 2016, Blum and Rasmussen, 2019b), while moment connections with nine bolts used for apex joints were capable to carry bending moments (Wreszien et al., 2012). It was also reported that rigid apex joints could be efficiently provided in the CFS portal frame by using bolt group length larger than 0.4 m (Phan et al., 2017a, Blum, 2016). In this study, it is assumed that the bolt group length is larger than triple of the beam depth, hence the effect of bi-moment caused by the presence of the bolts can be practically neglected (Lim and Nethercot, 2003a, Lim and Nethercot, 2004b, Lim et al., 2016b). Therefore, the buckling resistance of back-to-back channel sections is obtained by assuming that the single channels can buckle individually. It was observed from the experimental test results that a significant bending moment was developed in the columns and rafters at the intersection with the knee braces, while a considerably lower bending moment (up to 50%) was reported in the apex joint (Blum, 2016, Blum and Rasmussen, 2019b).

Previous studies have shown that detailed FE models can accurately predict the behaviour of CFS frames under axial and lateral loads (e.g. (Mojtabaei et al., 2018)). In this study, FE model of the reference frame was developed in ANSYS software (ANSYS Inc., 2009). To model the CFS columns and rafters, BEAM4 element available in ANSYS library was utilized, while LINK1 element, which can be representative of the axial members, was used for the knee bracing members. Pinned joints were simulated using rotational spring elements with zero length connected to two coincident nodes at the joint positions (COMBIN40). Structural analysis was then conducted to obtain internal forces of the elements and displacements of the joints under the design load combinations explained in the previous section. The effect of geometric nonlinearity (i.e. P-Δ and P-δ) was taken into account using second-order elastic analysis. However, based on the Bernoulli's beam theory, the effect of cross-section warping under shear stress action was neglected. In general, a very good agreement has been achieved between the internal forces of the beams and columns obtained from FE analysis and the experimental test results reported by Blum et al. (Blum, 2016, Blum and Rasmussen, 2019b).

C.6. OPTIMISATION PROBLEM

C.6.1. Cross-Section Size Optimisation

The size optimisation procedure aimed to optimise cross-sectional dimensions of the CFS beam members with regard to their flexural capacity, determined according to EC3 effective width method (see Section C.3). Standard CFS back-to-back lipped-channel sections with

steel grade S390 (f_y = 390MPa) were taken as the starting point of the optimisation process. Table C.2 lists the utilized standard cross-sections which were selected after consultation with the industrial partner of the project. The elastic modulus and the Poisson's ratio of CFS material were taken as 210 GPa and 0.3, respectively. To provide generic application of optimised CFS sections, simply supported beams subjected to uniformly distributed load (UDL) were considered in this study. The beams were assumed to be laterally braced. The effective length of the lateral restraints, which is identified as the spacing of purlins and side rails, was taken to be 1.3 m. It is worth noting that such spacing of 1.3 m was found to be appropriate for cost-effective design of purlins and side rails (Phan et al., 2017b). In this case, the optimisation target could be represented as a function of the effective property of the cross-section and the reduction factor for lateral-torsional buckling defined by:

$$\text{Max:} \quad f(x) = \chi_{LT}.W_{eff}.f_y \, / \, \gamma_{M_1} \quad \text{(C.16)}$$

$$\text{Subjected to:} \quad \frac{M_{Ed}}{M_{b,Rd}} \leq 1 \quad \text{(C.17)}$$

The reduction factor χ_{LT} was calculated for three typical UDLs of 4.0, 6.0 and 8.0 kN/m, and three different member lengths of 4.0, 6.0, and 8.0 m. It worth mentioning that according to EC3 the reduction factor explicitly considers the effect of imperfections through the cross-sectional buckling curve.

To ensure that the optimum solutions result in practically useful cross-sections, The following EC3 design constraints along with some practical and manufacturing limitations were imposed to each type of cross-sections as listed in Table C.3:

a) Similar to standard CFS elements, the overall shape of the cross-section was restricted to a lipped-channel section.

b) The width of the flanges was required to be at least 40mm in order to connect roofing system to the CFS beam elements by screws.

c) The lip had a minimum length of 10 mm to facilitate the CFS forming process. This manufacturing constraint was recommended by the industrial partner of the project.

d) The minimum depth of the channel sections was assumed to be 100 mm, which allows a bolted connection or bridging to be constructed. By considering the standard floor depth, the maximum height of the web (beam depth) was also limited to 400 mm.

e) The EC3 plate slenderness (width-to-thickness ratio) limits were also considered as design constraints (see Table C.3).
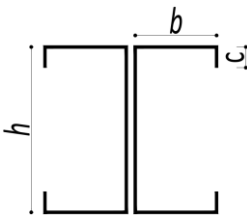
It should be noted that the aforementioned constraints, especially in terms of channel dimensions, are typically related to the effect of other elements connected to the CFS beam such as trapezoidal decking, plywood boards and angle cleats. These features are commonly encountered within commercially available sections and do not impose any excessive demands on the fabrication process.

Table C.2. Frame loadings and typical load combinations

Section	Depth (mm)	Width (mm)	Lip (mm)	t (mm)	I_y (mm⁴) ×10⁶	i_{yy} (mm)	I_W (mm⁶) ×10⁹	I_t (mm⁴)	A_{eff} (mm²)	I_{eff} (mm⁴) ×10⁶	$W_{y,eff}$ (mm³) ×10⁴	$M_{b,Rd}$ (kN.m)
C14014	140	62	13	1.4	2.53	56.33	3.34	520.26	382.32	2.05	2.51	9.80
C14015	140	62	13	1.5	2.70	56.28	3.55	639.00	435.37	2.27	2.85	11.10
C14016	140	62	13	1.6	2.87	56.24	3.75	774.42	490.77	2.50	3.20	12.47
C14018	140	62	13	1.8	3.21	56.14	4.13	1099.50	607.83	2.90	3.79	14.78
C14020	140	62	13	2.0	3.54	56.05	4.50	1504.00	726.88	3.29	4.38	17.09
C17014	170	62	13	1.4	3.95	67.00	4.88	575.14	381.96	3.10	3.06	11.92
C17015	170	62	13	1.5	4.22	66.95	5.18	706.50	432.53	3.44	3.46	13.51
C17016	170	62	13	1.6	4.49	66.90	5.48	856.34	486.14	3.78	3.89	15.17
C17018	170	62	13	1.8	5.03	66.80	6.05	1216.20	603.98	4.48	4.79	18.68
C17020	170	62	13	2.0	5.55	66.70	6.59	1664.00	724.54	5.14	5.64	22.01
C17025	170	62	13	2.5	6.85	66.46	7.85	3229.20	1016.00	6.48	7.22	28.18
C20014	200	70	15	1.4	6.30	78.56	9.97	666.61	392.60	4.59	3.71	14.45
C20015	200	70	15	1.5	6.73	78.51	10.59	819.00	445.38	5.10	4.21	16.42
C20016	200	70	15	1.6	7.16	78.46	11.20	992.87	500.74	5.62	4.74	18.47
C20018	200	70	15	1.8	8.02	78.36	12.40	1410.60	620.35	6.70	5.86	22.84
C20020	200	70	15	2.0	8.87	78.26	13.55	1930.70	753.76	7.80	7.06	27.52
C20025	200	70	15	2.5	10.96	78.01	16.24	3750.00	1088.60	10.27	9.71	37.87
C24015	240	74	17	1.5	10.78	92.96	18.69	936.00	455.92	7.77	5.22	20.35

C24016	240	74	17	1.6	11.48	92.91	19.78	1134.90	513.07	8.59	5.88	22.92
C24018	240	74	17	1.8	12.86	92.80	21.92	1612.70	635.62	10.26	7.28	28.37
C24020	240	74	17	2.0	14.23	92.70	23.99	2208.00	774.53	11.98	8.78	34.22
C24025	240	74	17	2.5	17.60	92.44	28.86	4291.70	1139.80	16.32	12.78	49.84
C24030	240	74	17	3.0	20.91	92.19	33.31	7380.00	1504.20	19.88	15.87	61.90
C30020	300	95	19	2.0	28.17	116.37	76.66	2773.30	783.54	20.51	11.15	43.48
C30025	300	95	19	2.5	34.92	116.11	92.96	5395.80	1172.90	28.65	16.65	64.93
C30030	300	95	19	3.0	41.55	115.85	108.19	9288.00	1626.50	37.25	22.94	89.46

Table C.3. CFS back-to-back lipped-channel beam section, design variables and optimisation constraints

Back-to-back lipped channel section	Design variables	Constraints based on EC3	Comments	Manufacturing & practical limitations (mm)
	$X_1=c/b$ $X_2=b/L$	$0.2 \leq c/b \leq 0.6$ $b/t \leq 60$ $c/t \leq 50$ $h/t \leq 500$	EN1993-1-3 Table 5.1 and Equation (5.2a), Clause 5.5.3.2(1)	$400 \geq h \geq 100$ $b \geq 40$ $c \geq 10$

While the total plate width and plate thickness were kept constant during the optimisation process (to use the same amount of material as standard sections), the size optimisation was carried out following two different options to provide wider range of optimum cross-sections: (i) varying depth, flange width and lip length (fully optimised sections); (ii) varying depth and flange width while lip length is fixed the same as standard sections (partially optimised sections). The detailed optimisation results for different UDLs and lengths are listed in Tables C.4, C.5, and C6.

Table C.4. Cross-section dimensions of standard and optimised CFS lipped-channel sections under 4, 6 and 8 kN/m uniformly distributed loads, 4 m span length

Section	Standard depth (mm)	Optimum depth (mm)			Standard width (mm)	Optimum width (mm)			Standard lip (mm)	Optimum lip (mm)			Standard I_{eff} (mm⁴)	Optimum I_{eff} (mm⁴)		
		UDL 4	ULD 6	UDL 8		UDL 4	ULD 6	UDL 8		UDL 4	ULD 6	UDL 8		UDL 4	ULD 6	UDL 8
C14014	140	144.04	-	-	62	50.95	-	-	13	22.03	-	-	2054000	2306400	-	-
C14015	140	148.11	156.72	-	62	49.62	45.44	-	13	21.33	21.19	-	2274000	2686500	2957471	-
C14016	140	151.13	136.22	-	62	48.02	48.63	-	13	21.41	28.26	-	2497600	3031200	2477226	-
C14018	140	159.26	133.54	-	62	47.24	56.58	-	13	18.13	21.65	-	2896100	3727000	2772600	-
C14020	140	164.05	142.01	157.98	62	45.36	55.39	48.11	13	17.62	18.61	17.9	3289800	4339700	3437800	4089800
C17014	170	181.73	189.21	-	62	46.08	43.01	-	13	23.05	22.39	-	3098500	3784200	4061300	-
C17015	170	186.09	162.64	-	62	45.38	54.5	-	13	21.58	24.19	-	3435200	4343000	3416900	-
C17016	170	188.16	166.71	-	62	44.13	53.18	-	13	21.79	23.46	-	3777400	4760100	3931400	-
C17018	170	189.7	172.46	155.11	62	44.13	50.3	58.4	13	21.02	23.47	24.04	4475200	5529300	4832400	4037600
C17020	170	191.02	180.67	164.04	62	44.13	49.92	57.44	13	20.36	19.74	20.54	5138600	6316700	5810300	4979900
C17025	170	202.82	190.76	176.25	62	44.13	45.95	52.58	13	14.46	18.67	19.3	6476000	8572800	7877600	6983800
C20014	200	243.1	219.37	202.72	70	42.14	48.32	55.2	15	21.31	26.99	28.44	4585100	6944400	5884800	5081200
C20015	200	243.38	223.41	207.27	70	40	47.25	53.87	15	23.31	26.04	27.49	5099700	7612800	6733800	5886500
C20016	200	238.69	228.81	211.26	70	41.03	47.25	52.73	15	24.62	23.35	26.65	5624300	8058900	7637500	6713400
C20018	200	242.01	230.52	216.23	70	40	43.59	49.69	15	24	26.15	27.2	6698700	9423100	8883400	8166000
C20020	200	242.01	235.38	220.36	70	40	42.07	47.29	15	24	25.24	27.53	7799700	10679000	10325000	9479600
C20025	200	240.95	240.95	235.34	70	43.66	43.66	45.99	15	20.87	20.87	21.34	10266000	13827000	13827000	1341000
C24015	240	277.35	277.35	272.36	74	50	50	50	17	22.33	22.33	24.82	7771200	10652000	10652000	10408000
C24016	240	276.86	276.86	276.86	74	50	50	50	17	22.57	22.57	22.57	8586400	11726000	11726000	11726000
C24018	240	267.74	267.72	267.74	74	50	50	50	17	27.13	27.14	27.13	10260000	13137000	13137000	13137000
C24020	240	261.98	261.98	261.98	74	50	50	50	17	30.01	30.01	30.01	11980000	14510000	14510000	14510000
C24025	240	266.05	266.05	266.05	74	50	50	50	17	27.98	27.98	27.98	16322000	19261000	19261000	19261000
C24030	240	283.22	283.22	283.22	74	50	50	50	17	19.39	19.39	19.39	19878000	25614000	25614000	25614000
C30020	300	362.25	362.25	362.25	95	51.8	51.8	51.8	19	31.05	31.05	31.05	20506000	30424000	30424000	30424000
C30025	300	342.48	342.48	342.48	95	57.97	57.97	57.97	19	34.78	34.78	34.78	28645000	37479000	37479000	37479000
C30030	300	342.91	342.91	342.91	95	58.82	58.82	58.82	19	33.73	33.73	33.73	37247000	46599000	46599000	46599000

Appendix C. Coupled element and structural level optimisation framework for
cold-formed steel frames
252

Table C.5. Cross-section dimensions of standard and optimised CFS lipped-channel sections under 4, 6 and 8 kN/m uniformly distributed loads, 6 m span length

Section	Standard depth (mm)	Optimum depth (mm)			Standard width (mm)	Optimum width (mm)			Standard lip (mm)	Optimum lip (mm)			Standard I_{eff} (mm⁴)	Optimum I_{eff} (mm⁴)		
		UDL 4	ULD 6	UDL 8		UDL 4	ULD 6	UDL 8		UDL 4	ULD 6	UDL 8		UDL 4	ULD 6	UDL 8
C17018	170	168.52	-	-	62	52.32	-	-	13	23.42	-	-	4475200	4672000	-	-
C17020	170	156.24	-	-	62	60.99	-	-	13	20.89	-	-	5138600	4589400	-	-
C17025	170	169.45	-	-	62	55.68	-	-	13	19.59	-	-	6476000	6565600	-	-
C20015	200	199.82	-	-	70	56.98	-	-	15	28.11	-	-	5099700	5501600	-	-
C20016	200	204.11	-	-	70	55.69	-	-	15	27.26	-	-	5624300	6308400	-	-
C20018	200	211.13	-	-	70	53.21	-	-	15	26.23	-	-	6698700	7902600	-	-
C20020	200	214.77	190.47	-	70	50.17	61.38	-	15	27.44	28.38	-	7799700	9155600	7697700	-
C20025	200	229.9	207.92	188.62	70	48.47	58.42	67.19	15	21.58	22.62	23.5	10266000	12966000	11152000	9539000
C24015	240	261.06	-	-	74	50.39	-	-	17	30.08	-	-	7771200	9773600	-	-
C24016	240	266.48	-	-	74	50	-	-	17	27.76	-	-	8586400	11130000	-	-
C24018	240	267.74	248.66	-	74	50	56.84	-	17	27.13	29.83	-	10260000	13137000	11770000	-
C24020	240	261.98	253.02	236.96	74	50	53.89	62.58	17	30.01	30.6	29.94	11980000	14510000	13873000	12595000
C24025	240	266.05	265.6	258.33	74	50	50.13	56.38	17	27.98	28.06	25.46	16322000	19261000	19222000	17568000
C24030	240	283.22	279.58	262.67	74	50	50	55.24	17	19.39	21.21	24.43	19878000	25614000	25212000	23121000
C30020	300	362.25	362.25	360.82	95	51.8	51.8	52.69	19	31.08	31.08	30.89	20506000	30424000	30424000	30281000
C30025	300	342.48	342.48	342.48	95	57.97	57.97	57.97	19	34.78	34.78	34.78	28645000	37479000	37479000	37479000
C30030	300	342.91	342.91	342.91	95	58.82	58.82	58.82	19	33.73	33.73	33.73	37247000	46599000	46599000	46599000

Table C.6. Cross-section dimensions of standard and optimised CFS lipped-channel sections under 4, 6 and 8 kN/m uniformly distributed loads, 8 m span length

Section	Standard depth (mm)	Optimum depth (mm)			Standard width (mm)	Optimum width (mm)			Standard lip (mm)	Optimum lip (mm)			Standard I_{eff} (mm^4)	Optimum I_{eff} (mm^4)		
		UDL 4	ULD 6	UDL 8		UDL 4	ULD 6	UDL 8		UDL 4	ULD 6	UDL 8		UDL 4	ULD 6	UDL 8
C20025	200	197.01	-	-	70	63.38	-	-	15	23.12	-	-	10266000	10238000	-	-
C24015	240	-	-	-	74	-	-	-	17	-	-	-	7771200	-	-	-
C24016	240	-	-	-	74	-	-	-	17	-	-	-	8586400	-	-	-
C24018	240	237.49	-	-	74	61.44	-	-	17	30.81	-	-	10260000	10847000	-	-
C24020	240	245.09	-	-	74	59.38	-	-	17	29.08	-	-	11980000	13286000	-	-
C24025	240	254.57	233.83	-	74	53.21	67.14	-	17	30.5	26.94	-	16322000	18175000	16171000	-
C24030	240	268.79	245.56	-	74	52.45	63	-	17	24.15	25.21	-	19878000	23906000	20944000	-
C30020	300	362.25	345.94	-	95	51.8	60.56	-	19	31.08	30.47	-	20506000	30424000	28742000	-
C30025	300	342.48	342.48	334.71	95	57.97	57.97	60.4	19	34.78	34.78	36.24	28645000	37479000	37479000	36451000
C30030	300	342.91	342.91	342.91	95	58.82	58.82	58.82	19	33.73	33.73	33.73	37247000	46599000	46599000	46599000

C.6.2. Frame Optimisation

The structural level optimisation aimed to minimise the weight of the CFS portal frame per unit floor area (W) while satisfying all Eurocode design requirements. The unit weight depends on the frame spacing, frame geometry, cross-section sizes of the CFS members, and can be expressed as:

$$W = \frac{1}{L_f b_f}[\sum_{1}^{m} w_i l_i] \tag{C.18}$$

where W is the weight of the frame per square meter of floor area; L_f and b_f are the CFS portal frame span length and frame spacing, respectively; l_i and w_i are the length and the weight per unit length of the CFS frame members, respectively; and m is the number of structural members in the main frame.

In this study, the normalised forms of the member check provisions for CFS members following EC3 are used as optimisation constraints:

$$g_1 = \frac{N_{Ed}}{N_{t,Rd}} - 1 \le 0 \tag{C.19-a}$$

$$g_2 = \frac{N_{Ed}}{N_{c,Rd}} - 1 \leq 0 \qquad\qquad\text{(C.19-b)}$$

$$g_3 = \frac{N_{Ed}}{N_{b,Rd}} - 1 \leq 0 \qquad\qquad\text{(C.19-c)}$$

$$g_4 = \frac{N_{Ed}}{N_{c,Rd}} + \frac{M_{y,Ed}}{M_{cy,Rd}} - 1 \leq 0 \qquad\qquad\text{(C.19-d)}$$

$$g_5 = \frac{M_{Ed}}{M_{b,Rd}} - 1 \leq 0 \qquad\qquad\text{(C.19-e)}$$

$$g_6 = (\frac{N_{Ed}}{N_{b,Rd}})^{0.8} + (\frac{M_{y,Ed}}{M_{b,Rd}})^{0.8} - 1 \leq 0 \qquad\qquad\text{(C.19-f)}$$

$$g_7 = \frac{\delta_e}{\delta_e^u} - 1 \leq 0 \qquad\qquad\text{(C.19-g)}$$

$$g_8 = \frac{\delta_a}{\delta_a^u} - 1 \leq 0 \qquad\qquad\text{(C.19-h)}$$

where g_1, g_2 and g_3 are constraints for the axial members; g_4, g_5 and g_6 are constraints for the beam-column members; and g_7 and g_8 are constraints for the deflection limit checks. δ_e^u is the horizontal displacement limit at eaves; and δ_a^u is the vertical deflection limit at apex.

As discussed before, at the element level, a set of optimised CFS cross-sections with different coil widths and plate thicknesses are developed for the elements with various lengths subjected to different applied load (UDL) levels. Subsequently, at the frame level, the best cross-section (with minimum amount of material) are selected from the optimised sections to satisfy the design constraints imposed on the frame, based on the internal forces calculated at each iteration. The frame optimisation solver also searches through a practical range of values for the roof pitch, frame spacing, and knee brace configuration (i.e. knee depth and knee angle) to obtain the best design solution. This implies that at structural level optimisation, discrete and continuous design variables are simultaneously used. In this study, it is assumed that roof pitch is varied from 6° to 30° and frame spacing is set in the range of 2.0 m to 20 m.

C.6.3. Real-Coded Genetic Algorithm (RC-GA)

Due to the high nonlinearity of the optimisation problem in this study, a Real-Coded Genetic Algorithm (RC-GA) was programmed to solve the objective functions, including maximising the ultimate load-bearing capacity of CFS elements (Equation C.16) by satisfying the cross-sectional design constraints (see Table C.3) and minimising the frame weight (Equation C.17) by considering all the predefined structural design constraints (Equations C.19). It should be mentioned that RC-GA is a metaheuristic population-based algorithm, which is inspired by the natural selection and adaptation. The main advantage of RC-GA compared to conventional binary GA methods is that genetic operators are directly applied to the design variables without coding and decoding.

The adopted optimisation algorithm randomly generates a set of solutions known as initial population. From this population, the next generation of solutions is evolved by conducting three genetic operations: binary tournament selection, SBX crossover, and polynomial mutation (Deb, 2001, Lwin et al., 2014). The process of random selection in the binary tournament ensures that the best solutions in the population will not dominate the mating pool. The diversity of the population is thus preserved to increase the exploration component of the algorithm. To maintain the diversity of population when generation progresses, a niching technique is applied for selection and crossover operators. The details of this process can be found in Phan et al. (2013c).

To consider the design constraints for single objective optimisation in this study, an effective penalty approach (Pezeshk et al., 2000, Yeniay, 2005) is applied, in which the penalised value for each violated design constraint is gradually decreased as the generation progresses (Erbatur et al., 2000, Phan et al., 2017a):

$$CVP_i = \frac{Kg_i}{Gen^{0.5}}$$ (C.20)

where CVP_i is the violated penalty for the ith design constraint; K is scale factor; g_i is the violated constraint; and Gen stands for the current generation. Since all design constraints are normalised to unity, an empirical scale factor of 100 was found to be sufficient to scale the penalty value to the same order with the objective function. Subsequently, the fitness function (F) in this study can be expressed as:

$$F = W(1 + \sum_{1}^{8} CVP_i)$$ (C.21)

As mentioned before, the adopted optimisation procedure aims to minimise the fitness function through evolutionary process to search for the lightest design that satisfies all design constraints. Specifically, for each solution, fitness function value is determined from objective function along with the penalty values for violated constraints. Better solutions will get smaller fitness values, and consequently, are selected preferentially by the tournament selection operator. The criterion for terminating the program is a predefined total number of generations.

To conduct optimisation process, the aforementioned design procedure in Section C.4 and the Real-Coded Genetic Algorithm (RC-GA) were implemented in MATLAB (Mathworks, 2011). The GA population size was taken equal to 50 and 80 for element and structural level optimisations, respectively; while the number of GA generations was kept 100 for both optimisation levels. The sensitivity analysis on the other GA parameters was also carried out, and subsequently the following values were selected: crossover probability $p_c = 0.9$; mutation probability $p_m = 0.01$; niching radius = 0.25; termination criterion = 100 generations (i.e. the maximum number of function evaluations allowed was 8000); distribution coefficient for mutation = 1.0; distribution coefficient for crossover = 1.0.

C.7. RESULTS AND DISCUSSIONS

In this study, a MATLAB code was developed to provide a link between ANSYS (ANSYS Inc., 2009) and the RC-GA optimisation code. First, the results of element level optimisation conducted in MATLAB (Mathworks, 2011) were automatically transferred to ANSYS software (ANSYS Inc., 2009) through an input file to develop the frame model. The element forces obtained from second-order elastic analysis were then recorded in an output file. Subsequently, the output data was transferred back to MATLAB (Mathworks, 2011) to carry out the optimisation process at the frame level. The internal forces changed during the optimisation process by changing the size of the CFS structural elements. At each iteration, the new internal forces were then used to check the serviceability and ultimate limit states design conditions.

Although the optimisation process in this paper is based on Eurocode 3 design regulations, the proposed optimisation framework is general and other standards (e.g. AISI (AISI S100-16, 2016) and AS/NZS 4600 (AS/NZS 4600, 2018)) can be easily adopted. It should be mentioned that previous studies by the authors have also confirmed that the optimisation based on Eurocode 3 effective width method can accurately predict the actual trends in changing the capacity of CFS elements and hence lead to optimum design solutions (Ye et al., 2019a, Ye et al., 2018b, Ye et al., 2018d, Ye et al., 2018c).

C.7.1.   Element Level Optimisation

For each CFS channel section listed in Table C.2, the element level optimisation was repeated three times using different sets of random initial populations and the answer with the maximum bending capacity was retained as the optimum section. In all cases, the optimum solution was reasonably achieved with consistently small standard deviation. For example, Fig. C.6 shows the iteration history of the bending capacity for the C30020 beam (see Table C.2) using back-to-back configuration, where the convergence was practically achieved after about 50 iterations. It should be noted that the cross-sections used in this study are all categorised as EC3 class 4 (CEN, 2005e), and therefore, no yielding is expected before failure.
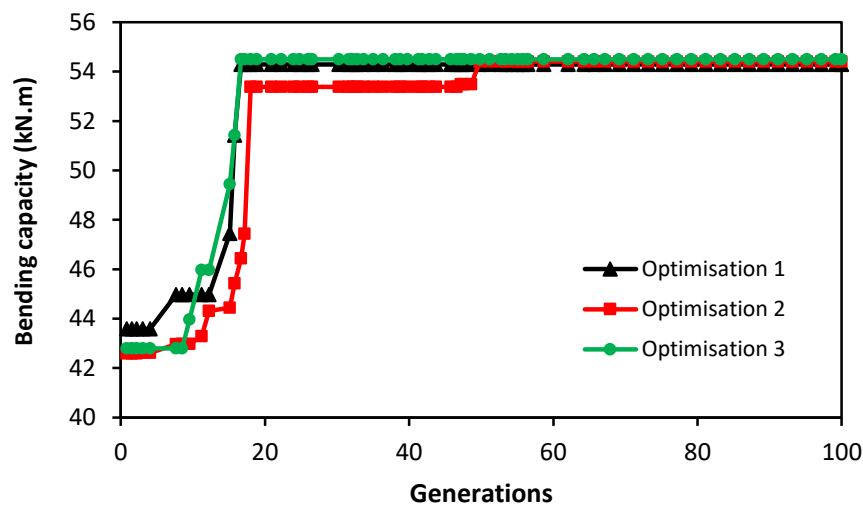
Fig. C.6. Convergent history of element level optimisation for back-to-back channel using C30020 section

The comparison between the flexural capacities of the standard CFS sections and those optimised based on maximum bending moment capacity for 4 m length and different UDLs of 4, 6 and 8 kN/m are shown in Fig. C.7 (a), (b), and (c), respectively. It can be seen that, for the same amount of material, the proposed optimisation method could significantly (up to 84%) increase the maximum bending capacity of the CFS beams with standard sections. It is also observed that optimising the lip length can result in a slight improvement (up to 8%) in the flexural capacity of the CFS beam members compared to the optimisation using a fixed lip length (i.e. partially optimised sections). This minor difference can be attributed to the effect of lip length on the lateral-torsional buckling of the sections, which is taken into account through the buckling reduction factor (χ_{LT}) in the design process. It is worth mentioning that for the beams with small cross-sectional sizes and plate thickness (namely BBC14015, BBC17014, and BBC20014) standard sections cannot carry the large uniformly distributed loads (i.e. 6.0 kN/m and 8.0 kN/m), whilst the optimum sections provide enough capacity to

sustain those design load levels. The optimum results for different element lengths and design load levels are listed in Tables C.4, C.5, and C.6. It should be noted that for those CFS beam sections which are not capable to satisfy the EC3 beam capacity design check (Equations C.17), no information is provided.
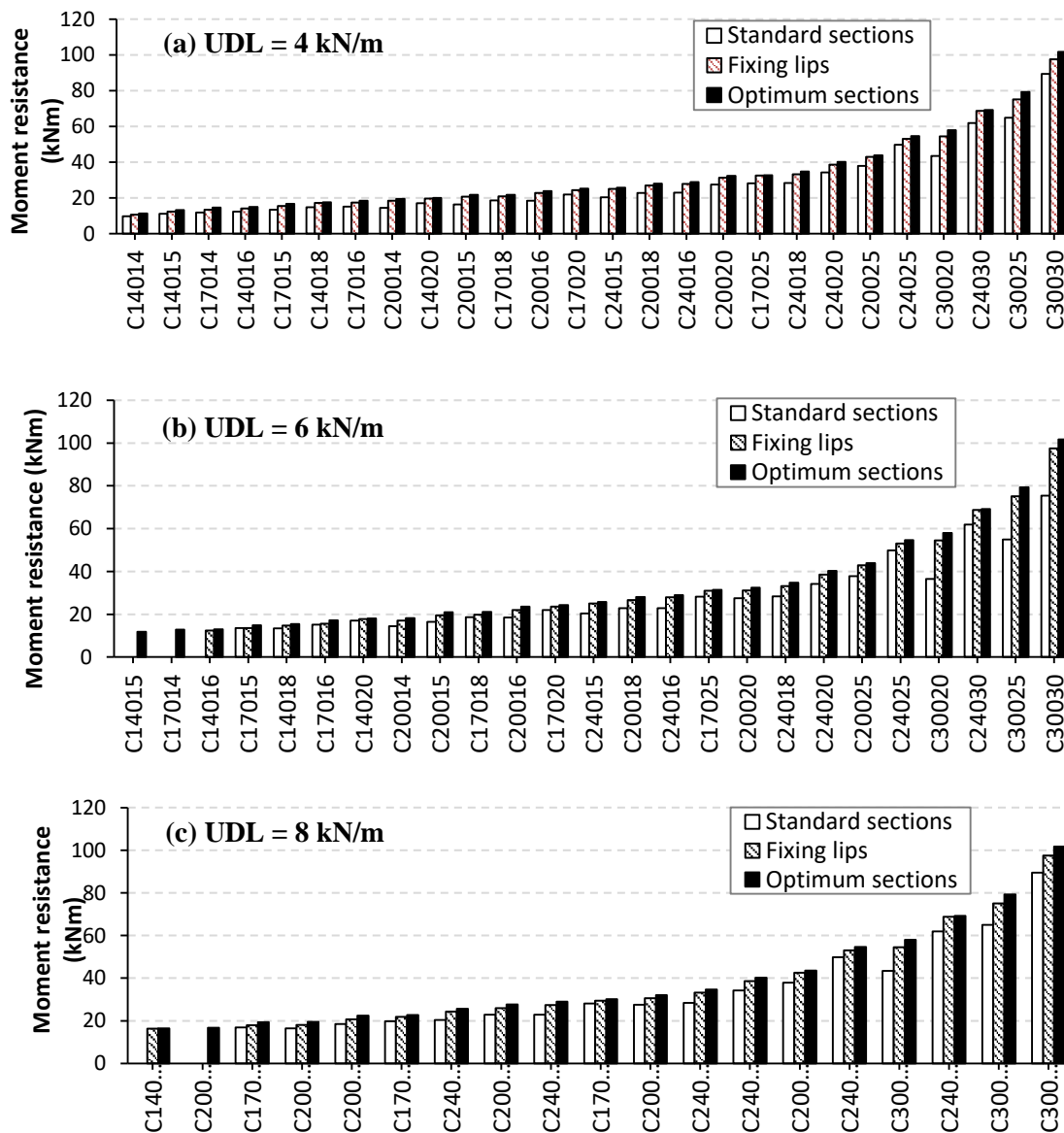
Fig. C.7. Moment resistance of standard, partially optimised (fixed lip length) and fully optimised sections

C.7.2. Structural Level Optimisation

In this Section, the results of structural level optimisation on the selected CFS long-span portal frame with knee braces are presented by incorporating standard CFS back-to-back lipped-channel sections at two different limit state design conditions: (i) ULS, and (ii) combined ULS and SLS. For each case, the influence of optimising the frame geometry and knee brace

configuration on the efficiency of the final solution is also investigated. All optimisation problems were conducted three times, and the answer with minimum structural weight was considered as the final optimum solution. In general, the standard deviation of the results was relatively small (less than 0.0058), which implies that the selected population size was sufficient. To obtain the internal forces and joint displacements for the structural level optimisation, second-order elastic analysis was conducted on the detailed FE models of the CFS frames using FE software ANSYS (ANSYS Inc., 2009) (see Section C.5). The results were then transferred to the RC-GA program in MATLAB as discussed in Section C.6.

The selected CFS frame was initially optimised under ULS and combined ULS and SLS design conditions by using the most appropriate standard CFS elements (as listed in Table C.2), while the initial geometry and knee brace configuration was assumed to be the same as the reference frame explained in Section C.5. Subsequently, the frame was optimised again under ULS and combined ULS and SLS design conditions, but this time the frame geometry and knee brace configuration were also optimised. Table C.7 compares the optimum results for all the above cases.

Table C.7. Optimum design of the reference frame using CFS standard sections

Optimum design conditions	Knee brace configuration		Frame geometry		Member sections (back-to-back)			Unit weight (kg/m2)
	Knee depth	Knee angle	Frame spacing	Pitch	Column	Rafter	Knee brace	
	(m)		(m)					
Optimum design using reference geometry (ULS)	1.36	50º	3.60	10º	C-30030	C-30030	C-14015	12.75
Optimum design using reference geometry (ULS & SLS)	1.36	50º	3.60	10º	N/A	N/A	N/A	N/A
Optimum design (ULS)	1.87	40.1º	4.30	6.0º	C-30030	C-30030	C-14015	10.62
Optimum design (ULS & SLS)	1.40	52.8º	2.21	6.0º	C-30030	C-30030	C-14015	20.63

The optimum weight of the frame optimised under ULS using the geometry of the reference frame was calculated 12.75 kg per square meter of floor area (kg/m^2) by using the strongest cross-section available in Table C.2 for rafters and columns (C-30030) and standard section C-14015 for knee brace members. In this case, the design constraint related to the lateral-torsional buckling of the column members under bending and compression interaction (g_6)

governed the design (i.e. g_6 =0 under the critical load combination LC3). As can be seen in Table C.7, when the geometry of the frame is not optimised, no optimum solution is obtained under combined ULS and SLS conditions. The reason is that none of the standard sections used in this study (Table C.2) can satisfy the predefined design constraint on the horizontal displacement at eaves (SLS load combination LC5).

As mentioned above, the selected CFS log-span portal frame was also optimised by including the frame geometry (i.e. frame spacing and pitch angel) and knee brace configuration (i.e. knee depth and knee angel) in the optimisation process. The most suitable standard cross-sections were obtained to provide the lightest solution by considering the design constraints at ULS and combined ULS and SLS. The results in Table C.7 indicate that, by optimising the frame geometry and knee brace configuration, the required structural weight for ULS design reduced by 17%, while the frame spacing was increased from 3.60 m to 4.30 m. Similar to the previous case, the optimum result at ULS was controlled by the design constraint on the lateral-torsional buckling of the column members under bending and compression interaction (i.e. g_6 =0 under the critical load combination LC3). Incorporating the optimum knee brace configuration and frame geometry enabled the frame designed at combined ULS and SLS to satisfy the horizontal displacement constraint at eaves (i.e. g_7=0 under the critical load combination LC5). This led to a considerable increase in the required structural weight compared to the frame optimised at ULS, which indicates that the serviceability design conditions governed the design as expected for the long-span frame considered in this study. The results in Table C.7 also demonstrate that the optimum design solution always tends to provide larger knee brace depth (up to 38%) regardless of the selected limit state design conditions. On the contrary, the optimum knee brace angle is affected by the selected limit state design condition, since changing the knee brace angle can also change the bending moment in the rafters and, hence, affect the frame displacement.

C.7.3.   Coupled Element and Structural Level Optimisation

This section presents the structural level optimisation are carried out on the selected CFS long-span portal frame with knee braces by incorporating optimised CFS lipped-channel sections at two different limit state design conditions: (i) ULS, and (ii) combined ULS and SLS. To examine the efficiency of the CFS sections optimised at element level (see Section C.7.1) for structural level optimisation, the reference CFS frame was optimised again by using optimum CFS sections instead of the standard elements (i.e. coupled element and structural level optimisation). Table C.8 compared the optimum design solutions under ULS and combined

ULS and SLS conditions with and without optimising the frame geometry and knee brace configuration.

Table C.8. Optimum design of the reference frame using optimised sections

Optimum design conditions	Knee brace configuration		Frame geometry		Member sections (back-to-back)			Unit weight (kg/m2)
	Knee depth (m)	Knee angle	Frame spacing (m)	Pitch	Column	Rafter	Knee brace	
Optimum design using reference geometry (ULS)	1.36	50º	3.60	10º	C-30030*	C-30025*	C-20015*	11.85
Optimum design using reference geometry (ULS & SLS)	1.36	50º	3.60	10º	N/A	N/A	N/A	N/A
Optimum design (ULS)	1.85	40.5º	4.55	6.0º	C-30030*	C-30030*	C-20015*	10.19
Optimum design (ULS & SLS)	1.40	52.7º	2.77	6.0º	C-30030*	C-30030*	C-14014*	16.42

* Elements with optimum dimensions as indicated in Tables C.4, C.5, and C.6

Similar to the previous case, the critical design constraints were the torsional buckling of the column members (g_6) and horizontal displacement at eaves (g_6) under ULS and combined ULS and SLS design conditions, respectively. The CFS frame with the geometry and knee brace configuration similar to the reference experimental test could not satisfy the serviceability design conditions, while full optimisation could reduce the required structural weight for ULS design by 14%.

Comparison between the results in Tables C.7 and C.8 indicates that by using optimised CFS elements the required structural weight was reduced by up to 20% compared to the frame optimised using the standard elements listed in Table C.2. The material saving due to using optimised CFS sections was especially evident when the frame was optimised under combined ULS and SLS design conditions. It is also shown that using optimised sections in general results in a higher frame spacing (up to 25%), while it does not considerably affect the optimum knee brace configuration (i.e. knee depth and knee angle).

C.8. SUMMARY

In this appendix, a novel coupled element and structural level optimisation framework was presented for optimum design of CFS portal frames under different limit state design conditions. Proposed optimisation method at the element level is based on the methodologies presented in Chapters 3 and 4 at different limit states. To search for the optimum design solutions, a Real-Coded Genetic Algorithm (RC-GA) was adopted, in which the genetic operators were directly applied to the design variables without coding and decoding. In the proposed framework, first the relative dimensions of a wide range of standard CFS lipped-channel sections were optimised with respect to their flexural capacity determined according to the Eurocode-3 effective width method, while the EC3 slenderness limits and a number of manufacturing and end-use constraints were considered in the optimisation process.

C.9. CONCLUDING REMARKS

It was shown that, by using the same amount of material, the ultimate flexural capacity of the optimum CFS members can be significantly higher (up to 84%) than their standard counterparts. Subsequently, structural level optimisation was conducted on a long-span CFS portal frame with knee braces under SLS and ULS conditions to find the best economic design with the lightest weight per unit area using both standard and optimised cross-sections. The results indicated that the proposed coupled framework can considerably reduce (up to 20%) the required structural weight of the CFS frame system by using the CFS sections optimised for generic applications. It was also shown that optimising the frame geometry and knee brace configuration, could further reduce the structural weight (up to 17%), especially under combined ULS and SLS design conditions. Based on the outcomes of this study, the proposed coupled optimisation framework should prove useful in practical design of CFS frame systems.

REFERENCES

Abaqus/CAE User's Manual (2014). *version 6.14-2, USA.*

Ádány, S. (2016). "Shell element for constrained finite element analysis of thin-walled structural members". *Thin-Walled Structures,* 105**,** 135-146.

Ádány, S. and Schafer, B. (2006a). "Buckling mode decomposition of single-branched open cross-section members via finite strip method: derivation". *Thin-Walled Structures,* 44**,** 563-584.

Ádány, S. and Schafer, B. W. (2006b). "Buckling mode decomposition of single-branched open cross-section members via finite strip method: Application and examples". *Thin-Walled Structures,* 44**,** 585-600.

Ádány, S. and Schafer, B. W. (2014). "Generalized constrained finite strip method for thin-walled members with arbitrary cross-section: secondary modes, orthogonality, examples". *Thin-Walled Structures,* 84**,** 123-133.

Adeli, H. and Karim, A. (1997). "Neural network model for optimization of cold-formed steel beams". *J. Struct. Eng. ASCE 123***,** 1535–1543.

AISI (2007). "Supplement No. 2 to the North American specification for the design of cold-formed steel structural members". *American Iron and Steel Institute (AISI), Washington, DC, USA.*

AISI S100-12 (2012). "North American specification for the design of cold-formed steel structural members". *American Iron and Steel Institute (AISI), Washington, DC, USA.*

AISI S100-16 (2016). "North American specification for the design of cold-formed steel structural members. ". *American Iron and Steel Institute (AISI), Washington, DC, USA.*

Ajeesh, S. S. and Arul Jayachandran, S. (2016). "Simplified semi-analytical model for elastic distortional buckling prediction of cold-formed steel flexural members". *Thin-Walled Structures,* 106**,** 420-427.

Anbarasu, M. (2016). "Local-distortional buckling interaction on cold-formed steel lipped channel beams". *Thin-Walled Structures,* 98**,** 351-359.

Andre, J., Siarry, P. and Dognon, T. (2001). "An improvement of the standard genetic algorithm fighting premature convergence in continuous optimization". *Advances in Engineering Software,* 32**,** 49-60.

ANSI/AISC 341-16 (2016). "Seismic provisions for structural steel buildings". *American Institute of Steel Construction (AISC).*

ANSYS Inc. (2009). "Programmer's manual for mechanical APDL. USA: SAS IP".

AS/NZS-4673 (2001). "Cold-formed stainless steel structures. Australian Standard/New Zealand Standard.".

AS/NZS 4600 (2005). "Coldformed steel structures, Homebush, Australia". *Standards Australia/Standards New Zealand (SA/SNZ).*

AS/NZS 4600 (2018). "Coldformed steel structures, Homebush, Australia". *Standards Australia/Standards New Zealand (SA/SNZ).*

ASCE/SEI 41-17 (2017). "Seismic Evaluation and Retrofit of Existing Buildings". *American Society of Civil Engineers (ASCE).*

ASTM A325-14 (2014). "Standard Specification for Structural Bolts, Steel, Heat Treated, 120/105 ksi Minimum Tensile Strength". *American Society for Testing and Materials*.

Bagheri Sabbagh, A. (2011a). "Cold-formed steel elements for earthquake resistant moment frame buildings, PhD thesis, University of Sheffield".

Bagheri Sabbagh, A., Petkovski, M., Pilakoutas, K. and Mirghaderi, R. (2011). "Ductile moment-resisting frames using cold-formed steel sections: An analytical investigation". *Journal of Constructional Steel Research,* 67**,** 634-646.

Bagheri Sabbagh, A., Petkovski, M., Pilakoutas, K. and Mirghaderi, R. (2012a). "Development of cold-formed steel elements for earthquake resistant moment frame buildings". *Thin-Walled Structures,* 53**,** 99-108.

Bagheri Sabbagh, A., Petkovski, M., Pilakoutas, K. and Mirghaderi, R. (2012b). "Experimental work on cold-formed steel elements for earthquake resilient moment frame buildings". *Engineering Structures,* 42**,** 371-386.

Bagheri Sabbagh, A., Petkovski, M., Pilakoutas, K. and Mirghaderi, R. (2013). "Cyclic behaviour of bolted cold-formed steel moment connections: FE modelling including slip". *Journal of Constructional Steel Research,* 80**,** 100-108.

Baigent, A. H. and Hancock, G. J. (1982). "Structural analysis of assemblages of thin-walled members". *Engineering Structures,* 4**,** 207-216.

Batista, E. d. M. (2009). "Local–global buckling interaction procedures for the design of cold-formed columns: Effective width and direct method integrated approach". *Thin-Walled Structures,* 47**,** 1218-1231.

Batista, E. d. M. and Rodrigues, F. G. (1992). "RESIDUAL STRESS MEASUREMENTS ON COLD-FORMED PROFILES". *Experimental Techniques,* 16**,** 25-29.

Becque, J. and Li, X. (2015). "A new approach to modal decomposition of buckled shapes". *Structures,* 4**,** 2-12.

Becque, J., Li, X. and Davison, B. (2019). "Modal decomposition of coupled instabilities: The method of the equivalent nodal forces". *Thin-Walled Structures,* 143**,** 106229.

Becque, J. and Rasmussen Kim, J. R. (2009). "Numerical Investigation of the Interaction of Local and Overall Buckling of Stainless Steel I-Columns". *Journal of Structural Engineering,* 135**,** 1349-1356.

Becque, J. and Rasmussen, K. J. R. (2009). "A numerical investigation of local–overall interaction buckling of stainless steel lipped channel columns". *Journal of Constructional Steel Research,* 65**,** 1685-1693.

Bernuzzi, C. and Maxenti, F. (2015). "European alternatives to design perforated thin-walled cold-formed beam–columns for steel storage systems". *Journal of Constructional Steel Research,* 110**,** 121-136.

Bernuzzi, C. and Simoncelli, M. (2015). "European design approaches for isolated cold-formed thin-walled beam–columns with mono-symmetric cross-section". *Engineering Structures,* 86**,** 225-241.

Bezabeh, M. A., Tesfamariam, S. and Stiemer, S. F. (2016). "Equivalent Viscous Damping for Steel Moment-Resisting Frames with Cross-Laminated Timber Infill Walls.". *J Struct Eng-ASCE,* 142**,** 1-12.

Blum, H. B. (2016). "Long-span cold-formed steel portal frames composed of double channels. PhD Thesis. The University of Sydney, Australia".

Blum, H. B. and Rasmussen, K. J. R. (2019a). "Experimental and numerical study of connection effects in long-span cold-formed steel double channel portal frames". *Journal of Constructional Steel Research,* 155**,** 480-491.

Blum, H. B. and Rasmussen, K. J. R. (2019b). "Experimental investigation of long-span cold-formed steel double channel portal frames". *Journal of Constructional Steel Research,* 155**,** 316-330.

Bock, M. and Real, E. (2015). "Effective width equations accounting for element interaction for cold-formed stainless steel square and rectangular hollow sections". *Structures,* 2**,** 81-90.

Boger, R. K. (2006). "PhD thesis, Non-monotonic strain hardening and its constitutive representation, The Ohio State University".

Bolandim Emerson, A., Beck André, T. and Malite, M. (2013). "Bolted Connections in Cold-Formed Steel: Reliability Analysis for Rupture in Net Section". *Journal of Structural Engineering,* 139**,** 748-756.

Bolong, Z. (1989). "Seismic test of structure". *Beijing : Earthquake Express [in chinese]*.

BS EN 1990:2002 + A1:2005 (2002). "Eurocode – Basis of structural design, Incorporating corrigenda December 2008 and April 2010, BSI".

BS EN 1991-1-1 (2002). "Eurocode 1, Actions on structures: Part 1-1 General actions, Densities, self-weight, imposed loads for buildings, Incorporating corrigendum No. 1, BSI".

BS EN 1991-1-4 (2005). "Eurocode 1, Actions on structures: Part 1-4 General actions, Wind actions. BSI, 2005".

BS EN (1993). "Eurocode 3: design of steel structures part 1–12: additional rules for the extension of EN 1993 up to steel grades S 700, London (UK): British Standards Institution".

Bučmys, Ž. and Daniūnas, A. (2015a). "Analytical and experimental investigation of cold-formed steel beam-to-column bolted gusset-plate joints". *Journal of Civil Engineering and Management,* 21**,** 1061-1069.

Bučmys, Ž., Daniūnas, A., Jaspart, J.-P. and Demonceau, J.-F. (2018). "A component method for cold-formed steel beam-to-column bolted gusset plate joints". *Thin-Walled Structures,* 123**,** 520-527.

C.H Pham and Hancock, G. J. (2012). "Direct strength design of cold-formed C-sections for shear and combined actions". 138(6)**,** 759–68.

Calderoni, B., De Martino, A., Formisano, A. and Fiorino, L. (2009a). "Cold formed steel beams under monotonic and cyclic loading: Experimental investigation". *Journal of Constructional Steel Research,* 65**,** 219-227.

Carruth, M. A., Allwood, J. M. and Milford, R. L. (2011). "Reducing CO_2 Emissions through Lightweight Design and Manufacturing". *AIP Conference Proceedings,* 1353**,** 1632-1637.

Cava, D., Camotim, D., Dinis, P. B. and Madeo, A. (2016). "Numerical investigation and direct strength design of cold-formed steel lipped channel columns experiencing local–distortional–global interaction". *Thin-Walled Structures,* 105**,** 231-247.

CEN (2002). "Eurocode 0: "Basis of structural design." , European Committee for Standardization, Brussels".

CEN (2005a). "EN 1998-1, Design of Structures for Earthquake Resistance - Part 1: General Rules, Seismic Actions and Rules for Buildings".

CEN (2005c). "Eurocode 3: design of steel structures, part 1.3: general rules—supplementary rules for cold formed members and sheeting, in, Brussels: European Comittee for Standardization".

CEN (2005e). "Eurocode 3: Design of Steel Structures. Part 1-1: General Rules and Rules for Buildings, in, Brussels: European Comittee for Standardization".

CEN (2005f). "Eurocode 3: Design of Steel Structures. Part 1-8: Design of joints, in, Brussels: European Comittee for Standardization".

CEN (2006a). "Eurocode 3: Design of steel structures, Part 1-5: Plated structural elements, in, Brussels: European Comittee for Standardization".

CEN (2006b). "Eurocode 3: Design of Steel Structures. Part 1-4: general rules: supplementary rules for stainless steels, in, Brussels: European Comittee for Standardization".

Chen, J., He, Y. and Jin, W.-L. (2010). "Stub column tests of thin-walled complex section with intermediate stiffeners". *Thin-Walled Structures,* 48**,** 423-429.

Chen, W. K. and Lui, E. M. (1987). "Structural Stability: Theory and Implementation". *PTR Prentice Hall*.

Chopra, A. K. "Dynamics of Structures: Theory and Applications to Earthquake Engineering, (2nd ed.)Prentice Hall, New Jersey (2001)".

Chung, K. F. and Lau, L. (1999). "Experimental investigation on bolted moment connections among cold formed steel members". *Engineering Structures,* 21**,** 898-911.

D'Aniello, M., Cassiano, D. and Landolfo, R. (2016). "Monotonic and cyclic inelastic tensile response of European preloadable gr10.9 bolt assemblies". *Journal of Constructional Steel Research,* 124**,** 77-90.

D'Aniello, M., Cassiano, D. and Landolfo, R. (2017a). "Simplified criteria for finite element modelling of European preloadable bolts". *Steel and Composite Structures, An International Journal,* 24**,** 643-658.

D'Aniello, M., Tartaglia, R., Costanzo, S. and Landolfo, R. (2017b). "Seismic design of extended stiffened end-plate joints in the framework of Eurocodes". *Journal of Constructional Steel Research,* 128**,** 512-527.

Dao, T. N. and Lindt, J. W. v. d. (2013). "Seismic Performance of an Innovative Light-Frame Cold-Formed Steel Frame for Midrise Construction". *Journal of Structural Engineering,* 139**,** 837-848.

Davies, J. M. (2000). "Recent research advances in cold-formed steel structures". *Journal of Constructional Steel Research,* 55**,** 267-288.

Deb, K. (2001). "Multi-objective optimization using evolutionary algorithms. Chichester: John Wiley and Sons, Inc.".

Degtyareva, N. V. and Degtyarev, V. V. (2016). "Experimental investigation of cold-formed steel channels with slotted webs in shear". *Thin-Walled Structures,* 102**,** 30-42.

Dinis, P. B., Batista, E. M., Camotim, D. and dos Santos, E. S. (2012). "Local–distortional–global interaction in lipped channel columns: Experimental results, numerical simulations and design considerations". *Thin-Walled Structures,* 61**,** 2-13.

Dinis, P. B. and Camotim, D. (2015). "Cold-formed steel columns undergoing local–distortional coupling: Behaviour and direct strength prediction against interactive failure". *Computers & Structures,* 147**,** 181-208.

Dinis, P. B., Camotim, D., Landesmann, A. and Martins, A. D. (2019). "On the direct strength method design of columns against global failures". *Thin-Walled Structures,* 139**,** 242-270.

Dubina D, Ungureanu V and Landolfo, R. 2012. *Design of cold-formed steel structures (Eurocode 3: Design of steel structures − Part 1-3: Design of cold-formed steel structures)* ECCS - Europian Convention for Constructional Steelwork.

Dubina, D., Stratan, A. and Nagy, Z. (2009). "Full-scale tests on cold-formed steel pitched-roof portal frames with bolted joints". *Advanced Steel Construction,* 5**,** 175-194.

Dubina, D. and Ungureanu, V. (2014). "Instability mode interaction: From Van Der Neut model to ECBL approach". *Thin-Walled Structures,* 81**,** 39-49.

Dundu, M. (2011). "Design approach of cold-formed steel portal frames". *International Journal of Steel Structures,* 11**,** 259.

Easterling, S. W. and Gonzalez, G. L. (1993). "Shear Lag Effects in Steel Tension Members". *Engineering Journal, American Institute of Steel Construction, Inc.,* 30**,** 77-89.

Elkersh, I. (2010). "Experimental investigation of bolted cold formed steel frame apex connections under pure moment". *Ain Shams Engineering Journal,* 1**,** 11-20.

Erbatur, F., Hasançebi, O., Tütüncü, İ. and Kılıç, H. (2000). "Optimal design of planar and space structures with genetic algorithms". *Computers & Structures,* 75**,** 209-224.

Erol, O. K. and Eksin, I. (2006). "A new optimization method: Big Bang–Big Crunch". *Advances in Engineering Software,* 37**,** 106-111.

FEMA-356 (2000). "Pre standard and commentary for the seismic rehabilitation of buildings. USA, Virginia: American Society Of Civil Engineers".

Fiorino, L., Iuorio, O. and Landolfo, R. (2014a). "Designing CFS structures: The new school bfs in naples". *Thin Wall Structures,* 78**,** 37-47.

Fiorino, L., Terracciano, M. T. and Landolfo, R. (2016). "Experimental investigation of seismic behaviour of low dissipative CFS strap-braced stud walls". *Journal of Constructional Steel Research,* 127**,** 92-107.

Fisher, J. W. 1964. On the Behavior of Fasteners and Plates with Holes. Fritz Engineering Laboratory, Department of Civil Engineering, Lehigh University.

Fülöp, L. A. and Dubina, D. (2004). "Performance of wall-stud cold-formed shear panels under monotonic and cyclic loading: Part I: Experimental research". *Thin-Walled Structures,* 42**,** 321-338.

Gad, E. F., Chandler, A. M., Duffield, C. F. and Hutchinson, G. L. (1999). "Earthquake ductility and overstreng thin residential structures". *Structural Engineering and Mechanics,* 8(4)**,** 361-82.

Galambos, T. V. (1968). "Structural Members and Frames". *Prentice-Hall Inc., Englewood Cliffs, NJ***,** 27-53.

Gao, W. C. and Xiao, Y. (2017). "Seismic behavior of cold-formed steel frame shear walls sheathed with ply-bamboo panels". *Journal of Constructional Steel Research,* 132**,** 217-229.

Gardner, L. and Ashraf, M. (2006). "Structural design for non-linear metallic materials". *Engineering Structures,* 28**,** 926-934.

Georgieva, I., Schueremans, L. and Pyl, L. (2012). "Composed columns from cold-formed steel Z-profiles: Experiments and code-based predictions of the overall compression capacity". *Engineering Structures,* 37**,** 125-134.

Gerald, F., T., A., Goodson, T. and Zsutty, M. (1989). "Slotted Bolted Connections in A seismic Design for Concentrically Braced Connections". *Earthquake Spectra,* 5**,** 383-391.

Gilbert, B. P. and Rasmussen, K. J. R. (2010). "Bolted moment connections in drive-in and drive-through steel storage racks". *Journal of Constructional Steel Research,* 66**,** 755-766.

Gilbert, B. P., Savoyat, T. J. M. and Teh, L. H. (2012a). "Self-shape optimisation application: Optimisation of cold-formed steel columns". *Thin-Walled Structures,* 60**,** 173-184.

Gilbert, B. P., Teh, L. H. and Guan, H. (2012b). "Self-shape optimisation principles: Optimisation of section capacity for thin-walled profiles". *Thin-Walled Structures,* 60**,** 194-204.

Goldberg, D. E. 1989. *Genetic algorithms in search, Optimization and machine learning*, Addison-Wesley.

Gonçalves, R., Ritto-Corrêa, M. and Camotim, D. (2010). "A new approach to the calculation of cross-section deformation modes in the framework of generalized beam theory". *Computational Mechanics,* 46**,** 759-781.

Gutierrez, R., Loureiro, A., Reinosa, J. M. and Lopez, M. (2015). "Numerical study of purlin joints with sleeve connections". *Thin-Walled Structures,* 94**,** 214-224.

Hadley Industries plc "P. O. B., Downing Street, Smethwick, West Midlands, B66 2PA, UK, "http://www.hadleygroup.co.uk/ URL." <http://www.hadleygroup.co.uk/ URL>".

Haidarali, M. R. and Nethercot, D. A. (2011a). "Finite element modelling of cold-formed steel beams under local buckling or combined local/distortional buckling". *Thin-Walled Structures,* 49**,** 1554-1562.

Hanaor, A. (2000). "Tests of composite beams with cold-formed sections". *Journal of Constructional Steel Research,* 54**,** 245-264.

Hancock, G. J. *Design of Cold-formed Steel Structures (to AS/NZ 4600:2007), 4th ed ., Australian Steel Institute, North Sydney, Australia, 2007*.

Hancock, G. J. and Pham, C. H. (2013). "Shear buckling of channel sections with simply supported ends using the Semi-Analytical Finite Strip Method". *Thin-Walled Structures,* 71**,** 72-80.

Hancock, G. J. and Pham, C. H. (2015). "Buckling analysis of thin-walled sections under localised loading using the semi-analytical finite strip method". *Thin-Walled Structures,* 86**,** 35-46.

Hasançebi, O. and Kazemzadeh Azad, S. (2012). "An exponential big bang-big crunch algorithm for discrete design optimization of steel frames". *Computers & Structures,* 110-111**,** 167-179.

Hassan, R., Cohanim, B., De Weck, O. and Venter, G. Year. A comparison of particle swarm optimization and the genetic algorithm. *In:* Proceedings of the 1st AIAA multidisciplinary design optimization specialist conference, 2005. 18-21.

He, Z. and Zhou, X. (2014). "Strength design curves and an effective width formula for cold-formed steel columns with distortional buckling". *Thin-Walled Structures,* 79**,** 62-70.

HMG (2013). "Construction 2025".

Holland, J. H. (1962). "Outline for a logical theory of adaptive systems". *Journal of ACM,* 9**,** 279-314.

Hong Pham, S., Hung Pham, C. and Hancock, G. J. (2014). "Direct strength method of design for shear including sections with longitudinal web stiffeners". *Thin-Walled Structures,* 81**,** 19-28.

Hsiao, L. E., Yu, W. W. and Galambos, T. V. (1988). "AISI LRFD method for cold-formed steel structural members". *9th Int. Specialty Conf. on Cold-Formed Steel Structures*.

Huang, Y. and Young, B. (2014). "Experimental investigation of cold-formed lean duplex stainless steel beam-columns". *Thin-Walled Structures,* 76**,** 105-117.

Jeong, S., Hasegawa, S., Shimoyama, K. and Obayashi, S. (2009). "Development and investigation of efficient GA/PSO-hybrid algorithm applicable to real-world design optimization". *Computational Intelligence Magazine, IEEE,* 4**,** 36-44.

Jia, L.-J., Koyama, T. and Kuwamura, H. (2013). "Prediction of cyclic large plasticity for prestrained structural steel using only tensile coupon tests". *Frontiers of Structural and Civil Engineering,* 7**,** 466-476.

Johnston, R. P. D., Lim, J. B. P., Lau, H. H., Xu, Y., Sonebi, M., Armstrong, C. G. and Mei, C. C. (2015a). "Finite-element investigation of cold-formed steel portal frames in fire". *Proceedings of the Institution of Civil Engineers-Structures and Buildings,* 169**,** 3-19.

Johnston, R. P. D., Sonebi, M., Lim, J. B. P., Armstrong, C. G., Wrzesien, A. M., Abdelal, G. and Hu, Y. (2015b). "The Collapse Behaviour of Cold-formed Steel Portal Frames at Elevated Temperatures. Journal of Structural Fire Engineering". *Journal of Structural Fire Engineering,* 6**,** 77-102.

Karim, A. and Adeli, H. (1999). "Global optimum design of cold-formed steel hat-shape beams". *Thin-Walled Structures,* 35**,** 275-288.

Kaveh, A. and Talatahari, S. (2009). "Size optimization of space trusses using Big Bang–Big Crunch algorithm". *Computers & Structures,* 87**,** 1129-1140.

Kennedy J and Eberhart R "Particle swarm optimization". *Neural Networks, 1995. Proceedings., IEEE International Conference on, IEEE, 1995, pp. 1942–1948.*

Kirk, P. (1986). "Design of a cold-formed section portal frame building system". *Proc. 8th International Speciality Conference on Cold-formed Steel Structures, St. Louis, MO, University of Missouri-Rolla; p.295.*

Koschmidder, D. M. and Brown, D. G. (2012). "Elastic design of single span steel portal frame buildings to Eurocode 3". *SCI Publication P397, Berkshire UK.*

Kulak, G. L. and Wu, E. Y. (1997). "Shear Lag in Bolted Angle Tension Members". *Journal of Structural Engineering,* 123**,** 1144-1152.

Kwon, Y. B., Kim, B. S. and Hancock, G. J. (2009). "Compression tests of high strength cold-formed steel channels with buckling interaction". *Journal of Constructional Steel Research,* 65**,** 278-289.

Kyvelou, P., Gardner, L. and Nethercot, D. A. (2015). "Composite Action Between ColdFormed Steel Beams and Wood-Based Floorboards". *International Journal of Structural Stability and Dynamics,* 15.

Kyvelou, P., Gardner, L. and Nethercot, D. A. (2017). "Design of Composite Cold-Formed Steel Flooring Systems". *Structures,* 12**,** 242-252.

Landesmann, A. and Camotim, D. (2013). "On the Direct Strength Method (DSM) design of cold-formed steel columns against distortional failure". *Thin-Walled Structures,* 67**,** 168-187.

Landesmann, A., Camotim, D. and Garcia, R. (2016). "On the strength and DSM design of cold-formed steel web/flange-stiffened lipped channel columns buckling and failing in distortional modes". *Thin-Walled Structures,* 105**,** 248-265.

Lawan, M., Tahir, M., Ngian, S. and Sulaiman, A. (2015). "Structural Performance of ColdFormed Steel Section in Composite Structures: A Review". *Jurnal Teknologi,* 74.

Lawson, R., Ogden, R., Pedreschi, R., Grubb, P. and Popo-Ola, S. (2005). "Developments in pre-fabricated systems in light steel and modular construction". *Structural Engineer,* 83**,** 28-35.

Lee, J., Kim, S. M., Park, H. S. and Woo, B. H. (2005). "Optimum design of cold-formed steel channel beams using micro-genetic algorithm". *Eng. Struct,* 27**,** 17–24.

Lee, J., Kim, S. M., Park, H. S. and Woo, B. H. (2006). "Optimum design of cold-formed steel columns by using micro genetic algorithms". *Thin-Walled Structures,* 44**,** 952–960.

Leng, J., Guest, J. K. and Schafer, B. W. (2011). "Shape optimization of cold-formed steel columns". *Thin-Walled Structures,* 49**,** 1492-1503.

Leng, J., Li, Z., Guest, J. K. and Schafer, B. W. (2014). "Shape optimization of cold-formed steel columns with fabrication and geometric end-use constraints". *Thin-Walled Structures,* 85**,** 271-290.

Li, Y., Shan, W., Shen, H., Zhang, Z.-W. and Liu, J. (2015). "Bending resistance of I-section bamboo–steel composite beams utilizing adhesive bonding". *Thin-Walled Structures,* 89**,** 17-24.

Li, Z. and Schafer, B. W. (2010). "Buckling analysis of cold-formed steel members with general boundary conditions using CUFSM conventional and constrained finite strip methods".

Lim, J. (2001). "Joint effects in cold-formed steel portal frames. University of Nottingham, PhD thesis".

Lim, J. B., Hancock, G. J., Clifton, G. C., Pham, C. H. and Das, R. (2016a). "DSM for ultimate strength of bolted moment-connections between cold-formed steel channel members". *Journal of Constructional Steel Research,* 117**,** 196-203.

Lim, J. B. P. and Nethercot, D. A. (2003b). "Ultimate strength of bolted moment-connections between cold-formed steel members". *Thin-Walled Structures,* 41**,** 1019-1039.

Lim, J. B. P. and Nethercot, D. A. (2004a). "Finite element idealization of a cold-formed steel portal frame". *Journal of Structural Engineering-ASCE,* 130**,** 78-94.

Lim, J. B. P. and Nethercot, D. A. (2004c). "Stiffness prediction for bolted moment-connections between cold-formed steel members". *Journal of Constructional Steel Research,* 60**,** 85-107.

Lin, S.-H., Pan, C.-L. and Hsu, W.-T. (2014). "Monotonic and cyclic loading tests for cold-formed steel wall frames sheathed with calcium silicate board". *Thin-Walled Structures,* 74**,** 49-58.

Liu, H., Igusa, T. and Schafer, B. W. (2004). "Knowledge-based global optimization of cold-formed steel columns". *Thin-Walled Structures,* 42**,** 785-801.

Liu, Q., Yang, J. and Wang, F. L. (2015). "Numerical simulation of sleeve connections for cold formed steel sigma sections". *Engineering Structures,* 100**,** 686-695.

Lui, W.-M., Ashraf, M. and Young, B. (2014). "Tests of cold-formed duplex stainless steel SHS beam–columns". *Engineering Structures,* 74**,** 111-121.

Lwin, K., Qu, R. and Kendall, G. (2014). "A learning-guided multi-objective evolutionary algorithm for constrained portfolio optimization". *Applied Soft Computing,* 24**,** 757-772.

Ma, W., Becque, J., Hajirasouliha, I. and Ye, J. (2015). "Cross-sectional optimization of cold-formed steel channels to Eurocode 3". *Engineering Structures,* 101**,** 641-651.

Madeira, J. F. A., Dias, J. and Silvestre, N. (2015). "Multiobjective optimization of cold-formed steel columns". *Thin-Walled Structures,* 96**,** 29-38.

Magnucki, K. and Paczos, P. (2009). "Theoretical shape optimization of cold-formed thin-walled channel beams with drop flanges in pure bending". *Journal of Constructional Steel Research,* 65**,** 1731-1737.

Magnucki, K., Rodak, M. and Lewiński, J. (2006). "Optimization of mono- and anti-symmetrical I-sections of cold-formed thin-walled beams". *Thin-Walled Structures,* 44**,** 832-836.

Mahendran, M. and Keerthan, P. (2013). "Experimental studies of the shear behavior and strength of LiteSteel beams with stiffened web openings". *Engineering Structures,* 49**,** 840-854.

Martins, A. D., Camotim, D. and Dinis, P. B. (2017a). "Behaviour and DSM design of stiffened lipped channel columns undergoing local-distortional interaction". *Journal of Constructional Steel Research,* 128**,** 99-118.

Martins, A. D., Camotim, D. and Dinis, P. B. (2017b). "Local-distortional interaction in cold-formed steel beams: Behaviour, strength and DSM design". *Thin-Walled Structures,* 119**,** 879-901.

Martins, A. D., Camotim, D. and Dinis, P. B. (2018). "On the distortional-global interaction in cold-formed steel columns: Relevance, post-buckling behaviour, strength and DSM design". *Journal of Constructional Steel Research,* 145**,** 449-470.

Mathworks 2011. Matlab R2011a. Mathworks, Inc.

Mathworks (2015). "Matlab R2015b". *Mathworks Inc.*

Matsubara, G. Y., Batista, E. d. M. and Salles, G. C. (2019). "Lipped channel cold-formed steel columns under local-distortional buckling mode interaction". *Thin-Walled Structures,* 137**,** 251-270.

McCrum, D. P., Simon, J., Grimes, M., Broderick, B. M., Lim, J. B. P. and Wrzesien, A. M. (2019). "Experimental cyclic performance of cold-formed steel bolted moment resisting frames". *Engineering Structures,* 181**,** 1-14.

McKinstray, R., Lim, J. B. P., Tanyimboh, T. T., Phan, D. T. and Sha, W. (2015). "Optimal design of long-span steel portal frames using fabricated beams". *Journal of Constructional Steel Research,* 104**,** 104-114.

Meza, F. J. (2018). "The Behaviour of Cold-Formed Steel Built-up Structural Members, PhD thesis, University of Sheffield".

Meza, F. J., Becque, J. and Hajirasouliha, I. (2019). "Experimental study of cold-formed steel built-up columns". *Thin-Walled Structures (in press).*

Miller, T. H. and Pekoz, T. (1994). "Behavior of Gypsum‐Sheathed Cold‐Formed Steel Wall Studs". *Journal of Structural Engineering,* 120**,** 1644-1650.

Moghimi, H. and Ronagh, H. R. (2009). "Performance of light-gauge cold-formed steel strap-braced stud walls subjected to cyclic loading". *Engineering Structures,* 31**,** 69-83.

Mohebbi, S., Mirghaderi, R., Farahbod, F. and Bagheri Sabbagh, A. (2015). "Experimental work on single and double-sided steel sheathed cold-formed steel shear walls for seismic actions". *Thin-Walled Structures,* 91**,** 50-62.

Mohebbi, S., Mirghaderi, S. R., Farahbod, F., Bagheri Sabbagh, A. and Torabian, S. (2016). "Experiments on seismic behaviour of steel sheathed cold-formed steel shear walls cladded by gypsum and fiber cement boards". *Thin-Walled Structures,* 104**,** 238-247.

Mohebkhah, A. and Azandariani, M. G. (2015). "Lateral–torsional buckling of Delta hollow flange beams under moment gradient". *Thin-Walled Structures,* 86**,** 167-173.

Mojtabaei, S. M., Kabir, M. Z., Hajirasouliha, I. and Kargar, M. (2018). "Analytical and experimental study on the seismic performance of cold-formed steel frames". *Journal of Constructional Steel Research,* 143**,** 18-31.

Mojtabaei, S. M., Ye, J. and Hajirasouliha, I. (2019b). "Development of optimum cold-formed steel beams for serviceability and ultimate limit states using Big Bang-Big Crunch optimisation". *Engineering Structures,* 195**,** 172-181.

Munse, W. H. and Chesson, E. J. (1963). "Riveted and bolted joints: net section design". *J. Struct. Div.,* 89(1)**,** 107-126.

Naderian, H. R. and Ronagh, H. R. (2015). "Buckling analysis of thin-walled cold-formed steel structural members using complex finite strip method". *Thin-Walled Structures,* 90**,** 74-83.

Nakata, N., Schafer, B. W. and Madsen, R. (2012). "Seismic Design of Multi-Story Cold-Formed Steel Buildings: The CFS-NEES Archetype Building". *Proc., Structures Congress 2012, ASCE***,** 1507-1517.

Nandini, P. and Kalyanaraman, V. (2010). "Strength of cold-formed lipped channel beams under interaction of local, distortional and lateral torsional buckling". *Thin-Walled Structures,* 48**,** 872-877.

Narayanan, S. and Mahendran, M. (2003). "Ultimate capacity of innovative cold-formed steel columns". *Journal of Constructional Steel Research,* 59**,** 489-508.

Nguyen, V. B., Pham, C. H., Cartwright, B. and English, M. A. (2017). "Design of new cold rolled purlins by experimental testing and Direct Strength Method". *Thin-Walled Structures,* 118**,** 105-112.

Nguyen, V. B., Wang, C. J., Mynors, D. J., English, M. A. and Castellucci, M. A. (2012). "Compression tests of cold-formed plain and dimpled steel columns". *Journal of Constructional Steel Research,* 69**,** 20-29.

Orbison James, G., Barth Karl, E. and Bartels Peter, A. (2002). "Net Section Rupture in Tension Members with Connection Eccentricity". *Journal of Structural Engineering,* 128**,** 976-985.

Öztürk, F. and Pul, S. (2015). "Experimental and numerical study on a full scale apex connection of cold-formed steel portal frames". *Thin-Walled Structures,* 94**,** 79-88.

Padilla-Llano, D. A., Eatherton, M. R. and Moen, C. D. (2016). "Cyclic flexural response and energy dissipation of cold-formed steel framing members". *Thin-Walled Structures,* 98**,** 518-532.

Padilla-Llano, D. A., Moen, C. D. and Eatherton, M. R. (2014). "Cyclic axial response and energy dissipation of cold-formed steel framing members". *Thin-Walled Structures,* 78**,** 95-107.

Pan, C.-L. and Shan, M.-Y. (2011). "Monotonic shear tests of cold-formed steel wall frames with sheathing". *Thin-Walled Structures,* 49**,** 363-370.

Parastesh, H., Hajirasouliha, I., Taji, H. and Bagheri Sabbagh, A. (2019). "Shape optimization of cold-formed steel beam-columns with practical and manufacturing constraints". *Journal of Constructional Steel Research,* 155**,** 249-259.

Park, R. (1989). "Evaluation of ductility of structures and structural assemblages from laboratory testing". *Bulletin of the New Zealand National Society for Earthquake Engineering,* 22(3)**,** 155–66.

Pastor, M. M., Casafont, M., Chillarón, E., Lusa, A., Roure, F. and Somalo, M. R. (2009). "Optimization of cold-formed steel pallet racking cross-sections for flexural–torsional buckling with constraints on the geometry". *Engineering Structures,* 31**,** 2711-2722.

Peng, J., Bendit, J. and Blum, H. B. (2018). "Experimental Study of Apex Connection Stiffness and Strength of Cold-Formed Steel Double Channel Portal Frames". *International Specialty Conference on Cold-Formed Steel Structures*.

Perera, N. and Mahendran, M. (2018). "Section moment capacity tests of hollow flange steel plate girders". *Journal of Constructional Steel Research,* 148**,** 97-111.

Perez, R. E. and Behdinan, K. (2007). "Particle swarm approach for structural design optimization". *Computers & Structures,* 85**,** 1579-1588.

Pezeshk, S., Camp, C. V. and Chen, D. (2000). "Design of Nonlinear Framed Structures Using Genetic Optimization". *Journal of Structural Engineering,* 126**,** 382-388.

Pham, C. H., Bruneau, L. A. and Hancock, G. J. (2015). "Experimental Study of Longitudinally Stiffened Web Channels Subjected to Combined Bending and Shear". *Journal of Structural Engineering,* 141**,** 04015018.

Pham, C. H., Davis, A. F. and Emmett, B. R. (2014). "Numerical investigation of cold-formed lapped Z purlins under combined bending and shear". *Journal of Constructional Steel Research,* 95**,** 116-125.

Pham, C. H. and Hancock, G. J. (2013). "Experimental Investigation and Direct Strength Design of High-Strength, Complex C-Sections in Pure Bending". *Journal of Structural Engineering,* 139**,** 1842-1852.

Pham, C. H. and Hancock, G. J. (2015). "Numerical investigation of longitudinally stiffened web channels predominantly in shear". *Thin-Walled Structures,* 86**,** 47-55.

Pham, S. H., Pham, C. H., Rogers, C. A. and Hancock, G. J. (2019). "Experimental validation of the Direct Strength Method for shear spans with high aspect ratios". *Journal of Constructional Steel Research,* 157**,** 143-150.

Phan, D. T., Lim, J. B. P., Meheron, S. J. and Lau, H. H. (2017a). "Design Optimization of Long-Span Cold-Formed Steel Portal Frames Accounting for Effect of Knee Brace Joint Configuration". *Technologies (MDPI),* 5(81)**,** 1-13.

Phan, D. T., Lim, J. B. P., Sha, W., Siew, C., Tanyimboh, T. T., Issa, K. H. and Mohammad, F. A. (2013a). "Design optimization of cold-formed steel portal frames taking into account the effect of topography". *Engineering Optimization,* 45**,** 415-433.

Phan, D. T., Lim, J. B. P., Tanyimboh, T. T., Lawson, R. M., Xu, Y., Martin, S. and Sha, W. (2013b). "Effect of serviceability limits on optimal design of steel portal frames". *Journal of Constructional Steel Research,* 86**,** 74-84.

Phan, D. T., Lim, J. B. P., Tanyimboh, T. T. and Sha, W. (2013c). "An efficient genetic algorithm for the design optimization of cold-formed steel portal frame buildings". *Steel and Composite Structures, An International Journal,* 15(5)**,** 519-538.

Phan, D. T., Lim, J. B. P., Tanyimboh, T. T. and Sha, W. (2017b). "Optimum design of cold-formed steel portal frame buildings including joint effects and secondary members". *International Journal of Steel Structures,* 17(2)**,** 427-442.

Phan, D. T., Lim, J. B. P., Tanyimboh, T. T., Wrzesien, A. M., Sha, W. and Lawson, R. M. (2015). "Optimal design of cold-formed steel portal frames for stressed-skin action using genetic algorithm". *Engineering Structures,* 93**,** 36-49.

Prayogo, D., Cheng, M.-Y., Wu, Y.-W., Herdany, A. A. and Prayogo, H. (2018). "Differential Big Bang - Big Crunch algorithm for construction-engineering design optimization". *Automation in Construction,* 85**,** 290-304.

Quach, W. M., Teng, J. G. and Chung, K. F. (2010). "Effect of the manufacturing process on the behaviour of press-braked thin-walled steel columns". *Engineering Structures, 32,* 3501-3515.

Rasmussen, K. J. R., Zhang, X. and Zhang, H. (2016). "Beam-element-based analysis of locally and/or distortionally buckled members: Theory". *Thin-Walled Structures, 98,* 285-292.

Reda, M., Sharaf, T., ElSabbagh, A. and ElGhandour, M. (2019). "Behavior and design for component and system of cold-formed steel roof trusses". *Thin-Walled Structures, 135,* 21-32.

Ren, C., Zhao, X. and Chen, Y. (2016). "Buckling behaviour of partially restrained cold-formed steel zed purlins subjected to transverse distributed uplift loading". *Engineering Structures, 114,* 14-24.

Rinchen and Rasmussen, K. J. R. (2019). "Behaviour and modelling of connections in cold-formed steel single C-section portal frames". *Thin-Walled Structures, 143,* 106233.

Roy, K., Ting, T. C. H., Lau, H. H. and Lim, J. B. P. (2018). "Nonlinear behavior of axially loaded back-to-back built-up cold-formed steel un-lipped channel sections". *Steel and composite structures International Journal, 28.*

Roy, K., Ting, T. C. H., Lau, H. H. and Lim, J. B. P. (2019). "Experimental and numerical investigations on the axial capacity of cold-formed steel built-up box sections". *Journal of Constructional Steel Research, 160,* 411-427.

Sabbagh, A. B., Mirghaderi, R., Petkovski, M. and Pilakoutas, K. (2010). "An integrated thin-walled steel skeleton structure (two full scale tests)". *Journal of Constructional Steel Research, 66,* 470-479.

Sabbagh, A. B., Petkovski, M., Pilakoutas, K. and Mirghaderi, R. (2012). "Experimental work on cold-formed steel elements for earthquake resilient moment frame buildings". *Engineering Structures, 42,* 371-386.

Sato, A. and Uang, C.-M. (2009). "Seismic design procedure development for cold-formed steel–special bolted moment frames". *Journal of Constructional Steel Research, 65,* 860-868.

Schafer, B. W. (2006). "CUFSM Version 3.12". *Department of Civil Engineering, Johns Hopkins University, http://www.ce.jhu.edu/bschafer/cufsm/.*

Schafer, B. W. (2008). "Review: The Direct Strength Method of cold-formed steel member design". *Journal of Constructional Steel Research,* 64**,** 766-778.

Schafer, B. W. (2019). "Advances in the Direct Strength Method of cold-formed steel design". *Thin-Walled Structures,* 140**,** 533-541.

Schafer, B. W., Ayhan, D., Leng, J., Liu, P., Padilla-Llano, D., Peterman, K. D., Stehman, M., Buonopane, S. G., Eatherton, M., Madsen, R., Manley, B., Moen, C. D., Nakata, N., Rogers, C. and Yu, C. (2016). "Seismic Response and Engineering of Cold-formed Steel Framed Buildings". *Structures,* 8, Part 2**,** 197-212.

Schafer, B. W. and Peköz, T. (1998). "Computational modeling of cold-formed steel: characterizing geometric imperfections and residual stresses". *Journal of Constructional Steel Research,* 47**,** 193-210.

SCI Advisory Desk (2010). "AD-090: Deflection limits for pitched roof portal frames (Amended)". *Ascot: The Steel Construction Institute*.

Seaburg, P. A. and Salmon, C. G. (1971). "Minimum weight design of light gage steel members". *Journal of the Structural Division,* 97**,** 203-222.

SEI/ASCE-8-02 (2002). "Specifications for the design of cold-formed stainless steel structural members ". *American Society of Civil Engineers (ASCE)*.

Serrette, R. L., Encalada, J., Juadines, M. and Nguyen, H. (1997). "Static Racking Behavior of Plywood, OSB, Gypsum, and FiberBond Walls with Metal Framing". *Journal of Structural Engineering,* 123**,** 1079-1086.

Serror, M. H., Hassan, E. M. and Mourad, S. A. (2016b). "Experimental study on the rotation capacity of cold-formed steel beams". *Journal of Constructional Steel Research,* 121**,** 216-228.

Shahini, M., Bagheri Sabbagh, A., Davidson, P. and Mirghaderi, R. (2018). "Cold-Formed Steel Bolted Moment-Resisting Connections with Friction-Slip Mechanism for Seismic Areas. CCFSS , St. Louis, MO.".

Shamim, I., DaBreo, J. and Rogers, C. A. (2013). "Dynamic Testing of Single- and Double-Story Steel-Sheathed Cold-Formed Steel-Framed Shear Walls". *Journal of Structural Engineering,* 139**,** 807-817.

Sharafi, P., Teh, L. H. and Hadi, M. N. S. (2014). "Shape optimization of thin-walled steel sections using graph theory and ACO algorithm". *Journal of Constructional Steel Research,* 101**,** 331-341.

Shifferaw, Y. and Schafer, B. W. (2012). "Inelastic Bending Capacity of Cold-Formed Steel Members". *Journal of Structural Engineering,* 138**,** 468-480.

Shifferaw, Y. and Schafer, B. W. (2014). "Cold-formed steel lipped and plain angle columns with fixed ends". *Thin-Walled Structures,* 80**,** 142-152.

Siahaan, R., Keerthan, P. and Mahendran, M. (2018). "Lateral distortional buckling of rivet fastened rectangular hollow flange channel beams". *Journal of Constructional Steel Research,* 144**,** 295-309.

Simões da Silva, L., Simoes, R. and Gervasio, H. (2010). "Design of Steel Structures, Eurocode 3: Design of Steel Structures, Part 1-1: General rules and rules for buildings, Ernst & Sohn - A Wiley Company". *ECCS Eurocode Design Manuals*.

Tartaglia, R., D'Aniello, M., Rassati, G. A., Swanson, J. A. and Landolfo, R. (2018). "Full strength extended stiffened end-plate joints: AISC vs recent European design criteria". *Engineering Structures,* 159**,** 155-171.

Teh, L. H. and Yazici, V. (2013). "Shear lag and eccentricity effects of bolted connections in cold-formed steel sections". *Engineering Structures,* 52**,** 536-544.

Teh Lip, H. and Clements Drew, D. A. (2012). "Tension Capacity of Staggered Bolted Connections in Cold-Reduced Steel Sheets". *Journal of Structural Engineering,* 138**,** 769-776.

Teh Lip, H. and Gilbert Benoit, P. (2012). "Net Section Tension Capacity of Bolted Connections in Cold-Reduced Steel Sheets". *Journal of Structural Engineering,* 138**,** 337-344.

Teh Lip, H. and Gilbert Benoit, P. (2013a). "Net Section Tension Capacity of Cold-Reduced Sheet Steel Angle Braces Bolted at One Leg". *Journal of Structural Engineering,* 139**,** 328-337.

Teh Lip, H. and Gilbert Benoit, P. (2013b). "Net Section Tension Capacity of Cold-Reduced Sheet Steel Channel Braces Bolted at the Web". *Journal of Structural Engineering,* 139**,** 740-747.

Tian, Y. S. and Lu, T. J. (2004). "Minimum weight of cold-formed steel sections under compression". *Thin-Walled Structures,* 42**,** 515-532.

Ting, T. C. H., Roy, K., Lau, H. H. and Lim, J. B. P. (2017). "Effect of screw spacing on behavior of axialy loaded back-to-back cold-formed steel built-up channel sections". *Adv. Struct. Eng.,* 21**,** 474-487.

Torabian, S., Fratamico, D. C. and Schafer, B. W. (2016). "Experimental response of cold-formed steel Zee-section beam-columns". *Thin-Walled Structures,* 98**,** 496-517.

Torabian, S., Zheng, B. and Schafer, B. W. (2015). "Experimental response of cold-formed steel lipped channel beam-columns". *Thin-Walled Structures,* 89**,** 152-168.

Tran, T. and Li, L.-y. (2006). "Global optimization of cold-formed steel channel sections". *Thin-Walled Structures,* 44**,** 399-406.

Tsang, K. S., Ion, W., Blackwell, P. and English, M. (2018). "Industrial validation of strain in cold roll forming of UHSS". *Procedia Manufacturing,* 15**,** 788-795.

Tshuma, B. and Dundu, M. (2017). "Internal eaves connections of double-bay cold-formed steel portal frames". *Thin-Walled Structures,* 119**,** 760-769.

Uang, C. M. (1991). "Establishing R (or Rw) and Cd factors for building seismic provisions". *Journal of Structural Engineering,* 117(1)**,** 19–28.

Uang, C. M., Sato, A., Hong, J. K. and Wood, K. (2010). "Cyclic Testing and Modeling of Cold-Formed Steel Special Bolted Moment Frame Connections". *Journal of Structural Engineering-Asce,* 136**,** 953-960.

Ungermann, D., Brune, B. and Lübke, S. (2012). "Numerical and analytical investigations on plain channels in coupled instabilities". *Steel Construction,* 5**,** 205-211.

VijayaVengadesh Kumar, J. and Arul Jayachandran, S. (2016). "Experimental investigation and evaluation of Direct Strength Method on beam-column behavior of uprights". *Thin-Walled Structures,* 102**,** 165-179.

Von Karman, T., Sechler, E. E. and Donnell, L. (1932). "The strength of thin plates in compression". *Trans. ASME,* 54**,** 53-57.

Walker, A. C. 1975. *Design and analysis of cold-formed sections*, Halsted Press.

Wang, B., Bosco, G. L., Gilbert, B. P., Guan, H. and Teh, L. H. (2016a). "Unconstrained shape optimisation of singly-symmetric and open cold-formed steel beams and beam-columns". *Thin-Walled Structures,* 104**,** 54-61.

Wang, B., Gilbert, B. P., Guan, H. and Teh, L. H. (2016b). "Shape optimisation of manufacturable and usable cold-formed steel singly-symmetric and open columns". *Thin-Walled Structures,* 109**,** 271-284.

Wang, B., Gilbert, B. P., Molinier, A. M., Guan, H. and Teh, L. H. (2016c). "Shape optimisation of cold-formed steel columns with manufacturing constraints using the Hough transform". *Thin-Walled Structures,* 106**,** 75-92.

Wang, C., Zhang, Z., Zhao, D. and Liu, Q. (2016d). "Compression tests and numerical analysis of web-stiffened channels with complex edge stiffeners". *Journal of Constructional Steel Research,* 116**,** 29-39.

Wang, H., Yan, Y., Wan, M. and Wu, X. (2012). "Experimental investigation and constitutive modeling for the hardening behavior of 5754O aluminum alloy sheet under two-stage loading". *International Journal of Solids and Structures,* 49**,** 3693-3710.

Wang, L. and Young, B. (2016a). "Behavior of Cold-Formed Steel Built-Up Sections with Intermediate Stiffeners under Bending. I: Tests and Numerical Validation". *Journal of Structural Engineering,* 142**,** 04015150.

Wang, L. and Young, B. (2016b). "Behavior of Cold-Formed Steel Built-Up Sections with Intermediate Stiffeners under Bending. II: Parametric Study and Design". *Journal of Structural Engineering,* 142**,** 04015151.

Wang, X. and Ye, J. (2016). "Cyclic testing of two- and three-story CFS shear-walls with reinforced end studs". *Journal of Constructional Steel Research,* 121**,** 13-28.

Wanniarachchi, K. S. and Mahendran, M. (2017). "Experimental study of the section moment capacity of cold-formed and screw-fastened rectangular hollow flange beams". *Thin-Walled Structures,* 119**,** 499-509.

Way, A. G. J. and Lawson, R. M. (2013). "Design and installation of light steel external wall systems". *SCI Guide ED-017*.

Weng, C. C. and Pekoz, T. (1990). "Residual Stresses in Cold‐Formed Steel Members". *Journal of Structural Engineering,* 116**,** 1611-1625.

Wijesundara, K. K., Nascimbene, R. and Sullivan, T. J. (2011). "Equivalent viscous damping for steel concentrically braced frame structures". *Bulletin of Earthquake Engineering,* 9**,** 1535-15558.

Williams, L. W. 2016. 1 - Introduction to recent trends in cold-formed steel construction A2 - Yu, Cheng. *Recent Trends in Cold-Formed Steel Construction.* Woodhead Publishing.

Wong, M. F. and Chung, K. F. (2002). "Structural behaviour of bolted moment connections in cold-formed steel beam-column sub-frames". *Journal of Constructional Steel Research,* 58**,** 253-274.

Wreszien, A., Lim, J. B. P. and Nethercot, D. A. (2012). "Optimum joint detail for a general cold-formed steel portal frame, Advances in Structural Engineering". *Advances in Structural Engineering,* 15**,** 1623-1639.

Wrzesien, A. M., Phan, D. T., Lim, J. B. P., Lau, H. H., Hajirasouliha, I. and Tan, C. S. (2016). "Effect of stressed-skin action on optimal design of cold-formed steel square and rectangular-shaped portal frame buildings". *International Journal of Steel Structures,* 16(2)**,** 299-307.

Xingyou, Y., Yanli, G. and Yuanqi, L. (2016). "Effective width method for distortional buckling design of cold-formed lipped channel sections". *Thin-Walled Structures,* 109**,** 344-351.

Xu, Z., Chen, Z., Osman, B. H. and Yang, S. (2018). "Seismic performance of high-strength lightweight foamed concrete-filled cold-formed steel shear walls". *Journal of Constructional Steel Research,* 143**,** 148-161.

Yan, J. and Young, B. (2002). "Column Tests of Cold-Formed Steel Channels with Complex Stiffeners". *Journal of Structural Engineering,* 128**,** 737-745.

Yang, N., Zhong, Y. n., Meng, Q. t. and Zhang, H. (2014). "Hysteretic behaviors of cold-formed steel beam-columns with hollow rectangular section: Experimental and numerical simulations". *Thin-Walled Structures,* 80**,** 217-230.

Yao, Y., Quach, W.-M. and Young, B. (2019). "Finite element-based method for residual stresses and plastic strains in cold-formed steel hollow sections". *Engineering Structures,* 188**,** 24-42.

Ye, J. (2016). "More efficient cold-formed steel elements and bolted connections, PhD thesis, University of Sheffield".

Ye, J., Becque, J., Hajirasouliha, I., Mojtabaei, S. M. and Lim, J. B. P. (2018a). "Development of optimum cold-formed steel sections for maximum energy dissipation in uniaxial bending". *Engineering Structures,* 161**,** 55-67.

Ye, J., Hajirasouliha, I. and Becque, J. (2018b). "Experimental investigation of local-flexural interactive buckling of cold-formed steel channel columns". *Thin-Walled Structures,* 125**,** 245-258.

Ye, J., Hajirasouliha, I., Becque, J. and Eslami, A. (2016a). "Optimum design of cold-formed steel beams using Particle Swarm Optimisation method". *Journal of Constructional Steel Research,* 122**,** 80-93.

Ye, J., Hajirasouliha, I., Becque, J. and Pilakoutas, K. (2016b). "Development of more efficient cold-formed steel channel sections in bending". *Thin-Walled Structures,* 101**,** 1-13.

Ye, J., Meza, F. J., Hajirasouliha, I., Becque, J., Shepherd, P. and Pilakoutas, K. (2019a). "Experimental Investigation of Cross-Sectional Bending Capacity of Cold-Formed Steel Channels Subject to Local-Distortional Buckling Interaction". *Journal of Structural Engineering,* 145**,** 04019064.

Ye, J., Mojtabaei, S. M. and Hajirasouliha, I. (2018c). "Local-flexural interactive buckling of standard and optimised cold-formed steel columns". *Journal of Constructional Steel Research,* 144**,** 106-118.

Ye, J., Mojtabaei, S. M. and Hajirasouliha, I. (2019b). "Seismic performance of cold-formed steel bolted moment connections with bolting friction-slip mechanism". *Journal of Constructional Steel Research,* 156**,** 122-136.

Ye, J., Mojtabaei, S. M., Hajirasouliha, I. and Pilakoutas, K. (2019c). "Efficient design of cold-formed steel bolted-moment connections for earthquake resistant frames". *Thin-Walled Structures*.

Ye, J., Mojtabaei, S. M., Hajirasouliha, I., Shepherd, P. and Pilakoutas, K. (2018d). "Strength and deflection behaviour of cold-formed steel back-to-back channels". *Engineering Structures,* 177**,** 641-654.

Ye, J., Wang, X., Jia, H. and Zhao, M. (2015). "Cyclic performance of cold-formed steel shear walls sheathed with double-layer wallboards on both sides". *Thin-Walled Structures,* 92**,** 146-159.

Ye, J., Wang, X. and Zhao, M. (2016c). "Experimental study on shear behavior of screw connections in CFS sheathing". *Journal of Constructional Steel Research,* 121**,** 1-12.

Yeniay, O. (2005). "Penalty function methods for constrained optimization with genetic algorithms. ". *Mathematical and Computational Applications,* 10(1)**,** 45-56.

Yin, L., Tang, G., Zhang, M., Wang, B. and Feng, B. (2016). "Monotonic and cyclic response of speed-lock connections with bolts in storage racks". *Engineering Structures,* 116**,** 40-55.

Young, B. (2008). "Research on cold-formed steel columns". *Thin-Walled Structures,* 46**,** 731-740.

Young, B. and Hancock, G. (2001). "Design of Cold-Formed Channels Subjected to Web Crippling". *J. Struct. Eng.,* 127(10)**,** 1137-1144.

Yu, C. and Schafer, B. W. (2007). "Simulation of cold-formed steel beams in local and distortional buckling with applications to the direct strength method". *Journal of Constructional Steel Research,* 63**,** 581-590.

Yu, C. and Xu, K. (2013). "Shear Strength of a Cold-Formed Steel Sheet in Bolted Connections Using Oversized Holes". *Journal of Structural Engineering,* 139**,** 860-864.

Yu, C. and Yan, W. (2011). "Effective Width Method for determining distortional buckling strength of cold-formed steel flexural C and Z sections". *Thin-Walled Structures,* 49**,** 233-238.

Yu, W.-W. and LaBoube, R. A. 2010. *Cold-formed steel design*, John Wiley & Sons.

Yu, W. K., Chung, K. F. and Wong, M. F. (2005). "Analysis of bolted moment connections in cold-formed steel beam–column sub-frames". *Journal of Constructional Steel Research,* 61**,** 1332-1352.

Zaharia, R. and Dubina, D. (2006). "Stiffness of joints in bolted connected cold-formed steel trusses". *Journal of Constructional Steel Research,* 62**,** 240-249.

Zeynalian, M., Ronagh, H. R. and Hatami, S. (2012). "Seismic characteristics of K-braced cold-formed steel shear walls". *Journal of Constructional Steel Research,* 77**,** 23-31.

Zeynalian, M., Shelley, A. and Ronagh, H. R. (2016). "An experimental study into the capacity of cold-formed steel truss connections". *Journal of Constructional Steel Research,* 127**,** 176-186.

Zhang, J.-H. and Young, B. (2012). "Compression tests of cold-formed steel I-shaped open sections with edge and web stiffeners". *Thin-Walled Structures,* 52**,** 1-11.

Zhang, X., Rasmussen, K. J. R. and Zhang, H. (2015). "Beam-element-based analysis of locally and/or distortionally buckled members: Application". *Thin-Walled Structures,* 95**,** 127-137.

Zhang, X., Rasmussen, K. J. R. and Zhang, H. (2016a). "Experimental investigation of locally and distortionally buckled portal frames". *Journal of Constructional Steel Research,* 122**,** 571-583.

Zhang, X., Rasmussen, K. J. R. and Zhang, H. (2016b). "Second-order effects in locally and/or distortionally buckled frames and design based on beam element analysis". *Journal of Constructional Steel Research,* 122**,** 57-69.

Zheng, B., Hua, X. and Shu, G. (2015). "Tests of cold-formed and welded stainless steel beam-columns". *Journal of Constructional Steel Research,* 111**,** 1-10.

Zhou, X., Zhao, Y., Liu, J., Chen, Y. F. and Yang, Y. (2019). "Bending experiment on a novel configuration of cold-formed U-shaped steel-concrete composite beams". *Engineering Structures,* 180**,** 124-133.